TAMPEREEN TEKNILLINEN YLIOPISTO
TAMPERE UNIVERSITY OF TECHNOLOGY

Jouko Hintikka

Fretting Induced Friction, Wear and Fatigue in Quenched and Tempered Steel

Julkaisu 1392 • Publication 1392

Tampere 2016

Tampereen teknillinen yliopisto. Julkaisu 1392
Tampere University of Technology. Publication 1392

Jouko Hintikka

Fretting Induced Friction, Wear and Fatigue in Quenched and Tempered Steel

Thesis for the degree of Doctor of Science in Technology to be presented with due permission for public examination and criticism in Konetalo Building, Auditorium K1702, at Tampere University of Technology, on the 27th of June 2016, at 12 noon.

Tampereen teknillinen yliopisto - Tampere University of Technology
Tampere 2016

ISBN 978-952-15-3766-0 (printed)
ISBN 978-952-15-3780-6 (PDF)
ISSN 1459-2045

Abstract

Fretting stands for reciprocating surface sliding with a typical sliding amplitude of a few tens of micrometres and a potential outcome of fretting fatigue and fretting wear. Fretting efficiently nucleates surface cracks, which may then continue to grow under cyclic loads and may ultimately lead to fretting fatigue failure. Uncertainties about fretting-induced surface degradation, wear, and frictional behaviour make the design of highly loaded contacts a challenging task.

This thesis aims to improve the understanding of fretting wear, fretting fatigue, and especially fretting-induced frictional behaviour. Fretting experiments were conducted with a pre-existing sphere-on-plane fretting apparatus and with an annular flat-on-flat fretting apparatus, the latter designed and built from scratch. Quenched and tempered steel specimens were fretted against themselves and against aluminium bronze.

Frictional behaviour was dominated by so-called non-Coulomb friction, which was related to initial adhesive wear damage and material transfer, which again led to a formation of tangentially interlocked protrusions and depressions and inclined sliding conditions. In the long run, the wear behaviour changed, because the interface started to fill up with entrapped loose wear debris, which reduced further wear via velocity accommodation mechanisms.

Fretting fatigue cracking of quenched and tempered steel occurred mostly near the gross sliding threshold. Analysis of loading conditions revealed that quenched and tempered steel was especially susceptible to cracking when fretted against aluminium bronze, which was explained by the pronounced formation of tangentially interlocked protrusion and depressions even in partial slip conditions. Individual tangentially interlocked protrusions and depressions were under a much greater cyclic load that what was predicted by nominal contact stresses, enabling crack initiation even though nominal fatigue stresses were below the fatigue limit.

Preface

This thesis was done at Tampere University of Technology (TUT) between the spring 2010 and May 2016. I did the work in the Tribology and Machine Elements research group, supervised by Professor Arto Lehtovaara. The work was initiated in the department of Mechanics and Design (2010-2012), which changed its name to Department of Engineering Design (2013), followed by the departure of the research group to the department of Materials Science (2014-), where this thesis was finalized. I would like to express my thanks to Professor Lehtovaara for his support and guidance.

Fretting studies begun at TUT in 2004 in the form of the Frefa1 research project (Fretting fatigue in diesel engineering), initiated by Wärtsilä Finland Oy. Since then, fretting research has continued at TUT, and I began my studies in the Frefa2 (2009-2010) research project, which was supported by Wärtsilä Finland Oy, Metso Paper Oy, and Tekes (Finnish Funding Agency for Innovation). After Frefa2, I continued fretting research in the Freda research project (Fretting damage in mechanical engineering, 2010-2013), which was sponsored by Wärtsilä, Metso Paper Oy, and Tekes. The project was part of the Demanding Applications Programme (DEMAPP), organized by Finnish Metals and Engineering Competence Cluster (FIMECC). The Freda project was followed by the SCarFace research project (Short crack and fretting fatigue damage in mechanical engineering, 2013-2015). It was financed by Tekes, Wärtsilä Finland Oy, Nome Oy, and Global Boiler Works Oy. The thesis was finalized during the ongoing MaNuMiEs-project (Manufacturing, Numerics, and Micromechanics in Engineering sciences, 2016-2018), financed by Tekes, Wärtsilä Finland Oy, AGCO Power Oy and Global Boiler Works Oy. I would like to thank all the financial supporters of the Frefa2, Freda, SCarFace and MaNuMiEs projects that enabled my work and especially Wärtsilä Finland Oy for their long term interest in fretting research at TUT.

I am grateful to PhD Roger Rabb, MSc Christian Lönnqvist, MSc Antti Mäntylä, and PhD Juho Könnö from Wärtsilä Finland Oy for their co-operation in this fretting research. I would also like to thank Lic. Tech. Olli Nuutila and PhD Juha Miettinen for their guidance on measurements and instrumentation and, in addition, MSc. Jouko Meriläinen for his contribution to designing and assembling a new fretting apparatus and MSc. Atte Hokkanen for helping with the experiments.

Tampere 27.05. 2016

Jouko Hintikka

Contents

Symbols and Abbreviations

Latin symbols

a	[m]	Radius of Hertzian point contact
A	[-]	Energy ratio ($A=E_d/E_t$)
A_{real}	[m^2]	Real contact area
c	[m]	Radius of stick region in partial slip
COF	[-]	Coefficient of friction
COF_{max}	[-]	Maximum COF during load cycle (μ_{max})
COF_{max_a}	[-]	Calculated COF_{max}
COF_{mean}	[-]	Mean COF during load cycle (μ_{mean})
COF_{min}	[-]	Minimum COF during load cycle (μ_{mean})
COF_T	[-]	Maximum COF during load cycle
d_F	[-]	Findley damage criterion
E_c	[Pa]	Combined modulus of elasticity
E_d	[J]	Frictional energy dissipation
E_t	[J]	Total energy
f_{Fr}	[Pa]	Shear fatigue limit
FCR	[-]	Findley cracking risk
G	[Pa]	Shear modulus
H	[Pa]	Hardness
k	[µm/N]	Specimen compliance in sphere-on-plane apparatus
k	[rad/Nm]	Specimen compliance in annular flat-on-flat apparatus
k_A	[-]	Archard wear coefficient
k_{Fr}	[-]	Constant in Findley criterion
k_S	[-]	Statistical size factor
$p(r)$	[Pa]	Hertzian normal pressure distribution
p_0	[Pa]	Maximum Hertzian normal pressure
P	[N]	Normal force
Q	[N]	Tangential force
Q_a	[N]	Tangential force amplitude
r	[m]	Radius
r_i	[m]	Inner radius
r_o	[m]	Outer radius
R_c	[m]	Combined radius
R_{QP}	[-]	$R_{QP}=Q_a/(\mu \times P)$
Sa	[m]	3D surface roughness (corresponds to Ra)
Su	[Pa]	Ultimate stress
T	[Nm]	Torque
u	[m]	Sliding
u_a	[m]	Sliding amplitude
W_A	[m^3/m]	Archard wear rate
W_{Cle}	[kg]	Wear mass loss due to each contact cleaning
W_{LC}	[kg]	Wear mass loss due to load cycles
x, y, z	[m]	x, y, z- coordinate and –displacement

Greek symbols

α	[deg]	Angle of gradient
α_{eff}	[deg]	Effective angle of gradient
d	[m]	Tangential displacement
d_a	[m]	Tangential displacement amplitude
d_k	[m]	Corrected tangential displacement
d_m	[m]	Measured tangential displacement
Δz	[m]	z-displacement range during load cycle (z_{max}-z_{min})
ΔCOF	[-]	Magnitude of non-Coulomb COF (COF_T-COF_{Ed})
τ_a	[Pa]	Shear stress amplitude
$\tau(r)$	[Pa]	Shear traction in sliding areas
$\tau_{stick}(r)$	[Pa]	Shear traction in sticking areas
φ	[rad]	Rotation
φ_a	[rad]	Rotation amplitude
φ_k	[rad]	Corrected rotation
φ_m	[rad]	Measured rotation
σ_n	[Pa]	Shear plane normal stress
ΣE_d	[J]	Accumulated frictional energy dissipation
Σu	[m]	Accumulated surface sliding
μ_{max}	[-]	Maximum COF during load cycle (COF_{max})
μ_{mean}	[-]	Mean COF during load cycle (COF_{mean})
μ_{min}	[-]	Minimum COF during load cycle (COF_{min})
ν	[-]	Poisson's ratio

List of abbreviations

Cle	Contact cleaning test series
COF	Coefficient of friction
FCR	Findley cracking risk
FEM	Finite element method
Gro	Test series with grooved specimens
Sta	Standard test series

Subscripts

max	Maximum
mean	Mean
min	Minimum

List of Publications

I. J Hintikka, A Lehtovaara, C Lönnqvist, “Effect of start-up schemes and amplitude of tangential motion on friction behavior in fretting point contact”, Tribol.Int. 44 (2011) 1535-1543. doi:10.1016/j.triboint.2010.10.015

II. J Hintikka, A Lehtovaara, A Mäntylä, ”Fretting fatigue and friction of quenched and tempered steel in dry contact with aluminum bronze”, Wear. 308 (2013) 155-165. doi:10.1016/j.wear.2013.07.002

III. J Hintikka, A Lehtovaara, A Mäntylä, “Non-Coulomb friction in gross sliding fretting conditions with aluminium bronze against quenched and tempered steel”, Tribol.Int. 79 (2014) 151-161. doi:10.1016/j.triboint.2014.06.004

IV. J Hintikka, A Lehtovaara, A Mäntylä, “Fretting-induced friction and wear in large flat-on-flat contact with quenched and tempered steel”, Tribol.Int. 92 (2015) 191-202. doi:10.1016/j.triboint.2015.06.008

V. J Hintikka, A Lehtovaara, A Mäntylä, “Normal displacements in non-Coulomb friction conditions during fretting”, Tribol.Int. 94 (2016) 633–639. doi:10.1016/j.triboint.2015.10.029

VI. J Hintikka, A Lehtovaara, A Mäntylä, ”Third particle ejection effects on wear with quenched and tempered steel fretting contact”, Tribology Transactions, Accepted for publication, doi:10.1080/10402004.2016.1146813

Author’s contribution

Authors’ role in publications: Jouko Hintikka was the main author in all publications and his role comprised pre-test activities, planning and carrying out experiments, post-test analysis, and publication writing. Prof. Lehtovaara was the second author in all publications and he supervised the work, participated in experiment planning and contributed to publication writing. In publication I, MSc. Lönnqvist was the third authors and he participated in planning experiments, reading the manuscript, and giving comments. In publications II – VI, MSc. Mäntylä was the third author and he participated in planning experiments, reading the manuscript, and giving comments.

Publication I: As stated in Authors’ role in publications.

Publication II: As stated in Authors’ role in publications. Additionally, SEM imaging and EDS data were provided by the chief laboratory technician Kati Mökkönen.

Publication III: As stated in Authors’ role in publications.

Publication IV: As stated in Authors’ role in publications. Also, Jouko Hintikka’s role comprised the layout design of a new annular flat-on-flat fretting apparatus, the completion of its design and instrumentation, and the bringing of the apparatus online. Prof. Lehtovaara and MSc. Mäntylä participated in designing the annular flat-on-flat apparatus. MSc. Meriläinen did detailed design and drawings of the new annular flat-on-flat apparatus, assembled it, and participated in bringing it online. MSc. Hokkanen carried out some of experiments and weighed specimens.

Publication V: As stated in Authors’ role in publications. Additionally, MSc. Hokkanen carried out some of the experiments.

Publication VI: As stated in Authors’ role in publications. MSc. Hokkanen carried out some of the experiments, MSc. Ville Oksanen did SEM imaging and provided EDS data, and MSc. Leo Hyvärinen performed X-ray diffractometry measurements.

1 Introduction

1.1 Basics of friction, wear and fatigue

1.1.1 From ancient times to the Renaissance

Tribology was defined in the 1966 Jost report as a science and technology relating to interacting surfaces under relative motion, including topics such as friction, wear, and lubrication. However, the individual topics derive from further back in history. Some early evidence of a deliberate exploitation of tribological processes, such as friction and wear, was stone age fire kindling by reciprocating rubbing of pieces of wood. Development of tools quickly led to tribological advances aimed at controlling friction and wear, such as the use of bitumen as a lubricant in the potter's wheel in 3250 B.C and bronze nail studding to reduce the wear of the chariot wheel rim in 2700 B.C. The first written account acknowledging friction was by Aristotle in the 4th century B.C. During the Renaissance in the 15th century, Leonardo da Vinci studied many aspects of tribology, including friction, wear, and bearings. Da Vinci was the first to discover the basic "laws" of friction, that is, that friction is proportional to the normal load and that it is independent of the apparent contact area dictated by the dimensions of the contacting bodies. However, Da Vinci's discoveries remained unpublished during his time. [1]

1.1.2 Friction

The friction laws were rediscovered later by Guillaume Amontons, who in the 17th century studied the static friction necessary to initiate sliding. In the 18th century, Charles Augustin de Coulomb extended the study of friction to cover kinetic friction. Both Amontons and Coulomb explained that friction originates from the interlocking of surface protrusions and depressions (initial surface roughness), an explanation which has its limitations.

The classic friction laws are as follows:

1. The friction force is directly proportional to the applied normal load (Amontons).
2. The friction force is independent of the apparent contact area (Amontons).
3. Kinetic friction is independent of the sliding velocity (Coulomb).

Furthermore, the proportion between the friction force *Q* and the normal load *P* was often measured to be approximately constant, the so-called coefficient of friction (COF). The friction force may be described as follows:

$$Q = COF' \ P \tag{1}$$

Since then, different sources have been identified for friction, such as the ploughing term (the 1920s), where hard asperity ploughs softer material [1]. Another source of friction was adhesive friction, described in the 1950s by Bowden et al, who combined the concept of a real contact area and the shear strength of asperity junctions in a way that COF could be calculated from the shear strength and the hardness of the weaker material (COF ~ 0,2). Higher COFs were explained by the adhesive friction theory, accompanied by shear-force-driven growth of a plastic asperity junction leading to an increased real contact area. [2,3]

1.1.3 Wear

At the beginning of the 19th century, Hatchett studied the wearing down of gold coins and discovered that the amount of mass loss was inversely proportional to the hardness of the material. Starting in the 1940s, Holm studied wear in electrical contacts and established a linear relation between sliding distance and wear volume [1]. In the 1950s, Archard proposed a law for adhesive wear rate (Eq. 2) which is still widely used [4]. The wear law is based on the concept of a real contact area, formed by fully plastic asperity tip contacts, and that the shearing of asperity tip junctions produce hemispherical, or 'lumpy', wear particles with a certain probability. In Eq. 2 P is normal load, H is hardness and k_A is the Archard wear coefficient, representing the probability of wear particle formation which is determined experimentally.

$$W_A = k_A' \, P / H \tag{2}$$

According to Dowson, there are two type classifications for wear, the first describing rather the results of wear and the type of loading and the second the fundamental physical wear mechanisms. Terms such as fretting, pitting, and scoring were given as examples of descriptive wear types; however, the second type of wear was preferred with its five different acknowledged wear mechanisms: abrasion, adhesion, fatigue, erosion, and corrosion [1]. Stachowiak [5] and Sarkar [6] included fretting wear in their list of different wear mechanisms or types of wear. Although fretting wear has been described as including different fundamental wear mechanisms, such as adhesive wear, abrasion, and corrosion, it has been categorized as both descriptively wear and on a par with other fundamental wear mechanisms.

1.1.4 Metal fatigue

The 19th century became acquainted with metal fatigue, partly due to developments in steam engines and transportation resulting in occasional catastrophic failures of moving components with loss of profits and even life at times. This motivated pioneering work on failures under cyclic loads. The first documented experiments under cyclic loads were done in the 1840s, yet the term 'fatigue' to describe failure under such conditions was coined in the 1850s. In the 1850s and 1860s, August Wöhler studied extensively the fatigue failures of railway car axles and demonstrated that stress amplitudes lower than the material's static strength could lead to component failure. Furthermore, he showed that the fatigue life of a component depends on cyclic and mean stresses, and that component life could be designed to be finite or infinite. Since then the study of fatigue has progressed vastly and branched into metallurgical description of fatigue based on dislocation theory and fracture mechanics, focused the growth of cracks and brittle fractures. [7,8]

1.2 Fretting

Fretting is small-amplitude, reciprocating sliding motion between contacting surfaces. Fretting action leads to fretting damage, such as fretting wear, fretting corrosion, and fretting fatigue. Components prone to fretting are, for example, bearing backs, couplings, and joints [9].

Depending on loading, contact geometry, and its compliance, fretting may occur in certain regions of the interface while the rest remains stuck. Also the whole interface may experience fretting. Such conditions are called 'partial slip' and 'gross sliding', respectively. The term 'mixed slip' is used for partial slip conditions changing to gross sliding or vice versa. The terms partial slip, mixed-slip, and gross sliding are called fretting regimes [10], and they define the running-condition of the fretting contact [11].

Tangential force vs tangential displacement forms a closed loop during one fretting cycle, and it is commonly called the fretting loop [12].

1.2.1 Towards fretting testing

In his book *Fretting Corrosion*, R. B. Waterhouse summarized the first pioneering decades of fretting research [9]. Fretting wear was first reported in 1911 by Eden, Rose, and Cunningham, who observed that in a plain fatigue test, oxide wear particles were produced as a by-product of the fixture of a test specimen and its holder. However, in 1927, Tomlinson was the first to run deliberate fretting experiments, using ball-on-flat contact geometry to show that an oscillatory slip is required to produce oxide wear debris. Since then, basically two breeds of fretting apparatuses have been developed with increasing levels of fidelity to study the fretting phenomenon. [9,13]

The first plain fretting apparatuses began to emerge in the 1930s, 40s, and 50s following Tomlinson's first tests in the 1920s [9]. These apparatuses may be categorized by their contact configurations, some of which have retained their popularity up to recent years, such as the rotating annular flat-on-flat contact [14,15], sphere-on-plane contact [16-20], crossed cylinders [10,21], and cylinder-on-flat contact [22,23]. These apparatuses have been especially suitable for measuring fretting wear and friction, but they are also capable of measuring fretting fatigue crack initiation.

The second type of fretting experiments was done using the so-called fretting fatigue apparatuses. The early designs were based on rotating-bending and push-pull fatigue machines, in which plain fatigue conditions were enhanced with a bridge-type fretting contact [9]. These apparatuses were used to study the effects of fretting contact on specimen fatigue performance. Although variants of the early, bridge-type, fretting fatigue apparatuses remain in use [24-26], current popular designs are based on the push-pull fatigue rig, where fretting contact is generated by sandwiching the specimen between two pads (often cylinders) fixed to a carriage. The carriage may be firmly attached to the apparatus frame, or it may supported by springs, and a tangential force is caused by specimen elastic deformation and the compliance of the apparatus [27-29]. Another method is to use a separate actuator to a generate fretting motion, thereby to allow independent control of plain fatigue loading and tangential forces [30,31].

1.2.2 Fretting wear

Hurricks [32] and Waterhouse [9] identified three fretting wear processes: (1) the mechanical wear of naturally occurring oxide films and the oxidation of any exposed 'clean' metal; (2) the rubbing of clean surfaces, which promotes removal of metallic particles from surfaces via adhesive wear and leads to metallic material transfer; and (3) adhesive wear, which in later stages gradually decreases and changes to abrasive 3-body wear due to the entrapment of oxide wear particles forming an intermediate layer. The severity of abrasive wear depends on the difference in properties between the oxides and the bulk metal. Sauger et al showed that the source of wear particles is so-called tribologically transformed structure, which is highly work hardened layer at the contact interface [33].

The classic Archard wear formalism predicts that wear volume is linearly dependent on the normal force, sliding distance, and hardness of the material [4]. Pearson et al pointed out that the determination of fretting wear coefficient should be based on the actual surface sliding rather than the tangential displacement [34]. The measured tangential displacement may include elastic deformations and additionally the sliding may have a distribution of values inside the contact, hence the sliding is not necessarily determined easily. Recently, the so-called 'energy wear' approach, originally introduced by Mohrbacher et al [35], has shown promising results and has gained some traction among fretting researchers [36,37]. In the energy wear approach, material loss due to wear is assumed to be linearly dependent on accumulated

frictional energy dissipation, E_d. Its main advantage over the classic Archard wear equation is its capability to include the effect of COF variations which may occur in time and position. Furthermore, frictional energy dissipation is conveniently obtained from measured fretting loops, without determining surface sliding.

According to Berthier et al, under fretting conditions, the wear rate depends on the rate of wear particle ejection rather than wear particle generation, because rubbing or velocity accommodation within the entrapped third bodies does not produce new wear particles [38,39]. Coulombié et al illustrated that wear particles tend to get entrapped in a contact that provides a load carrying capacity that separates the first bodies, enables additional velocity accommodation mechanisms, and leads to a reduced wear rate [40]. Diomidis et al run fretting experiments using sphere-on-plane contact, with small contact and large sliding amplitude [41]. They concluded that the wear rate follows the classic Archard wear law and is independent of third body behaviour. However, Merhej et al studied the effect of contact size on the fretting wear rate using sphere-on-plane contact and showed that the larger the contact, the lower the wear rate, which they explained by the tendency of larger contacts maintaining a thicker third body than smaller contacts [42]. Warmuth et al performed a similar study using a cylinder-on-plane contact and obtained similar results. They suggested that contact geometry affects the flow of wear debris out of the contact [43].

1.2.3 Friction in fretting

Godfrey et al reported the COF behaviour of copper-copper, copper-glass, and copper-steel contacts, showing that the COF increased rapidly to ~1.5 during the first few load cycles, followed by a reduction and stabilization to a value of approximately 0.6 within ~100 load cycles. Consequently, the COF was characterized by the initial friction peak [17]. Similar initial peaking and gradual reduction and stabilization of COF were reported for a stainless steel contact [44], quenched and tempered steel [26], and 12%-Cr steel [45]. Leidich et al reported COF values of up to 1.7 with quenched and tempered steel in fretting contact with chromium alloy steel [14]. It is often reported that the COF increases during the first load cycles and stabilizes to a value in the range of 0.6 - 1.0, without a peaking COF [46-48]. COF values and stabilization times depend on the materials and other test conditions. For example, Pearson et al carried out fretting tests with high strength alloy steel (SCMV) and showed that steady state COF reduced from 0.8 to 0.5 when ambient temperature was increased from 25 °C to 200 °C [23]. Mohrbacher et al fretted bearing steel against TiN coated hardened high speed steel and showed that the value of COF was near unity when relative humidity was low (10 %); however, when the relative humidity was high (80 %) the resulting COF was dramatically lower [49].

Analysis of fretting loops has shown that the friction force does not necessarily remain at a constant value during the gross sliding phase of a fretting cycle, and many studies have shown that the force increases gradually when the fretting movement approaches its extreme positions [15,21,37,44,50,51]. In such so-called non-Coulomb friction conditions, the value of the COF depends on how it is calculated. In such conditions (Eq. 3), an energy-COF is frequently used and calculated from the frictional energy dissipation E_d, normal load P, and the sliding amplitude u_a, representing the mean COF during a fretting cycle [37,44,51]:

$$COF_{mean} = E_d / (4 \cdot P \cdot u_a) \tag{3}$$

Non-Coulomb friction has been explained by mechanical interlocking in the tangential direction; however, the scale on which the interlocking has been observed differs. ‘Macroscopic’ interlocking was reported to occur when a fretting pad ploughed a trench in the specimen due to the specimen’s plastic deformation [37] or wear [44,51], and as such its occurrence was strongly dependent on the type of the contact and

load levels. A second kind of explanation was given by Mulvihill et al, who showed that the non-Coulomb phenomenon can originate from tangentially interlocked protrusions and depressions within the interface [15]. Such 'microscopic' interlocking describes a tribologically significant process, independent of specimen geometry. They also modelled the effect of tangential fretting scar interaction on the total friction force by assuming that the interactions led to inclined sliding conditions.

Halliday et al reported COF behaviour for mild steel contact, where the COF rapidly increased to approximately 0.7, followed by a gradual reduction to the very low value of 0.05. The low COF was explained by accumulation of wear debris, which enabled pieces of wear debris to roll to and fro instead of sliding, leading thus to rolling friction [22]. Although such low COF values are uncommon, there has been further evidence that entrapped wear debris affects the value of the COF. Merhej et al studied the effect of contact size on friction with a sphere-on-plane, steel-steel contact by keeping the maximum surface pressure at a constant by varying the sphere radius [42]. They showed that the steady state COF depended on contact size so that increasing the contact radius from 0.122 mm to 0.754 mm reduced the COF from 0.8 to 0.5, which was also explained by velocity accommodation via entrapped third bodies. Additionally, Mohrbacher et al acknowledged that observed development of the COF and wear rate in fretting are affected by a velocity accommodation mechanism [35].

1.2.4 Fretting fatigue

Fretting fatigue is perhaps the most severe form of fretting damage, because fatigue failures in general are notorious for causing unexpected and sometimes catastrophic failures. In fretting, crack initiation and early crack growth occur in the confinements of the interface, which is out of sight and thus may go unnoticed even under scheduled maintenance, unless the contact is opened. Fretting can be detected from the appearance of oxide fretting wear debris, which in the case of iron metals is fine-textured, reddish-brown powder.

Waterhouse summarized early fretting fatigue research and observed that failures nucleated at the edges of the contact, where the stresses were the highest, inside the contact near a stick-slip boundary, where tangential traction was the highest, and also at the adhesive cold weld junctions. Fretting fatigue was tested by combining plain fatigue conditions with fretting, which enables production of SN-curves (Wöhler curves) under combined fretting and fatigue conditions. Overall, Waterhouse described fretting as having a detrimental effect on fatigue performance similar to that of notches or corrosion. [9]

According to Hills et al [52], in addition to cyclic bulk stresses, accurate estimation of contact stresses is necessary to fully analyse fretting fatigue loading conditions. Incomplete contacts, such as Hertzian cylinder-on-plane contacts, are often preferred to complete contacts, because the resulting stress fields avoid singularities. Fatigue failure typically initiates from pre-existing flaws in the material; however in fretting, the contact stresses can be so high as to nucleate fatigue cracks without such flaws. Fretting is described as being very efficient in producing surface cracks, which may continue to grow under cyclic bulk stresses. Rigorous analysis of contact tractions and stresses is necessary to properly estimate fatigue life; however, the effects of sliding are not well understood.

Complex fatigue loading can be analysed with multiaxial fatigue models. There are basically two kinds of multiaxial models: some are based on the equivalent stress approach, such as the von Mises stress, and others on the critical plane approach [53]. Various critical plane-multiaxial models, such as the Findley damage criterion, have been used to evaluate fretting fatigue loading conditions [31,37,54-56]. The Findley damage criterion has been proved reliable for analysis of multiaxial plain fatigue conditions [53]. Additionally, it has produced consistent results with different fretting contacts [56] and has been recommended for fatigue analysis of fretting conditions [55]. Utilization of advanced multiaxial fatigue criteria, combined with careful analysis of contact stresses, enables design against fatigue crack nucleation.

Fretting fatigue conditions are often closely analogous to notch fatigue, and as such are characterized by steep stress gradients, which can lead to significant size effects, as small contacts tend to withstand higher fatigue loads than large contacts [57]. The theory of critical distances can be used to analyse the severity of fatigue loading, which is characterized by a steep stress gradient [58]. Basically, the stresses used in fatigue analysis are extracted at a certain distance from the stress concentrator, or alternatively they may be averaged over a certain length, area, or volume around the stress concentrator. These methods are called point method, line method, area method, and volume method, respectively. For example, the volume method has been used to determine the critical length in fretting fatigue experiments [37] and the point method, successfully, to analyse fretting fatigue conditions [59]. Fracture mechanics approach allows damage tolerant design of components, where small cracks are allowed to nucleate.

1.2.5 Fretting maps

Vingsbo studied fretting conditions using a crossed cylinders test set-up and showed that the severity of surface cracking depends on the displacement amplitude. Fretting-induced cracking increases when the tangential displacement amplitude is increased in partial slip conditions ($Q<\mu \times P$). However, increasing the displacement amplitude in gross sliding conditions alleviated fretting-induced cracking. Basically, in partial slip or stick conditions, contact stresses increase if the tangential displacement amplitude is increased, whereas in gross sliding they remains more or less at a constant, regardless of the size of the displacement amplitude. The reduction in fretting-induced cracking under gross sliding conditions was explained by the increasing wear rate, which gradually exceeded the rate of crack nucleation and growth. Figure 1A illustrates schematically Vingsbo's fretting fatigue map, where fatigue life plummets dramatically when the displacement amplitude approaches the gross sliding threshold and increases sharply when the displacement amplitude is greater than the gross sliding threshold. Simultaneously, wear is low in the partial slip regime and increases sharply as a function of the displacement amplitude in the gross sliding regime. [10]

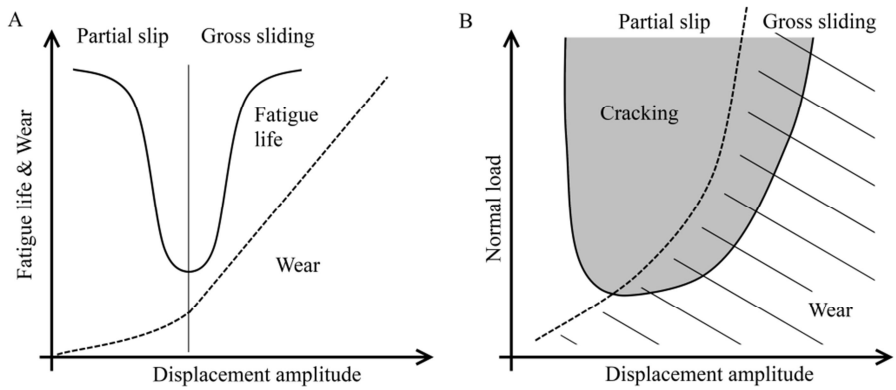

Figure 1 – Schematic illustrations of (A) Vingsbo's fretting life map and (B) material response fretting map with Hertzian point or line contact.

Fretting maps, which were originally introduced by Vingsbo [10] and reviewed by Zhou [11], are a useful tool for post-test analysis, because they allow graphic illustration of results as a function of multiple parameters. Such a tool helps to cope with a large number of variables that influence fretting conditions, such as COF, normal pressure, tangential force, sliding amplitude, atmosphere, contact size, and material pair. Frequently, in fretting maps, the ordinate is the normal load, and the abscissa may vary depending on the type of fretting map. The so-called 'running condition fretting map' is a plot of test points as a func-

tion of the tangential displacement amplitude and normal load, and the symbols in the graph indicate whether the running-condition was stick, partial slip, mixed slip, or gross sliding. The so-called 'material response fretting map' is built on the running condition fretting map so that the symbols indicate the type of fretting damage, such as slight wear, cracking, and particle detachment. Figure 1B shows an example of a material response fretting map, illustrating that certain normal load and displacement amplitude combinations can lead to specimen cracking and/or wear. The version of the material response fretting map where the abscissa is replaced with fatigue stress or some other fatigue parameter is called the fretting fatigue map.

1.3 The aim of the study

1.3.1 Motivation

The demand to improve machine performance, for example, the efficiency and power density of heavy duty combustion engines, means that components must withstand higher cyclic loads without unnecessarily increasing their size and/or mass. This can be achieved by exploiting the material's fatigue strength to a high degree and by using high fatigue strength materials, such as quenched and tempered steel. Design against plain fatigue load can be done reliably, assuming that loads and material fatigue properties are known. However, gaining correspondingly good reliability for highly loaded contacts, susceptible to fretting, is a much more demanding task. Compared to plain fatigue conditions, fretting can effectively accelerate crack initiation, and so far only a limited amount of literature is available on the fretting fatigue performance of quenched and tempered steel. Although pioneering fretting researchers studied steels, over the recent decades focus has shifted to aeronautical alloys, such as aluminium and titanium. The designer is not necessarily sure of what COF should be used when dimensioning contacts. Cyclic loads or vibrations may introduce fretting loading, whose severity is affected significantly by the value of the COF. A high COF leads to potentially high tangential tractions, which may significantly contribute to near surface stresses, which promote fretting fatigue, whereas a low COF may lead to considerable slip and fretting wear. In any case, such conditions may occur in large, highly loaded contacts with some slip to them, whereas stresses near the contact remain below the fatigue limit. The designer must know the effect of such fretting conditions on the contact and overall fatigue performance. Most reliably, data on COF and overall fretting performance can be obtained by tailored experiments under laboratory conditions.

1.3.2 Aims and scope

This thesis is part of a research project with the ultimate goal to develop constitutive "fretting models" that could be used to evaluate the risk and severity of fretting damage in industrial-scale contacts by using common dimensioning tools, such as the FEM. The thesis aims to further understand the phenomenon of fretting in quenched and tempered steel, and its main focus is to study friction and especially the so-called non-Coulomb friction and related adhesive wear damage. Also studied was fretting fatigue cracking in steel specimens. These objectives led to the formulation of the following research questions:

1. What kind of frictional behaviour and friction mechanisms exist in the fretting contact of quenched and tempered steel?
2. What kind of material response does the fretting contact of quenched and tempered steel have, and what are its driving mechanisms?

Fretting experiments were conducted with quenched and tempered steel in contact with itself and in contact with aluminium bronze. Fretting was tested with a pre-existing sphere-on-plane fretting apparatus and with an annular flat-on-flat fretting apparatus designed and built from scratch. The first step was to char-

acterize and develop descriptive models of frictional behaviour and material response for steel under fretting conditions, based on experimental evidence. Constitutive models can be developed once these aspects are sufficiently understood.

1.3.3 Outline and scientific contribution

The thesis is composed of four chapters: 1 Introduction, 2 Methods, 3 Results and Discussion and 4 Conclusions. The first chapter begins with a literature review on tribology and fretting, followed by the motivation, aims and scope, outline, and scientific contribution of the thesis.

The second chapter describes the materials and methods used in this study. Experiments were run with two different fretting test rigs, sphere-on-plane and annular flat-on-flat apparatuses. The design and instrumentation of these apparatuses and the test procedures are explained. Additionally, the most important equations are shown, and the tools for post-test analysis are described. Lastly, the end of chapter two describes each test series and covers the materials, surface finishes, test matrixes, and measurement schemes.

The main results of the thesis are compiled in the third chapter, which is divided into sections on fretting wear, friction, and fretting fatigue. The chapter starts with wear results and deals mostly with adhesive wear damage. A significant part of the thesis is about the characterization of frictional behaviour, especially non-Coulomb friction. The observed non-Coulomb friction phenomenon is described, and different measurement schemes were used to study the mechanics behind it. Lastly, chapter three shows and discusses the fretting fatigue results.

The conclusions and summary of this work are given in the chapter 4.

The main scientific contribution of this thesis can be summarized as follows:

a) Development of an advanced annular flat-on-flat fretting apparatus with on-the-run, clearance free, adjustable alignment.
b) Characterization of the frictional behaviour, fretting wear, and fretting fatigue performance of quenched and tempered steel in fretting contact with itself and in that with aluminium bronze, based on experimental evidence.
c) Improvement of the fundamental knowledge of the non-Coulomb friction phenomenon, the role of tangential fretting scar interactions, and adhesive wear damage during the initial stages of fretting.

2 Methods

2.1 Sphere-on-plane apparatus

2.1.1 Apparatus design

A sphere-on-plane fretting apparatus [19] was used to study friction and fretting fatigue in publications I, II, and III. The sphere-on-plane contact and the design of the apparatus are shown schematically in Figure 2. In tribological tests, the Herzian point contact (Figure 2A) is convenient, because analytical solutions are available for normal and tangential traction distributions, slip and subsurface stresses, and easy alignment [52]. Loading a sphere against a plane with a normal load P gives a circular contact with a radius a. Friction resists the tangential displacement d between the sphere and the plane, resulting in the tangential force Q. A well-defined partial slip occurs if the tangential force is below the gross sliding threshold value ($Q<\mu \times P$). In partial slip, the outer annulus of the contact exhibits slip while the centre remains stuck. The size of the sticking region ($-c \ldots c$) shrinks, when the tangential force increases, and finally disappear ($c=0$) when gross sliding commences ($Q=\mu \times P$).

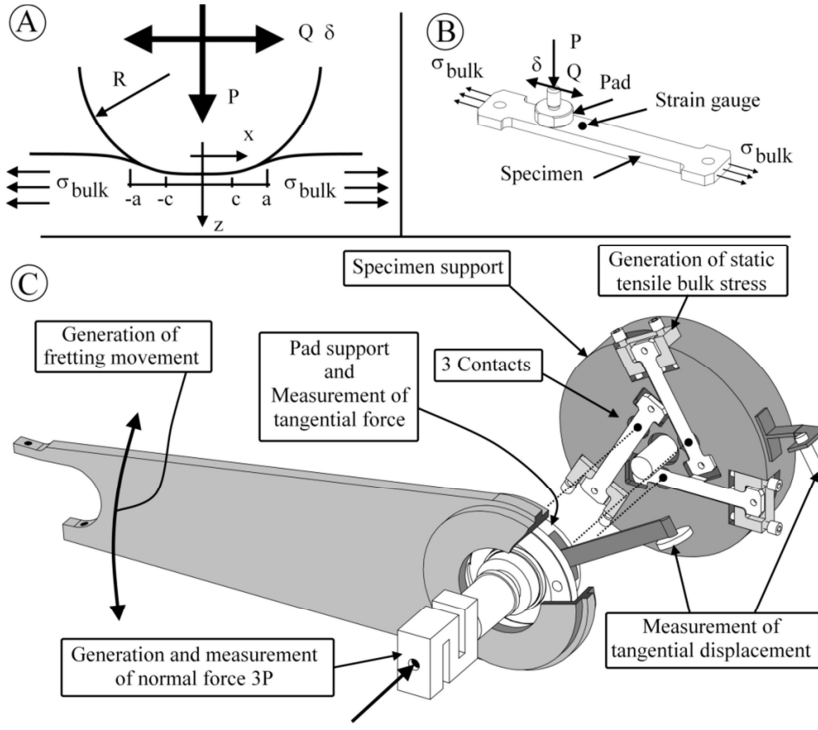

Figure 2 - Sphere-on-plane test device. [Publication II]

In the apparatus, the pad (sphere) was loaded against the specimen (plane), and three symmetrically positioned contacts were run simultaneously (Figure 2B&C). In addition to contact stresses, the specimen was under a constant tensile bulk stress s_{bulk}, which was applied with screws and measured with a strain gauge. A normal load was generated with a hydraulic cylinder and measured with an s-beam load cell. Tangential displacement was generated with an electric shaker via reciprocating rotation of the lever arm and

measured between the specimen and pad supports using an eddy current probe. The control system used measured displacement data as a feedback signal, and the experiments were run under displacement amplitude control. The tangential force was measured from the pad support with strain gauges. A combined normal load of $3\times P$ and a tangential force of $3\times Q$ were measured and assumed equal for all three contacts.

A standard test procedure was to run the apparatus at a frequency of 40 Hz for 2.8×10^6 load cycles in monitored laboratory atmosphere. The experiment was started in a controlled manner so that the displacement amplitude was gradually increased from zero to the target level within 5000 load cycles. After the start-up phase, the measured displacement amplitude was kept at a predefined constant value. The static bulk stress in the specimens was 400 MPa. Before and after each test, the specimens and pads were cleaned with acetone using an ultrasonic washing device.

2.1.2 Analysis of contact conditions

The radius of the Hertzian point contact a, the maximum pressure p_0, and the normal pressure distribution $p(r)$ can be solved using Eqs. 4, 5, and 6, respectively. R_c and E_c are the combined radius and modulus of elasticity, respectively. Under gross sliding conditions, the tangential traction distribution (Eq. 7) is simply the product of normal pressure distribution and COF. [60]

$$a = \sqrt[3]{(3 \cdot P \cdot R_c)/(4 \cdot E_c)} \tag{4}$$

$$p_0 = (3 \cdot P)/(2 \cdot \pi \cdot a^2) \tag{5}$$

$$p(r) = p_0 \cdot \sqrt{1 - r^2/a^2} \tag{6}$$

$$t(r) = COF \cdot p(r) \tag{7}$$

Mindlin equations can be used to solve the radius of the central stick zone (Eq. 8) and the tangential traction distribution (Eq. 9) in partial slip conditions [61]. In the slipping annulus, the tangential traction distribution follows Eq.7; however, in the central stick region it corresponds to $t_{stick}(r)$ in Eq. 9, taking into account the effect of the stick.

$$c = a \cdot \sqrt[3]{1 - Q/(COF \cdot P)} \tag{8}$$

$$t_{stick}(r) = COF \cdot p_0 \cdot \left(\sqrt{1 - r^2/a^2} - \frac{c}{a} \cdot \sqrt{1 - r^2/c^2} \right) \tag{9}$$

The tangential displacement δ can be solved using Eq. 10, where G is the shear modulus and ν is Poisson's ratio. Due to finite specimen and pad dimensions of the measured tangential displacement δ_m is greater than what Eq. 10 predicts. This was corrected using Eq. 11, where k is the extra specimen and pad compliance.

$$\delta = \frac{3 \cdot COF \cdot P}{16 \cdot a} \cdot \left(\frac{2 - \nu_1}{G_1} + \frac{2 - \nu_2}{G_2} \right) \cdot \left(1 - \left(1 - \frac{Q}{COF \cdot P}\right)^{(2/3)}\right) \tag{10}$$

$$\delta_k = \delta_m - k \cdot Q \tag{11}$$

In gross sliding conditions, the calculation of COF is straightforward (Eq. 1); however, in partial slip, the so-called energy ratio method can be used [62], based on the Mindlin solution [61]. The energy ratio A is the ratio between the frictional energy dissipation E_d and the total energy E_t, and both can be determined from a measured fretting loop (Q-d_k-plot). The energy ratio has an analytical equation (Eq. 12), from which the COF can be solved ($R_{QP}=Q_a/(COF\times P)$):

$$A=\frac{E_d}{E_t}=\frac{6}{5}\cdot\frac{1-\left(1-R_{QP}\right)^{(5/3)}-\frac{5}{6}\cdot R_{QP}\cdot\left(1+\left(1-R_{QP}\right)^{(2/3)}\right)}{R_{QP}\cdot\left(1-\left(1-R_{QP}\right)^{(2/3)}\right)} \tag{12}$$

Conveniently, the stress field under a frictional sliding Hertzian point contact can be solved analytically with Hamilton's equations [63]. The Hamilton solution is applicable under gross sliding conditions; however, it can be extended to cover partial slip conditions simply by superposing two solutions, which correspond to full gross sliding minus the effect of the stick zone [12].

2.1.3 Multiaxial Findley criterion and size effect

Fatigue loading was estimated using the multiaxial Findley damage criterion d_F. According to Findley, fatigue damage occurs at a critical plane, where the shear stress amplitude combined with normal stress is the highest. The Findley criterion is shown in Eq. 13, where τ_a is the shear stress amplitude, σ_n is the normal stress on the shear plane, k_{Fr} is the Finley criteria constant, and f_{Fr} is the shear fatigue limit. Fatigue failure is to be expected if $d_F \geq 1$. [64]

$$d_F=\max((\tau_a(t)+k_{Fr}\cdot\sigma_n(t)/f_{Fr}) \tag{13}$$

Initially, engineering materials are filled with microscopic, various size flaws. Fatigue failure starts from such a pre-existing flaw on the specimen surface. The statistical size factor enables estimation of a specimen's fatigue strength by using a stochastic approach to calculate the largest expected defect size in a highly stressed region on the specimen surface, and it conveniently takes into account the effect of size and notch size on fatigue strength [65,66]. The Findley damage criterion was enhanced with the statistical size factor k_s, and the parameter was named the Finley cracking risk (*FCR*), as shown in Eq. 14:

$$FCR=d_F/k_S \tag{14}$$

An in-house numerical calculation tool was developed by Lehtovaara et al [67], based on Eqs. 4-14, and it was used to analyse the sphere-on-plane experiment data in this study.

2.1.4 Estimation of fatigue load

In addition to elastic moduli and other material parameters, measured values of normal load, tangential force amplitude, COF, and tensile bulk stress were used as input values. Figure 3 illustrates the normal and tangential traction distributions, in partial slip and gross sliding conditions, in the centre line of the contact, parallel to the fretting direction ($x=\pm a$ and $y=z=0$). The maximum *FCR* (and d_F) exists on the surface of the specimen at the crossing of the contact edge and the contact centre line, and it was used for further analysis.

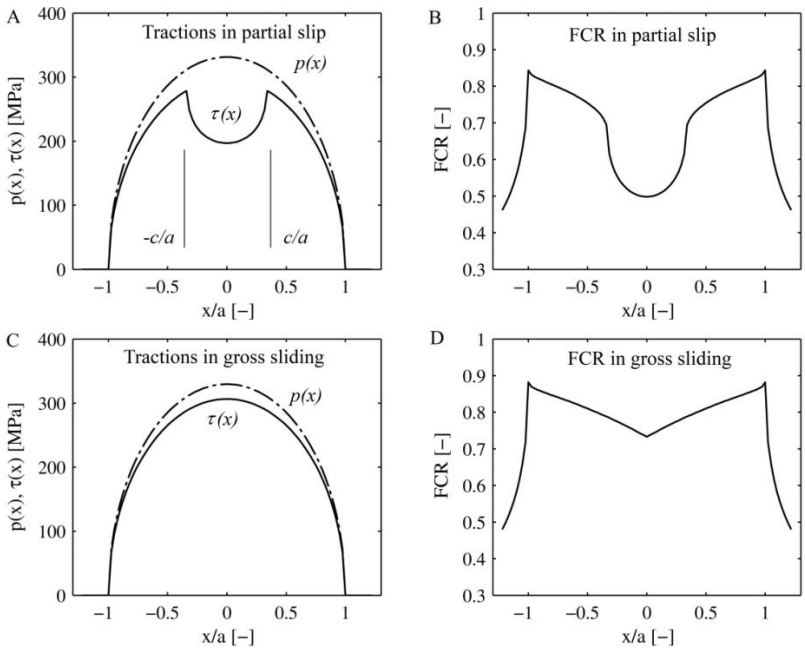

Figure 3 – Normal and tangential traction distributions and the resulting Findley cracking risk (FCR) in partial slip (A and B) and gross sliding (C and D).

Fretting fatigue maps can be constructed using the methods illustrated previously. Figure 4 shows such fretting fatigue map showing maximum d_F (Eq. 13) contours, extracted from the edge of the sphere-on-plane contact ($\pm a$ and $y=z=0$), in a tangential displacement amplitude vs normal load graph. Fatigue crack nucleation is expected when $d_F > 1$. In the partial slip regime the contour lines are nearly vertical, indicating that the d_F is fairly insensitive to normal load. However, d_F is sensitive to tangential displacement amplitude (and tangential force amplitude). In gross sliding d_F is independent of the tangential displacement amplitude but is dependent on the normal load.

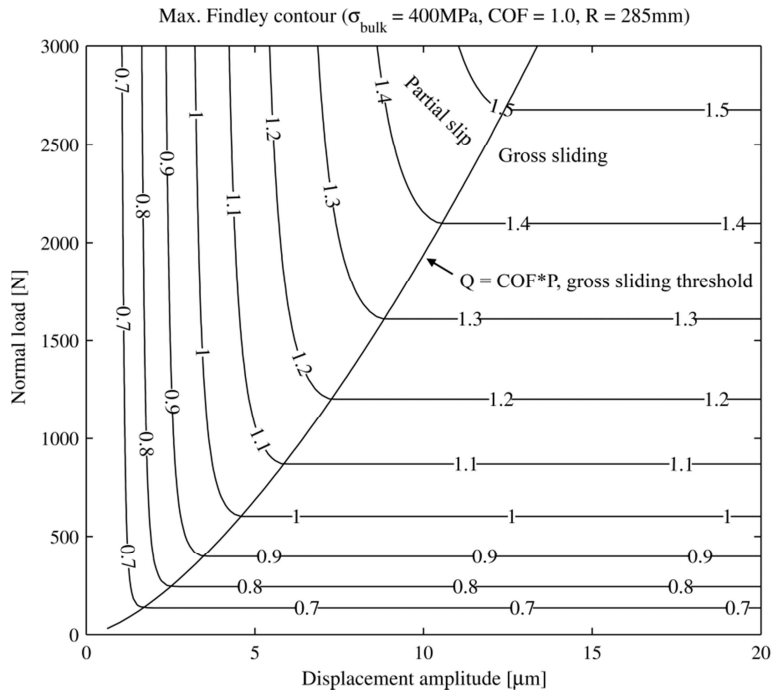

Figure 4 – Numerical fretting fatigue map.

2.1.5 Load balance effects

It was assumed that the forces and displacements between the three contacts were equal. However; a comparison of the measured fretting scar widths and the ones obtained using the analytical solution (Eq. 4) have shown ±10% deviations, which may indicate that the normal force balance between the three contacts was not achieved perfectly. Modest normal force variation has fairly insignificant impact on the fatigue results (Figure 4), especially in the partial slip regime.

The average COF, between the three contacts, is measured accurately in the gross sliding regime. However, an error in the measured combined E_d will lead to erroneous average partial slip COF. The sensitivity of the calculated average partial slip COF on the measured parameter deviations can be estimated by simulating the $3\times E_d$ and $3\times Q$, with slightly different P or COF values for each of the three contacts. The average partial slip COF can then be calculated with Eq. 12, using the average values from each simulated contact, after which it can be compared against the true average COF. The normal load imbalance had low effect on the average frictional energy dissipation. For example normal load variation of ±20 % ($0.8\times P$, $1.0\times P$ and $1.2\times P$) led to only about -3% error in the calculated average partial slip COF. However; COF variations had slightly larger effect on the average partial slip COF, because ±20% deviation in individual COFs lead to approximately 6% reduction in the calculated average partial slip COF. It may be summarized that the estimation of average COF if fairly insensitive to modest P and COF imbalances. However, the magnitude of COF and P deviations remains unknown. The value of COF has fairly significant effect on the resulting fatigue loading in the sphere-on-plane contact. For example increasing the COF from 1.0 to 1.2 increases the d_F from 8 to 16%, in the operational range of the sphere-on-plane apparatus, depending on the P and d_a. Hence COF imbalance leads also to d_F variations between the three contacts. Additionally, the loss of loading symmetry can lead to tangential displacement imbalance which effect is more difficult to estimate.

2.2 Annular flat-on-flat apparatus

2.2.1 Apparatus design

A fretting test device with a large annular, flat-on-flat contact was designed and used to measure friction, wear, and surface degradation. It was first described in publication IV and then used to obtain the results in publications V and VI. A large annular contact produced almost even pressure and sliding distributions and enabled fretting tests with modest normal pressure levels while retaining a large contact independent of loading conditions, which are unobtainable with a sphere-on-plane tester. Such a contact corresponds more closely to typical contact conditions in heavy duty machines, such as heavy duty combustion engines, than the previous sphere-on-plane contact.

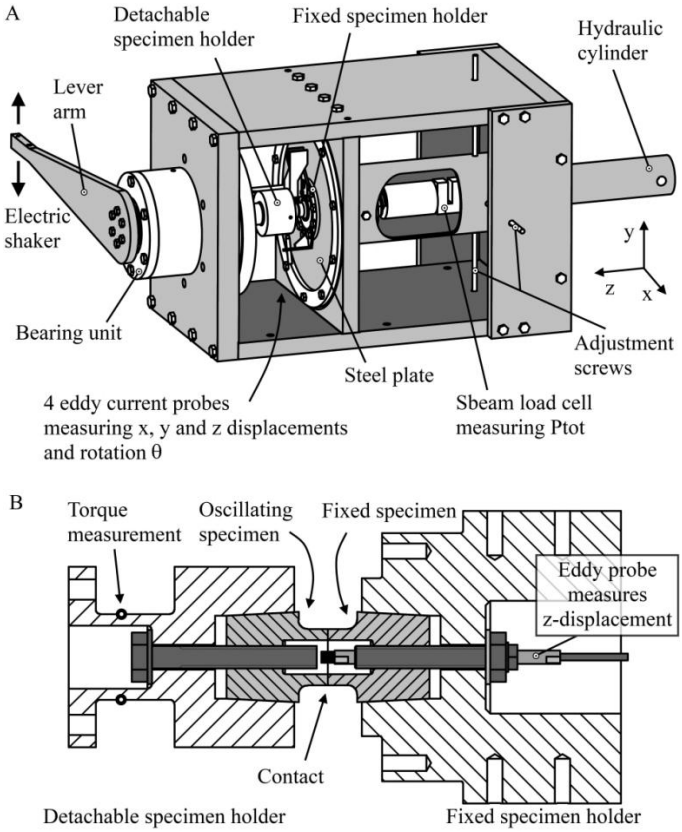

Figure 5 – Annular flat-on-flat apparatus. [Publication V]

The design of the apparatus is shown in Figure 5A. Specimens with tubular ends are attached to the detachable specimen holder and to the fixed specimen holder with conical seats (Figure 5B). The detachable specimen holder is bolted to the main shaft, which is rotated cyclically by the electric shaker via the lever arm q. The detachable specimen holder measures torque T with strain gauges. The fixed specimen holder is attached to the apparatus frame with a thin steel plate and an alignment screw assembly. Tightening and loosening the alignment screws enable adjustment of the normal pressure distribution with the help of a pressure sensitive film (Fuji Prescale) before a test is started. In unloaded conditions, there is an approximately 1.0-mm clearance between the contacting surfaces, which closes when the hydraulic cylinder pushes the fixed specimen holder towards the detachable specimen holder. The normal load P between

specimens was calculated as the total normal force at the end of the piston rod minus the force related to the initiation of contact, which was separately calibrated. The rotation q and the *x*-, *y*-, and *z*-displacements between fixed and detachable specimen holders were measured with eddy current probes. The control unit used the measured rotation signal as feedback, and experiments were run under rotation amplitude q_a control.

The loading frequency was 40 Hz, and during a 400-load-cycle-long star-up phase the rotation amplitude was gradually increased from zero to the target value. During a test run, specimen parallelism could be adjusted on the run by minimizing the measured *x*- and *y*-displacements. Before and after each test, specimens and pads were cleaned with acetone using an ultrasonic washing device.

2.2.2 Calculation of COF

The measured rotation q_m included specimen elastic deformation; therefore, the corrected rotation q_k was calculated using Eq. 15, where *k* is the specimen's compliance:

$$q_k = q_m - k \cdot T \tag{15}$$

The sliding *u* between the specimens was estimated using q_k and the average specimen radius r_a, which was 10 mm (Eq. 16):

$$u = q_k \cdot r_a \tag{16}$$

Two different methods were used to calculate COF. First, it was calculated from the measured torque amplitude T_a and the normal pressure distribution *p(r)*.

$$COF_{\max} = T_a / (2 \cdot p \cdot \int_{r_i}^{r_o} r^2 \cdot p(r)dr) \tag{17}$$

Second, it was determined from the measured frictional energy dissipation E_d, *p(r)* and the rotation amplitude q_a as follows:

$$COF_{mean} = E_d / (8 \cdot p \cdot q_a \cdot \int_{r_i}^{r_o} r^2 \cdot p(r)dr) \tag{18}$$

In ideal Coulomb conditions, both COFs are approximately equal; however, in non-Coulomb conditions $COF_{max} > COF_{mean}$. The difference between the two COFs was used to study the non-Coulomb friction phenomenon.

2.3 Post-test analysis

Pre- and post-test specimen surface 3D-profilometry was done using a Wyko NT1100 white light vertical scanning interferometer, which has a better than 1Å-Ra vertical resolution. A scanning electron microscope (SEM, Philips XL-30) and an energy dispersive X-ray spectroscope (EDS, EDAX DX 4) were used in publications II and VI. X-ray diffraction (Panalytical Empyrean) was used in publication VI. A Precisa EP 420A with a readability of 0.1mg and a repeatability of 0.15mg was used to weigh specimens in publications IV and VI. Optical microscopy was done using a Qioptiq OPTEM ZOOM 70XL zoom lens

system with an Infinity 1-3 camera (2048×1536 pixel resolution) in publications I-III and a Leica MZ 7.5 zoom stereo microscope with a DFC420 camera (2592×1944 pixel resolution) in publications IV-V.

2.4 Materials and test schemes

This chapter gives an overview of the materials and measurement schemes used in this study; an extensive description is given in the respective publications. Fretting experiments were done using quenched and tempered steel (EN 10083-1-34CrNiMo6+QT) and aluminium bronze (CuA10Fe5Ni5-C-GC EN 1982), in short 'steel' and 'bronze' in this study. Apparatus and specimen properties are also summarized in Table 1, and material properties are shown in Table 2.

The effect of start-up schemes on COF: Publication I examined the effect of different experiment start-up schemes on frictional behaviour and materials response using the sphere-on-plane apparatus. Pads and specimens were polished steel, machined from a 25-mm diameter bar. Their surface roughness (*Sa*) was in the range of 0,04 - 0,18 µm, and the radius of the sphere in the range of 285±15 mm. Experiments were run with two normal loads (680 N and 1270 N) and in both partial slip and gross sliding regimes (d_a in the range of 4 to 64 µm). The test duration was 2.8×10^6 load cycles. Three different start-up schemes (step, positive-slope, and negative slope) were used to study their effect on frictional behaviour using a 1270-N normal load. The 'step' start-up was the simplest, and in it the displacement amplitude was increased from zero to the target value during only a few load cycles. In the 'positive slope' start-up scheme, the displacement amplitude was increased linearly from zero to the target value within 8000 load cycles, the standard test procedure in most sphere-on-plane tests. The 'negative slope' start-up began with a step-like start-up to 35 µm displacement amplitude, which is in the gross sliding regime, followed by linear reduction to the target value within 8000 load cycles.

Material response of steel under fretting conditions: Publication II focused on material response, fretting fatigue cracking, and friction in steel when fretted with bronze on the sphere-on-plane apparatus. The surfaces were polished so that their *Sa* was in the range of 0.04 – 0.09 µm and the radius of the sphere in the range of 280 to 300 mm. Measurements were made with two normal loads (1270 N and 2240 N) and in both partial slip and gross sliding regimes (d_a in the range of 3 to 52 µm).

Study of non-Coulomb friction: Publication III examined in detail the non-Coulomb friction phenomenon observed with the bronze-steel contact in publication II. The phenomenon was studied using three variable displacement amplitude schemes, including a sudden and rapid increase and a reduction in the displacement amplitude. A third variable displacement amplitude scheme was one in which the displacement amplitude was repeatedly changed between two values. These tests were in the gross sliding regime (d_a in the range of 20 to 50 µm).

Development of an annular flat-on-flat device: A new fretting apparatus, based on a large annular flat-on-flat contact, is introduced in publication IV, which also includes experiments with steel specimens. Otherwise the material is the same as that used in the sphere-on-plane tests, except that the specimens were machined from a 45-mm diameter bar. The contacting surfaces were precision-ground so that *Sa* was in range of 0,22 to 0,32 µm. Fretting tests were run using three normal pressures (10 MPa, 30 MPa, and 50 MPa) and multiple sliding amplitudes in the gross sliding regime (u_a in the range of 5 to 65 µm). This study focused on the characterization of frictional behaviour and consisted of measurements of fretting wear and surface degradation.

Normal displacements in non-Coulomb friction: Non-Coulomb friction was further studied using the annular flat-on-flat apparatus, which was upgraded with an extra eddy current probe to measure normal displacement. Experiments were run with steel specimens at 10-MPa, 30-MPa, and 50-MPa normal pressures and multiple sliding amplitudes (u_a in the range of 20 to 50 µm).

Velocity accommodation effects on fretting wear: This study focused on fretting wear and velocity accommodation in entrapped third bodies occurring in large annular flat-on-flat contact with steel specimens. A series of fretting tests were run with the contact periodically opened and entrapped wear debris removed. The test duration was 3.0×10^6 load cycles, and the contact was cleaned 13 times during each test. A second test series was run using modified specimen geometry (grooved specimens), which introduced extra edges parallel to the direction of the fretting movement. Tests were run at two normal pressures (10 MPa and 30 MPa) and with sliding amplitudes ranging from 5 µm to 50 µm.

Table 1 – Compilation of the experiments

	Publication					
	I	II	III	IV	V	VI
Sphere-on-plane tester	X	X	X			
Annular flat-on-flat tester				X	X	X
Steel vs Steel	X			X	X	X
Bronze(Pad) vs Steel		X	X			
Slip range [µm]	2-56	1.5-43	11-43	5-65	20-50	5-65
Max Hertz pressure [MPa]	274-334	276-333	276-333	-	-	-
Mean normal pressure [MPa]	183-226	184-222	184-222	10-50	10-50	10-50
Contact area [mm^2]	3.7-5.5	6.9-10	6.9-10	314	314	273-314
Polished surfaces S_a [µm]	X < 0.18	X < 0.09	X < 0.1			
Ground surfaces S_a [µm]				X < 0.32	X < 0.32	X < 0.36
Fretting fatigue	X	X				
Fretting wear			X	X	X	
Friction	X		X	X		X
Non-Coulomb COF			X	X		X

Table 2 – Material properties

	Steel	Steel	Bronze
Apparatus	Flat-on-flat	Sphere-on-plane	Sphere-on-plane
G [GPa]	210	207	120
n [-]	0.27	0.27	0.3
Sy [MPa]	994	1056	280
Su [MPa]	1075	1160	650
f_{Fr} [MPa]	-	380	-
k_{Fr} [-]	-	0.29	-

3 Results & discussion

3.1 Fretting wear

Fretting wear was studied in various ways in all publications (I-VI). The main findings can be divided into observations of adhesive material transfer occurring in the early stages of fretting and high load cycle fretting wear characterized by abrasive third body conditions.

3.1.1 Material transfer and tangential interlocking

Material transfer was examined and discussed in publications I, II, III, IV, and V. During the initial stages of fretting, wear damage was adhesive and resulted in material transfer. Protrusions formed in locations where the material was deposited, and their removal resulted in depressions. The depression-protrusion pairs conformed geometrically and interlocked in a tangential direction with profound effects on frictional behaviour and fretting fatigue performance.

In publications II and III, bronze pads were fretted against flat steel specimens using the sphere-on-plane apparatus. The surfaces were polished, and the tests consisted of two normal load levels and multiple displacement amplitudes covering both the partial slip and gross sliding regimes. For most tests, the duration was 2.8×10^6 load cycles; however, some short duration tests were also performed. The load levels were severe for bronze but reasonably modest for steel. The resulting wear damage showed that bronze transferred from the pad to the surface of the steel specimen. In most tests, the steel specimens showed little or no wear damage. Material transfer was pronounced in the gross sliding regime, occurring throughout the contact. It also occurred in partial slip conditions but was confined to the sliding annulus. Figure 6A shows an example of a bronze transfer layer on a steel specimen. The outer contact annulus showed multiple protruding material transfer chunks of widths up to 1 mm and heights ranging from tens to about 100 µm. However, the circular central region was less rough and filled with protruding ridgelines ranging from a few to about 10 µm in height. These protrusions corresponded to the conforming depressions in the pad surface (Figure 6B, C and D). The angle of gradient corresponding to the interlocked protrusions and depressions was in the range of 10 to 35 degrees.

In publication IV, ground surfaces were tested for fretting with steel-steel contact using the flat-on-flat apparatus. A large, annular flat-on-flat contact offered uniform normal and tangential traction conditions and fairly constant sliding conditions. The normal pressure levels and sliding amplitudes ranged from 10 to 50 MPa and 5 to 65 µm, respectively. The test duration in these tests was 3.0×10^6 load cycles, but a few short duration tests were run as well. Almost all fretting scars showed multiple material transfer spots with widths in the millimetre range. In the initial stages of the experiments, material transfer and adhesive wear damage were pronounced. Figure 7A shows that, after 10^4 load cycles of fretting, three material transfer spots formed with widths in the millimetre range. The topographies of these three locations were measured and compared with the impression in the counter specimen. Again a protrusion corresponded to a conforming depression, forming tangential interlocking. In the tangentially interlocked protrusions and depressions, the angles of gradient ranged from a few to about 20 degrees. Adhesive wear was pronounced in the initial stages of the fretting test and gradually changed to abrasion partly due to the accumulation of wear particles in the interface, which effectively separated the contacting first bodies.

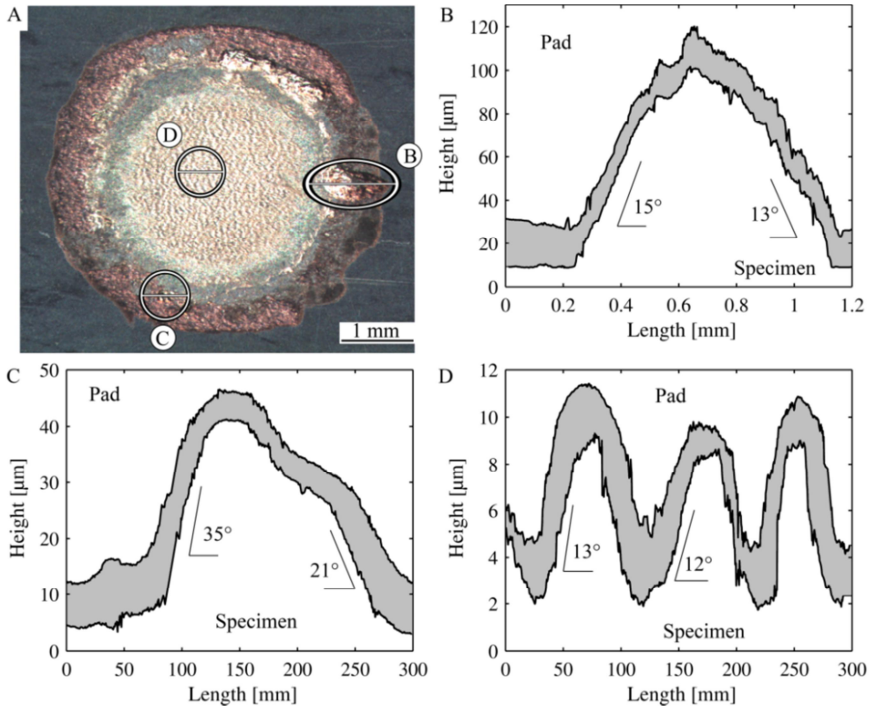

Figure 6 – Material transfer and tangential interlocking with sphere-on-plane, bronze-steel contact. [Publication III]

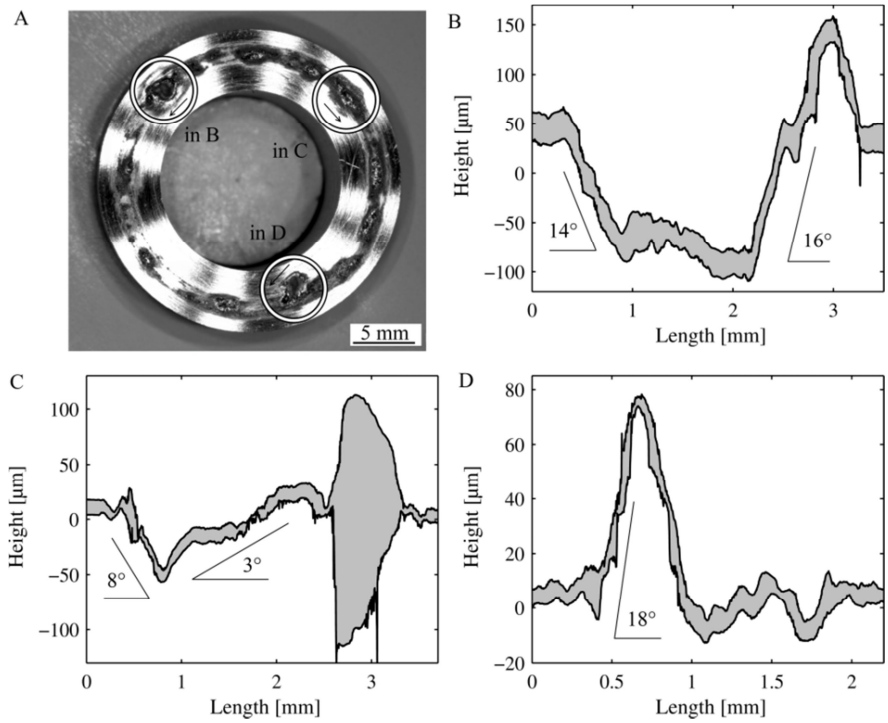

Figure 7 – Material transfer and tangential fretting scar interlocking with annular flat-on-flat contact. [Publication V]

Some evidence for extensive material transfer was observed in publication I with polished steel-steel contact using the sphere-on-plane test rig, when the contact was fretted in the gross sliding regime. This occurred in the standard test (Figure 8A-B) and was especially pronounced in the 'negative slope' tests (Figure 8C-D), where the fretting loading was such that the displacement amplitude was abruptly increased from zero to gross sliding (35 µm), followed by a gradual reduction to the target value within 8000 load cycles. The total test duration of these tests was 2.8×10^6 load cycles. Figure 8 shows examples of fretting scars and their surface profiles paired with a fretted pad profile and illustrating the already familiar material transfer and tangential interlocking. The whole contact area was friction-welded and then torn under a reciprocating shearing load. Because material transfer was especially pronounced in the 'negative slope' tests, it evidently occurred during the early stages of gross sliding; however, short duration fretting tests were not performed at this time.

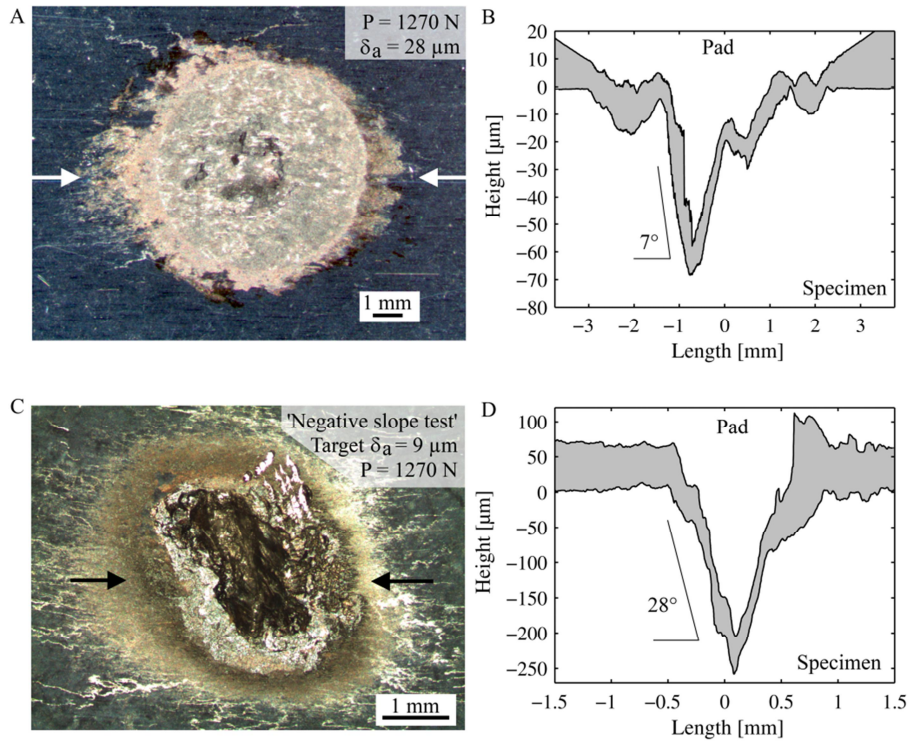

Figure 8 – Material transfer and tangential interlocking with sphere-on-plane steel-steel contact. A&B standard gross sliding fretting scar and C&D 'Negative slope'tests fretting scar. Arrows indicate the location of the profile. [Publication I]

Figure 8C and Figure 7 show a striking similarity in fretting scar in the form of large, millimetre-scale material transfer spots. In the sphere-on-plane tester, the severe damage can be explained by high loads produced by the Hertzian point contact owing to the combined effect of a normal load and a high initial COF. For example, during the highest loads, the Von Mises stresses at the edge of the point contact exceeded the yield strength. However, in the annular flat-on-flat contact, the normal pressure was merely 30 MPa, and remnants of adhesion spots were observed already at 10 MPa normal pressure. Therefore, in the annular flat-on-flat tests, the nominal stress levels were insignificant in comparison to the yield strength or fatigue strength of steel, even though the COF measured high. This implies that in the flat-on-flat contact fretting damage accumulated in a few "hot spots", where the load was significantly higher than what nominal loads could predict.

3.1.2 Wear rate in fretting

The wear rate of steel was studied in publications V and VI, using the annular flat-on-flat apparatus. In publication IV, the wear rate as measured was mostly dependent on the sliding amplitude or accumulated sliding distance, while the normal load was less significant (Figure 9). This contradicts the Archard wear model, which predicts that wear is linearly dependent on normal load [4]. Because oxide wear debris gradually filled the contact interface, the wear rate behaviour was explained by the velocity accommodation mechanism. In third bodies, velocity accommodation provides load carrying capacity and protects the first bodies from wear. The velocity accommodation mechanism was put to the test in two series in publication VI. First, the entrapped wear debris was periodically removed from the interface (Cle-tests), which resulted in about 4 times greater wear mass losses than in standard, uncleaned test conditions. This validates the wear reducing property of entrapped wear debris.

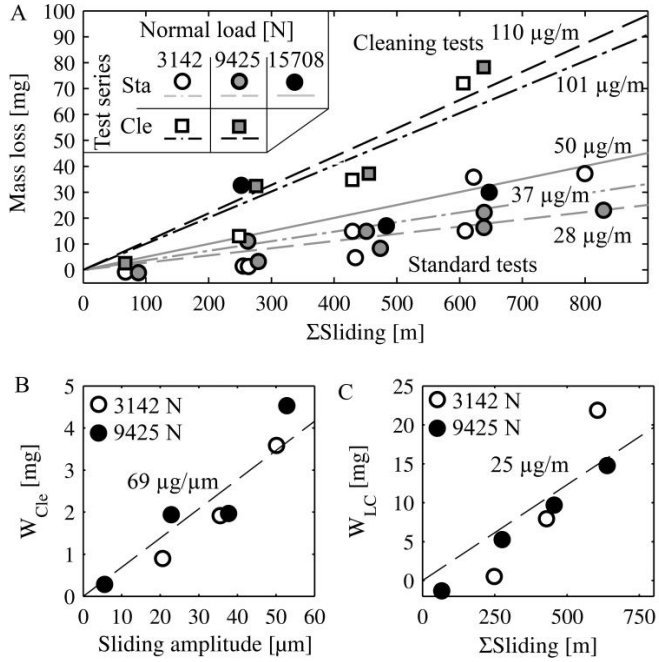

Figure 9 – Fretting wear in contact cleaning test vs standard test with the plane-on-plane test rig. [Publication VI]

A second test series in publication VI was performed with modified specimen geometry so that grooves perpendicular to the fretting movement were made in the specimens (grooved specimen vs regular specimen). The wear rate of the grooved specimens increased significantly with the wear increasing effect of the grooves almost linearly dependent on the number of grooves (Figure 10). The grooves reduced the nominal contact area by about 7% and 13% with 6 and 12 grooves, respectively; hence the increase in the wear rate was not sensitive to the change in the nominal contact area, but the increase in the wear rate can be explained by the change in the interface geometry.

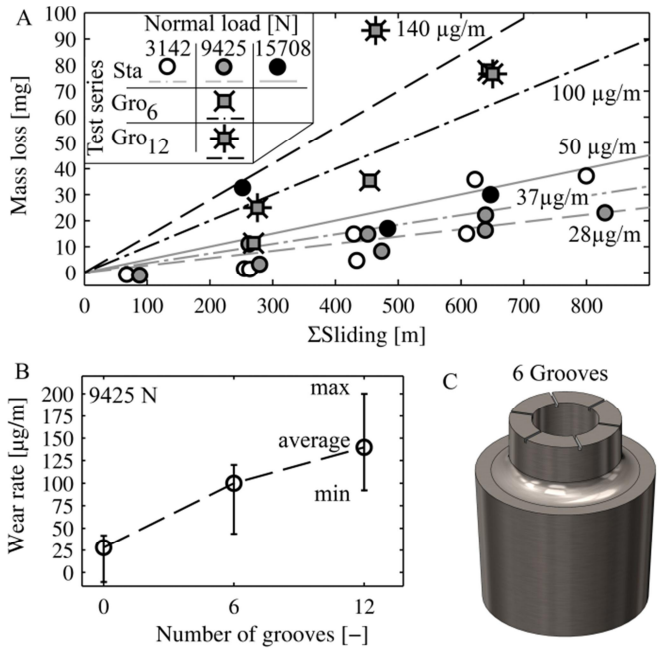

Figure 10 - Fretting wear with grooved specimens tests vs standard test with the plane-on-plane test rig. [Publication VI]

The increased wear rate in both Cle- and Gro-tests was explained by the velocity accommodation mechanism. In the Cle-tests, cleaning temporarily removed the bulk of entrapped wear debris, thereby reducing its wear protection capability and resulting in an increased wear rate. The increasing wear rate effect was not permanent because newly generated wear debris gradually accumulated in the interface reducing the wear rate. The overall increased mass loss was also dependent on the number of contact cleanings. In the Gro-tests, changing the interface geometry and the extra edges perpendicular to the fretting movement may have increased the natural ejection of entrapped wear debris. Because velocity accommodation must occur mostly in the direction of the fretting movement, it is reasonable that ejection is more pronounced on the edges perpendicular to the fretting movement than on those parallel to the fretting movement. An increased ejection rate reduced the amount of entrapped wear debris and also its wear protection potential and resulted ultimately in an increased wear rate.

3.2 Frictional behaviour

3.2.1 Fretting loops and non-Coulomb friction

The study of frictional behaviour constituted a major part of publications I, III, IV, and V. Analysis of this behaviour was largely based on interpretation of fretting loops. A fretting loop is a graph of frictional load versus fretting movement over the duration of one load cycle, such as tangential force vs tangential displacement or torque vs rotation. One unifying factor in frictional behaviour was a lack of ideal frictional sliding and the existence of so-called non-Coulomb friction. Non-Coulomb friction, in which frictional resistance to sliding changed during a load cycle, was observed in gross sliding conditions, as illustrated in Figure 11.

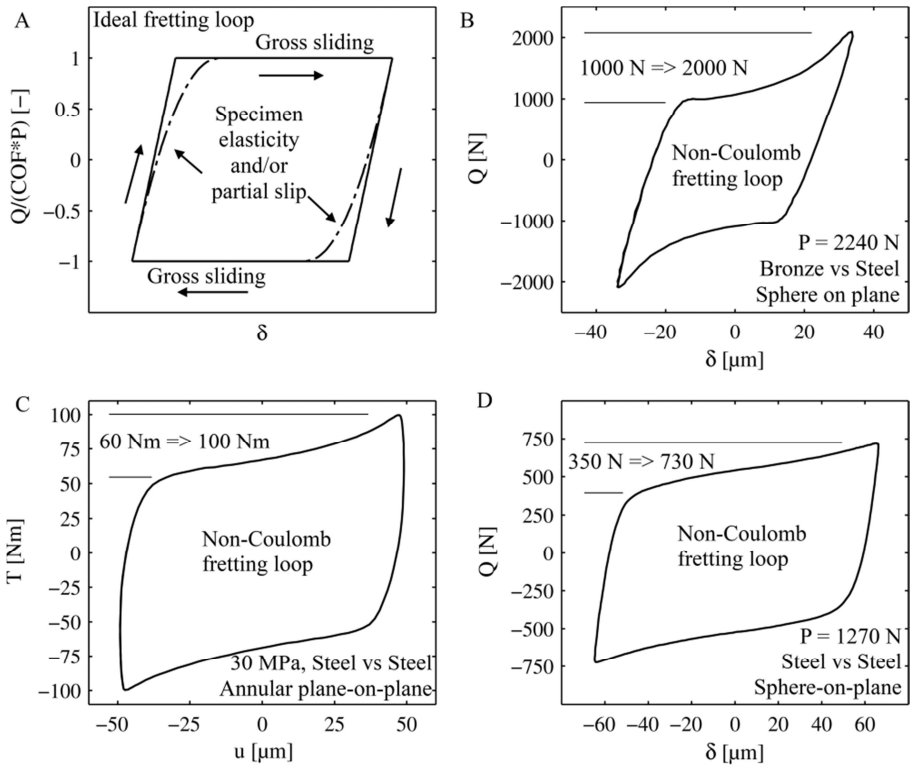

Figure 11 – Ideal fretting loop and examples of non-Coulomb fretting loops.

Figure 11A shows schematically a gross sliding fretting loop and assumes ideal Coulomb (or Amontons) friction conditions. A to and fro movement produces a parallelogram-shaped fretting loop, in which the friction force remains at a constant value during gross sliding. A change in the loading direction may result in angled or curved ends because of contacts compliance in the tangential direction; however, during gross sliding, the friction force remains at a constant value.

Publication II and especially publication III showed evidence of non-Coulomb friction occurring in gross sliding fretting with bronze sphere against steel plane. An example of a non-Coulomb fretting loop is illustrated in Figure 11B. The basic property of non-Coulomb friction is that the friction force increases gradually, when the fretting movement approaches its extreme positions. In bronze vs steel contact, this resulted in a pronounced 'hooked' fretting loop. During gross sliding, increase in the friction force was significant.

Non-Coulomb fretting loops occurred also with steel-steel contact, when the annular flat-on-flat apparatus was used (publication IV and publication V). In this case, the non-Coulomb fretting loop shaped into a skewed parallelogram with less 'hookiness' than with bronze-steel contact (Figure 11C).

The phenomenon of non-Coulomb friction was observed and briefly discussed in publication I, though it was not yet sufficiently understood. A reanalysis of the sphere-on-plane tests with steel-steel contact showed clear evidence of non-Coulomb friction behaviour, as illustrated in Figure 11D.

The phenomenon of non-Coulomb friction was observed with steel vs steel contact with both the sphere-on-plane and annular flat-on-flat apparatuses. The Hertzian point contact was under high loads, whereas the plane-on-plane contact was subjected to nominally low loads. Furthermore, the phenomenon was pronounced with the bronze-steel contact in the sphere-on-plane apparatus. Basically, all gross sliding

fretting tests showed signs of non-Coulomb friction; consequently it may well be a common occurrence in fretting. The non-Coulomb increase in the friction force was significant, which means that such friction conditions must be carefully analysed. Simplifying such frictional behaviour to a single COF value gives a limited picture of the overall frictional behaviour.

3.2.2 Different coefficients of friction

In publications I and II, COF was calculated using the energy ratio method in partial slip conditions and from the maximum *Q/P*-ratio in gross sliding. In these first publications, the calculation of COF was based on the assumption of ideal Coulomb friction behaviour. However, it follows from the shape of the non-Coulomb fretting loop that a single ideal COF is insufficient to describe the overall frictional behaviour. In publication III, the fretting loop was characterized using three different COFs: COF_{min}, COF_{mean}, and COF_{max} (μ_{min}, μ_{mean} and μ_{max}), which describe the shape of the fretting loop in gross sliding conditions. In publications IV and V, COF was calculated from the dissipated frictional energy dissipation (COF_{Ed}) and from the maximum torque (COF_T). In ideal conditions, these COFs are all equal; however, different values are obtained in non-Coulomb conditions. Different symbols and abbreviations were used in publications I-VI for the COFs; however, the following three different COFs were used: COF_{max}, COF_{mean}, and COF_{min} (Figure 12).

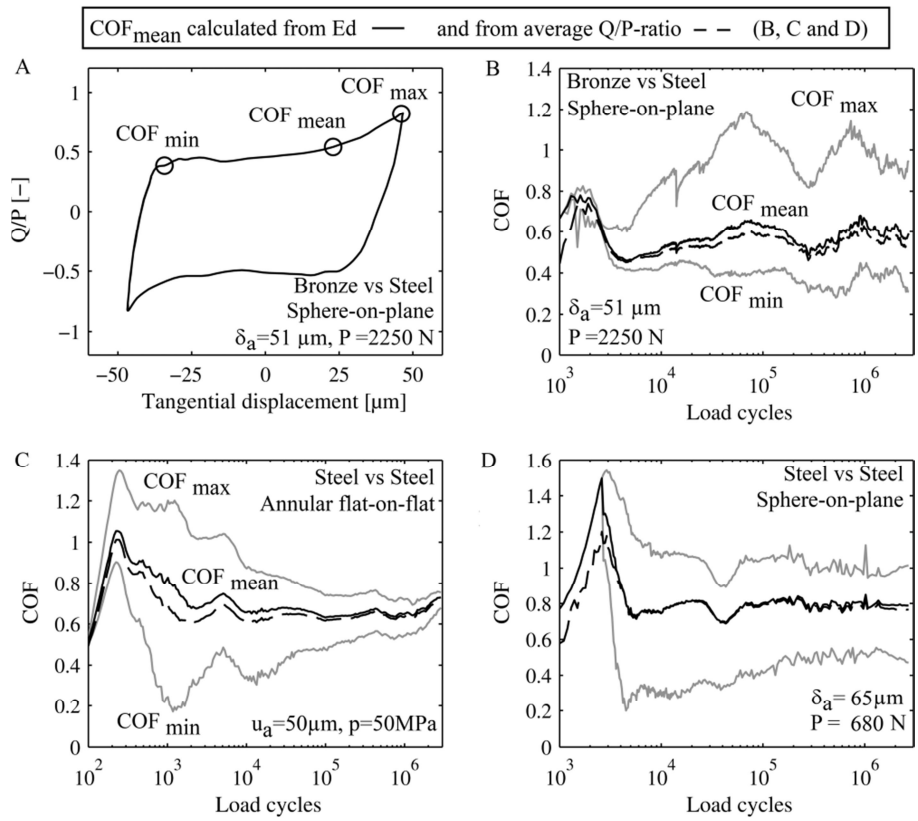

Figure 12 – Different coefficients of friction.

Maximum COF during a fretting cycle (COF_{max}): The gross sliding COF in publications I and II corresponds to the COF_{max}. Furthermore, the μ_{max}, which was used in publication III, and the COF_T used in publications IV and V represent the COF_{max}. Each corresponds to the maximum friction measured at the extreme positions of the fretting movement (Figure 12A). Therefore, $COF_{max}=COF_T=\mu_{max}$.

Mean COF during a fretting cycle (COF_{mean}): In publication III, the μ_{mean} was calculated as the mean of the COF weighed with the sliding distance, and as such it represents the mean COF during a load cycle. In publications IV and V, the COF_{Ed} was calculated from the frictional energy dissipation, and it also represents the mean COF during a load cycle though the calculation method is different. Both approaches produce very similar values for the mean COF, which is illustrated in Figure 12B-D, where the solid black line represents the mean COF weighed with the sliding distance, and the dashed black line represents the COF_{Ed}. Therefore, $COF_{mean}=COF_{Ed}=\mu_{mean}$.

Minimum COF during a fretting cycle (COF_{min}): In publication III, the COF represents the minimum friction force during gross sliding (μ_{min}), which was often measured right after a partial slip stage following a reversal in the direction of the fretting movement (Figure 12A).

Partial slip COF: In publications I and II, a partial slip COF was calculated using the energy ratio method. The result represents COF in the sliding annulus, and the method assumes ideal Coulomb friction conditions and ideal tangential compliance of the sphere-on-plane contact($COF_{min}=COF_{mean}=COF_{max}$). Under non-Coulomb friction conditions, the meaning of the calculated partial slip COF is not fully understood and thus warrants further study. Additionally, one must be careful when interpreting partial slip COF results, if non-Coulomb friction occurs in gross sliding.

3.2.3 Gross sliding COFs with steel-steel contact

The gross sliding COF of steel-steel contact was reported in publications IV and V, covering annular flat-on-flat results. The behaviour is illustrated in Figure 13. With the steel-steel contact, frictional behaviour was characterized by a high COF_{max}, which peaked during the first 10^2-10^3 load cycles (maximum of COF_{max}) and gradually stabilized within the first ~1.0×10^5 load cycles. This phase was dominated by non-Coulomb friction conditions, as indicated by $COF_{mean}<COF_{max}$. The non-Coulomb friction phase ended after about 1.0×10^5 load cycles. The development of the COFs correlated well with accumulated frictional energy dissipation and accumulated surface sliding, as illustrated in Figure 13A-C. The peak COF_{mean} and COF_{max} values are compiled in Figure 13D&E, which shows them as approximately 1.4 and 1.1, respectively, and increasing slightly as a function of the normal load. The corresponding steady state values about 0.8 for COF_{max} and 0.7 for COF_{mean} were mostly independent of normal load and sliding amplitude. Further analysis of frictional behaviour showed that its peaking and stabilization correlated well with the accumulated frictional energy dissipation and especially well with the accumulated sliding distance, as shown in Figure 13F-G. Median values were shown in publication IV; however mean values were used in Figure 13, both methods producing similar results.

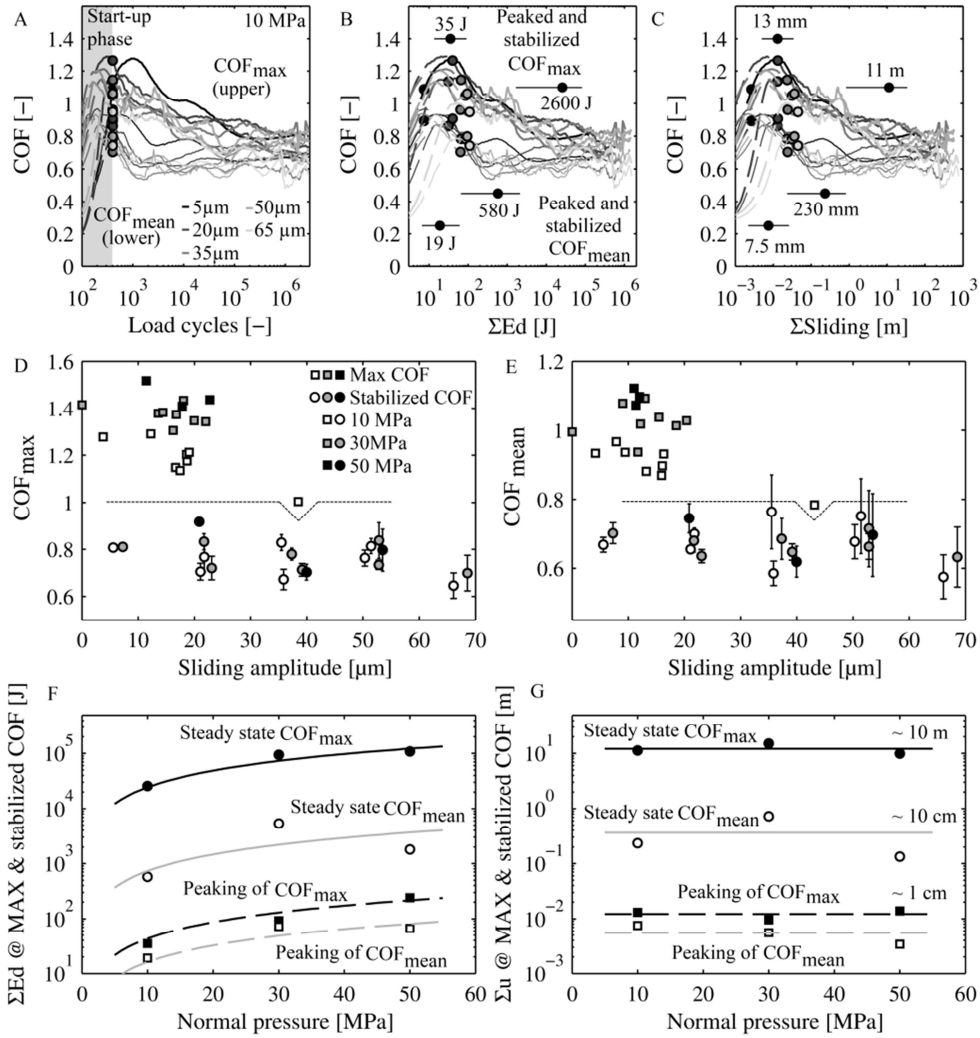

Figure 13 – Steel vs steel gross sliding COFs with annular flat-on-flat contact. [Publication IV]

Steel-steel sphere-on-plane gross sliding COF was studied also in publication I, though the concept of different COFs and non-Coulomb friction was not used at the time. The COF_{max} peaked at approximately 1.5 during the start-up phase, when the displacement amplitude was still being increased, followed by a gradual reduction to steady state values in the range of 0.8 - 1.0 (Figure 14), which is close to the previously discussed flat-on-flat COF_{max} behaviour. Furthermore, the sphere-on-plane results were reanalysed using the methods illustrated in publication III and taking into account the non-Coulomb fretting loop effects. This showed that also the COF_{mean} behaved as it did in the earlier flat-on-flat results.

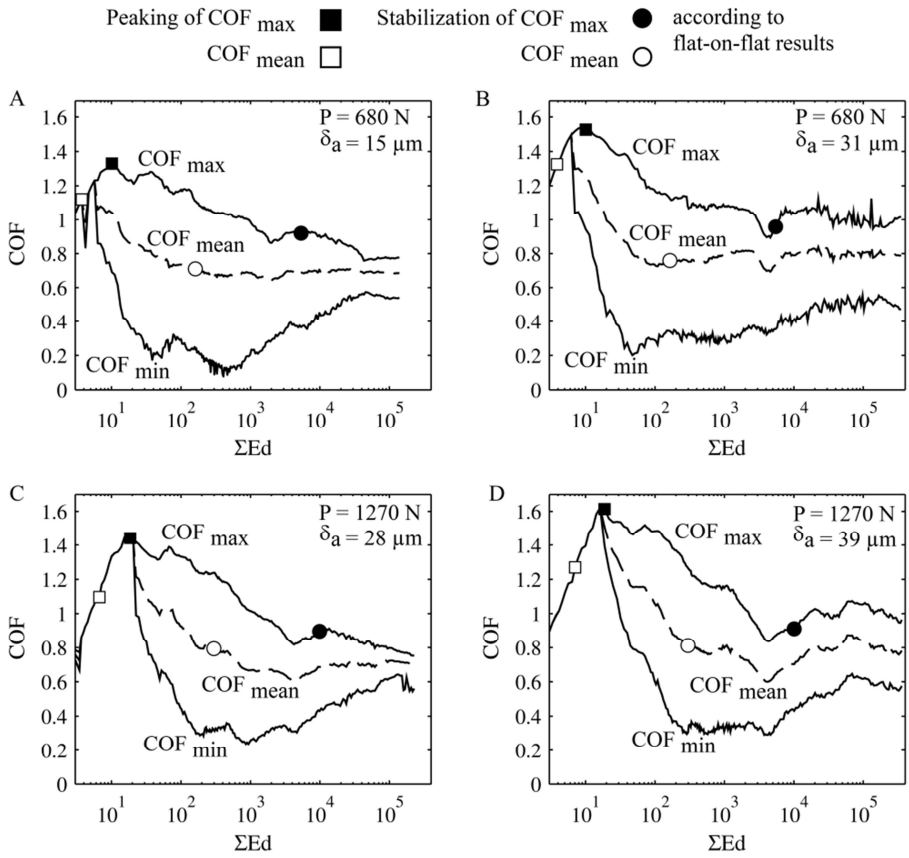

Figure 14 – Steel vs steel gross sliding COFs with sphere-on-plane contact.

In publication IV, the COF_{max} and COF_{mean} peaked and stabilized at the values of accumulated frictional energy dissipation, which increased linearly as a function of the normal pressure. The average pressure levels were an order of magnitude higher in the sphere-on-plane tests than in the flat-on-flat tester; therefore, the energies related to the peaking and stabilization of COFs should be similarly higher, if they indeed depend on the normal pressure. This turned out not to be the case: the energies were, in fact, lower in the sphere-on-plane contact than what was predicted by the flat-on-flat results. However, simply by replacing normal pressure with normal load produced closely correlating peaking and stabilizing energies in both flat-on-flat and sphere-on-plane COF results. It may be speculated that the peaking and stabilization of COFs depend on the accumulation of frictional energy dissipation in the real contact area $\Sigma E_d/A_{real}$, because this area depends on the normal and tangential forces under high COF plastic asperity tip contact conditions [2,3]. In Figure 14, the squares and circles indicate when the COFs should peak and stabilize according to the flat-on-flat results as a function of normal force rather than normal pressure, showing surprisingly good correlation between the results obtained with different apparatuses and contact geometries.

3.2.4 Gross sliding COFs with bronze-steel contact

Publications II and III reported the overall gross sliding frictional behaviour of bronze vs steel as a function of load cycles. Here frictional behaviour was characterized by non-Coulomb 'hooked' fretting loops with significant differences between COF_{min}, COF_{mean}, and COF_{max} (Figure 15). In bronze vs steel contact,

the non-Coulomb phenomenon built up gradually as a function of load cycles within the first ~100×10^3 load cycles, and non-Coulomb friction conditions persisted for the whole 2.8×10^6 load cycle. In all cases, the COF_{max} fluctuated around unity, whereas the COF_{mean} and COF_{min} were more stable with values of about 0.7 and 0.4, respectively.

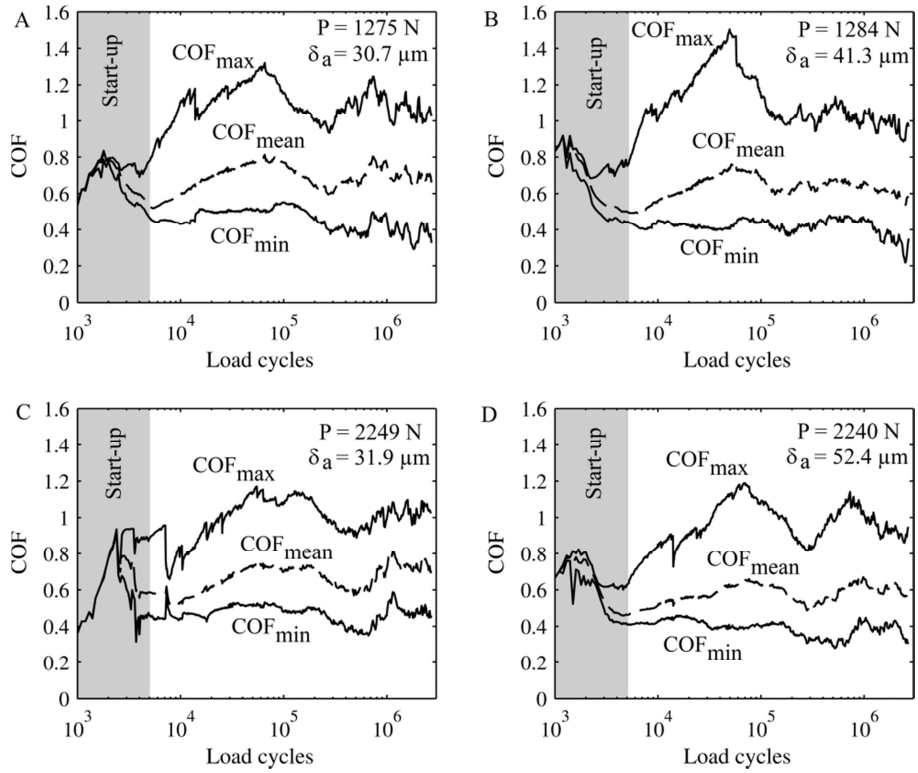

Figure 15 – Bronze vs steel gross sliding COFs with sphere-on-plane contact. [Publication III]

There were few major differences in the overall frictional behaviour between steel-steel and bronze-steel contacts. The steel-steel contact was characterized by an initial adhesive friction peak, dominated by non-Coulomb friction. The bronze-steel contact showed no such initial friction peak, and non-Coulomb friction conditions took more load cycles to develop and persisted throughout the experiment.

3.2.5 Effect of third bodies on COF in steel-steel contact

Publication VI focused on the effect of velocity accommodation in entrapped third bodies on wear and friction. A series of tests was run with the annular flat-on-flat contact with the contact periodically opened and wear debris removed with pressurised air and a paper tissue soaked in acetone. Because this procedure had barely any observable effect on COF_{max} and COF_{mean}, it was concluded that steady state COF conditions are not affected by removal of wear debris from the contact (Figure 16). This finding is in stark contrast with Halliday's work, which showed that the COF increased dramatically after wear debris was removed [22].

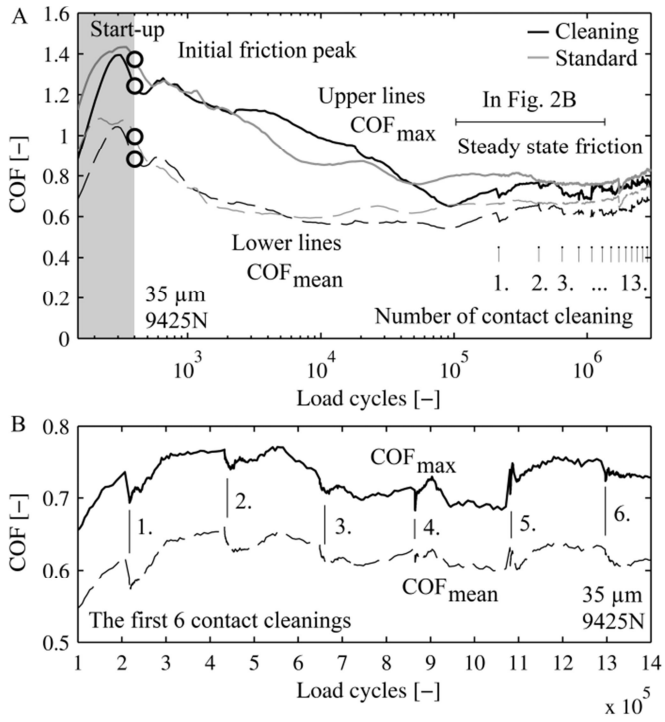

Figure 16 - Effect of wear debris removal on COFs with annular flat-on-flat, steel vs steel contact. [Publication VI]

It was assumed in publication IV that the gradual reduction and stabilization of COF_{max} and COF_{mean} during the first ~10^5 load cycles was linked with wear debris accumulation in the interface. Loose wear debris in the interface enables additional modes of velocity accommodation mechanism, such as rolling, which was suggested by Halliday [22]. The results in Figure 16 indicate that COF_{max} and COF_{mean} values are insensitive to the thickness of the third body bulk. After each cleaning of the contact, the specimen surfaces retained a brown colouring, indicating that the first body surfaces were oxidized or covered with adhered oxide wear debris. In fact, even small amounts of entrapped wear debris and sticking oxide layers may be sufficient to maintain steady state friction conditions. In addition, frictional behaviour may depend on the overall accumulation of fretting damage and work hardening of the first body surfaces.

3.2.6 Coefficient of friction in partial slip conditions

In publications I and II, measurements were made using the sphere-on-plane apparatus in partial slip conditions with steel-steel and bronze-steel contacts. The COF was calculated with the energy ratio method from the frictional energy dissipation. The COF was measured to be dependent on the displacement amplitude so that the greater the displacement amplitude, the greater the COF until gross sliding commenced. The running condition often changed from partial slip to gross sliding. In steel-steel contact, COF behaviour was characterized by friction peaking during the first ~10^5 load cycles, which resembles gross sliding COF_{max} behaviour though the peaking was subtle at the lowest displacement amplitudes. A steady state COF was achieved gradually, and its value corresponds closely to the steady state gross sliding COF_{max} in the gross sliding experiments.

The bronze-steel contact produced no COF peak; however, the COF value was measured to be dependent on the displacement amplitude like in the steel-steel contact. The highest COF values near gross sliding corresponded closely to the gross sliding COF_{max} and the lowest COFs were close to the COF_{mean}.

In publication I, the displacement-amplitude-dependent COF was assumed to originate from the slip amplitude-dependent growth of a plastic asperity junction. However, in retrospect, non-Coulomb friction effects may have significantly affected the results. The energy ratio method cannot separate different COFs, such as COF_{max} and COF_{mean}, which prevail during a non-Coulomb fretting load cycle. Because non-Coulomb friction conditions were measured to occur in gross sliding, similar effects may reasonably occur during partial slip conditions as well. Hence partial slip COF results must be interpreted with care. Additionally, load imbalance may cause inaccuracy which was discussed in the chapter 2.1.5.

3.2.7 Tangential fretting scar interactions scheme and friction

Previous chapters showed how the initial stages of fretting wear damage are characterized by adhesive wear resulting in material transfer and tangential interlocking between protrusions and depressions. Additionally, a non-Coulomb friction phenomenon was observed, which was also pronounced at the beginning of the fretting tests. Interlocked protrusions and depressions may harbour limited clearances so that in fretting movement the sides of the interlocked surface features may interact. The non-Coulomb friction phenomenon has been suggested to originate from such interactions. Because the angles of gradient related to the interactions are in the range of a few degrees to a few tens of degrees, most tangential interactions may lead to gentle inclined sliding rather than a brutal “head-on” collision.

For tangential interactions to occur during fretting, the clearance between interlocked protrusions and depressions, if any at all, must be smaller than the sliding amplitude (publication III). Figure 17 shows a comparison of a pair of fretting scars (profiles from Figure 6D), illustrating that a significant clearance may occur between protrusions and depressions. Simply by ‘sliding’ the upper topography to and fro shows that a tangential clearance may accommodate about a 14-µm sliding amplitude. In that experiment, the slip amplitude was estimated to be approximately 25 µm in the centre of the contact [60]. Clearances are hard to measure precisely, because surfaces are, for example, unstressed during 3D-profilometry, and because loose wear particles may have filled the clearances. However, because the sliding amplitude is by far greater than what the clearance can accommodate, tangential interactions do occur between protrusions and depressions.

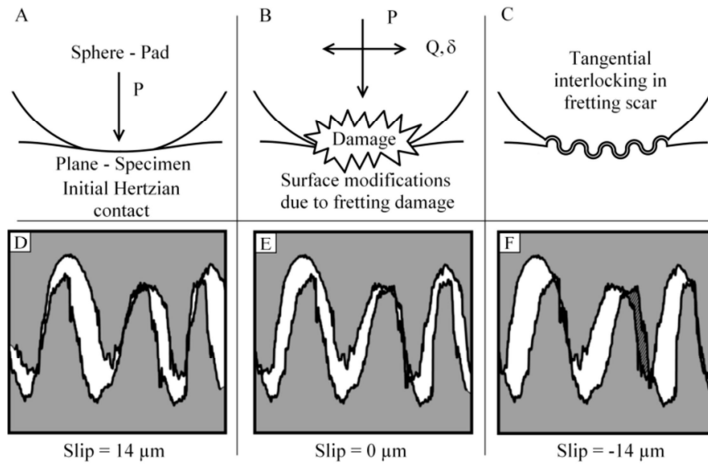

Figure 17 – Formation of tangential interlocking in a fretting scar. [Publication III]

The shape of the non-Coulomb fretting loop indicates that the friction force depends on the phase of the fretting movement. Such behaviour is also to be expected in the tangential fretting scar interaction scheme, because individual protrusion-depression interactions progress gradually, when the sliding approaches its extreme positions. Different experimental approaches were used to study this non-Coulomb friction phenomenon and the tangential fretting scar interaction scheme.

In publication III, three different types of variable displacement amplitude schemes were used with the displacement amplitude changed abruptly during 40 load cycles (1s). The effect on frictional behaviour of abrupt reduction and abrupt increase in the displacement amplitude was tested in separate measurements. In the third measurement, the displacement amplitude was repeatedly changed abruptly. Variable displacement amplitude schemes were used also in publication I. Especially the 'negative slope' tests are considered here, because they clearly showed non-Coulomb friction behaviour, though the change in the displacement amplitude was gradual rather than abrupt, because it occurred within 8000 load cycles. The resulting effects on measured fretting loops are shown in Figure 18.

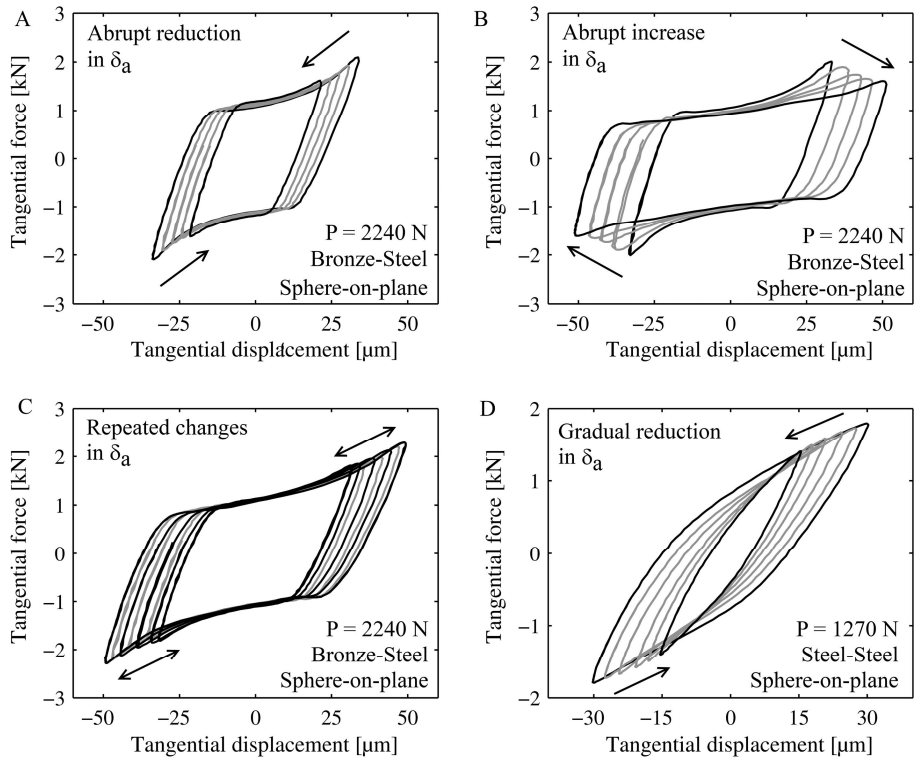

Figure 18 – Effect of abrupt changes in displacement amplitude on fretting loops during non-Coulomb friction conditions in gross sliding.

Figure 18 shows abrupt changes in the displacement amplitude resulting in significant changes in the shapes of the fretting loops. Most notable is the dependence of the maximum friction force on the changing displacement amplitude. In bronze-steel contact, an abrupt reduction in the displacement amplitude produced a significant reduction in the maximum friction force (Figure 18A). When the displacement amplitude was abruptly increased, the maximum friction force also dropped (Figure 18B), indicating a wipe-out of tangentially interlocked protrusions and depressions due to a sudden overloading. When the displacement amplitude was periodically reduced, increased, and then reduced back again and so forth, the resulting maximum friction force decreased and increased as a function of the displacement amplitude,

as illustrated in Figure 18C. Reduced maximum friction force vs reduced displacement amplitude behaviour was also measured with the steel-steel contact (Figure 18D).

Abrupt reductions in the displacement amplitude resulted in respective reductions in the sliding amplitude, which ultimately dictated how much the tangential protrusion-depression interactions propagated, because the fretting scar topographies remained mostly unchanged. This clearly shows that during non-Coulomb friction conditions, the friction force depends on sliding in a manner that is predicted by the tangential fretting scar interaction scheme. Reduction in the maximum friction force due to an abrupt change in the displacement amplitude was not permanent, and when the latter was kept at a constant value, the former gradually increased and ultimately stabilized at values almost independent of the displacement amplitude. This is explained by the finite number of load cycles, which is required before fretting wear modifies the fretting scar profiles to match the loading conditions, which occurs gradually over thousands of load cycles.

Non-Coulomb friction was studied in another way in publication V with experiments run with the annular flat-on-flat apparatus, which was upgraded to accurately measure any normal displacements during fretting cycles. In non-Coulomb friction conditions, also cyclic normal displacements were then observed. Specimens moved slightly away from one another, when the fretting movement approached its extreme positions, as illustrated in Figure 19 ("u-shaped" *u*-*z*-fretting loops).

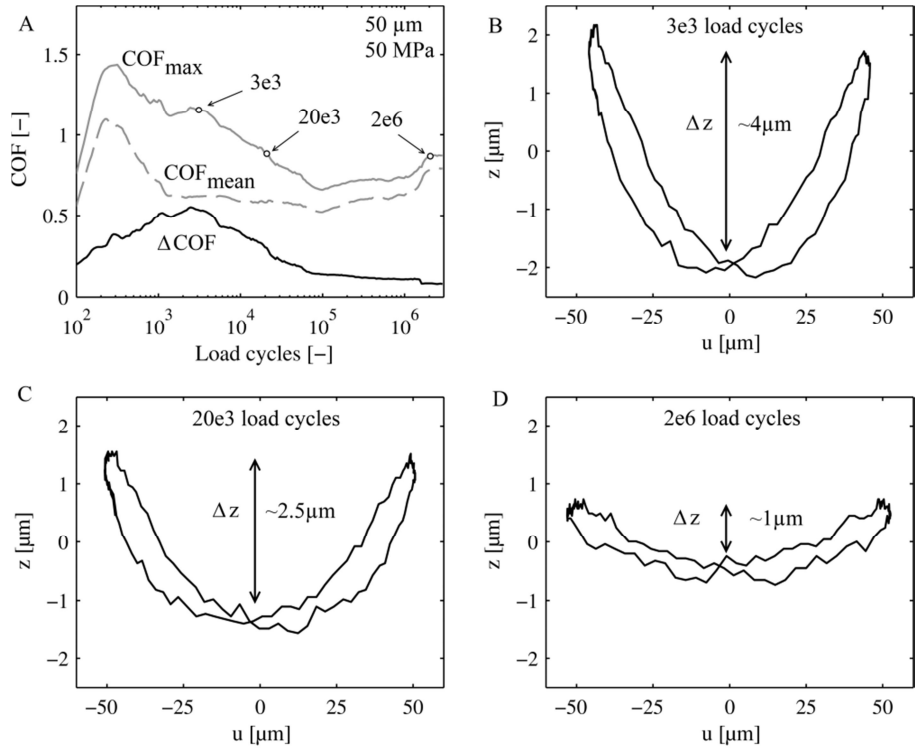

Figure 19 – Normal displacements during non-Coulomb friction conditions. [Publication V]

Both the magnitude of the normal displacements Δz and the magnitude of non-Coulomb friction ($\Delta COF = COF_{max} - COF_{mean}$) gradually declined as a function of load cycles, suggesting a common source. Each tangentially interlocked protrusion-depression pair was characterized by a unique angle of gradient a, whose effective value a_{eff} was estimated from measured sliding and *u*-*z*-displacement data. The extraction of a_{eff} and its development as a function of load cycles is illustrated in Figure 20A&B. The magni-

tude of this angle had a strong, nearly linear correlation with the magnitude of the non-Coulomb friction (Figure 20C). The a_{eff} and COF_{mean} were used to calculate COF_{max_a}, based on frictional inclined sliding (Eq. 19) according to the tangential fretting scar interaction scheme [15]. The resulting COF_{max_a} was very close to the measured COF_{max}, which provides further evidence that non-Coulomb friction is caused by tangential fretting scar interactions.

$$COF_{\max\_a} = \frac{COF \cdot \cos(a) + \sin(a)}{\cos(a) - COF \cdot \sin(a)} \tag{19}$$

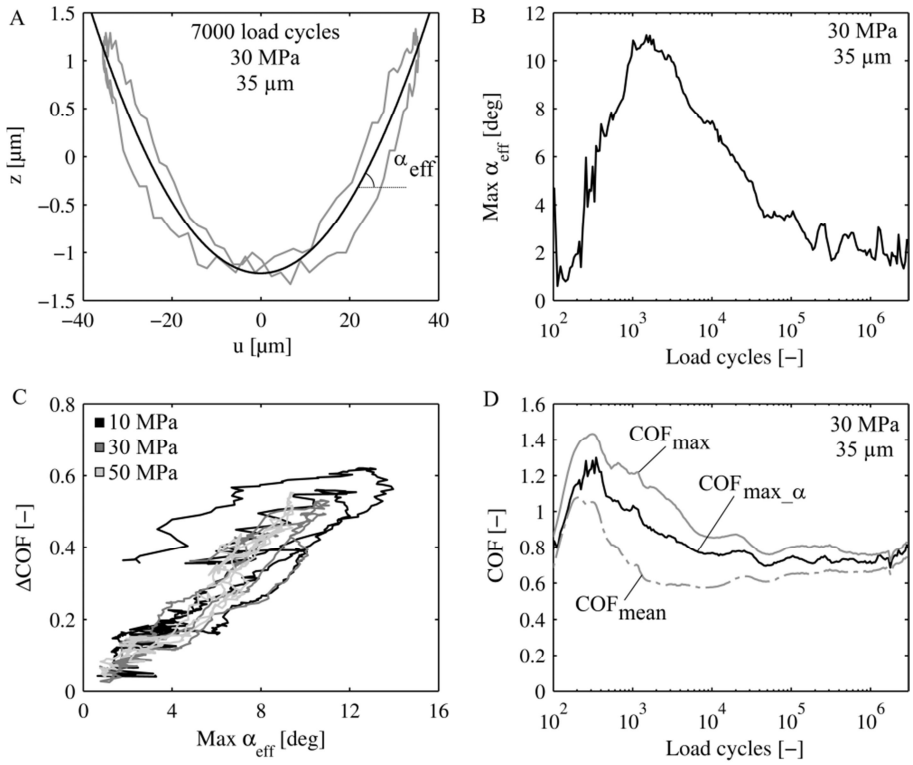

Figure 20 – Estimated maximum angle of gradient and its effect on non-Coulomb friction. [Publication V]

The results of publications I, III, and V agree with mechanical tangential fretting scar interactions to account for the origin of non-Coulomb friction. Every test series in which non-Coulomb friction occurred gave evidence of adhesive material transfer leading to tangentially interlocked protrusions and depressions. It follows from the model that frictional resistance against surface sliding should be affected by abrupt changes in the displacement amplitude, which was confirmed in publication III. It also follows from inclined sliding that tangential movement is accompanied by normal displacement, which was confirmed in publication V. Therefore, the mechanical fretting scar interaction scheme is a sound explanation for the non-Coulomb friction phenomenon.

It is ironic that this frictional behaviour is called ‘non-Coulomb’, because Coulomb theorized that friction originates in interactions of tangentially interlocked surface protrusions and depressions, albeit he meant initial surface roughness rather than anything caused by adhesive material transfer.

3.3 Fretting fatigue

3.3.1 Fatigue cracks

The fretting fatigue performance of quenched and tempered steel was studied with steel-steel and bronze-steel contacts using the sphere-on-plane apparatus in publication II and including experiments performed in publication I. Due to a lack of cyclic bulk stress, the sphere-on-plane apparatus could not produce specimen fatigue failure; however, contact stresses combined with constant tensile bulk stress were sufficient to produce cracks that could be observed with an optical microscope. Examples of fretting scars with cracks are shown in Figure 21.

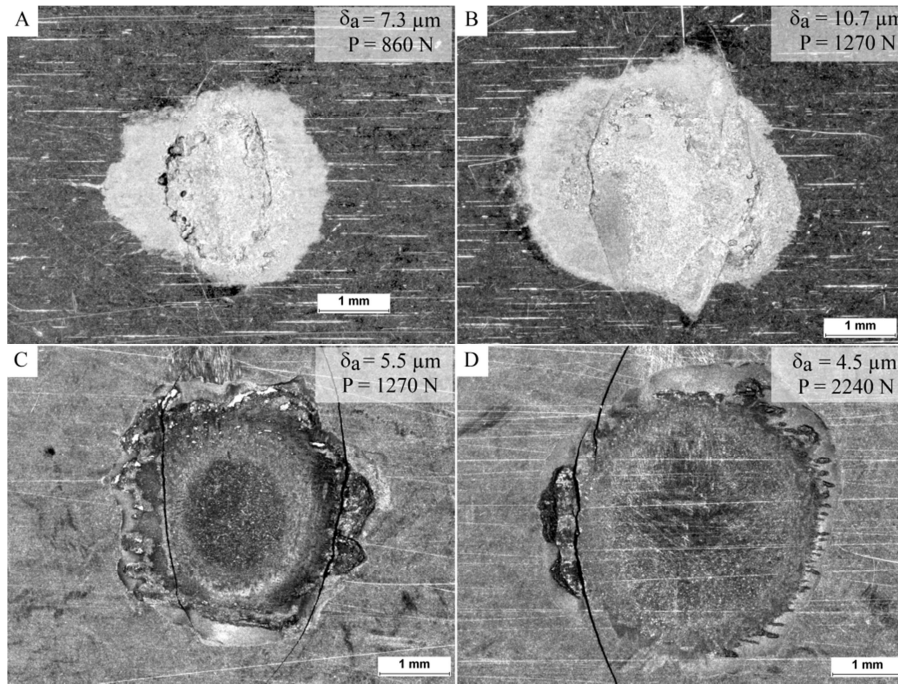

Figure 21 – Examples of fretting fatigue cracks with steel-steel (A&B) and bronze-steel (C&D) contacts using the sphere-on-plane apparatus. [Publication II]

All specimens with observable cracks, such as those in Figure 21, were counted as cracked specimens. Each test with the sphere-on-plane tester had three contacts running simultaneously; the number of cracked specimens thus varied from zero to three. The number of cracked specimens varied also depending on whether fretting loading was below, near, or above the fatigue cracking threshold. If loading was below the threshold, no cracks appeared, and if it was clearly above the threshold, all specimens had cracks. However, if loading was close to the threshold, some specimens were cracked, others not.

The number of load cycles required for crack initiation could be approximated from the measured tensile bulk stresses. Figure 22 show a steep drop in the tensile bulk stress caused by a crack growing in the specimen. The steel-steel contact showed crack initiation roughly during the first 10^5 load cycles (Figure 22A), whereas it took longer for cracks to develop with the bronze-steel contact (Figure 22B), about 10^5 to 10^6 load cycles. It is difficult to pinpoint a location in the tensile bulk stress data where a crack initiation occurred, because it must be fairly large before it can be observed by this method. Obviously, it

developed before it caused any measurable reduction in the tensile bulk stress. However, the main finding was that fatigue cracks developed in the early stages of the test, especially in steel-steel contact.

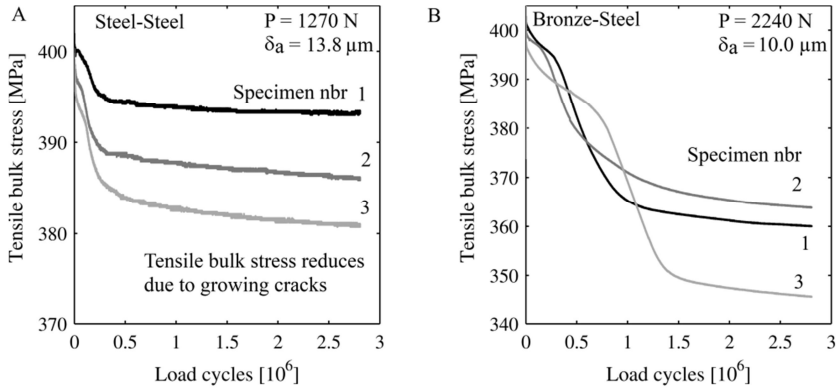

Figure 22 - Crack initiation estimation from tensile bulk stress.

3.3.2 Fretting maps

The fretting fatigue performance of steel specimens was analysed with the help of fretting maps in publication II. Different types of fretting maps were used by varying the abscissa with parameters such as the tangential displacement amplitude, tangential force amplitude, and *FCR* (fretting maps are compiled in Figure 23). The measured values used in analysis (COF_{max}, d_a, Q_a, P, s_{bulk}) correspond to the average of the first 1.0×10^5 load cycles, which takes into account that fatigue cracks developed early in the experiments and particularly markedly in steel-steel contact. The dashed line represents the partial slip/gross sliding threshold displacement amplitude, which was calculated using the measured maximum of COF_{max}; consequently, it corresponds to the highest achievable tangential force amplitude (COF for steel-steel contact 1.5, and for bronze-steel contact 1.2).

First, as a function of the tangential displacement amplitude, the fretting maps (Figure 23A&B) showed typical behaviour, such as that reported by Vingsbo [10]. At the lowest displacement amplitudes, no cracking occurred in the steel specimens; however, when the amplitude was increased, the first cracks were observed, and cracking was most pronounced, when the amplitude was near the gross sliding threshold. Further increases in the displacement amplitude led to a gradual reduction in the number of observed cracks. The cracking thresholds were approximately 6 µm with steel-steel contact and 4 µm with bronze-steel contact. Interestingly, the bronze-steel contact produced cracks at a higher displacement amplitude than the steel-steel contact, perhaps because of a lack of wear in the steel specimen fretted with bronze pads, except at the highest displacement amplitudes. Reduced crack initiation deep in the gross sliding regime has frequently been explained by a high enough wear rate, which can wipe out crack embryos faster than they can grow [10,52,68]. Clearly, such a crack embryo wipe-out mechanism cannot exist, if the steel specimen remains unworn.

As a function of the tangential force amplitude, the fretting maps show that the cracking threshold was ~20% and ~30% lower in bronze-steel contact than what was measured for steel-steel contact at 1270 N and 2240 N normal loads, respectively (Figure 23C&D). In the steel-steel contact, the first cracks appeared when the *FCR* was approximately 0.8, which is somewhat below the expected value 1.0 (Figure 23E). In comparison, the bronze-steel contact produced fatigue cracking at much lower *FCR* values, at about 0.6 (Figure 23F). Hence it was concluded that the use of bronze pads compromised the fretting fatigue performance of the steel specimen.

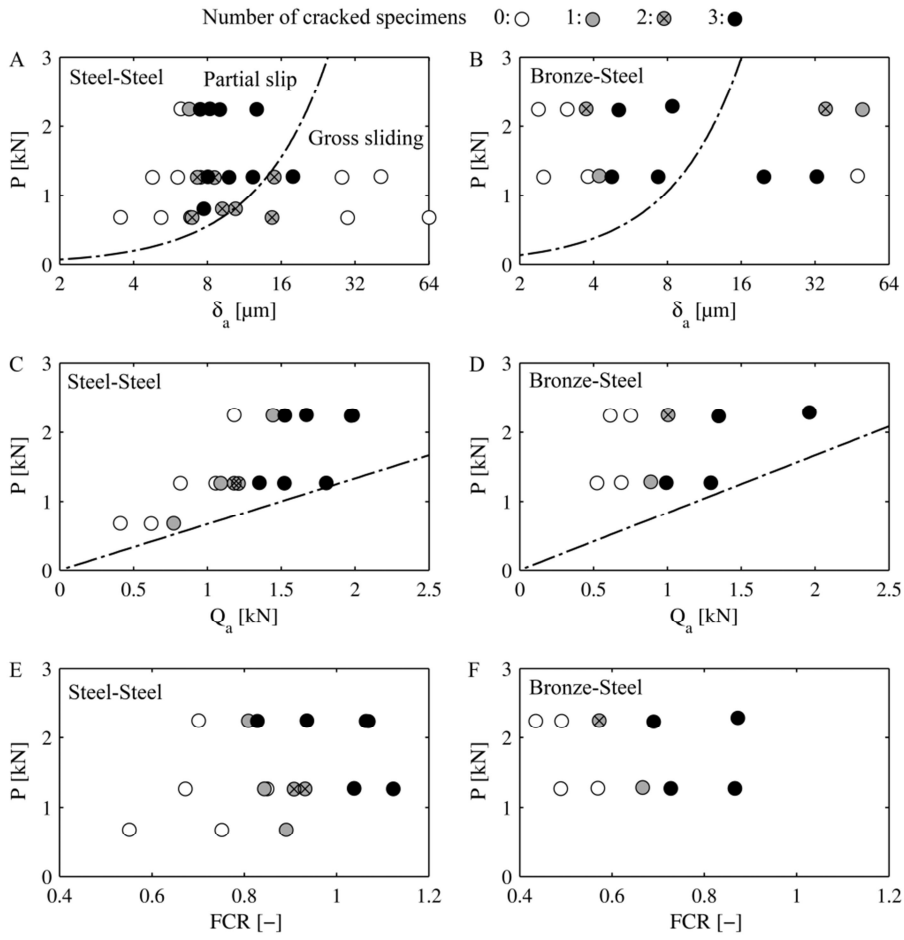

Figure 23 – Steel specimen fretting maps with steel-steel and bronze-steel contacts. [Publication II]

Because of steep stress gradients, size effects exist in fretting fatigue conditions [57,58]. Using a statistical size factor takes into account the small size of the sphere-on-plane contact and the stress gradient on the surface of the specimen. However, the sphere-on-plane contact exhibits a significant stress gradient also in the depth direction, which is not included in the statistical size factor. Therefore, using maximum cyclic stresses on the specimen surface may overestimate the severity of the fatigue loading. Additionally, because the steel-steel contact has a smaller contact radius than the bronze-steel contact under the same normal loads, the former produces a steeper stress gradient than the latter. Taylor's theory of critical distances can be used to evaluate fatigue loading under such steep stress gradients. His so-called point method was used to analyse the fatigue loading of the sphere-on-plane contact, where stress was calculated at a depth of 20 μm, which corresponds the average defect size of the tested steel [69,70]. According to Rabb [69] the average defect size corresponds roughly to half of the critical distance, which is supposed to be used in the point method. Plain Findley fatigue criterion results, calculated on the specimen surface and at a depth of 20 μm, are shown for both the steel-steel and bronze-steel contacts in Figure 24.

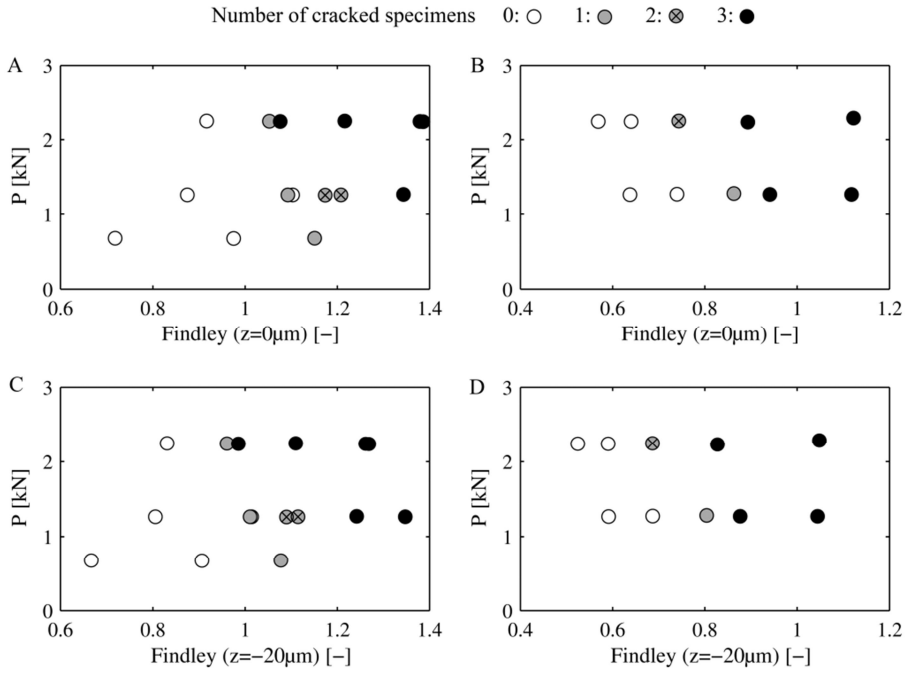

Figure 24 – Fretting fatigue maps with steel-steel and bronze-steel contacts using the plain Findley damage criterion on the surface and at a depth of 20 μm.

Figure 24A-B illustrates that in the steel specimen, fatigue cracking occurred when the surface Finley criterion value was approximately 1.1 and 0.8 for the steel-steel and bronze-steel contacts, respectively. Figure 24C-D shows subsurface fatigue loadings with cracking thresholds of 1.0 and 0.75 for the steel-steel and bronze-steel contact, respectively. Though these values are greater than the originally reported *FCR* values, both the surface and subsurface Findley damage criterion values indicate that, compared to steel pads, using bronze pads lowered the steel specimens' fretting fatigue performance. The low fretting fatigue performance of the bronze-steel contact cannot be explained by the size effect. The reduction in the subsurface d_F is approximately 7 and 9% compared to the surface values with the steel-steel and bronze-steel contacts, respectively. Consequently, the *FCR* values are accurate.

3.3.3 Tangential fretting scar interactions and fatigue

When the *FCR* equals 1.0, the number of cycles to fatigue crack initiation should be significant. However, cracking occurred even at an *FCR* of below 1.0, and cracks developed in the early stages of the experiment. This indicates that stresses were, in fact, much higher than what the analysis indicated. Observation of adhesive material transfer leading to tangential interlocking explains this peculiar behaviour, especially in the case of the bronze-steel contact, which was prone to cracking.

Non-Coulomb friction was measured to occur with both steel-steel and bronze-steel contacts in gross sliding conditions. It is reasonable to assume that non-Coulomb friction conditions exist also in partial slip conditions, especially in bronze-steel contact, because tangentially interlocked protrusions and depressions were measured for the bronze-steel contact even in partial slip conditions. With the steel-steel contact, no significant adhesive material transfer was measured at low sliding amplitudes, though it may have occurred to a certain extend but remained unnoticed after 2.8×10^6 load cycles.

The low fretting fatigue performance of the bronze-steel contact in comparison to the steel-steel contact may have been caused by a mechanism similar to that which led to a pronounced non-Coulomb friction (publication III and IV). Because non-Coulomb friction was caused by tangential fretting scar interactions (protrusions and depressions), it follows that regions near individual interacting protrusions and depressions are under very high stress. These regions are likely sites for fatigue cracks to develop. Moreover, the steel specimen remained mostly unworn, while the bronze suffered severe damage. This may further promote crack initiation, as crack embryos are not wiped out because the steel specimen undergoes no wear. When these regions coincide with nominally highly loaded spots, fatigue cracking may occur at surprisingly low loads. There was evidence of cracks developing near bronze material transfer spots and in multiple locations near the edge of the contact (Figure 25).

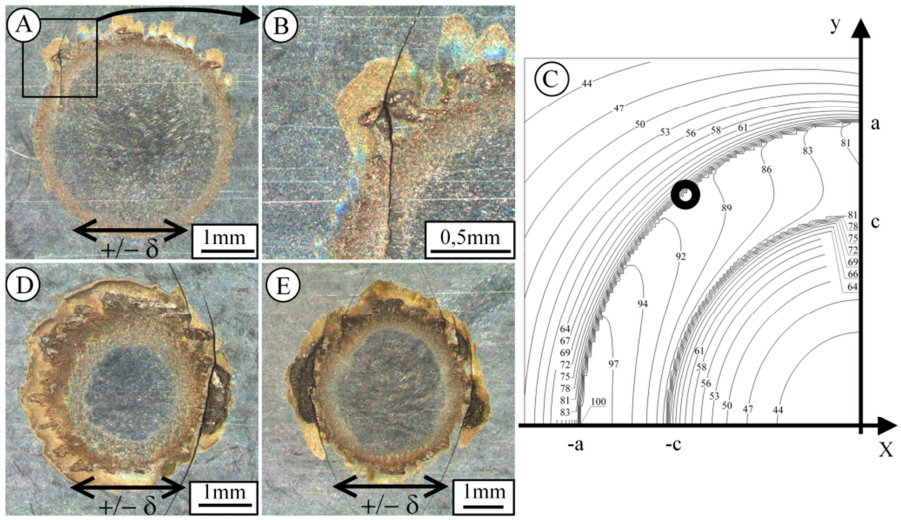

Figure 25 - Cracking at locations of material transfer with a bronze-steel contact. [Publication II]

At this stage, it remains unknown what kind of stresses are related to any protrusion-depression interactions. However, the existence of cyclic normal displacement indicates that most normal and tangential loads are transmitted via protrusion-depression interaction, which may indicate extremely high local stresses. Surely, the stress fields, near tangential interactions, will be characterized by extremely steep stress gradients, meaning that the highest stresses exist on the surface, and that they will not penetrate deep in the specimen reducing their severity concerning fatigue cracking. Of course, if a large enough crack develops, it may continue to grow due to nominal contact stresses, even without any stress increasing effect from fretting scar interactions. The role of tangential fretting scar interactions in fatigue crack nucleation invites further study, including experiments, simulations, and fracture mechanics.

4 Conclusions

The ever present demand to improve machine efficiency and power density, for example, in heavy duty combustion engines, leads to individual components having to withstand high loads. In such conditions, the engineer prefers to exploit the material's strength without excessive safety margins while ensuring reliable machine performance. Dimensioning of highly loaded contacts has become a challenge because of the risk of fretting. Under fretting conditions, contacting surfaces or parts of them experience reciprocating surface sliding, which can lead to fretting wear and fretting fatigue. Fretting is notoriously efficient in nucleating surface cracks, which may continue to grow under cyclic bulk loads, especially when the components' plain fatigue stresses utilize a large proportion of the material's fatigue strength. Because fretting damage may accumulate in the confinements of the interface, it may lead to sudden and unexpected failure of machine components. Evaluation of the risk of fretting is made difficult by uncertainties about frictional behaviour and fretting-induced surface degradation, which further underline the importance of studying fretting.

This thesis seeks to understand the phenomenon of fretting in quenched and tempered steel (abbreviated as 'steel'). Experiments were conducted with steel vs steel and with aluminium bronze (abbreviated as 'bronze') vs steel contacts. Fretting was tested with a pre-existing sphere-on-plane fretting apparatus and an annular flat-on-flat fretting apparatus, designed and built from scratch.

Non-Coulomb friction was measured in gross sliding fretting conditions in all test series, though it was especially pronounced with the heavily loaded bronze-steel contact. In non-Coulomb conditions, the friction force is a function of surface sliding during a load cycle and increases gradually during gross sliding and peaks, when the fretting movement approaches its extreme positions. During a fretting load cycle, the maximum friction force may be up to twice as large as the mean friction force.

Under non-Coulomb friction conditions, a single COF value cannot fully describe the contact's frictional behaviour. A better understanding of this behaviour is achieved by determining the maximum and mean COFs (COF_{max} & COF_{mean}) during a fretting cycle. With a steel-steel contact, COF_{max} development was characterized by an initial friction peak, during which it reached a range of 1.3-1.6, then declined gradually and stabilized at a typical range of 0.7-1.0. High COF conditions occurred simultaneously with non-Coulomb friction and lasted about 10^5 load cycles, or about 10 meters of accumulated surface sliding. The COF_{mean} showed similar behaviour, though its peak and steady state values were lower, in range of 0.9 to 1.1 and 0.6 to 0.9, respectively, and though it stabilized already after about 10 centimetres of accumulated surface sliding. With the bronze-steel contact, no such initial friction peak appeared, yet non-Coulomb friction was the dominant friction pattern and persisted throughout the test of 2.8×10^6 load cycles. The maximum and mean COFs were in a range of 0.9 to 1.5 and 0.5 to 0.8, respectively.

In the early stages of fretting, adhesive wear and material transfer occurred and led to a formation of tangentially interlocked protrusions and depressions. Variable tangential displacement amplitude and normal displacement measurements showed that mechanical interlocking between protrusions and depressions leads to inclined sliding conditions. The results show that a significant proportion of the non-Coulomb friction phenomenon was caused by inclined sliding conditions, even though the surfaces were nominally flat. With the steel-steel contact, the adhesive wear phase occurred during the first few thousands of load cycles, whereas with the bronze-steel contact it lasted much longer.

In the long run, the wear behaviour changed, especially with steel-steel contacts, because the interface started to fill up with entrapped loose wear debris, which then oxidized. This provided some protection against further wear via velocity accommodation in entrapped third bodies. In such conditions, the wear rate is driven by ejection of wear particles. The wear rate increased significantly when the entrapped wear

particles were periodically removed. Furthermore, the wear rate increased similarly when the specimen geometry was modified with grooves to enable more efficient natural ejection of wear particles during a test run. The wear enhancing effect of the grooves was almost linearly dependent on their number.

Cracking of steel under fretting fatigue was studied using steel-steel and bronze-steel contacts, which later proved especially susceptible to fretting fatigue. The overall cracking behaviour corresponded to Vingsbo's findings, according to which cracking occurs mostly near the gross sliding regime and decreases gradually as a function of an increasing displacement amplitude in the gross sliding regime. Fatigue load was analysed by using the so-called Findley cracking risk (*FCR*). Cracking occurred at *FCR* values of approximately 0.8 and 0.6 with steel-steel and bronze-steel contacts, respectively. The increased sensitivity to fretting fatigue with the bronze-steel contact was explained by formation of tangentially interlocked protrusions and depressions, which also occurred in partial slip conditions. The bronze-steel contact also witnessed significant non-Coulomb friction, which was caused by tangential fretting scar interactions. It follows that individual tangentially interlocked spots are under a much greater cyclic load than predicted by nominal contact stresses, accelerating fatigue crack initiation.

References

[1] D Dowson, History of tribology, Longman Group Limited, London, 1979.

[2] F Bowden, D Tabor, The friction and lubrication of solids part 1, Oxford University Press, Oxford, 1950.

[3] F Bowden, D Tabor, The friction and lubrication of solids part 2, Oxford University Press, Oxford, 1964.

[4] JF Archard. Contact and Rubbing of Flat Surfaces, Journal of Applied Physics. 24 (1953) 981-988.

[5] GW Stachowiak, AW Batchelor, Engineering tribology, 4th ed., Butterworth-Heinemann, Oxford, 2013.

[6] AD Sarkar, Wear of metals, Pergamon Press, Oxford, 1976.

[7] NE Frost, KJ Marsh, LP Pook, Metal fatigue, Clarendon Press, Oxford, 1974.

[8] W Schütz. A history of fatigue, Eng.Fract.Mech. 54 (1996) 263-300.

[9] RB Waterhouse, Fretting corrosion, Pergamon press, Oxford, 1972.

[10] O Vingsbo, S Söderberg. On fretting maps, Wear. 126 (1988) 131-147.

[11] ZR Zhou, K Nakazawa, MH Zhu, N Maruyama, P Kapsa, L Vincent. Progress in fretting maps, Tribol.Int. 39 (2006) 1068-1073.

[12] S Fouvry, P Kapsa, L Vincent, K Dang Van. Theoretical analysis of fatigue cracking under dry friction for fretting loading conditions, Wear. 195 (1996) 21-34.

[13] GA Tomlinson. The rusting of steel surfaces in contact, Proc. R. Soc. A 115 (1927) 472.

[14] E Leidich, A Maiwald, J Vidner. A proposal for a fretting wear criterion for coated systems with complete contact based on accumulated friction energy density, Wear. 297 (2013) 903-910.

[15] DM Mulvihill, ME Kartal, AV Olver, D Nowell, DA Hills. Investigation of non-Coulomb friction behaviour in reciprocating sliding, Wear. 271 (2011) 802-816.

[16] D Godfrey. Investigation of fretting by microscopic observation, NACA Report 1009. (1950).

[17] D Godfrey, JM Bailey. Coefficient of friction and damage to contact area during the early stages of fretting, NACA Tech. Note 3011. (1953).

[18] KL Johnson. Surface Interaction between Elastically Loaded Bodies under Tangential Forces, Proceedings of the Royal Society of London A: Mathematical, Physical and Engineering Sciences. 230 (1955) 531-548.

[19] A Pasanen, S Järvisalo, A Lehtovaara, R Rabb. Development of a test device for the evaluation of fretting in point contact, Lubr Sci. 21 (2009) 41-52.

[20] JF Zheng, J Luo, JL Mo, JF Peng, XS Jin, MH Zhu. Fretting wear behaviors of a railway axle steel, Tribol.Int. 43 (2010) 906-911.

[21] PR Degat, ZR Zhou, L Vincent. Fretting cracking behaviour on pre-stressed aluminium alloy specimens, Tribol.Int. 30 (1997) 215-223.

[22] JS Halliday, W Hirst. The fretting corrosion of mild steel, Proc. R. Soc. A 236 (1956) 411.

[23] SR Pearson, PH Shipway, JO Abere, RAA Hewitt. The effect of temperature on wear and friction of a high strength steel in fretting, Wear. 303 (2013) 622-631.

[24] MA Rahmat, RN Ibrahim, RH Oskouei. A stress-based approach to analyse fretting fatigue life behaviour of electroless Ni–P coated Al 7075-T6, Materials Science and Engineering: A. 631 (2015) 126-138.

[25] K Nakazawa, N Maruyama, T Hanawa. Effect of contact pressure on fretting fatigue of austenitic stainless steel, Tribol.Int. 36 (2003) 79-85.

[26] JA Pape, RW Neu. A comparative study of the fretting fatigue behavior of 4340 steel and PH 13-8 Mo stainless steel, Int.J.Fatigue. 29 (2007) 2219-2229.

[27] BU Wittkowsky, PR Birch, J Dominguez, S Suresh. An apparatus for quantitative fretting testing, Fatigue & Fracture of Engineering Materials & Structures. 22 (1999) 307-320.

[28] LHL Martins, LS Rossino, WWB Filho, JA Araújo. Detailed design of fretting fatigue apparatus and tests on 7050-T7451 Al alloy, Tribology - Materials, Surfaces & Interfaces. 2 (2008) 39-49.

[29] AA Walvekar, BD Leonard, F Sadeghi, B Jalalahmadi, N Bolander. An experimental study and fatigue damage model for fretting fatigue, Tribol.Int. 79 (2014) 183-196.

[30] A Mugadu, DA Hills, D Nowell. Modifications to a fretting-fatigue testing apparatus based upon an analysis of contact stresses at complete and nearly complete contacts, Wear. 252 (2002) 475-483.

[31] MP Szolwinski, TN Farris. Mechanics of fretting fatigue crack formation, Wear. 198 (1996) 93-107.

[32] PL Hurricks. The mechanism of fretting — A review, Wear. 15 (1970) 389-409.

[33] E Sauger, S Fouvry, L Ponsonnet, P Kapsa, JM Martin, L Vincent. Tribologically transformed structure in fretting, Wear. 245 (2000) 39-52.

[34] SR Pearson, PH Shipway. Is the wear coefficient dependent upon slip amplitude in fretting? Vingsbo and Söderberg revisited, Wear. 330–331 (2015) 93-102.

[35] H Mohrbacher, B Blanpain, JP Celis, JR Roos, L Stals, M Van Stappen. Oxidational wear of TiN coatings on tool steel and nitrided tool steel in unlubricated fretting, Wear. 188 (1995) 130-137.

[36] S Fouvry, P Kapsa, L Vincent. Quantification of fretting damage, Wear. 200 (1996) 186-205.

[37] S Fouvry, P Duó, P Perruchaut. A quantitative approach of Ti–6Al–4V fretting damage: friction, wear and crack nucleation, Wear. 257 (2004) 916-929.

[38] Y Berthier, L Vincent, M Godet. Velocity accommodation in fretting, Wear. 125 (1988) 25-38.

[39] M Godet. The third-body approach: A mechanical view of wear, Wear. 100 (1984) 437-452.

[40] C Colombié, Y Berthier, A Floquet, L Vincent, M Godet. Fretting: Load Carrying Capacity of Wear Debris, Journal of Tribology. 106 (1984) 194-201.

[41] N Diomidis, S Mischler. Third body effects on friction and wear during fretting of steel contacts, Tribol.Int. 44 (2011) 1452-1460.

[42] R Merhej, S Fouvry. Contact size effect on fretting wear behaviour: application to an AISI 52100/AISI 52100 interface, Lubr Sci. 21 (2009) 83-102.

[43] AR Warmuth, SR Pearson, PH Shipway, W Sun. The effect of contact geometry on fretting wear rates and mechanisms for a high strengthsteel, Wear. 301 (2013) 491-500.

[44] R Rybiak, S Fouvry, B Bonnet. Fretting wear of stainless steels under variable temperature conditions: Introduction of a 'composite' wear law, Wear. 268 (2010) 413-423.

[45] K Asai, T Kudo, H Yoda. Experimental Validation of Fretting Fatigue Strength and Fretting Wear Rate at Contact Surface of Turbine-Blade-Shroud Cover, Journal of Engineering for Gas Turbines and Power. 136 (2013) 042101-042101.

[46] J Ding, G Bandak, SB Leen, EJ Williams, PH Shipway. Experimental characterisation and numerical simulation of contact evolution effect on fretting crack nucleation for Ti–6Al–4V, Tribol.Int. 42 (2009) 1651-1662.

[47] NKR Naidu, SGS Raman. Effect of contact pressure on fretting fatigue behaviour of Al–Mg–Si alloy AA6061, Int.J.Fatigue. 27 (2005) 283-291.

[48] KJ Kubiak, TW Liskiewicz, TG Mathia. Surface morphology in engineering applications: Influence of roughness on sliding and wear in dry fretting, Tribol.Int. 44 (2011) 1427-1432.

[49] H Mohrbacher, B Blanpain, J- Celis, JR Roos. The influence of humidity on the fretting behaviour of PVD TiN coatings, Wear. 180 (1995) 43-52.

[50] MR Hirsch, RW Neu. Fretting damage in thin sheets: Analysis of an experimental configuration, Tribol.Int. 44 (2011) 1503-1510.

[51] M Lavella, D Botto. Fretting wear characterization by point contact of nickel superalloy interfaces, Wear. 271 (2011) 1543-1551.

[52] Hills D.A Nowell D, Mechanics of fretting fatigue, Kluwer Academic Publishers, Dordrecht, 1994.

[53] AR Kallmeyer, A Krgo, P Kurath. Evaluation of Multiaxial Fatigue Life Prediction Methodologies for Ti-6Al-4V, Journal of Engineering Materials and Technology. 124 (2002) 229-237.

[54] JA Araújo, D Nowell. The effect of rapidly varying contact stress fields on fretting fatigue, Int.J.Fatigue. 24 (2002) 763-775.

[55] B Alfredsson, A Cadario. A study on fretting friction evolution and fretting fatigue crack initiation for a spherical contact, Int.J.Fatigue. 26 (2004) 1037-1052.

[56] SA Namjoshi, S Mall, VK Jain, O Jin. Fretting fatigue crack initiation mechanism in Ti-6Al-4V, Fatigue & Fracture of Engineering Materials & Structures. 25 (2002) 955-964.

[57] D Nowell, D Dini, DA Hills. Recent developments in the understanding of fretting fatigue, Eng.Fract.Mech. 73 (2006) 207-222.

[58] D Taylor, The theory of critical distances: a new perspective in fracture mechanics, Elsevier, Oxford, 2007.

[59] JA Araújo, L Susmel, D Taylor, JCT Ferro, JLA Ferreira. On the prediction of high-cycle fretting fatigue strength: Theory of critical distances vs. hot-spot approach, Eng.Fract.Mech. 75 (2008) 1763-1778.

[60] KL Johnson, Contact mechanics, Cambridge University Press, Cambridge, 1985.

[61] RD Mindlin. Compliance of elastic bodies in contact, Jnl. Appl. Mech. 16 (1949) 259-268.

[62] S Fouvry, P Kapsa, L Vincent. Analysis of sliding behaviour for fretting loadings: determination of transition criteria, Wear. 185 (1995) 35-46.

[63] GM Hamilton. Explicit Equations for the Stresses beneath a Sliding Spherical Contact, Proceedings of the Institution of Mechanical Engineers, Part C: Journal of Mechanical Engineering Science. 197 (1983) 53-59.

[64] DF Socie, GB Marquis, Multiaxial fatigue, Society of Automotive Engineers, Inc, Warrendale, 2000.

[65] M Makkonen. Statistical size effect in the fatigue limit of steel, Int.J.Fatigue. 23 (2001) 395-402.

[66] M Makkonen. Notch size effects in the fatigue limit of steel, Int.J.Fatigue. 25 (2003) 17-26.

[67] A Lehtovaara, R Rabb. A numerical model the calculation of fretting fatigue crack initiation for smooth spherical contact, Finnish Journal of Tribology. 25 (1) (2006) 23-29.

[68] O Jin, S Mall. Effects of slip on fretting behavior: experiments and analyses, Wear. 256 (2004) 671-684.

[69] R Rabb, Todennäköisyysteoriaan pohjautuva väsymisanalyysi, Books on Demand, Helsinki, 2013, ISBN 978-952-286-210-5.

[70] R Rabb. Todennäköisyysteoriaan pohjautuva väsymisanalyysi, Rakenteiden Mekaniikka. Vol. 45, Nro 3 (2012) s. 162-187.

ORIGINAL PUBLICATIONS

Publication I

Effect of start-up schemes and amplitude of tangential motion on friction behavior in fretting point contact

by

J Hintikka. A Lehtovaara & C Lönnqvist

Tribology International, 44 (2011), 1535-1543

doi:10.1016/j.triboint.2010.10.015

Tribology International 44 (2011) 1535–1543

Contents lists available at ScienceDirect

Tribology International

journal homepage: www.elsevier.com/locate/triboint

Effect of start-up schemes and amplitude of tangential motion on friction behavior in fretting point contact

Jouko Hintikka [a,*], Arto Lehtovaara [a], Christian Lönnqvist [b]

[a] Department of Mechanics and Design, Tampere University of Technology, P.O. Box 589, 33101 Tampere, Finland
[b] Research & Development, Wärtsilä Finland Oy, P.O. Box 244, 65101 Vaasa, Finland

ARTICLE INFO

Article history:
Received 20 May 2010
Received in revised form
30 September 2010
Accepted 14 October 2010
Available online 21 October 2010

Keywords:
Friction
Fretting
Partial and gross slip
Quenched and tempered steel

ABSTRACT

The friction coefficient is an important factor in fretting fatigue. The frictional behavior of quenched and tempered steel 34CrNiMo6 was studied in smooth fretting point contact with measurements at partial and gross slip conditions. The effect of the start-up scheme is studied by altering the way the displacement amplitude is developed to the target value. This only has a minor effect on the maximum friction coefficient but it does alter the frictional behavior. The friction coefficient increases as tangential displacement amplitude is increased and it has a maximum value of 1.5–1.6 at the transition to gross sliding.

1. Introduction

Fretting may occur between any two contacting surfaces where short amplitude reciprocating sliding is present over a large number of cycles. This oscillatory movement can take place at the micrometric level, even without gross sliding of the contacting surfaces. This causes fretting wear of the surfaces and fretting fatigue, which can lead to a rapid decrease in fatigue life. Fretting wear is related to surface degradation processes and it can be detected by the appearance of wear debris. The appearance and severity of fretting fatigue is essentially dependent on the stress field in a contact (sub)surface caused by external bulk and contact loading. This stress field, affected by the oscillatory movement of the contacting surfaces, promotes crack nucleation. An extensive description of the fretting phenomenon and its associated contact mechanics is given in Refs. [1–3].

The oscillatory tangential movement of the contacting bodies is the basis of the fretting phenomenon. This causes tangential traction in the contact, which is known to have a very strong impact on the stress field and thus on cracking risk. The level of the tangential traction is strongly dependent on the friction between the contacting surfaces, and it is therefore crucial to determine the friction coefficient in fretting contact. This input value is one of the main uncertainties when designing components at risk of fretting damage.

Friction evolution on fretting contact in partial and gross slip conditions has mostly been studied on titanium and aluminium alloys [4,5]. In general, high friction coefficients have been found in fretting contacts. However, little attention has been given to quenched and tempered steel, which is a commonly used material in heavily loaded conditions, such as in diesel engines, where the contact surfaces have to transfer high tractions. In diesel engines this material is used for jointed components such as connecting rods, camshafts and crankshafts whose loading conditions pose a potential risk of fretting.

The vast majority of the fretting studies have been conducted in gross sliding conditions, where the whole contact is sliding. The slip zone friction coefficient has been investigated using different displacement amplitude build-up methods and it was concluded that the most stable results are obtained through a continuous increase of the cyclic tangential load in small incremental amounts until it reaches the point of global sliding [4]. In fretting tests performed with quenched and tempered steel it was found that the friction coefficient has a high value at the beginning of the test which gradually decreases to lower values, especially in mixed slip conditions [6,7]. Fretting fatigue cracks are also initiated during the first 500×10^3 load cycles [7]. In these experiments the tangential displacement amplitude was continuously increased from zero to the target level during start-up. The purpose of this study is to find out if displacement amplitude build-up schemes, and the range of tangential displacement amplitudes, have an effect on the frictional behavior of quenched and tempered steel. The high friction coefficient at the beginning of the test [6,7] is of particular interest.

* Corresponding author. Tel.: +358 3 311511; fax: +358 3 31152307.
E-mail address: jouko.hintikka@tut.fi (J. Hintikka).

0301-679X/$ - see front matter © 2010 Elsevier Ltd. All rights reserved.
doi:10.1016/j.triboint.2010.10.015

2. Methods

2.1. The point contact

A sphere (Test pad) on a plane (Tension bar) makes a contact with the forces and coordinates as shown in Fig. 1.

Loading the contact with normal force P gives a circular contact area with a radius of a. Adding tangential force Q causes the annulus inside the Hertzian area to slip. The normal Hertzian contact pressure distribution of smooth surfaces is assumed. When the tangential load is small enough ($Q<\mu P$), contact is in partial slip and the circular area with the radius of c will stick. Increasing the tangential load decreases the radius of the stick area until the tangential load is equal to μP after which gross sliding will take place. The tension bar is subjected to a constant bulk stress which is in the same direction as the tangential displacement amplitude. A tangential load causes deformations to the test specimen and a relative tangential displacement δ, which is given as Eq. (1) [8]

$$\delta=\frac{3\mu P}{16a}\left(\frac{2-\nu_1}{G_1}+\frac{2-\nu_2}{G_2}\right)\left(1-\left(1-\frac{Q}{\mu P}\right)^{2/3}\right) \tag{1}$$

where μ is the friction coefficient, ν_i Poisson's constant and G_i the shear module. Evaluation of the friction coefficient depends on the running condition as the contact is fretted. Under partial slip conditions energy ratio is used. A reciprocating tangential load in the contact generates frictional work E_d which can be derived from the area of the fretting hysteresis loop. The total energy of one load cycle can be solved from the tangential force amplitude and displacement amplitude as $E_t=4\delta Q$. The ratio of these energies is the energy ratio $A=E_d/E_t$. An analytical solution for the energy ratio is given as Eq. (2) [9]

$$A=\frac{6}{5}\frac{\left[1-\left(1-\frac{Q}{\mu P}\right)^{5/3}-\frac{5Q}{6\mu P}\left(1+\left(1-\frac{Q}{\mu P}\right)^{2/3}\right)\right]}{\frac{Q}{\mu P}\left[1-\left(1-\frac{Q}{\mu P}\right)^{2/3}\right]} \tag{2}$$

The energy ratio is calculated from the measured fretting hysteresis loop and Eq. (2) can be used to calculate the friction coefficient numerically. In gross sliding, Coulombs law is used to define the friction coefficient from tangential force amplitude and normal force alone.

$$\mu=\frac{Q}{P} \tag{3}$$

2.2. The test device

The test device has three similarly loaded contacts running simultaneously. Each contact is a Hertzian sphere in plane configuration. The test device used is presented schematically in Fig. 2.

Cyclic tangential motion in a test specimen is generated through cyclic rotation of the lever arm. The normal force is generated using a hydraulic cylinder. Three test pads are attached to the lever arm and are then pushed against the tension bars, which then form Hertzian contact pairs. The symmetrical alignment causes the normal force, tangential force and tangential movement to be distributed evenly between the specimens. The tangential displacement amplitude and the motion frequency of the test pads can be adjusted and controlled accurately by the electric shaker control unit. The normal load, tangential displacement amplitude and the bulk stress are adjusted and measured separately. The tangential force resisting the movement is measured. By combining the displacement and the tangential force, a fretting hysteresis loop can be plotted. A more detailed description of the test device can be found from Ref. [10].

Tangential force causes compliance in the test specimen and the fretting test device. The measured total tangential motion is the combination of the test device related compliance and actual movement between the test pad and tension bar. The test device compliance was evaluated in two steps. The compliance related to the test pads was solved using a FE-calculation and that of the tension bar was measured from the test device. These test device related compliances are now removed from the measured data in normal data analysis. The effects of removing the compliances are:

- The actual displacement amplitude gets smaller. Compliances are linearly proportional to tangential load. Structural elastic deformations of the test device were determined to be $\sim 1.6\times10^{-9}$ m/N. This is about 15–20% of the measured displacement amplitude, depending on the applied normal force.
- The energy ratio gets bigger, which decreases the friction coefficient in partial slip Eq. (2).
- There was a closer correspondence between the measured data and the analytical results for the limits of gross slip (Eqs. (1) and (2) when $Q=\mu P$).

Normal force and the bulk stresses are collected at the frequency of 2 Hz. The tangential force and displacement amplitude data is collected at the higher frequency of 5000 Hz. As a part of data

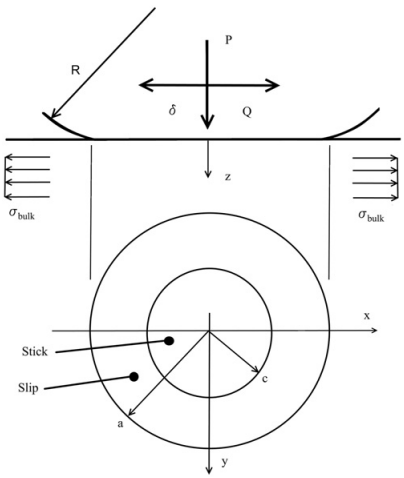

Fig. 1. Hertzian contact has radius of a. Tangential load Q promotes slip in the annulus $c<x<a$ in partial slip. In gross slip all contacting surface slips.

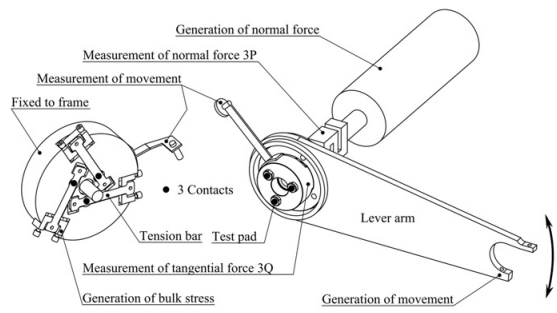

Fig. 2. Schematic view of the test device.

analysis, the tangential force and the displacement amplitudes are processed in sets of 40 sequential load cycles. The data sets are then used to calculate the corresponding average load cycles for the tangential force and displacement amplitudes. These average load cycles are then used to define one average fretting hysteresis loop for the processed 40 cycles. This method reduces noise but it also decreases resolution so that occasional rapid and small changes in data can be lost. These data sets of 40 cycles are collected from raw data files at different time intervals. Normally this is done once every 10 min for the duration of the whole test. However, when analyzing the start of the test, much shorter time gaps of 1 and 12 s are mostly used, although the number of load cycles analyzed and the time intervals for data collection can be chosen at will to suit the analysis.

2.3. The test procedure

All the specimens were carefully cleaned with solvent, and the tests were carried out in a normal laboratory atmosphere. A constant bulk stress of 400 MPa was first applied to all three tension bars. Then the contacts were loaded with normal load. At the beginning of the fretting test, specific start-up phases were used to build up the tangential displacement amplitude. This experiment start-up phase lasts for up to 8000 load cycles, after which the displacement amplitude is kept at a constant value. The fretting tests were set to last for 2.8×10^6 load cycles. After the test, all the specimens were cleaned with solvent and the fretting scars were examined with an optical microscope and an optical profilometer.

2.4. The test specimen

The contact pads and tension bars were made from quenched and tempered steel EN 10083-1-34CrNiMo6+QT. The material has yield strength of 1056 MPa and an ultimate strength of 1160 MPa. The spherical shape of the test pad was achieved through grinding and polishing. The radius of the test pads was set to 285 ± 15 mm. The tension bar has a width of 15 mm and a thickness of 5 mm. The tension bars had a similar kind of surface finish to the test pads, first ground to plane and then polished. All the specimens were measured with an optical profilometer. The measured surface roughness values are listed in Table 1.

Sa represents the roughness average, the arithmetic mean of the absolute value of the surface departures from the mean plane. *Sz* is the average of the ten greatest peak-to-valley separations in the sample. The analyzed surface has an area of 3.8×4.9 mm^2, measured with a 6.72 μm sampling.

Table 1
Surface roughness of specimens.

Contact body	*Sa* (μm)	*Sz* (μm)
Test pad	0.04–0.14	1.08–2.94
Tension bar	0.04–0.18	0.78–3.29

2.5. The test matrix

The tests were performed with a variety of displacement amplitudes including both partial slip and gross slip. The effect of the experiment start-up was investigated by altering the way the displacement amplitude was built up to the target level. Three different types of start-up phases were used:

Positive slope: Displacement amplitude is increased linearly from zero to the target level. The length of this phase is 8000 load cycles.

Step: The control signal for displacement amplitude is increased very rapidly (~4 load cycles) to the target level.

Negative slope: Displacement amplitude is increased rapidly to 30 μm so that gross sliding will take place instantly. Then displacement amplitude is linearly decreased to the target level. The length of this start-up phase is also 8000 load cycles.

Most of the tests were made with the positive slope start-up phase, whereas only a few displacement amplitude target levels were chosen for additional testing with the other start-up phases. In previous experiments, positive slope has been used as a standard procedure and high friction coefficients were achieved as the test pads rub themselves against the contact during the period of slowly increasing displacement amplitude [6]. The step start-up phase was chosen to investigate whether the gradual increase in the tangential displacement amplitude is the reason for the high friction coefficient obtained. Negative slope is clearly an extreme way to start the experiment as the pure gross sliding damages the surface topography and could thus affect the friction coefficient. The test matrix is shown in Table 2.

A test frequency of 40 Hz combined with a test length of 2.8×10^6 load cycles gives a good working rhythm as a finished test can be dismantled and a new one set to run once a day. Some of the highest displacement amplitudes were set to run at the lower 20 Hz frequency because of the limitations of the electric shaker control system. This also reduces frictional heating, which increases rapidly in gross sliding. The measurements made at the lower frequency are handled separately.

3. Results and discussion

The results are presented separately for each start-up style so that at first the positive slope is explained in great detail while the other two start-up styles are used as points of comparison. The long-term friction coefficient behavior has its own chapter, which only deals with the positive slope start-up style, as it will be shown that the start-up has little effect on the long-term friction coefficient.

3.1. The positive slope

The measured friction coefficient is presented as a function of load cycles in Fig. 3. In this start-up phase the tangential displacement amplitude is increased steadily from zero to the target value during the first 8000 load cycles.

Table 2
Test matrix. Displacement amplitude levels marked with "+" are in gross slip regime. The frequency of fretting loading is 40 Hz but amplitude levels marked with { } were done with a lower frequency of 20 Hz. Hertzian contact has maximum pressure of p_0.

	P **(N)**	p_0 **(MPa)**	**Displacement amplitude (μm),** δ						
Positive slope	680	274	4	8	16+	{32+}	{64+}		
	1270	337	6	9	12	15	20+	{30+}	40+
Step	1270	337	6	9		15	20+		
Negative slope	1270	337		9		15	20+		

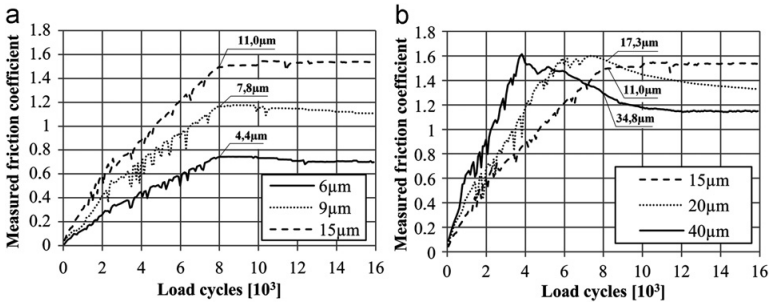

Fig. 3. The friction coefficient as a function of load cycles during start-up phase. Displacement amplitude levels are nominal values from the test matrix and actual values are marked next to the ending of the start-up phase.

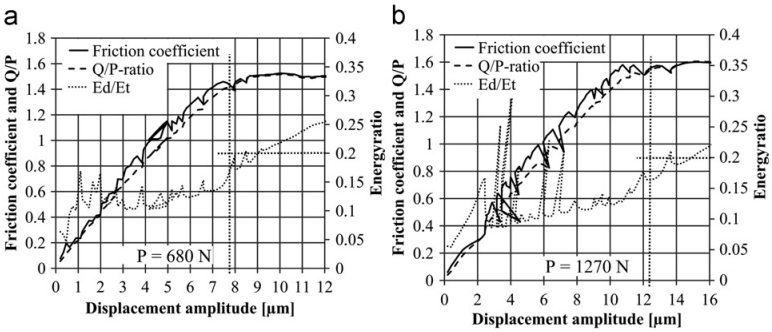

Fig. 4. Friction coefficient, Q/P-ratio and energy ratio as a function of displacement amplitude. $P=680$ N, $\delta=0$–16 μm and $P=1270$ N, $\delta=0$–20 μm. Analytical limits for gross slip are drawn on the charts from Eqs. (1) and (2).

As Fig. 3b shows, the maximum friction coefficient is observed at the transition from partial slip to gross sliding during the start-up phase, this being the highest value observed in any of the fretting tests carried out in this research. Any further increase in the value of the displacement amplitude in gross sliding has no effect on the friction coefficient. However, it rapidly decreases as a function of load cycles. In partial slip conditions the maximum value of the friction coefficient is measured right after the displacement amplitude build-up phase in all the tests, as shown in Fig. 3a. The influence of displacement amplitude on the friction coefficient can be clearly seen in Fig. 4, where the friction coefficient is plotted against measured and calibrated displacement amplitude.

Fig. 4 shows that during displacement amplitude build-up, the friction coefficient rises just over the ratio Q/P. The calculated value for gross sliding corresponds quite closely with its measured counterpart. The analytical limit for gross sliding can be solved from Eqs. (1) and (2) by setting $Q=\mu P$, which gives an energy ratio limit of 0.2 and displacement amplitude limits of $\delta_{680N}\sim 7.7$ μm and $\delta_{1270N}\sim 12.3$ μm. All the tests show the same friction coefficient development as illustrated in Fig. 4, so that the maximum friction coefficient can be read from the plot for any given displacement amplitude from the partial slip domain. The maximum values for the friction coefficient are: $\mu_{max-1}=1.52$ for $P=680$ N and; $\mu_{max-2}=1.61$ for $P=1270$ N.

The displacement amplitude build-up phase is characterized by rapid changes in the energy ratio and the friction coefficient. This can be clearly seen from Fig. 5, which is a short-time-interval analysis from part of the displacement amplitude build-up phase shown in Fig. 4b. The average fretting loops are calculated from two load cycles.

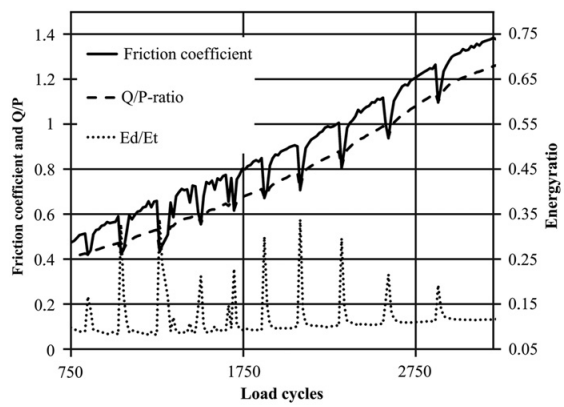

Fig. 5. Friction coefficient, Q/P-ratio and energy ratio as a function of load cycles. $P=1270$ N, $\delta=2.6$–8.7 μm.

Fig. 5 shows that contact is momentarily in gross slip and that this occurs even with very low displacement amplitudes when the tangential force is low. The test device has three contacts running simultaneously so it is quite possible that these brief moments of gross sliding take place separately. There can be deviations in the value of the energy ratio assuming that only one or two of the contacts are in gross slip. These brief moments of gross slip cease after the displacement amplitude build-up phase ends, or when

constant gross slip is achieved. Partial slip behavior is somewhat unstable as the displacement amplitude increases steadily, which can be explained by an uneven friction coefficient distribution inside the contact, as will be shown later.

The friction coefficient tends to increase as the contacting surfaces are fretted [2]. Most metals produce an oxide film in a normal atmosphere which is softer and weaker than the bulk of the material [11]. Manufacturing processes and contaminants may also have an effect on the frictional properties of the top surface layers. In these experiments, partial slip may occur even if the test specimens are covered with a weak surface layer, but this is characterized by a low friction coefficient. The low shear strength of the top surface layers limits the value of the friction coefficient, and periodic gross sliding occurs at lower loading levels than those observed for constant gross sliding. The top surface layers wear when the whole contacting surface slides, and this exposes a pure metallic surface to the contact resulting in an increase in the friction coefficient. The contact will go back to partial slip as soon as the friction coefficient has raised high enough to support it. Because there is still potential for the friction coefficient to increase in the contact, this process will repeat itself multiple times before the maximum friction coefficient is reached and continuous gross sliding takes place. As the tangential displacement amplitude increases, so does the tangential force amplitude, which reduces the size of the stick area. The stick area is much smaller than the Hertzian contact area, even with very small tangential forces. Because the friction coefficient rises as the tangential force increases, the actual reduction in the size of the stick area is quite small. With the measured values, the traction bears most of the tangential force in the slip area, as can be seen when comparing the measured tangential force and the integral of traction over the slip area. In partial slip, the friction coefficient is low in the stick zone because the surface is relatively intact and it cannot support the tangential load if the slip zone fails to carry it for any reason. A slightly higher maximum friction coefficient with higher normal load could be the result of better penetration of the top surface layers. The existence of the surface film explains low values for the friction coefficient but does not explain its high values.

The rise in the friction coefficient to very high values as the tangential displacement amplitude increases can be explained by the adhesive friction theory presented by Bowden and Tabor [11,12]. The junction growth comes from plastic flow between the asperities as they are loaded with local normal load and local tangential force and this leads to a high friction coefficient. In these experiments, the tangential force results mostly from the asperity junction growth in the slip zone, which occurs as the contacting surfaces are loaded with normal load and tangential displacement. These junctions are stuck locally and the resulting tangential force occurs as plastic flow which resists local sliding. This implies that the partial slip cases have frictional work coming from plastic deformations of the junctions in the slip zone, which is then measured and used to calculate energy ratio and friction coefficient. The measured friction coefficient is then lower in partial slip than it is in gross slip as a result of incomplete junction growth as junction growth is just sufficient to produce the real contact area and traction field to hold the tangential force. The wear of the surface films is a process which increases the shear strength of the adhesive junctions. According to this hypothesis, the friction coefficient is not constant in the slip zone because local slip has a wide range of values in a slip zone (0, $\sim 1/2\delta$ [3]). More precise models for the friction coefficient are needed to increase the accuracy of contact models. Different variable friction coefficient models have been developed [13,14] and it is shown that a variable friction coefficient has an effect on the contact stresses, and that a close correspondence between FE fretting contact simulations and measured data may be achieved. However, much work still remains to be done in this area.

3.2. The step

In the step-like start-up method, the displacement amplitude is increased rapidly to the target level. In all the tests, the desired displacement amplitude level stabilizes in about 2 s, although values close to the target value of the displacement amplitude are recorded after $\sim$10 load cycles. The measured friction coefficient behavior can be seen in Fig. 6.

Step-like displacement amplitude build-up causes the friction coefficient to rise to high values during the initial load cycles. Because an unfretted surface has a low friction coefficient, the contact starts to run in gross sliding. A few hundred (150–500) load cycles are enough to increase the friction to levels that support partial slip. In experiments which are clearly in the partial slip domain, the friction coefficient is clearly higher than the Q/P-ratio. Both the maximum friction coefficient and the maximum Q/P-ratio are also somewhat higher than the maximum values from the positive slope start-up method, with corresponding tangential displacement amplitude values. For the nominal displacement amplitudes 6 and 9 μm, the differences are about 0.15 but the measured values for the friction coefficient are still significantly lower than the maximum values measured at the transition to gross sliding. Step-like start-up produces the same friction coefficient in gross sliding as positive slope does. The friction coefficient values merge with the ones measured with positive slope after 8000 load cycles, which is also the end of the start-up phase in positive-slope. It is possible that slightly higher Q/P-ratio for step-like start-up style in partial slip is related to surface degradation as positive slope has been fretted 8000 load cycles before it reaches the target displacement amplitude.

One difference between these two start-up types is the occurrence of brief moments of gross slip with positive slope start-up, whereas the step-like start-up style produces smooth curves as illustrated in Figs. 5 and 6. This difference comes from the frictional behavior associated with gross sliding and wear of surface films. As seen in Fig. 6, a step-like start-up to the experiment causes gross sliding which affects the whole contacting surface area (E_d/E_t is much greater than 0.2). The middle of the contact is subjected to the highest surface pressure and local slip is also quite noticeable because of the low traction resulting from the low initial friction coefficient. This causes a higher rate of wear in the middle than on the sides of the contact where the surface pressure is low. As the top surface layers and any possible contaminants are worn away, a pure metallic contact is formed. This action will firstly increase the friction coefficient in the middle of the contact, resulting in a

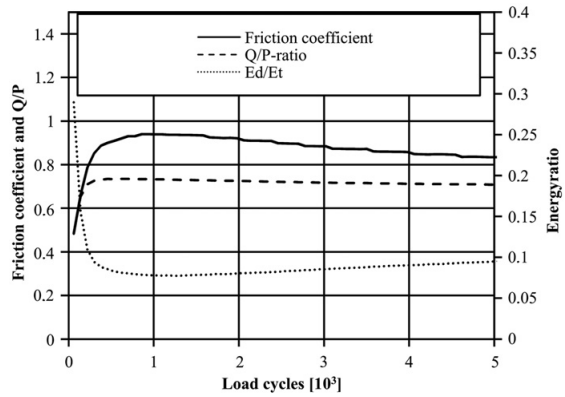

Fig. 6. Friction coefficient as a function of load cycles. Step start-up phase, $P=1270$ N, $\delta=4.6$ μm (6 μm nominal).

stronger stick area than that which was obtained in the positive slope tests, where the slip annulus wears more. The development of fretted surfaces as they occur under different start-up methods is illustrated in the schematic Fig. 7.

A strong stick area gives a stable contact, which can be seen when comparing Figs. 5 and 6, as the contact stays in partial slip once the short period of gross slip ends. The slightly greater difference between the friction coefficient and the *Q*/*P*-ratio in step-like start-up than positive slope start-up can be explained by uneven distribution of friction coefficient and by the use of the energy ratio to evaluate the friction coefficient, (although Eq. (2) assumes a constant friction coefficient in the contact). The remnants of the surface layers in the sliding annulus decrease the friction coefficient locally. If the sliding annulus has low friction then the frictional work is also low and the energy ratio stays low. A low energy ratio yields higher values for the friction coefficient if Eq. (2) is used to evaluate it. This explains the slightly higher maximum friction coefficient measured with the small displacement amplitudes used in the step start-up phase. The conclusion is that there is no difference in the values of the friction coefficient between step-like and positive slope start-up, but the step-like start-up produces a stronger stick area as it has been fretted during the initial gross slip.

3.3. The negative slope

In negative slope tests, the displacement amplitude is increased to gross slip regime by first using a step-like start-up to increase the displacement amplitude to 30 μm and then gradually decreasing it to the desired target level. The resulting friction coefficient can be seen in Fig. 8.

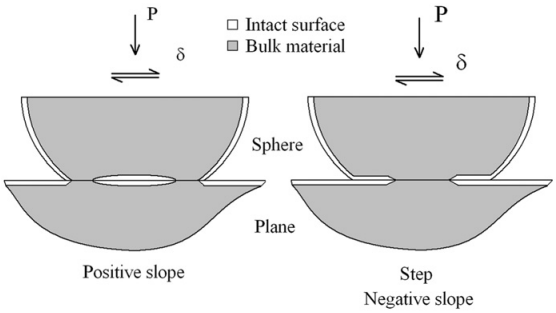

Fig. 7. Development of fretted surface in point contact with different start-up styles.

Just as with the step start-up phase, the friction coefficient needs a few hundred load cycles to build up. The maximum friction coefficient is 1.4–1.5, which is slightly lower than gross slip friction in the other two start-up methods. The friction coefficient decreases as the displacement amplitude decreases. A comparison between the positive slope and the negative slope reveals that the latter's friction coefficient decreases to smaller values than those observed in positive slope. This could be the result of poor metallic contact caused by the debris which is produced as the contact is fretted in gross slip during the start-up. Another explanation is suggested by the fretting scars, as these tests revealed a new kind of material response not seen in any other start-up method. A comparison between the normal and new kind of fretting scar is shown in Fig. 9.

Slides a and b present normal fretting scars. In the test with negative slope start-up there were always one or more fretting scars like those illustrated in slide c. There, part of the tension bar has literally been torn off, and that torn off material was usually found strongly adhered to the test pad. The size of the hole corresponds closely to the size of the Hertzian contact area and has a depth of roughly 1 mm. If this fracture happens during the start-up phase it surely has an impact on the measured friction coefficient and could explain the lower values of the friction coefficient when using this start-up method. Surprisingly, this severe fracture has little or no effect on the friction coefficient after the first 250×10^3 load cycles. However, it is possible that the friction coefficient does not come purely from sliding friction alone, as the transferred piece of material is pressed against the hole and it could be supported by its sides. The magnitude of the surface damage far exceeded expectation in the negative slope start-up phase. The surface was expected to suffer only light damage during the short period of gross slip at the start of the experiment. Because the tests were run for the whole 2.8×10^6 load cycles, it is possible that the fracture happens after the start-up. However, as the strain gauge data from the tension bar does not show a clear starting point for this damage, it is suspected that it happens quite rapidly at the beginning of the start-up phase, when the contact forces are highest.

3.4. Development of the friction coefficient as a function of load cycles

Fig. 10 shows the friction coefficient measurements for the duration of the whole test using the different start-up methods. The analysis starts after 10 min has elapsed, so the displacement amplitude build-up phase is not included in these results.

The differences in friction coefficient development in the positive slope and step are limited to the first few thousand load cycles and can be explained by small differences in actual

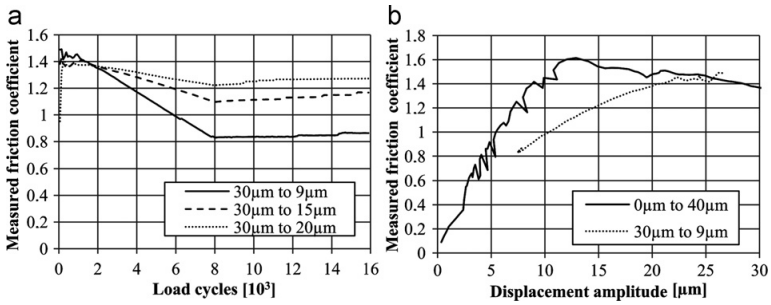

Fig. 8. Friction coefficient curves from negative slope start up (left). Comparison of friction coefficient between the negative slope and the positive slope as a function of displacement amplitude (right).

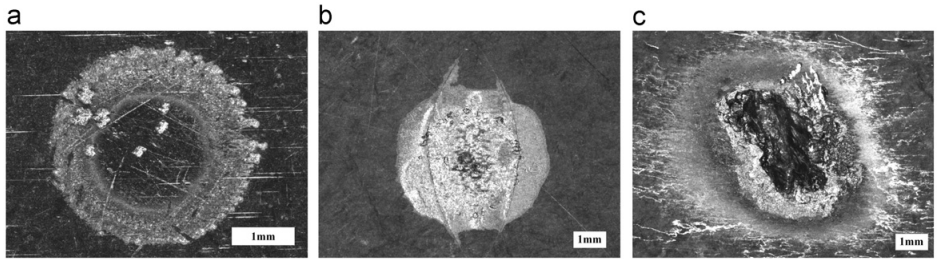

Fig. 9. The fretting scars from different tests. (a) Partial slip, (b) mixed slip and two macro cracks and (c) severe material transfer from negative slope test.

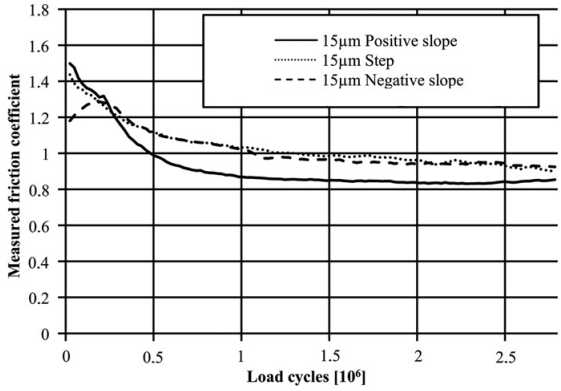

Fig. 10. The development of friction coefficient as function of load cycles, $P=1270$ N and $\delta=15$ μm, all start-up schemes.

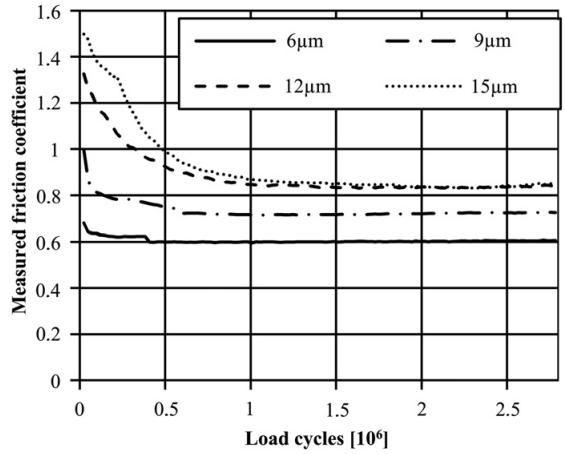

Fig. 11. The friction coefficient in mixed slip regime, $P=1270$ N.

displacement amplitude. Negative slope produces a noticeably lower friction coefficient after the start-up phase, but this then increases slowly and after about 250×10^3 load cycles the negative slope produces the same friction coefficient as the other start-up styles. Although Fig. 10 clearly shows that, after the same 250×10^3 load cycles, the positive slope has a more rapidly decreasing friction coefficient than the other two, this can be explained by the difference in material response, as it had large macro cracks in all three tension bars, whereas the other two had fewer and smaller macro cracks. At displacement amplitude of 20 μm, the friction coefficient curves are almost identical for all three start-up styles, which points to the conclusion that the start-up style has no effect on the long-term friction coefficient. The impact of the displacement amplitude level and the load cycles is only investigated in detail for positive slope start-up.

The initial friction coefficient develops during the displacement amplitude build-up phase as explained in chapter 3.1. The results are shown separately in cases of gross slip and mixed slip. Fig. 11 shows the measurements from the mixed slip regime.

In mixed slip regime, contacts changed running condition from partial slip to gross slip during the first 0.5×10^6 load cycles as energy ratio slowly increased over the value of 0.2. The friction coefficient drops from its initial value and stabilizes at a value which is dependent on the level of displacement amplitude: the lower the amplitude, the lower the value of the friction coefficient. The two highest displacement amplitude levels in Fig. 11 have identical steady state values for the friction coefficient. This can be explained by identical material response, as all three tension bars had large macro cracks in both tests. Cracking increases the amount of wear debris, and large cracks can reduce the rigidity of the contact. The two lowest test levels had only one cracking specimen in one test, so the friction coefficient is not greatly affected by cracking. The reason for the decrease in the friction coefficient could be, for example, the accumulation of wear debris or the work hardening of the asperities, which in turn reduces the potential for junction growth.

The tests where the contact was loaded to gross slip produces behavior like that illustrated in Fig. 12. Just as with the mixed slip regime, the positive slope has a friction coefficient development like the one explained in chapter 3.1. This means that during displacement amplitude build-up, all tests will make the transition from partial slip to gross slip if the target test level is in gross slip regime characterized by high tangential forces.

In gross slip the friction coefficient falls to a value ~0.83 after about 40×10^3 load cycles. This happens to measurements with displacement amplitudes of 30, 32, 40 and 64 μm, which are clearly in gross slip regime. This is then followed by an increase in the friction coefficient, which continues up to about 500×10^3 load cycles. This is illustrated by the 40 μm nominal displacement amplitude friction curve in Fig. 12. This phase of increasing friction coefficient is similar to the one observed in negative slope start-up. The friction coefficient stabilizes to a value of about 0.9. This can be explained by material response, as there was evidence of strong material transfer between the test specimens in all cases of gross slip. Instead of producing macro cracks, material was typically transferred from the tension bar to the test pad from the original Hertzian contact area. This results in severe damage to the contacting surfaces, which could explain the lowered friction

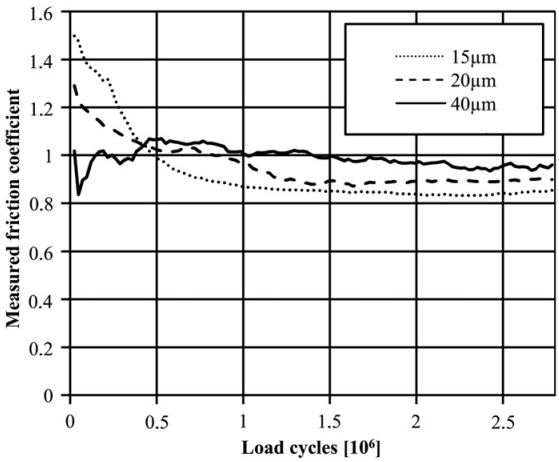

Fig. 12. The friction coefficient in gross slip. $P=1270$ N.

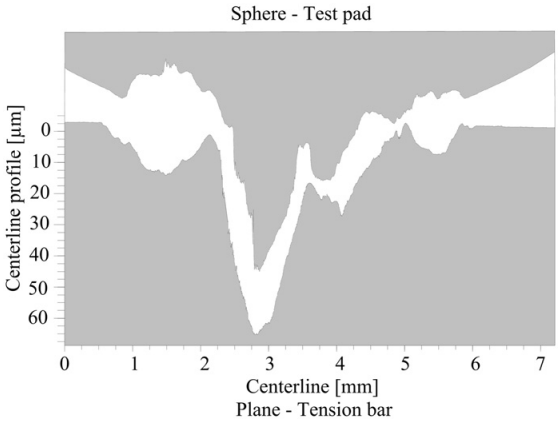

Fig. 13. Wear profiles from the tension bar (below) and test pad (above).

coefficient. As the contacts are also worn significantly in gross sliding, this leads to a slowly increasing friction coefficient as the work hardened layer is worn away and the contact area spreads to the intact area around the original Hertzian area. The contact area increases as the spherical surface of the test pad wears away. Material transfer can be seen clearly in Fig. 13, where the wear profiles of the test pad and the tension bar are compared.

Note that Fig. 13 does not correspond to the fretting scar type illustrated in Fig. 9c, although both indicate material transfer. With small displacement amplitudes there is no large scale material transfer, but in gross slip the area of original Hertzian contact shows clear signs of material transfer. Some material transfer can be observed from tests near gross slip regime. Material transfer occurs with both normal forces and indicates strong adhesion between specimens.

3.5. Plasticity in the contact

Because high friction coefficients have been measured, it is assumed that the friction is strongly adhesive. According to adhesive friction theory, high friction comes from the junction growth of the contacting asperities. The maximum friction force is limited by the shear strength of the junctions. A simple equation is given to explain junction growth [12]

$$p^2+\alpha q^2=\alpha s_y^2 \tag{4}$$

The symbols p and q are normal pressure and surface traction and s_y the shear strength of the material. Constant α relates to the junction growth. The real contact area A_{real} can be estimated if tractions are estimated as [12]

$$\left(\frac{P}{A_{real}}\right)^2+\alpha\left(\frac{Q}{A_{real}}\right)^2=\alpha S_y^2 \tag{5}$$

To estimate the real contact area the shear strength is assumed to be the shear yield strength of the bulk material which is then estimated as $(1/\sqrt{3})$ von Mises yield strength. Constant α has a value 9, which is a good estimate for plastic contact, although it could be high as 12 [11,15]. The resulting real contact areas from maximum forces are listed in Table 3.

As illustrated in Table 3, according to the adhesive friction theory (which ignores the bulk stresses in the tension bar) a high proportion of the contact is plastic. Because the friction coefficient is as high as it is, the effect of the normal force on the real contact area is minimal, as it is outweighed by the large tangential force, and the precise value of α also has little effect on the value of the real contact area.

A linearly elastic stress analysis [16] was used to analyze the contact stresses in this study and it reveals that contact stresses rise to high values which exceed not only yield strength, but in some cases, the ultimate strength. The measurement with normal force $P=1270$ N and a displacement amplitude of 15 μm has von Mises stress along the contacts center line, as presented in Fig. 14.

Fig. 14 shows that there is macroscopic yielding in the contact. The contact stresses rise to high values due to the increasing

Table 3
Real contact area according to adhesive friction theory.

	$P=680$ N $Q=1030$ N	$P=1270$ N $Q=2040$ N
A_{real} (mm^2)	1.73	3.42
A_{real}/A_{Hertz}	0.47	0.61

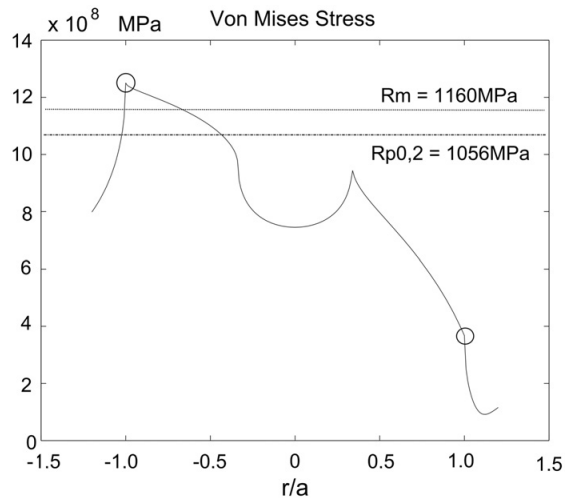

Fig. 14. Von Mises stress from measurement, $P=1270$ N and $\delta=11$ μm (15 μm nominal). Yield limit *Rp* 0.2 and ultimate strength *Rm* are shown.

tangential force which occurs as the tangential displacement amplitude is increased to values near gross slip. The high stresses can explain the severe surface damage observed in the tests made with negative slope start-up phase. High plasticity is observed in the measurements made with the higher normal load, whereas the lower normal load results in von Mises stresses just reaching the yield limit at the highest tangential loads. Macroscopic plasticity could explain the severe surface damage with a higher normal load, but material transfer also occurred with the lower normal load without any significant plasticity.

3.6. Effect of load frequency

The test frequency is one of the variables in studies of fretting fatigue, and few tests were carried out at the lower test frequency. It has been previously shown that the test frequency has a small but measurable effect on the friction coefficient with quenched and tempered steel [6]. In this study all the recorded results with a test frequency of 20 Hz are consistent with tests made with 40 Hz, although there are some differences. Given the limited data, one can merely state that frequency does not have a major affect on the friction coefficient, at least within the range of displacement amplitudes and frequencies used. The deviations in friction coefficient are most likely linked to material response in gross slip regime, or more specifically, to the severity of material transfer, rather than to the test frequency itself.

4. Conclusions

The development of the friction coefficient was investigated in smooth fretting point contact using different experiment start-up styles. The friction coefficient was evaluated using energy ratio in the case of partial slip and Coulombs law in gross slip condition. The following conclusions were reached:

- Friction coefficient increases as displacement amplitude is increased in partial slip condition. The increase in the friction coefficient was explained with the adhesive friction junction growth model, assuming that junction growth is proportional to local slip.
- The effect of the start-up scheme on frictional behavior is limited to the first quarter of the experiments and it has no major effect on the steady state friction coefficient. There is no difference in the values of the friction coefficient in the step-like and positive slope start-up schemes. However, the step-like start-up produces a more stable contact and frictional behavior, because the stick area has been fretted during the initial gross slip.
- After the start-up phase, the friction coefficient decreases as the number of load cycles increases and it stabilizes after 10^5–10^6 load cycles. The value of the steady state friction coefficient depends on the displacement amplitude and is also affected by the material response.
- The maximum values for the friction coefficient were obtained at the transition to gross slip, where it has a value of 1.5–1.6 depending on the normal force. The measured steady state friction coefficients are 0.6–1.0, mainly depending on displacement amplitude.
- Severe material transfer occurs when the contact is loaded to gross slip condition. This, together with a high measured friction coefficient, indicates strong adhesion and traction between the contacting surfaces. In many cases the severe material transfer can be explained by macroscopic plasticity observed with elastic von Mises stress analysis.

Acknowledgements

This study is a part of a FREFA (Fretting Fatigue in diesel engineering) research project. The authors are grateful for the financial support of Wärtsilä Finland Oy and The Finnish Funding Agency for Technology and Innovation.

References

[1] Waterhouse RB, editor. Fretting fatigue. Barking: Applied science publishers; 1981. 244 p.
[2] Hills DA, Nowell D. Mechanics of Fretting fatigue. Dordrecht: Kluwer Acadmic Publishers; 1994. 236 p.
[3] Johnson KL. Contact Mechanics. Cambridge: Cambridge University Press; 1985. 452 p.
[4] Alfredsson B, Cadario A. A study on fretting friction evolution and fretting fatigue crack initiation for a spherical contact. International Journal of Fatigue 2004;26:1037–52.
[5] Degat PReybet, Zhou ZR, Vincent L. Fretting cracking behavior on pre-stressed aluminum alloy specimens. Tribology International 1997;30:215–23.
[6] Pasanen A, Lehtovaara A, Rabb R, Riihimäki P. Friction behavior of quenched and tempered steel in partial and gross slip conditions in fretting point contact. Wear 2009;267:2200–7.
[7] Pasanen A, Lehtovaara A, Rabb R, Riihimäki P. On the fretting fatigue behavior of quenched and tempered steel in smooth point contact. Finnish Journal of Tribology 2009;28:26–37.
[8] Mindlin RD. Compliance of elastic bodies in contact. Journal of Applied Mechanics 1949;16:259–68.
[9] Fouvry S, Kapsa Ph, Vincent L. Analysis of sliding behavior for fretting loadings: determination of transition criteria. Wear 1995;185:35–46.
[10] Pasanen A, Järvisalo S, Lehtovaara A, Rabb R. Development of a test device for the evaluation of fretting in point contact. Lubrication Science 2009;21:41–52.
[11] Bowden F, Tabor D. The Friction and lubrication of solids (part I). Ely House, London W.I: Oxford University Press; 1950. 391 p.
[12] Bowden F, Tabor D. The Friction and lubrication of solids (part 2). Ely House, London W.I: Oxford University Press; 1964. 544 p.
[13] Wang RH, Jain VK, Mall S. A non-uniform friction distribution model for partial slip fretting contact. Wear 2007;262:607–16.
[14] Cheikh M, Quilici S, Cailletaud G. Presentation of KI-COF, a phenomenological model of variable friction in fretting contact. Wear 2007;262:914–24.
[15] Brizmer V, Kligerman Y, Etsion I. A model for junction growth of a spherical contact under full stick condition. Journal of Tribology 2007;129:783–90.
[16] Lehtovaara A, Rabb R. A numerical model for the calculation of fretting fatigue crack initiation for spherical contact. Finnish Journal of Tribology 2006;25:23–9.

Publication II

Fretting fatigue and friction of quenched and tempered steel in dry contact with aluminum bronze

by

J Hintikka, A Lehtovaara and A Mäntylä

Wear, 308 (2013), 155-165

doi:10.1016/j.wear.2013.07.002

Wear 308 (2013) 155–165

Contents lists available at ScienceDirect

Wear

journal homepage: www.elsevier.com/locate/wear

Fretting fatigue and friction of quenched and tempered steel in dry contact with aluminum bronze

Jouko Hintikka [a,*], Arto Lehtovaara [a], Antti Mäntylä [b]

[a] Department of Mechanics and Design, Tampere University of Technology, PO Box 589, 33101 Tampere, Finland
[b] Research & Development, Wärtsilä Finland Oy, PO Box 244, 65101 Vaasa, Finland

ARTICLE INFO

Article history:
Received 23 November 2012
Received in revised form
25 June 2013
Accepted 2 July 2013
Available online 6 July 2013

Keywords:
Fretting fatigue
Quenched and tempered steel
Bronze
Partial slip
Gross sliding

ABSTRACT

Bronze–steel contacts are common in machinery where the loading might give rise to fretting conditions. The flat surfaces of the quenched and tempered steel (QT) specimens were fretted with aluminum bronze spheres in partial slip and gross sliding conditions. The dry friction coefficient was around unity in gross sliding. Material transfer occurred from bronze pad to the QT-specimen and cracks initiated at these locations. Fretting map comparisons with QT–QT fretting tests showed that aluminum bronze–QT contact produces fatigue cracks with lower values in terms of displacement amplitude, tangential force amplitude and Findley cracking risk.

1. Introduction

Fretting fatigue is a phenomenon occurring between contacting bodies under oscillating tangential loads. The coefficient of friction (COF) is usually high in fretted contact, which can lead to high frictional tangential traction and ultimately to high surface stresses. The slipping between the contacting surfaces can cause fretting wear. Depending on the severity of the fretting wear, it can have either favourable or unfavourable impacts on the fretting fatigue life of the contact [1].

The properties of fretted steels and aeronautical alloys have been studied extensively [2–9], but there are few publications dealing with the fretting fatigue of steels in spherical partial slip conditions. Fretting studies with aluminium bronze normally show that it can have favourable properties under fretting conditions. Aluminium bronze has shown resistance to fretting wear [10] and soft aluminium bronze coatings on titanium substrate have reduced friction [11] and increased fretting fatigue life [12].

Bronze–steel contacts are common in machinery where the loading might give rise to fretting conditions. Such contact conditions can be found, for example, when bronze shims are used between steel bodies in medium speed diesel engines. Due to high firing and inertia forces in the engine, many contacts are under a heavy cyclic load and experience huge number of loading cycles. Reliability of such contacts is extremely important. This makes studying fretting of bronze–steel contacts an interesting and important topic. In this study the properties of quenched and tempered steel (QT) are investigated when fretted with spherical bronze pads in partial slip and gross sliding conditions. The results are compared to the measurements already published for QT–QT material pair [13–15].

2. Theoretical background

2.1. The Hertzian point contact

A sphere (test pad) on a plane (test specimen), as shown in Fig. 1A, makes contact with the forces and coordinates as follows. The Hertzian sphere-on-plane contact with radius R, has a contact radius of a when it is loaded with a normal load P. When a tangential force Q is introduced under partial slip conditions, the outer annulus slips and the radius of the stick zone becomes c. The radius of stick zone is dependent on loading conditions and the COF so that the value of c decreases from a to zero when the ratio of $Q/\mu P$ increases from zero to one. The analytical solution for tangential displacement is, according to Mindlin [16]:

$$\delta_a = \frac{3\times\mu\times P}{16\times a}\times\left(\frac{2-\nu_1}{G_1}+\frac{2-\nu_2}{G_2}\right)\times\left\{1-\left(1-\frac{Q}{\mu\times P}\right)^{2/3}\right\} \quad (1)$$

The surface sliding in the outer annulus of the point contact causes frictional energy dissipation E_d which can be used to

* Corresponding author. Tel.: +358 3 311511; fax: +358 3 31152307.
E-mail address: jouko.hintikka@tut.fi (J. Hintikka).

0043-1648/$ - see front matter © 2013 Elsevier B.V. All rights reserved.
http://dx.doi.org/10.1016/j.wear.2013.07.002

Nomenclature

Symbol	Explanation
a	Radius of point contact
A	Energy ratio
c	Radius of stick area
f_F	Findley fatigue criterion
E	Modulus of elasticity
E_d	Frictional energy dissipation
E_t	Total energy ($4\times\delta\times Q$)
EDS	Energy dispersive X-ray spectroscopy
f_{Fr}	Shear fatigue limit
FCR	Findley cracking risk
G	Shear module
k	Additional compliance
k_{Fr}	Findley fatigue criteria constant
k_s	Statistical size factor
P	Normal force
p_0	Maximum normal surface pressure
p_H	Normal traction
Q	Tangential force
R	Radius of sphere
Ruiz	Ruiz damage criterion
S_u	Ultimate stress
S_y	Yield stress (0.2%)
S_f	Fatigue stress
S_a	Average 3D surface roughness
S_t	3D max peak to valley distance
SEM	Scanning electron microscope
u	Surface sliding in x-direction
β	Dundur's parameter
σ_{VMmax}	Maximum Von Mises stress
σ_{bulk}	Static tensile bulk stress
δ	Tangential displacement
δ_a	Analytical tangential displacement
δ_m	Measured tangential displacement
$\sigma_n(t)$	Normal stress
ν	Poisson ratio
μ, COF	Coefficient of friction
τ_0	Maximum tangential surface pressure
τ_a	Shear stress amplitude
τ_s	Shear traction in x-direction

estimate the COF in partial slip conditions according to Fouvry [17]:

$$A=\frac{E_d}{E_t}=\frac{6}{5}\times\frac{1-(1-Q/\mu\times P)^{5/3}-5\times Q/6\times\mu\times P\times(1+(1-Q/\mu\times P)^{2/3})}{Q/\mu\times P\times(1-(1-Q/\mu\times P)^{2/3})} \quad (2)$$

The value of E_d can be calculated from the area of the measured fretting hysteresis loop and the total energy from the formula $E_t=4\times\delta\times Q$, where both values are obtained from the fretting test data. In gross sliding conditions, Coulombs law is used to define the COF from the tangential force amplitude and the normal force:

$$\mu=Q/P \quad (3)$$

There can also be mixed slip conditions where the running condition changes between partial slip and gross sliding during a fretting test [18]. Using Eqs. (2) and (3), the COF can be estimated for all running conditions. The mechanics of Hertzian point contact are thoroughly explained by Johnson [19]. The severity of contact loading is evaluated via the Findley cracking risk (FCR). The calculations were performed numerically using Hamilton's explicit stress equations [20] and the Findley fatigue criterion [21], enhanced by a statistical size factor concept, as illustrated in Ref. [22]. The FCR is shown in Eq. (4):

$$\mathrm{FCR}=k_S^{-1}\times d_F=k_S^{-1}\times\max[(\tau_a(t)+k_{Fr}\times\sigma_n(t))/f_{Fr}] \quad (4)$$

The FCR is a purely stress based damage criterion which does not take into a count the effects of fretting surface sliding. The fretting damage criterion developed by Ruiz [23] includes relative surface sliding, so this criterion might be more suitable for estimating the severity of the fretting conditions. Vidner et al. [24] proposed a modification to the Ruiz criterion where the uniaxial stress component was replaced by a multi-axial one and the frictional work by a frictional power. In this study the Ruiz criterion is calculated as shown in Eq. (5).

$$\mathrm{Ruiz}=\mathrm{FCR}\times 4\times\tau_S\times u \quad (5)$$

The product of $4\times\tau_s\times u$ is the frictional work done by an arbitrary surface point. The shear traction τ_s can be expressed as the product of surface normal pressure and the COF even under partial slip conditions because the relative surface sliding u is zero in sticking regions.

2.2. The elasticity miss match

The limitations of Eqs. (1) and (2) are that they are based on analytical half-space assumptions where it is assumed that normal and tangential displacements are uncoupled and can be calculated separately from traction fields. This is known to be a good approximation, at least when the COF is small. Another challenge arises when the contact pair elements have different elastic properties which will introduce an initial tangential traction distribution when a pure normal load is applied. This may affect the size and location of the stick zone and hence the frictional energy dissipation under fretting conditions. However, the impact of this initial traction field might be low because the COF itself is normally quite low at the start of a fretting test and it rises to higher values only after the contact has been fretted for some time [1]. Munisamy et al. [25] have studied the partial slip of elastically dissimilar spheres and they showed that the contact will shake down after a number of load cycles. After the shake down period the tangential displacement and frictional energy dissipation of the contacts are close to the values predicted by the Mindin solution. During the first load cycles the δ–Q-dependence and the value of the frictional energy dissipation are influenced by the elasticity miss match and the severity of this can be evaluated from the Dundurs' constant β [26] divided by the COF:

$$\frac{\beta}{\mu}=\frac{(1-2\times\nu_1)\times(1+\nu_1)/E_1-(1-2\times\nu_2)\times(1+\nu_2)/E_2}{2\times\mu\times((1-\nu_1)/E_1+(1-\nu_2)/E_2)} \quad (6)$$

Munisamy et al. showed that a contact with $\beta/\mu=1.0$ shakes down to similar contact conditions to those predicted by the Mindlin solution after about 10 load cycles. This indicates that fretting experiments with bronze–QT material pairs in partial

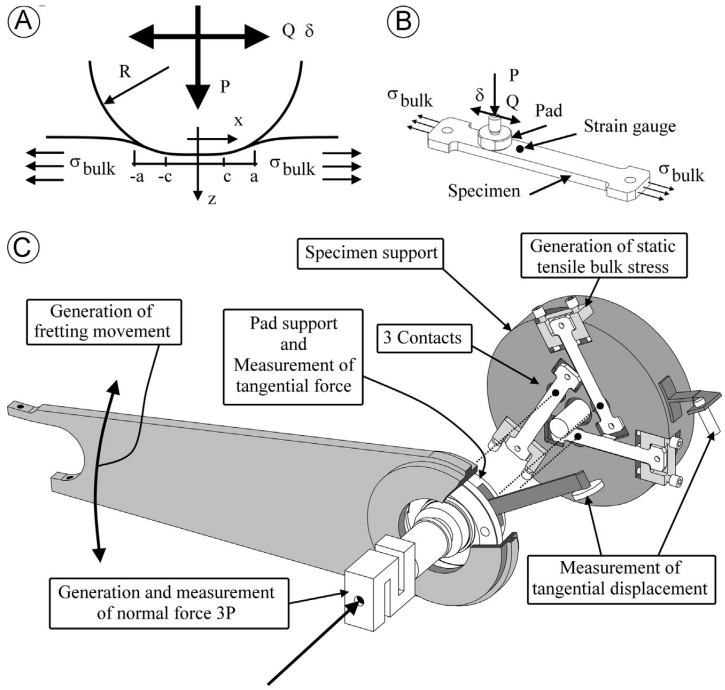

Fig. 1. Hertzian point contact under normal and tangential loads (A), the test specimen and pad (B) and schematic illustration of the test device with three sphere-on-plane contacts (C).

slip conditions can be analyzed using an energy ratio method based on the Mindlin solution.

3. Materials and methods

3.1. The test device

Schematic illustrations of the contact configuration and the test device are presented in Fig. 1.

The Hertzian sphere-on-plane contact, as in Fig. 1A, is achieved using a test specimen and a pad with a spherical contact profile as shown in Fig. 1B. The test device has three similar sphere-on-plane test contacts running simultaneously as shown in Fig. 1C. The normal force on the pads is generated by a hydraulic cylinder through a spherical bearing and pad support, which generates equal force distribution for each of the three contacts. The test specimens are loaded to constant tensile bulk stress with screws and the tangential fretting movement is generated by reciprocating rotation of the lever arm which is achieved by moving the end of the lever arm with an electric shaker. The combined normal and tangential forces of all three contacts are measured. The relative rotational movement between the pad and specimen supports is measured with an eddy current probe and this data is used to estimate the relative movement between the contact pair. It is assumed that the tangential displacement and the normal and tangential forces are identical for each of the three contact pairs.

The test device and the test contacts have a certain amount of tangential compliance. The measured displacement δ_m is a combination of the displacements in the test device and the displacements between the specimen and the pad, which composes of contact deformations and possible surface sliding. The tangential displacement of the point contact δ was calculated as follows:

$$\delta = \delta_m - k \times Q \tag{7}$$

The product $k \times Q$ represents the displacement in the test device which is typically about 20% of the total measured displacement δ_m. The value of k has been defined by FE-calculations and measurements from the test device with reasonable accuracy. However, in this study the parameter k was fine tuned so that the value of δ corresponds to the value of δ_a obtained from Eq. (1). A more detailed description of the test device can be found in [27] and the method for removing the test device compliance in [15].

All specimens were carefully cleaned with solvent in an ultrasonic cleaner before and after testing. The tests were conducted in a normal laboratory atmosphere which was monitored (temperature: 24–27 °C, relative humidity: 15–43%). A constant tensile bulk stress of 400 MPa was initially applied to all three test specimens followed by the constant normal load and finally, the oscillating tangential displacement, which was gradually increased from zero to the target value during the first 5000 load cycles. The fretting tests were set to run for 2.8×10^6 load cycles and the loading frequency was 40 Hz for all tests.

3.2. The test specimen and test matrix

The contact pads were made from aluminum bronze (CuA10-Fe5Ni5-C-GC EN 1982), abbreviated to “bronze” in this paper. The test specimens were made from quenched and tempered steel (EN 10083-1-34CrNiMo6+QT), abbreviated “QT” in this paper. Both contacting surfaces were polished. The properties of the QT specimens have been studied when fretted with a QT pad [13–15] and for this study, only the pad material is changed. The material properties and the surface roughness parameters are shown in Table 1.

Table 1
The material properties and specimen topography.

	QT	Bronze
S_y [MPa]	1056	280
S_u [MPa]	1160	650
S_f [MPa]	496	–
k_{Fr} [-]	0.29	–
f_{Fr} [MPa]	380	–
E [GPa]	206	120
ν [-]	0.27	0.3
S_a [μm]	0.04–0.08	0.05–0.09
S_t [μm]	1.0–2.0	1.5–2.5
R [mm]	–	280–300

The specimen and pad surfaces were polished so that the S_a values were less than 0.09 μm. The recommended usage for the bronze alloy tested is in, for example, demanding bearing applications under high fatigue loading and with good lubrication. The dry friction properties are known to be poor. Nevertheless, the elastic properties, yield strength and ultimate strength are lower than for QT.

The test points in partial slip conditions were chosen iteratively so that the cracking threshold was identified. The displacement amplitudes in the gross sliding tests include test points deep into the gross sliding regime. The test points are shown in Table 2. Assuming that the COF is 1.0 gross sliding occurs when the displacement amplitude is greater that the value of GS.

4. Results and discussion

The results consist of the analysis of fretting scars, COF and contact stresses. The fretting maps and other aspects of bronze–QT contact are compared to previous studies with QT–QT contact. These topics are discussed in detail below.

4.1. Fretting scar observations

4.1.1. Optical microscopy

The fretting scars were first examined with an optical microscope. The fretting map is constructed by counting the clearly visible cracks (macro cracks). Each test produces up to three cracked specimens. This means that near to the cracking threshold, it is possible to have cracked and non-cracked specimens from a single test since fatigue damage is a stochastic phenomenon. The partial slip condition can be confirmed from these observations because wear only occurs in the sliding annulus. Mixed and gross sliding conditions generate wear throughout the contact, thus only the occurrence of gross sliding can be identified with certainty. Fig. 2 shows typical fretting scars obtained with a normal load of 2240 N.

With small displacement amplitudes a partial slip was achieved, as shown in Fig. 2A. Increasing the displacement amplitude in the partial slip domain led to large fatigue cracks, as shown in Fig. 2B. A further increase in the displacement amplitude results in gross sliding and accelerated wear (Fig. 2C). Initially, it seems that the bronze–QT contact produces similar fretting scars to the QT–QT contact [13,15] but some clear differences exist. These are now discussed.

The maximum cracking risk is known to be located at the edge of the point contact ($x=\pm a$, $y=0$ in Fig. 1A). However, some cracks were found in surprising locations, as clearly seen in Fig. 3.

Fig. 3A shows a fatigue crack that was initiated in the upper left corner of the fretting scar. In Fig. 3B, the higher magnification reveals a piece of wear debris on the surface of the specimen which is situated in the suspected location of crack initiation. These pieces of wear debris were not loose particles because the specimens were carefully cleaned after the test with an ultrasonic cleaner. Fig. 3C shows the FCR contour plot of the upper left corner of the contact, where the values are percentages of the maximum cracking risk. The location of the crack initiation (Fig. 3B) has about a 10% lower cracking risk than the calculated maximum value at the edge of the contact area ($x=\pm a$, $y=0$). The crack initiation location seems to be at the contact area edge or even slightly outside the contact area, where the FCR falls sharply to about 60% of the maximum. Similar, though more severe cases were also observed in which some fretting scars had multiple fatigue cracks like those shown in Fig. 3D and E. Fig. 3D shows cracking on the right hand side of the contact in which there are two distinct separate cracks. Fig. 3E shows multiple cracks on both sides of the contact area. This indicates that there must be multiple locations for crack initiation and that many of the initiated cracks have grown. Some of these cracks were initiated away from the location of the maximum cracking risk in a similar way to that shown in Fig. 3A. It is probable that these multiple cracks initiated after a different number of load cycles. It is also possible that the stress state of a particular surface point has been altered by the proximity of cracks so that the contour plot in Fig. 3C should be used with caution when estimating the precise FCR for the location of every crack which forms. Similar fretting behavior, where crack initiation and growth occurs throughout the slip zone has also been reported with titanium–titanium point contacts [28].

Table 2
Test matrix with two normal force levels.

P [N]	GS [μm]	Average δ [μm]							
1270	9.3	2.8	4.0	5.1	5.7	7.8	19.1	30.7	41.3
2240	13.6	2.8	3.5	4.5	6.6	10.0	31.9	52.4	

4.1.2. Profilometry

The fretting scars produced by partial slip running conditions showed many locations where wear debris was attached to the surface of the QT-specimen, as shown in Fig. 2A where some of the locations are indicated by arrows. This behavior becomes more pronounced when the displacement amplitude is increased. These pieces of wear debris are mostly distributed around the edge of the contact area though such particles can also be found in arbitrary positions throughout the slip zone. In some cases the wear particles even seem to be slightly outside the contact area. Careful profilometry was undertaken at some of the locations where these pieces of wear debris were found. The corresponding counter surface of the test pad was then profiled. Another example of a fretted specimen surface with wear debris is shown in Fig. 4A where the location marked with the rectangle was measured with an optical profilometer.

Fig. 4A shows a photograph of a fretting scar obtained in partial slip conditions with many locations where there is wear debris (arrows). Many 3D surface profiles from the surface of the test specimen were taken with large magnification. An example of such a 3D surface profile can be seen in Fig. 4B at the location indicated by the rectangle in Fig. 4A. Fig. 4B shows that material is protruding from the flat surface of the specimen. A corresponding location profiled from the test pad (Fig. 4C) shows a striking similarity. 2D surface profiles from the dotted lines in Fig.4B and C are compared in Fig. 4D. The 2D profile of the fretted test specimen shows a close match to the 2D profile of the fretted test pad. In general the profilometry showed that the surface of the fretted QT-

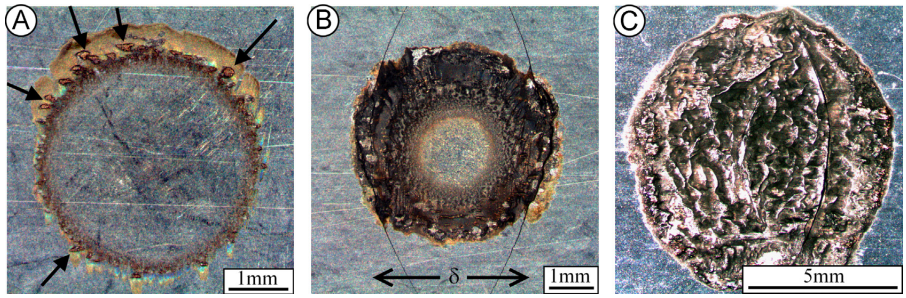

Fig. 2. Typical fretting scars under different running conditions (partial slip without (A) and with cracks (B) and gross sliding (C)), P=2240 N.

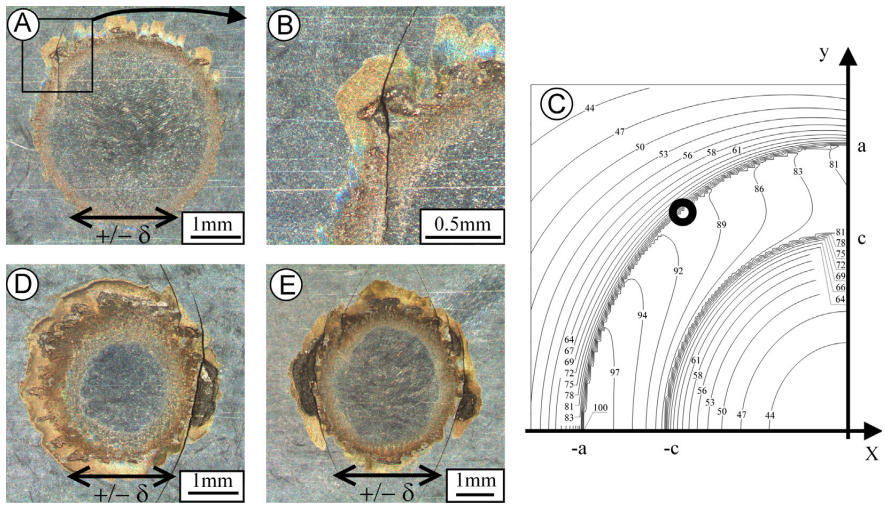

Fig. 3. Fatigue crack initiation from location of fretting damage ((A) and (B)) and FCR contour plot (% of maximum value) of the upper left corner of the contact where the maximum FCR is 0.75 (C). Multiple crack initiation locations with both normal loads ((D) and (E)).

specimen had mostly flat surfaces with many locations where wear debris was protruding from the surface. The surface profiles of the bronze fretting pads also had relatively low roughness, however, the profile had many locations where there were depressions or dents. In every case the location of protruding wear debris in the specimen corresponded well with the location of the depression in the surface of the fretting pad similar to the example shown in Fig. 4. It seems that material transfer had occurred at these locations so that fretting damage causes pieces of bronze wear particles to attach to the surface of the specimen. Typically, the QT specimen showed little wear and it was only observed near fatigue cracks and in gross sliding situations at the largest displacement amplitudes.

4.1.3. SEM and EDS

Some of the fretting scars were analyzed using a scanning electron microscope (SEM) and energy dispersive X-ray spectroscopy (EDS). The locations of the contacts in the specimens where bronze wear debris seemed to have attached were the main focus in this analysis but some other arbitrary locations were also investigated for reference. An example of such analysis can be seen in Fig. 5.

The fretting scar shown in Fig. 5A was analyzed using SEM and EDS. Examples of SEM images from a specimen can be seen in Fig. 5B and C at the locations which are marked in Fig. 5A. The fretting pad surface is shown in Fig. 5D at a location which corresponds to Fig. 5C. The SEM image in Fig. 5B shows three different regions. A smooth dark grey region is a layer of oxidized bronze (EDS1), the larger chunks of attached bronze wear debris are the second type (EDS2) and third type is the smooth light gray region of almost pure QT (EDS3). Fig. 5D clearly shows a chunk of transferred wear debris (EDS4) on the bronze fretting pad which seems to have a close match to the shape of the lower right corner of the light gray area in Fig. 5C. It seems to be that in some locations bronze wear debris had peeled off from the surface of the QT-specimen and in some cases part of that peeled material had attached itself back to the bronze fretting pad. The location EDS5 is the location on the bronze fretting pad from which the wear particle seems to have detached leaving a depression. The EDS analysis revealed the composition of elements in these regions which is showed in Table 3.

The rows in Table 3 correspond to the regions illustrated in Fig. 5 and the v2, v3, v4 and v5 corresponds to similar kind of regions from different specimen. The regions named EDS1 appear to be a thin layer of bronze oxides with varying degrees of oxidation. EDS1 regions have quite a lot of copper which is not present in QT so it must come from the bronze pad. This layer has a significant amount of oxygen which suggests that this layer is partly oxidized, however, there is not enough oxygen to indicate that the layer was completely oxidized. The elemental composition of a thin layer is not captured with complete accuracy because

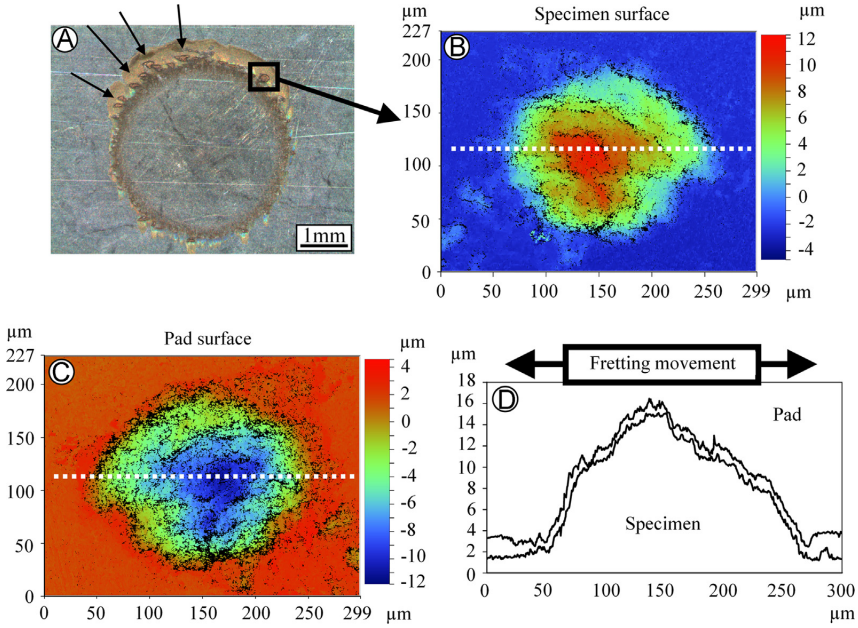

Fig. 4. The wear debris on the steel specimen (A). The corresponding wear scar 3D profiles on the test specimen (B) and the pad (C). Comparison of the wear scar 2D profiles of the pad and specimen surfaces (D).

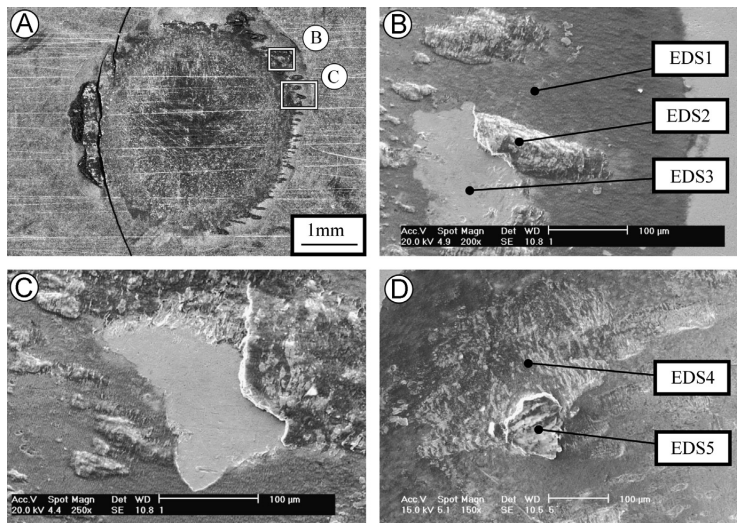

Fig. 5. Optical microscope image from the specimen (A), SEM images from fretting scars ((B) and (C)) and SEM image from fretting pad corresponding to the location C (D).

the electron beam penetrates up to a depth of about 1.5 µm which might already be through to clean QT under the oxidized surface layer thus showing excessive amounts of the elements found in QT. Lowering the excitation voltage lowers the depth of the electron beam penetration and the analysis $EDS1_{v3}$ with the lower excitation voltage shows less elements of QT and a higher degree of oxidation than the other EDS1 analysis. The EDS2 regions correspond to the protruding surface profiles found in the profilometry analysis. EDS2 regions are the attached wear debris discussed in Sections 4.1.1 and 4.1.2. The attached wear debris has the elemental composition of the bronze used with small amounts of additional oxygen. These EDS2 regions are not significantly oxidized because there is so little oxygen present. This analysis does not reveal which elements have oxidized. The EDS3 regions are the regions from which the attached bronze wear debris had peeled off. These locations have the elemental composition of QT with little remaining copper. The regions labeled EDS4 are the locations in the fretting pad where there seems to be attached wear debris. The elemental composition of these regions corresponds to oxidized bronze. The amount of iron in the EDS4

regions is similar to that found in unfretted bronze. The EDS5 analysis shows that the elemental composition in the fretting wear scar of the fretting pad is oxidized bronze. The amount of iron found in the bronze fretting pads corresponds closely to the amount found in unfretted bronze in all cases (EDS4 and EDS5). Because the QT-specimen showed little wear there is no significant amount of QT-wear debris around to attach to the bronze.

The SEM and EDS analyses confirmed the observations from the profilometry and optical microscopy that bronze wear debris seems to be attached to the surface of the QT-specimen. The fretting wear process in the bronze–QT contact seems to be dominated by wear of the bronze. The wear particles seem to attach to the surface of the QT-specimen forming large chunks at arbitrary locations. These chunks of bronze wear debris did not show a high degree of oxidization. In some situations the bronze wear debris transferred back to the surface of the bronze fretting pad. It is not known exactly how these locations, where wear debris has become attached, have formed and it cannot be fully explained within the scope of this study. It is possible that those bronze particles have torn from the pad in large chunks but it is also possible that the bronze debris has conglomerated more gradually from small wear particles.

4.2. The friction coefficient

In partial slip conditions the COF was calculated from the measured frictional energy dissipation using Eq. (2) and in the case of gross sliding from the *Q*/*P*-ratio. Typically, the COF tends to evolve during the fretting test since it is dependent on the magnitude of surface damage. In this study the minimum, mean and maximum values of COF are presented for the first 100×10^3 load cycles excluding the displacement amplitude ramp-up phase during the first 5000 cycles. In this way, wear and possible fatigue cracks do not cause much distortion. There might be local plastic straining in the bronze pad but this is not taken into account in the evaluation of COF. The COF values are listed in Table 4.

In general, Table 4 shows an almost linear rise in the COF with increasing displacement amplitude in the partial slip regime. The mean value for friction coefficient reaches its maximum value when running conditions approach the gross sliding boundary. The mean COF in gross sliding seems to depend slightly on the normal load and has a value of about 1.2 with the lower normal force and about 1.0 with the higher normal force. A similar kind of friction vs. displacement amplitude behavior has been reported with QT–QT contact but the maximum COF was found to be 1.5–1.6 [15]. The deviations between minimum, mean and maximum values are small in partial slip but much greater in gross sliding conditions. The measurement with $\delta = 41.3$ μm $P = 1270$ N shows the maximum COF as high as with QT–QT contact but these highest values lasted for only a few thousand load cycles. During the rest of the test (1.0×10^5–2.8×10^6 load cycles) the COF produced by gross slip conditions varied between 0.8 and 1.2, being mostly around 1.0 with both normal forces. This is similar to the QT–QT steady state gross slip COF. Some of the partial slip experiments, which produced fatigue cracks, showed a gradually decreasing measured COF, starting at roughly the same moment as when the crack was first observed in the strain gauge data which measured the static tensile bulk stress near the contact. One notable property of bronze–QT contact was that it did not show the existence of a mixed slip regime because all the tests done under partial slip conditions preserved the same running conditions for the duration of the test. In contrast, the QT–QT contact behaved differently. Almost all of the experiments which were initially in partial slip conditions had a transition into gross sliding within the 2.8×10^6 load cycles. The effect of elasticity miss match on the energy ratio is believed to insignificant even at the very

Table 3
The elemental composition of certain fretting scar locations in relative weight percentages (wt%).

Analysis	Voltage	O	Al	Si	S	Cr	Mn	Fe	Ni	Cu
QT	20 kV	2.52	2.97	0.41	–	1.72	0.93	89.96	1.48	–
Bronze	15 kV	0.86	10.90	0.57	–	–	–	4.30	4.66	78.72
EDS1	20 kV	10.67	4.08	0.27	1.4	1.40	0.61	63.66	1.84	17.25
$EDS1_{v2}$	20 kV	15.82	6.31	–	–	0.85	0.59	41.74	2.13	32.57
$EDS1_{v3}$	10 kV	19.84	7.44	0.35	–	–	–	6.25	–	66.13
EDS2	20 kV	7.39	10.47	–	–	–	0.39	6.31	4.48	70.64
$EDS2_{v2}$	20 kV	6.96	9.98	0.19	–	–	0.32	6.99	3.73	71.83
EDS3	20 kV	2.50	1.39	0.33	–	1.74	0.87	89.90	1.70	1.37
$EDS3_{v2}$	20 kV	1.53	0.75	0.29	–	1.89	0.74	92.77	1.49	0.53
EDS4	15 kV	26.01	8.91	0.34	–	–	–	4.50	3.04	57.21
$EDS4_{v2}$	15 kV	13.15	9.25	0.39	–	–	–	6.15	3.63	67.43
$EDS5_{v2}$	15 kV	21.38	9.29	–	–	–	–	3.37	3.68	62.27
$EDS5_{v3}$	15 kV	17.07	9.96	–	–	–	–	4.29	3.97	64.38

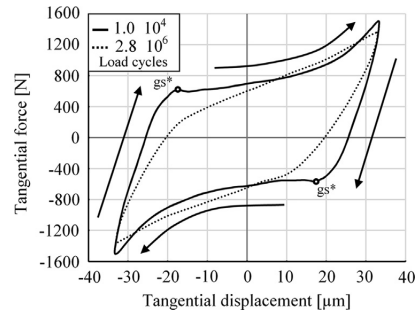

Fig. 6. Shape of the fretting loop after 10×10^4 and 2.8×10^6 load cycles in gross sliding, $P = 1270$ N.

Table 4
Measured friction coefficient values from the first 100×10^3 load cycles, ps = partial slip and gs = gross sliding.

Normal force *P* [N]	Average displacement amplitude [μm]							
	2.8 (ps)	4.0 (ps)	5.1 (ps)	5.7 (ps)	7.8 (ps)	19.1 (gs)	30.7 (gs)	41.3 (gs)
1270								
μ_{min}	0.57	0.73	0.95	1.03	1.24	0.78	0.91	0.94
μ_{mean}	0.62	0.75	0.98	1.09	1.26	1.06	1.20	1.27
μ_{max}	0.67	0.77	1.02	1.11	1.29	1.10	1.32	1.50
	2.8 (ps)	3.5 (ps)	4.5 (ps)	6.6 (ps)	10.0 (ps)	31.9 (gs)	52.4 (gs)	
2240								
μ_{min}	0.39	0.48	0.64	0.81	0.91	0.66	0.70	
μ_{mean}	0.42	0.51	0.68	0.86	1.04	1.05	1.05	
μ_{max}	0.45	0.55	0.70	0.89	1.07	1.17	1.19	

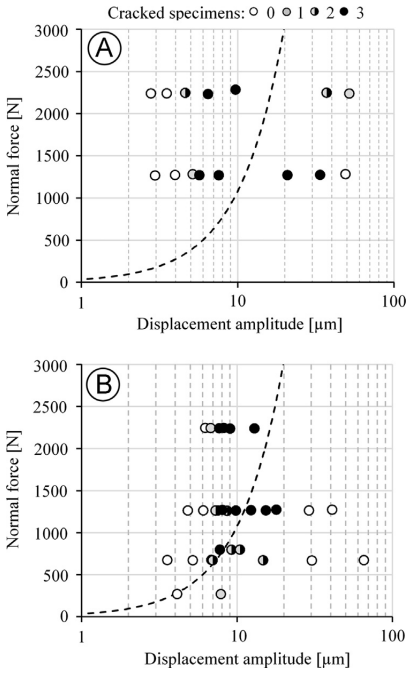

Fig. 7. Measured fretting map for bronze–QT contacts (A) and QT–QT contacts (B). The dashed line indicates the gross slip limit.

beginning of the experiment because the value of β/μ is in the range of 0.05–0.16 depending on the values of COF. In addition the average COF was calculated from the first 100×10^3 load cycles after the start up phase and these average values deviated only a little from the corresponding minimum and maximum values in partial slip conditions.

Fig. 6 shows the curved shape of the fretting loop that was obtained with all gross slip experiments with bronze–QT contact. The loading direction is marked by arrows and the points gs* indicate the points at which gross sliding commences during one load cycle.

Fig. 6 shows that instead of remaining constant, the tangential force increases exponentially after gross sliding appears to start (gs*), which indicates that the COF is not constant during the load cycle. The fretting loop changes gradually to a more elliptical shape like that shown by the dotted curve in Fig. 6, which corresponds to 2.8×10^6 load cycles. Similar fretting loop shapes have also been found in Ref. [29,30]. Mulvihill et al. [30] suggested that this kind of non-Coulomb behavior can originate from fretting scar interactions. It is possible that the non-Coulomb fretting loop obtained with bronze–QT contact in gross sliding is also due to fretting scar interactions. It is possible that fretting scar interactions originates from the interactions between the attached bronze wear debris, on the QT-specimen, and the scarred bronze pad (Fig. 4).

4.3. Fretting maps

Fretting tests are commonly analyzed using fretting maps [18]. In this study, a number of different fretting maps were constructed using various parameters (δ, Q, FCR and Ruiz). Every test was analyzed using the measured values for parameters, such COF, Q, δ and P. For example measurement i was analyzed using the values COF_i, Q_i, etc. meaning that no averaging was done to combine parameter values from multiple measurements. The maximum FCR is used to analyze the fatigue loading although it can lead to slightly non conservative estimates for the cracking threshold because cracking did not always occur in the exact location of $x = \pm a$, $y = 0$. All the bronze–QT and QT–QT tests are compiled in the fretting map shown in Fig. 7 as a function of the displacement amplitude and the normal load.

As shown in Fig. 7A, fretting fatigue cracking occurred with displacement amplitudes greater than $\sim 4\ \mu m$ and the cracking continued up to the largest displacement amplitudes. In comparison the QT–QT had slightly smaller crack producing region. Generally, the behavior is similar to that reported by Vingsbo [31] in the case of both material pairs.

Next, the bronze–QT tests are discussed with the aid of several fretting maps and compared with the QT–QT contact results. The average values for parameters (μ and Q) were calculated from the first 100×10^3 load cycles excluding the displacement amplitude ramp-up phase during the first 5000 cycles. Such values were then used in the following analysis. Fretting tests with smooth QT–QT contact was earlier analyzed with the FCR and these showed a high degree of accuracy in predicting fatigue damage [22]. In this study, the QT–QT contact results were obtained by re-analyzing the earlier test data [13,15]. The fretting maps are shown in Fig. 8 for bronze–QT contact and with QT–QT contact as a reference. For clarity, the QT–QT results are mostly shown for partial and mixed slip regimes.

Fig. 8 contains fretting maps where the amount of calculation and assumptions increase from top to bottom. Only measured data was used to compile Fig. 8A and B. When comparing these fretting maps (A and B), a reduction in fatigue performance can be seen with the bronze–QT contact pair. In the case of QT–QT contact, the two highest normal loads withstand tangential loads greater than 1000 N and the bronze–QT contact produces cracked specimens with tangential force amplitude slightly less than 1000 N. The tangential force amplitude required to produce fretting fatigue cracks is about 20–30% lower with the bronze–QT contact than with the QT–QT contact. This occurred even when the bronze–QT contact has more favorable contact conditions in terms of the reduced elastic modulus which should lead to a decrease of about 10% in FCR. In addition, the bronze–QT contact has a lower maximum COF than the QT–QT contact, which also decreases the FCR in partial slip conditions if the tangential force is kept constant [32]. The bonze–QT contact should withstand higher tangential force amplitudes than QT–QT contact but clearly the opposite behavior was observed in this study.

Fig. 8C shows the fretting map as a function of the displacement amplitude. It shows that, in the case of bronze–QT contact, fatigue cracks start to appear with displacement amplitudes greater than about 4 μm with both normal loads. Severe cracking is observed in a partial slip regime well before the gross slip border. In comparison, the QT–QT contact seems to have a similar kind of cracking threshold, but the limit is about 6 μm for the displacement amplitude (Fig. 8D). The bronze–QT fretting tests produced cracking with about 30% lower displacement amplitude than what was observed with the QT–QT contact.

Fig. 8E and F show that cracking occurs with bronze–QT contact at a low FCR value of 0.64 and severe damage to all specimens was observed with FCR 0.8. The QT–QT tests show cracking when the FCR is about 0.9. This comparison shows that the use of bronze pads produces fretting fatigue cracks at an FCR value up to about 20–25% lower than that deduced from the QT–QT results. Many of the specimens cracked in the way shown in Figs. 3 and 4, where the value of the FCR at the exact location of the crack is about 10% lower than the values used for the fretting map in Fig. 8E. The reduction in fretting fatigue performance using Findley criteria is inevitable and logical because the tangential force data is used to

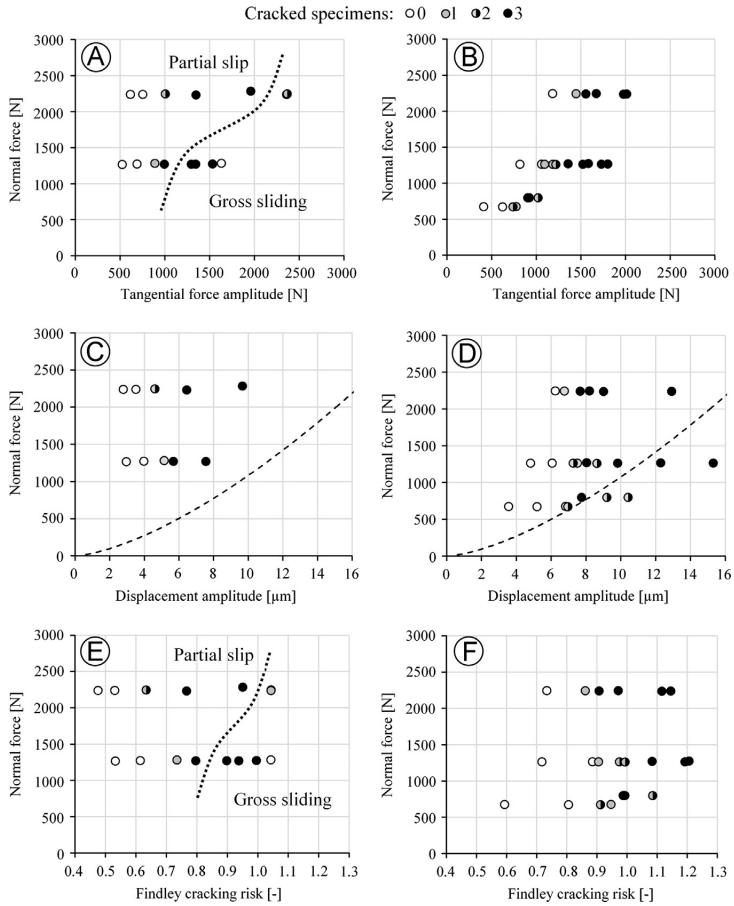

Fig. 8. Fretting maps for bronze–QT ((A), (C) and (E)) vs. QT–QT ((B), (D) and (F)) contacts.

calculate the FCR. Most of the bronze–QT tests were performed under conditions where FCR is clearly less than one. This implies that there must be locations in the contact area which are under higher load than predicted by stress calculations based on ideal Hertzian contact stresses; otherwise there must be some other mechanism that leads to crack nucleation. Interestingly, the highest normal load produces somewhat more severe cracking with bronze–QT material pair when compared with the lower normal force level.

The fretting maps, constructed with the Ruiz criterion, are shown in Fig. 9 for the partial and mixed slip regimes.

The Ruiz fretting maps are shown in Fig. 9 for both the bronze–QT (A) and the QT–QT (B) contact. The Ruiz criterion underestimates the severity of the bronze–QT fretting conditions with the highest normal load even more than by the plain stress based analysis (FCR). However, a better fretting damage threshold can be obtained for the QT–QT contact. Fig. 9A shows that there is no clear fretting damage threshold for the bronze–QT contact. However, if such threshold exists it is much lower for the bronze–QT than is for the QT–QT contact.

The main result here is that the use of bronze (CuA10Fe5Ni5-C-GC EN 1982) pads reduces fretting fatigue performance when compared to the QT–QT contact. An understanding of the tribological processes within the contact is essential: it is not enough to merely calculate the ideal Hertz stresses accurately. The resistance to fretting damage gained when using aluminum bronze in Ref. [10–12] was only repeated in terms of a small reduction in the maximum COF when compared to the QT–QT results. This is probably due to differences in the properties of the bronze and the loading conditions. The soft bronze coating in contact with titanium [11,12] is very different set of conditions than the homogenous bronze pad against QT. Ref. [10] provides a very different set of conditions from the homogenous bronze pad against QT. Ref. [10] relates to plane on plane contact with a nominal surface pressure of about 4 MPa, whereas this study concerns point contact with maximum Hertzian pressure being almost 100 times greater.

4.4. Discussion

The explanation for the reduced fretting fatigue performance must be somehow related to the use of a bronze fretting pad. The QT specimens used in the bronze–QT and QT–QT fretting tests are made from the same QT material batch and the measurements were made with same test device and procedures. The bronze fretting pad was under severe fretting loading due to relatively large normal and tangential forces which might be important factors leading to the measured observations in this study. The fatigue loading was calculated only for the QT specimen. The only difference is the pad material, thus the differences found in the

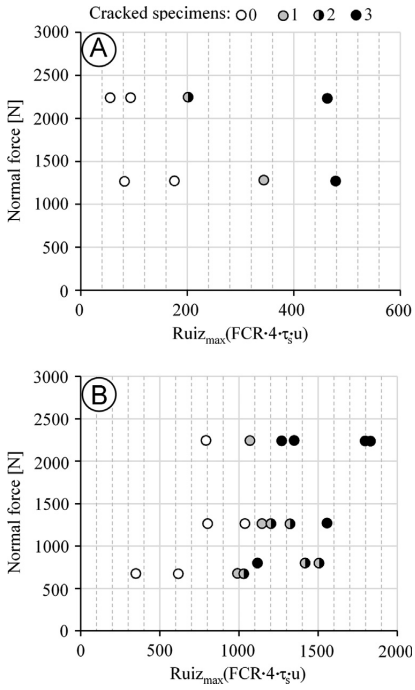

Fig. 9. Ruiz fretting maps for bronze–QT (A) vs. QT–QT (B) contacts.

fretting fatigue performance are related to the fretting pad material alone. It was shown that material transfer occurred from bronze pad to the QT-specimen and cracks initiated in these locations. The fretting wear damage in the bronze pad seems to lead to interlocking wear scar profiles (Fig. 4). The fretting movement between contacting surfaces at the precise location of the attached wear debris might cause collisions to occur between the piece of wear debris and the scarred pad surface (Fig. 4D). A collision will lead to reaction forces which will ultimately lead to additional local stresses in the QT specimen. This could explain why the cracks had initiated in multiple and sometimes surprising locations. The shape of fretting loop in gross sliding supports the view of fretting scar interactions although it is not obvious that it also occurs in partial slip conditions. Even if there were no "collisions" the fretting damage changes the geometry of the contacting surfaces which in itself can modify the contact tractions. Exactly how the fretting wear scar interactions or surface geometry modifications might contribute to the surface stresses and the fretting fatigue performance is not fully understood. Ultimately it is suspected that the reduction in the fretting fatigue performance of the specimen is strongly influenced by fretting damage in the fretting pad. It has been reported that increased wear in gross sliding improves fretting fatigue life because it might destroy crack embryos at a faster rate than they nucleate or grow [31]. The lack of wear in QT specimens, especially in partial slip conditions, when fretted with a bronze pad could also allow crack embryos to form and grow undisturbed by the fretting wear.

5. Conclusions

Quenched and tempered steel (QT) specimens were fretted with aluminum bronze pads under high loads. The fatigue, wear and friction properties were analyzed and the following conclusions were drawn:

- The friction coefficient is in the range of 1.0–1.2 in gross sliding; in partial slip this seems to depend on the displacement amplitude. The maximum friction coefficient is lower than with QT–QT contact (~1.5).
- Fretting scars showed evidence of material transfer as particles of bronze were found to have attached to the surface of the steel specimen. These locations also show interlocking fretting scar topography. In many cases fatigue cracks initiated at these locations. Overall the QT-specimen showed only a little wear.
- Fretting map comparison with previous QT–QT fretting tests shows that bronze–QT contact produces fatigue cracks with lower values in terms of displacement amplitude, tangential force amplitude and Findley cracking risk. With the bronze–QT material pair there was greater tendency for fretting fatigue damage than with the QT–QT contact under the test operating conditions.
- The explanation for the decreased fretting fatigue performance was suspected to be the unfavorable fretting damage in the bronze pad.

Acknowledgements

This study was undertaken within FIMECC Ltd (Finnish Metals and Engineering Competence Cluster) and its DEMAPP program. The authors are grateful for the financial support provided by Wärtsilä Finland Oy, Metso Paper Oy and Tekes (Finnish Funding Agency for Technology and Innovation). The authors would also like to thank chief laboratory technician Kati Mökkönen (TUT, Department of Materials Science) for providing the SEM images and EDS data.

References

[1] D.A. Hills, D. Nowell, Mechanics of Fretting Fatigue, Kluwer Academic Publishers, Dordrecht, 1994.
[2] J.A. Pape, R.W. Neu., A comparative study of the fretting fatigue behavior of 4340 steel and PH 13-8 Mo stainless steel, International Journal of Fatigue 29 (2007) 2219–2229.
[3] A.L. Hutson, C. Neslen, T. Nicholas, Characterization of fretting fatigue crack initiation processes in CR Ti–6Al–4V, Tribology International 36 (2003) 133–143.
[4] K. Nakazawa, N. Maruyama, T. Hanawa, Effect of contact pressure on fretting fatigue of austenitic stainless steel, Tribology International 36 (2003) 79–85.
[5] S.R. Shinde, D.W. Hoeppner, Fretting fatigue behavior in 7075-T6 aluminum alloy, Wear 261 (2006) 426–434.
[6] S. Fouvry, C. Paulin, S. Deyber, Impact of contact size and complex gross-partial slip conditions on Ti–6Al–4V/Ti–6Al–4V fretting wear, Tribology International 42 (2009) 461–474.
[7] M.P. Szolwinski, T.N. Farris, Observation, analysis and prediction of fretting fatigue in 2024-T351 aluminum alloy, Wear 221 (1998) 24–36.
[8] V. Fridrici, S. Fouvry, P. Kapsa, P. Perruchaut, Prediction of cracking in Ti–6Al–4V alloy under fretting-wear: use of the SWT criterion, Wear 259 (2005) 300–308.
[9] S. Fouvry, P. Kapsa, L. Vincent, Quantification of fretting damage, Wear 200 (1996) 186–205.
[10] J. Cronin, J. Warburton, Amplitude-controlled transitions in fretting: the comparative behaviour of six materials, Tribology International 21 (1988) 309–315.
[11] W. Ren, S. Mall, J.H. Sanders, S.K. Sharma, Evaluation of coatings on Ti–6Al–4V substrate under fretting fatigue, Surface and Coatings Technology 192 (2005) 177–188.
[12] B.P. Conner, T. Nicholas, Using a dovetail fixture to study fretting fatigue and fretting palliatives, Journal of Engineering Materials and Technology-transactions of the Asme 128 (2006) 133–141.
[13] A. Pasanen, A. Lehtovaara, R. Rabb, P. Riihimäki, On the fretting fatigue behavior of quenched and tempered steel in smooth point contact, Tribologia 28 (n3-4) (2009) 26–37.

[14] A. Pasanen, A. Lehtovaara, R. Rabb, P. Riihimäki, Friction behavior of quenched and tempered steel in partial and gross slip conditions in fretting point contact, Wear 267 (2009) 2200–2207.
[15] J. Hintikka, A. Lehtovaara, C. Lönnqvist, Effect of start-up schemes and amplitude of tangential motion on friction behavior in fretting point contact, Tribology International 44 (2011) 1535–1543.
[16] R.D. Mindlin, Compliance of elastic bodies in contact, Journal of Applied Mechanics 16 (1949) 259–268.
[17] S. Fouvry, P. Kapsa, L. Vincent, Analysis of sliding behaviour for fretting loadings: determination of transition criteria, Wear 185 (1995) 35–46.
[18] Z.R. Zhou, K. Nakazawa, M.H. Zhu, N. Maruyama, P. Kapsa, L. Vincent, Progress in fretting maps, Tribology International 39 (2006) 1068–1073.
[19] K.L. Johnson, Contact Mechanics, Cambridge University Press, Cambridge, 1985.
[20] G.M. Hamilton, Explicit equations for the stresses beneath a sliding spherical contact, Proceedings of the Institution of Mechanical Engineers 197C (1983) 53–59.
[21] D.F. Socie, G.B. Marquis, Multiaxial Fatigue, Society of Automotive Engineers, Inc, Warrendale, 2000.
[22] A. Lehtovaara, R. Rabb, A. Pasanen, Modelling and evaluation of the fretting fatigue cracking risk in smooth spherical contacts, Tribology International 44 (2011) 1526–1534.
[23] C. Ruiz, P.H.B. Boddington, K.C. Chen., An investigation of fatigue and fretting in a dovetail joint, Experimental Mechanics 24 (1984) 208–217.
[24] J. Vidner, E. Leidich, Enhanced Ruiz criterion for the evaluation of crack initiation in contact subjected to fretting fatigue, International Journal of Fatigue 29 (2007) 2040–2049.
[25] R.L. Munisamy, D.A. Hills, D. Nowell, Static axisymmetric Hertzian contacts subject to shearing forces, Journal of Applied Mechanics American Society of Mechanical Engineers 61 (1994) 278–283.
[26] J. Dundurs, Discussion of edge-bonded dissimilar orthogonal elastic wedges under normal and shear loading, Journal of Applied Mechanics, 36, 650–652.
[27] A. Pasanen, S. Järvisalo, A. Lehtovaara, R. Rabb, Development of a test device for the evaluation of fretting in point contact, Lubrication Science 21 (2009) 41–52.
[28] B. Alfredsson, A. Cadario., A study on fretting friction evolution and fretting fatigue crack initiation for a spherical contact, International Journal of Fatigue 26 (2004) 1037–1052.
[29] S. Fouvry, P. Duó, P. Perruchaut., A quantitative approach of Ti–6Al–4V fretting damage: friction, wear and crack nucleation, Wear 257 (2004) 916–929.
[30] D.M. Mulvihill, M.E. Kartal, A.V. Olver, D Nowell, D.A. Hills, Investigation of non-Coulomb friction behaviour in reciprocating sliding, Wear 271 (2011) 802–816.
[31] O. Vingsbo, S. Söderberg., On fretting maps, Wear 126 (1988) 131–147.
[32] A. Lehtovaara, R. Rabb, Fretting fatigue crack initiation for a smooth spherical contact—a parameter study, Tribologia 25 (n1) (2006) 31–39.

Publication III

Non-Coulomb friction in gross sliding fretting conditions with aluminium bronze against quenched and tempered steel

by

J Hintikka, A Lehtovaara and A Mäntylä

Tribology International, 79 (2014), 151-161

doi:10.1016/j.triboint.2014.06.004

Tribology International 79 (2014) 151–161

Contents lists available at ScienceDirect

Tribology International

journal homepage: www.elsevier.com/locate/triboint

Non-Coulomb friction in gross sliding fretting conditions with aluminium bronze against quenched and tempered steel

Jouko Hintikka [a,*], Arto Lehtovaara [a], Antti Mäntylä [b]

[a] Department of Materials Science, Tampere University of Technology, P.O. Box 589, 33101 Tampere, Finland
[b] Research & Development, Wärtsilä Finland Oy, P.O. Box 244, 65101 Vaasa, Finland

ARTICLE INFO

Article history:
Received 28 March 2014
Received in revised form
6 June 2014
Accepted 9 June 2014
Available online 17 June 2014

Keywords:
Fretting
Friction
Wear
Topography

ABSTRACT

A series of fretting tests were performed in gross sliding conditions to study the properties of non-Coulomb friction occurring in the contact of an aluminium bronze sphere against a quenched and tempered steel plane. Measurements were analysed by studying measured fretting loops and the topographies of fretting scars with 3D optical profilometry. Measured fretting loops showed non-Coulomb tangential behaviour, in which the tangential force depended on the tangential displacement. Measurements in which the tangential displacement amplitude was suddenly increased or reduced showed a temporary reduction in the maximum friction force. Fretting wear modified initially polished surfaces producing a tangentially interlocked fretting scar surface profile, which may explain the non-Coulomb increase in the friction force.

1. Introduction

Fretting may occur between any two contacting surfaces where short-amplitude reciprocating sliding exists over a large number of load cycles. The running conditions of a fretting contact can be divided into partial slip and gross sliding. Under partial slip conditions, some contact regions are stuck and undergo no relative surface sliding, while the rest of the contact is slipping. However, under gross sliding conditions no such sticking regions appear within the contact. Sliding in the contact causes fretting wear, which can lead to surface degradation detectable by the appearance of material transfer and wear debris. Fretting movement can cause fretting fatigue due to high tractions and wear, potentially enhancing crack nucleation and decreasing fatigue life, typically affected by a high friction coefficient. Though precise knowledge of frictional behaviour is crucial, the phenomenon is sometimes poorly understood and often assumed to follow ideal Coulomb friction law. A more extensive account of fretting can be found, e.g., in [1,2].

When elastically dissimilar materials are fretted, the elasticity mismatch itself affects the slip and traction fields. The significance of this can be estimated by using Dundurs' parameter β/μ [1,3]. Munisamy et al. [4] studied the problem of elastically dissimilar spheres in partial slip conditions and discovered that after a shakedown period of about 10 load cycles, the contact behaves close to the Mindlin solution [5]. In a bronze–steel contact [6], such as in this study, Dundurs' parameter β/μ had a modest value of 0.16 and thus a small effect, especially in gross sliding conditions.

Knowledge of the frictional properties of a fretting contact can be obtained by studying the measured tangential force (Q) vs. tangential displacement (δ) plots, i.e., fretting loops; however fretting loop must be measured accurately and with a sufficiently high data collection frequency to capture the shape of the fretting loop in detail. The forces are often measured with a load cell [7–10], which is typically based on strain gage measurements [11]. Strain gages have been used to measure tangential force by gluing them directly to the test rig or specimen [12–14]. Piezo-force transducers have also been used to measure tangential force [15–17]. Tangential displacement can be measured, e.g., with LVDT [7,10,18], laser or other light based censors [15,19,20], eddy current probe, or other sensors based on induction [14,21]. Extensometers [8,22] are commonly used and may be based on different operating principles (strain gage, LVDT, capacitive, inductive, or other). Forces and displacements are often measured at a location which is different from where the fretting contact occurred introducing test-rig-dependent compliance that may affect the measured tangential displacement and tangential force. Advances have been made in measuring slip or displacement directly from specimens and thereby avoiding compliance by using laser interferometry (vibrometer) [15,19] and digital image correlation [7,10].

Fig. 1 illustrates the development of friction forces and the terminology for the properties of the non-Coulomb fretting loop in

* Corresponding author. Tel.: +358 3 311511.
E-mail address: jouko.hintikka@tut.fi (J. Hintikka).

http://dx.doi.org/10.1016/j.triboint.2014.06.004
0301-679X/

Nomenclature

a	contact radius [m]
E	elasticity modulus [Pa]
$F\mu$	friction force [N]
G	shear modulus [Pa]
gs*	onset of gross sliding [m]
k	rigidity of the test device [m/N]
P	normal force [N]
Q	tangential force [N]
Q_a	tangential force amplitude [N]
R	sphere radius [m]
S_y	yield strength [Pa]
S_u	ultimate strength [Pa]
S_f	fatigue strength [Pa]
S_a	arithmetic surface roughness [m]
S_t	peak to peak surface roughness [m]
β	Dundurs' parameter [–]
σ_{bulk}	bulk stress [Pa]
δ	tangential displacement [m]
δ_a	tangential displacement amplitude [m]
δ_m	measured tangential displacement [m]
μ	friction coefficient [–]
ν	Poisson's ratio [–]

Subscripts

min	minimum
mean	average
max	maximum

the case of Hertzian sphere-on-plane contact. The friction force ($F\mu$) is defined here as the force resisting tangential movement between contacting bodies in gross sliding. After the loading direction changes ($\pm\delta_a$), the sphere-on-plane contact undergoes a brief partial slip phase, followed by gross sliding. The tangential force (Q) at the onset of gross sliding (gs*) corresponds to the minimum friction force ($F\mu_{min}$). Under non-Coulomb friction conditions, the friction force increases during gross sliding and achieves its maximum value ($F\mu_{max}$) when the tangential displacement (δ) is at its extreme position, producing a "hooked" end in the fretting loop.

Many fretting studies on gross sliding conditions have shown that the tangential force, instead of remaining constant, increases in gross sliding during one load cycle. Such non-Coulomb friction behaviour has been reported in fretting studies with different contact types, material pairs, and even coatings [7,8,15,20,22–29]; however, the studies have discussed the phenomenon only briefly, because it was not their main focus. Fouvry et al. [23] suggested that the "hooked" shape in the fretting loop may derive from changes in the contact conditions brought about by a macroscopic plastic deformation in the specimen caused by the test pad ploughing slightly into the specimen. Lavella et al. [15] arrived at a similar conclusion, though the change in the contact condition was also affected by fretting wear. Zhou et al. [26] explained the phenomenon by cyclic plastic deformation. Mulvihill et al. [9] studied non-Coulomb behaviour extensively and produced a non-Coulomb fretting loop by using a rotational fretting loading that eliminated macroscopic ploughing at the contact edges. Observations based on fretting wear scar profilometry showed evidence of tangentially interlocked fretting scar topographies. Furthermore, Mulvihill et al. found that tangential fretting scar interactions between interlocked protrusions and dents within the contact caused the fretting loop to produce a non-Coulomb shape, and that the curvature of the fretting loop was linked with the geometry of the interacting protrusions and dents. In a study of fretting fatigue in a bronze against steel contact, Hintikka et al. [6] reported that fretting scars showed evidence of interlocking fretting scar topography and suggested that this had an adverse impact on cracking behaviour. In the same study, curved non-Coulomb tangential behaviour was observed also in gross sliding conditions.

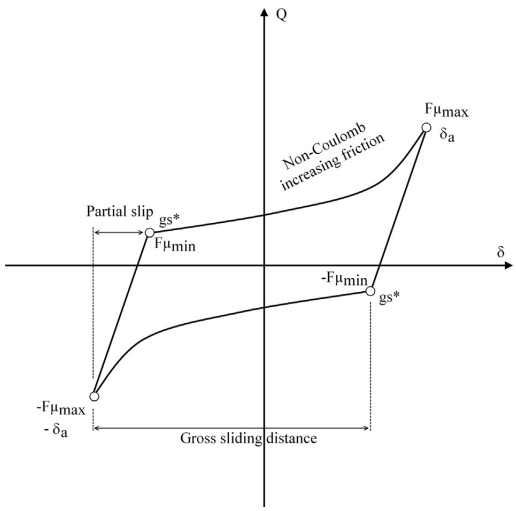

Fig. 1. The non-Coulomb fretting loop.

The need to increase power density, e.g., in diesel engineering, leads to high utilisation of the fatigue strength of the materials used. In such cases, accurate dimensioning of contacts susceptible to fretting is very important, because engine components undergo countless load cycles during their life time. Cyclic loadings and often also variable loading conditions bear on many joints that transfer high tangential traction, as in diesel engines, where load consists of firing forces, inertial forces, vibrations, and thermal effects, to name a few, which may vary not only due to different engine operating conditions but also during a combustion cycle [30]. Fretting has been tested using different variable stress amplitude or variable displacement amplitude schemes focused on fretting fatigue [31–33] and fretting wear [34,35], respectively; however not much attention has been paid to frictional behaviour. Exception is the study by Liskiewicz et al. [35] where it was reported that energy friction coefficient remained at a constant value regardless of changing displacement amplitude; however that study did not show non-Coulomb behaviour. If the coefficient of friction behaves in a non-Coulomb manner, the fretting loop and the values of friction forces ($F\mu_{min}$, $F\mu_{mean}$ and $F\mu_{max}$) may be affected by variable loading conditions.

Bronze–steel is one of the material pairs used in the frictional joints of engines, and this alloy has been shown to display non-Coulomb gross sliding friction behaviour. This study examined the properties of non-Coulomb friction occurring in an aluminium bronze vs. quenched and tempered steel pair by using dry fretting point contact under constant and variable loading conditions.

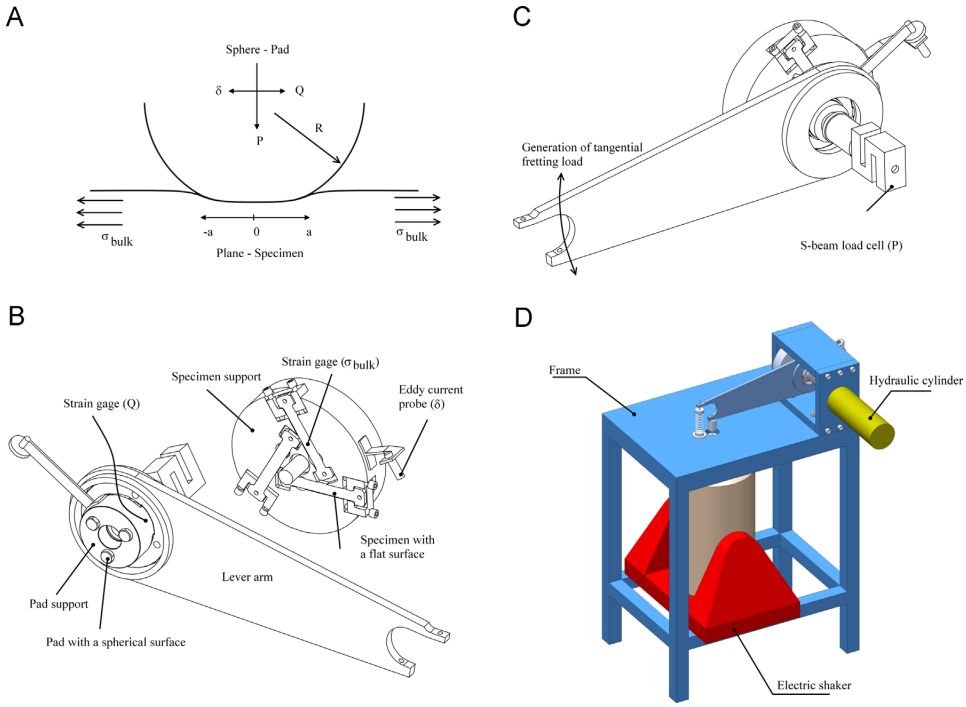

Fig. 2. (A) Sphere-on-plane contact, (B) test device dismantled and (C, D) test device assembled.

Accurate prediction of the friction coefficient allows precise modelling of frictional traction fields in machine component surfaces producing realistic cracking risk.

2. Experiments

2.1. The test device

Experiments were performed using a sphere-on-plane fretting test rig [14] (instrumentation and test device layout shown in Fig. 2). The test pad with a spherical surface made contact with the planar surface of the test specimen (Fig. 2A). The device had three equally-loaded contacts running simultaneously (Fig. 2B). First, the specimens were strained with a constant tensile bulk stress (σ_{bulk}), independent of the fretting movement of the pad and measured using strain gages. The pads were then pressed against the specimens with a hydraulic cylinder, and the combined normal force ($3 \times P$) was measured using an s-beam load cell. Fretting loading was generated with an electric shaker via reciprocating rotation of the lever arm (Fig. 2C), controlled with a feed-back signal from an eddy current probe, a Micro-Epsilon DT3701-U3-A-C3, used for measuring the tangential displacement (δ_m), which was equal for all contacts. The combined tangential force ($3 \times Q$) was measured with strain gages (torsion) calibrated with dead weights. The control unit of the shaker allowed computer-controlled changes in the tangential displacement amplitude (δ_a), either gradually or abruptly, during the test. The measured tangential displacement δ_m included some extra displacement due to the compliance of the test device. This additional displacement was removed from the measured displacement data with the formula $\delta = \delta_m - k \times Q$, where k corresponds to the rigidity of the test rig [6,36].

Table 1
The material and surface properties of the specimens.

	Steel	*Bronze*
S_y [MPa]	1056	280
S_u [MPa]	1160	650
S_f [MPa]	496	–
E [GPa]	206	120
ν [–]	0.27	0.3
S_a [μm]	0.04–0.08	0.05–0.1
S_t [μm]	1.0–2.0	0.8–2.9

In summary, the test rig was capable of measuring the tangential displacement and tangential force in detail and of accurately controlling the tangential displacement amplitude. It was thus well suited for testing the non-Coulomb phenomenon.

2.2. Test specimens and the test matrix

In this study, some previous gross sliding measurements [6] were reanalysed, and new complementary measurements were made to study non-Coulomb behaviour in detail. Contact pads were made from aluminium bronze (CuA10Fe5Ni5-C-GC EN 1982), here bronze for short, and test specimens from quenched and tempered steel (EN 10083-1-34CrNiMo6+QT), steel for short. The specimens were machined and fine-ground from a 25-mm diameter round bar tempered at 900 °C (63 min) and quenched in oil and then tempered at 560 °C (84 min). The pads were machined from a 26-mm diameter round bar, and the spherical shape was ground. Last, the contact surfaces of the specimens and pads were polished. The properties of the test pieces are listed in Table 1.

In Table 1, S_y is the yield strength, S_u the ultimate strength, S_f the fatigue strength, E the elastic modulus, ν Poisson's ratio, and

S_a and S_t are surface roughness parameters. S_a was calculated as the arithmetic mean of the absolute value of surface departures from an average plane. S_t is the average valley-to-peak height between five highest peaks and five lowest valleys. Surface roughness was measured using a Wyko NT1100 optical profilometer. The surface area analysed was 4.9×3.8 mm^2 with 6.72-μm lateral and 3-nm vertical resolutions. In radius, the spherical pads ranged from 280 to 300 mm. Surface roughness and sphere radius were measured for all specimens and pads. The specimens were carefully cleaned in an ultrasonic washing device before and after the fretting tests.

Tests were run in standard monitored laboratory air. A constant bulk stress of 400 MPa was first applied and followed by a constant normal force. The fretting loading frequency was 40 Hz. Each test had a 5000-load-cycle start-up phase, during which δ_a was increased linearly from zero to the target value. Two sets of experiments were run with different δ_a schemes, where δ_a was either kept constant or changing after start-up. The sets were labelled constant δ_a measurements and variable δ_a measurements.

In constant δ_a measurements, δ_a was kept at a constant value after start-up. A total of six experiments were run with two normal loads and different displacement amplitudes (Table 2). Constant δ_a measurements were fretted 2.8×10^6 load cycles, except that measurement 33* was fretted for only 10,000 load cycles after the start-up phase (5000 load cycles). Duration for measurement 30* was chosen retrospectively after full duration tests, and it corresponded to such test duration that a non-Coulomb fretting loop was well developed, thus providing representative fretted surfaces for post-test analysis. Measurements are compiled in Table 2, where the displacement amplitude corresponds to the average value over the whole experiment.

In variable δ_a measurement, δ_a was either changed once and suddenly or under repeating changes after start-up, and these measurements were used to determine the behaviour of Q if δ_a suddenly changed. Varying δ_a during a fretting test should lead to changes in measured Q, if it is a function of δ. In the first variable δ_a measurement (Fig. 3A), the contact was fretted with a constant δ_a of 33 μm for 10,000 load cycles; then δ_a was decreased linearly to 20 μm within 1 s (40 load cycles), which was maintained for a further 10,000 load cycles, referred to as measurement 33→20. In the second variable δ_a measurement, the scheme was the same except for δ_a, which was increased to 50 μm rather than decreased, a procedure referred to as measurement 33→50. In the third measurement, δ_a was varied constantly between 30 and 50 μm and referred to as measurement 30↔50. Fig. 3B shows that in measurement 30↔50, δ_a was first kept at 30 μm for 10,000 load cycles, after which it had five distinct phases where δ_a had a specific control scheme. In phases 2 and 4, δ_a was kept constant at 30 and 50 μm, respectively. In phases 1, 3, and 5, δ_a was repeatedly varied between 30 and 50 μm in such a way that it was kept constant for 2 s (80 load cycles) and then linearly changed to another δ_a over 1 s (40 load cycles), held there for 2 s, and then switched back again. During the experiment, the number of load cycles in each phase was chosen to ensure steady state conditions in tangential behaviour. The 40-load cycle (1 s) change duration allowed observation of the evolution of fretting loops during the time when δ_a was changing, whereas 1 s (40 cycles) and 2 s (80 cycles) were short enough to represent temporary fretting conditions without long-term wear or fretting damage.

Table 2
The test matrix.

δ_a-scheme	P [N]	δ_a [μm]		
Constant	1270	19.1	30.7	41.3
Constant	2240	31.9	33*	52.4
Variable	2240	33→50	33→20	30↔50

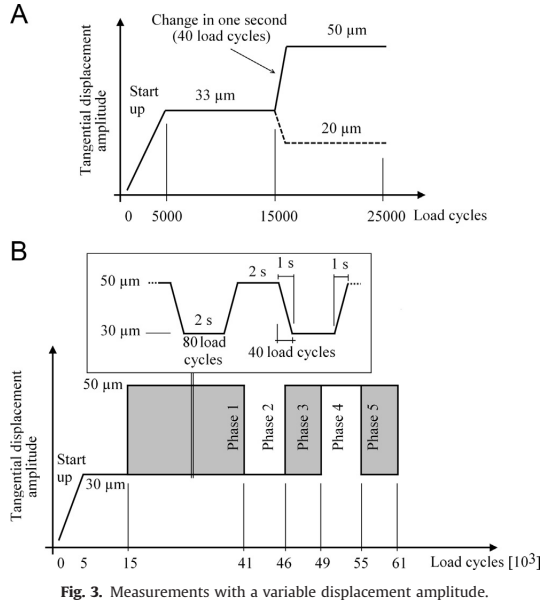

Fig. 3. Measurements with a variable displacement amplitude.

3. Results

3.1. Constant tangential displacement amplitude

Measurements with the constant δ_a-scheme produced non-Coulomb fretting loops, shown from 5000 to 100×10^3 load cycles in Fig. 4A–E, where the dotted and solid black lines represent the first and the last fretting loop, respectively, and the grey lines represent the loops in between with 10,000 load cycle spacing. Though all measured fretting loops clearly show non-Coulomb behaviour, the exact shape varies slightly as a function of loading and load cycles, thus making it difficult to interpret the properties of individual fretting loops. The values of $F\mu_{min}$, $F\mu_{mean}$, and $F\mu_{max}$ were extracted from the fretting loops (Fig. 4F) using a Matlab code.

The location of the onset of gross sliding (gs*) was primarily determined by calculating the slope of the fretting loop ($\Delta Q/\Delta\delta$) and its zero or minimum value to pinpoint a precise location for gs*. When obtainable, the location was named as unique. Otherwise Eq. (1) was used, which describes the Q–δ dependence in an ideal sphere-on-plane contact assuming ideal coulomb friction [5]:

$$\delta = \frac{3\mu P}{16a} \times \left(\frac{2-\nu_1}{G_1} + \frac{2-\nu_2}{G_2}\right) \times \left\{1 - \left(1 - \frac{Q}{\mu P}\right)^{2/3}\right\} \quad (1)$$

The measured maximum Q/P-ratio was used to estimate μ, which gives a slightly longer partial slip than exists in the non-Coulomb fretting loop. Using the maximum Q/P-ratio ensures that subsequent data processing operates in the gross sliding part of the fretting loop. $F\mu_{min}$ was then searched from between gs* and the next extreme position of δ. If $F\mu_{min}$ had a local minimum in between those boundaries, it was named unique; however, often this value coincided with the location of gs*, and in such cases $F\mu_{min}$ was named unique only if the location of gs* was unique. $F\mu_{mean}$ was calculated as an average value from the gross sliding phase, weighted with the gross sliding distance, and $F\mu_{max}$

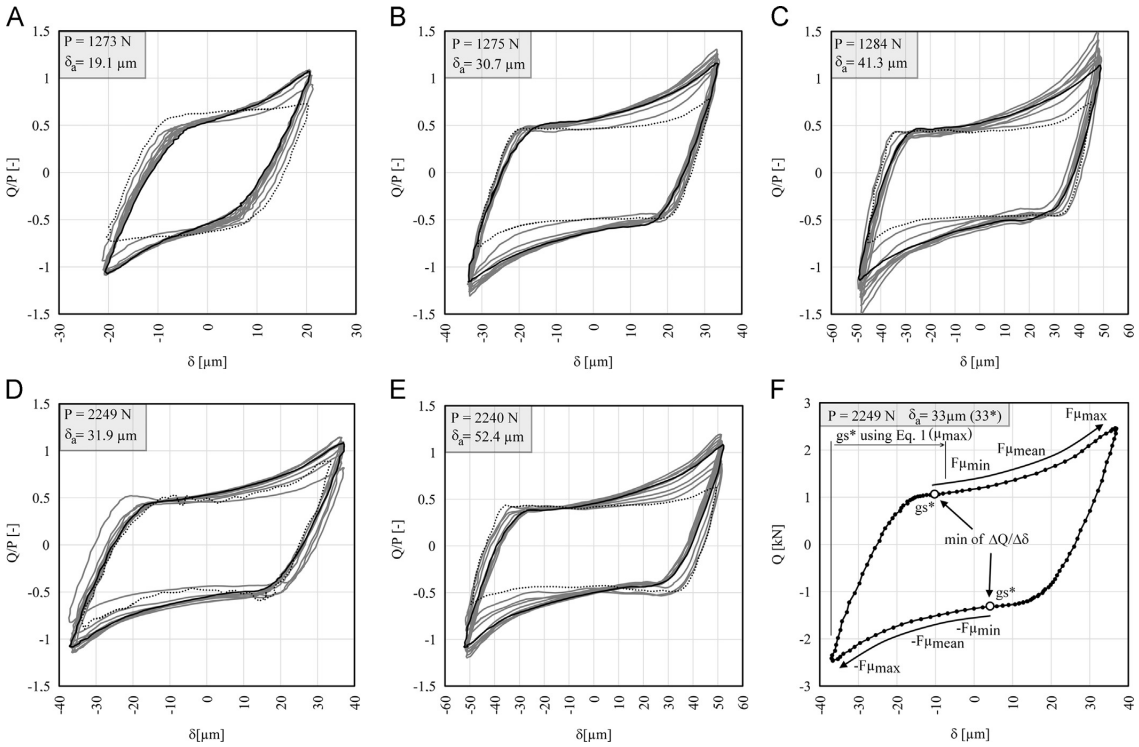

Fig. 4. (A–C) Fretting loops from measurements with a ~1270 N normal load, (D and E) fretting loops from measurements with a ~2240 N normal load, and (F) illustration of data processing to obtain minimum, average, and maximum friction forces.

corresponded to the single maximum value of $F\mu$, which was typically located at the extreme end of the fretting movement.

Often the location of gs* and $F\mu_{min}$ was found directly from the fretting loops (unique), but the values were also often obtained solely by using Eq. (1). Non-unique $F\mu$ values could depend on the method of extraction; however, this had only a minor effect on the extracted values of $F\mu_{min}$ and $F\mu_{mean}$, because Q remained almost constant near gs*. If a unique location was found, it is indicated in the subsequent friction results for both loading directions, a procedure applied to both sides of the fretting loop with average absolute values calculated for $F\mu_{min}$, $F\mu_{mean}$, and $F\mu_{max}$. These values were then divided by the normal force to obtain the corresponding Q/P-ratios (μ_{min}, μ_{mean}, and μ_{max}) (Fig. 5).

Fig. 5 shows the development of measured friction coefficient values. At the bottom of each figure, the lines marked in black dots indicate that unique values were obtained for μ_{min} so that the upper and lower lines correspond to forward and reverse movements, respectively. Similarly, grey dots indicate whether unique locations were found for gs*. The non-Coulomb fretting loop is absent in the initial fretting cycles, and the first signs of it are observed after gross sliding is reached, as δ_a is increased during the first 5000 load cycles. After the start-up phase, μ_{min} is fairly independent of load cycles and the normal force. It may slightly depend on δ_a so that an increase in δ_a decreases μ_{min}. μ_{max} increases and also peaks before the first $\sim 100\times10^3$ load cycles and thereafter fluctuates around unity. μ_{max} has its maximum values in the range of 1.1–1.5, which is 2–3 times greater than the corresponding μ_{min}. μ_{mean} shows a slightly increasing trend as a function of load cycles but stabilises at values about 50% greater than μ_{min}. The value of μ_{mean} can be used to estimate the curvature of the fretting loops. Because μ_{min} is clearly below μ_{max}, and because μ_{mean} is typically closer to μ_{min} than μ_{max}, the fretting loops remained non-Coulomb throughout the experiments. The non-Coulomb hook in the fretting loop is most pronounced in the early stages of the experiments ($\mu_{mean}/(\mu_{max}-\mu_{min})\ll0.5$), and the curve gradually transforms into a parallelogram, where Q increases almost linearly as a function of δ ($\mu_{mean}/(\mu_{max}-\mu_{min})=\sim0.5$). Further study is focused on load cycles less than 100×10^3.

3.2. Variable tangential displacement amplitude

Two kinds of variable δ_a measurements were made. In the first two measurements, the contact was first fretted in steady state conditions, and then δ_a was increased or reduced within 40 load cycles (Fig. 3A) and kept at a constant value. δ_a was large enough for the contact to remain in gross sliding at all times (resulting friction coefficient values shown in Fig. 6).

Fig. 6A and B shows how friction coefficients developed in measurements 33→20 and 33→50 during the 5000–25,000 load cycles. μ_{max} shows a gradual increasing trend, though its value often drops suddenly and temporarily even in locations where δ_a remains constant. The vertical arrows indicate when δ_a was suddenly changed; this data section is shown in detail in Fig. 6C and F as a function of load cycles and δ_a. Clearly, a sudden change in δ_a results in a decrease of about 0.2 in μ_{max} regardless of the direction of the δ_a-change. A smaller change in μ_{min} can also be seen, but this now depends on the direction of the δ_a-change such that increasing δ_a decreases μ_{min} and vice versa. Interestingly, the constant δ_a measurements showed a similar relation between the μ_{min} and δ_a values, i.e., the larger the δ_a, the smaller the μ_{min}. The decrease in μ_{max} is only temporary, and it gradually increases and even exceeds the values it had prior to any changes in δ_a.

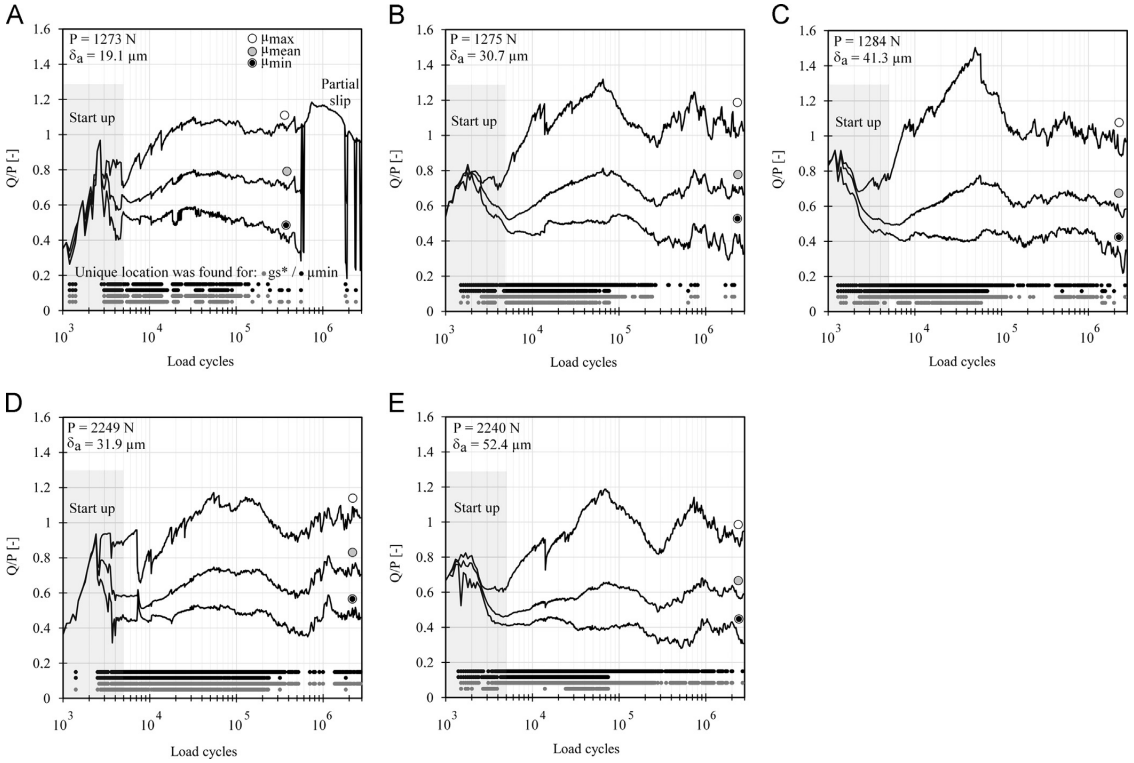

Fig. 5. Minimum, mean and maximum friction coefficient values from constant tangential displacement amplitude measurements.

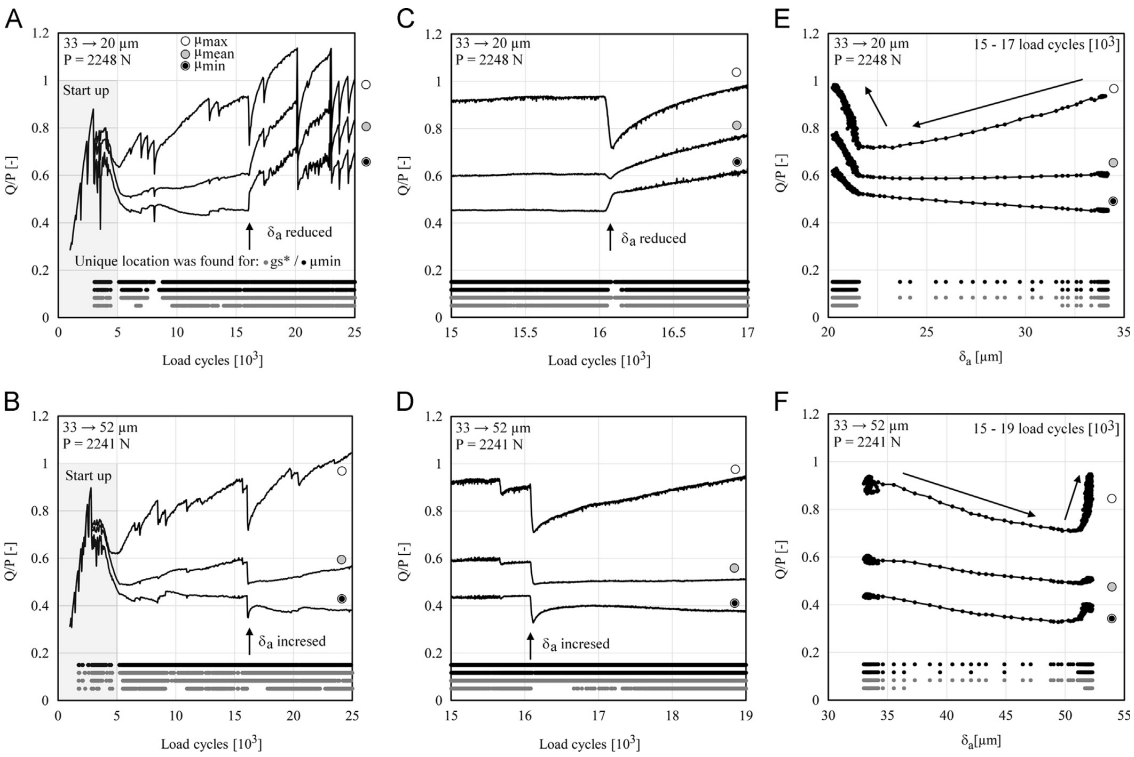

Fig. 6. Measured friction coefficients when the displacement amplitude was suddenly reduced (A, C and E) and increased (B, D and F).

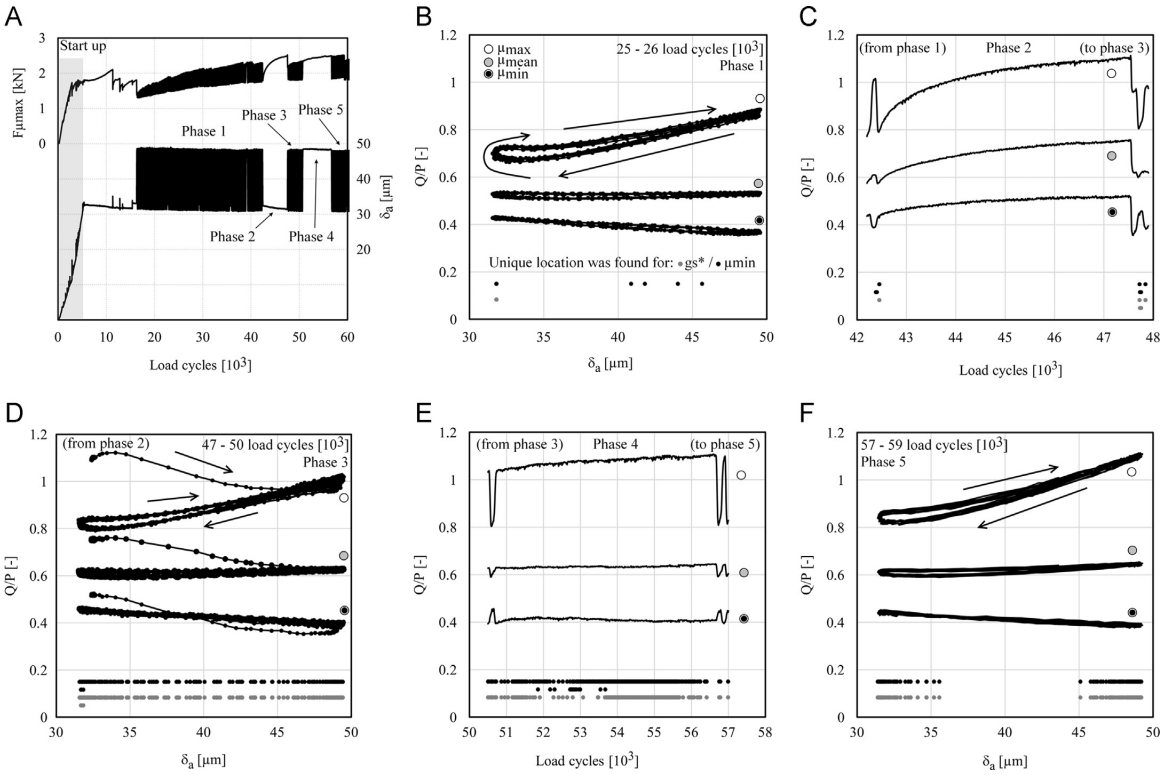

Fig. 7. Results from measurement 30↔50 with P=2251 N during different phases.

The second type of variable δ_a measurement (30↔50) was made so that δ_a underwent repeated changes, as illustrated in Fig. 3B and Fig. 7A. In Phase 1, δ_a was varied continuously between 30 and 50 μm, and the resulting friction behaviour is shown in Fig. 7B. As shown, μ_{max} decreases and increases when δ_a is decreased and increased, respectively. Rather than a straight line, μ_{max} forms a narrow teardrop-shaped loop. This is most likely due to a load cycle effect, because one cycle in the variable δ_a scheme, i.e., one teardrop loop, corresponds to 240 load cycles. The maximum value of μ_{max} occurs at the largest δ_a. As in the earlier measurements, μ_{min} decreased and increased slightly when δ_a is increased and decreased.

The δ_a control scheme at the end of Phase 1 (reduced δ_a), Phase 2 (constant δ_a), and the beginning of Phase 3 (increased δ_a) was similar to that used in experiments 33→20 and 33→50, which is why the results shown in Fig. 7C correspond closely to those shown in Fig. 6C and D. It follows that in Phase 2, μ_{max} started to increase until it gradually reached and even exceeded the μ_{max} that had been achieved during Phase 1.The friction data from the beginning of Phase 3 shows that μ_{max} decreased to its level at the end of the Phase 1, when δ_a was suddenly increased. In phase 2, μ_{min} showed only a minor increase.

Fig. 7D shows the friction behaviour in Phase 3 as a function of δ_a. At the beginning of this phase, the increase in δ_a resulted in a reduction of 0.1 in μ_{max}. Almost immediately, δ_a was reduced to 30 μm, which resulted in an additional reduction of 0.2 in μ_{max}. The later behaviour in Phase 3 was similar to that in Phase 1. In Phase 4, δ_a was kept constant at a higher δ_a of 50 μm. During this phase, friction values did not evolve much, and only a minor increase in μ_{max} was observed (Fig. 7E). In Phase 5 (Fig. 7F), δ_a was again varied, and the behaviour was identical to the corresponding steady state conditions in Phases 1 and 3, showing good repeatability. The only difference between Phases 1, 3, and 5 is that the values of μ_{max} gradually increase as the number of load cycles increase.

The variable δ_a measurements show that frictional behaviour can be significantly influenced by a sudden change in δ_a. Major changes occur in μ_{max}, whereas μ_{min} exhibits only moderate changes. The fretting loops remained non-Coulomb regardless of the variable δ_a schemes ($\mu_{mean}/(\mu_{max}-\mu_{min}) \leq 0.5$). The μ_{min}–δ_a dependence was quite consistent, whether or not δ_a was constant or continuously varying, i.e., μ_{min} always decreased when δ_a increased. Whenever δ_a was kept at a constant value over a few thousand load cycles, a temporary reduction in μ_{max} followed when δ_a was suddenly reduced or increased. Conversely, a different behaviour was seen when δ_a was continuously changing between two δ_a values within a range of a few tens of load cycles. In such a case, μ_{max} increased when δ_a was suddenly increased and vice versa. However, μ_{max} could not be permanently reduced by manipulating δ_a. It stabilised gradually up to a specific maximum value, if δ_a was kept at a constant value long enough, which in these measurements typically occurred within about 5000 load cycles.

3.3. Fretting scar observations

After the fretting tests, the test specimen and pad were inspected and loose wear particles were removed from the fretting scars, first with compressed air and then by thorough cleaning in an ultrasonic washing device prior to surface analysis. The fretting

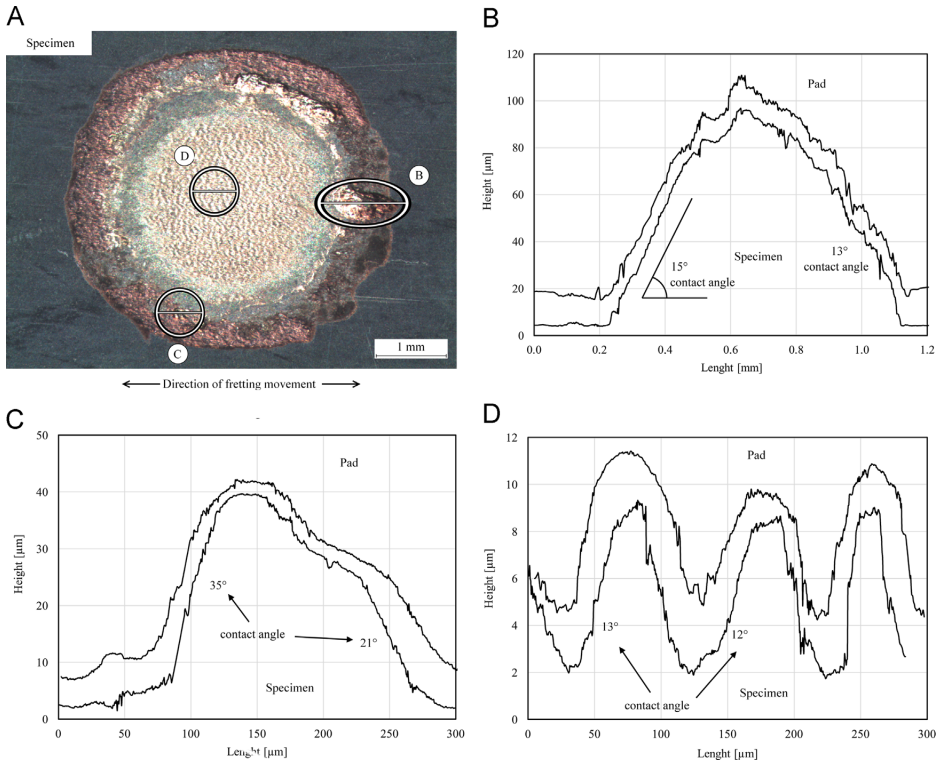

Fig. 8. Fretting scar and surface topographies from different locations after 10,000 load cycles. P=2240 N and δ_a=33 μm.

scar on the surface of the steel specimen (Fig. 8A) has the bright metallic shine of bronze; thus the sticking layer seems mostly metallic bronze. The fretting scars were then analysed for their element composition by energy dispersive X-ray spectroscopy (EDS), and the results showed that there was indeed a bronze transfer layer on the surface of the steel specimen. In addition, the iron content of the fretting scars in the specimen and pad was similar to that in the undamaged bronze, indicating that wear occurred mostly in the bronze pad, while the steel specimen remained intact. The fretting wear damage was characterised by a transfer of bronze to the surface of the steel specimen. After 25,000 load cycles, the fretting scars had 1–6% oxygen in relative weight percentage, which means that the bronze transfer layer was mostly metallic. Due to fretting damage, surface sliding actually occurred between the bronze pad and the bronze transfer layer deposited on the surface of the specimen.

However, the fretting tests, which were set to run for 2.8×10^6 load cycles, produced fretting scars that were covered in a thick black layer, clearly indicating that some elements in the metallic bronze had gradually oxidised. These specimens were not analysed by EDS. Lack of oxygen in the early stages of the experiment may have been a factor contributing to the formation of a bronze transfer layer by causing wear particles to remain highly adhesive. Fretting surface sliding combined with adhesion and possibly work-hardened bronze wear particles may have led to the formation of the interlocked fretting scar features shown below.

The topographies of the fretted specimens were carefully analysed. Fig. 8A shows an example of fretting wear damage caused by 10,000 load cycles in gross sliding (measurement 33*). The surface topographies of the test specimens (bronze transfer layer) were examined with an optical profilometer at the marked locations. The exact same spots were then identified on the bronze test pad. These matching contact surface topographies are compared in Fig. 8B–D. The fretting wear scar in Fig. 8A has two distinct regions. The central region seems to have low surface roughness but has a wavy surface profile. The radius of this central area corresponds closely to that of the initial Hertzian contact. The outer annulus seems to have a much rougher surface profile with a number of large material pieces protruding from the surface. Surface topography comparison of the specimen and pad showed that the wear scars had interlocking surface profiles. The locations on the specimen with bumps (protruding material) correspond to depressions in the surface of the fretting pad, as clearly seen in Fig. 8B–D. Similar surface topographies with varying size bumps/depressions could be found everywhere. These fretting scar topographies were formed gradually by fretting load cycles due to wear damage (material transfer), as opposed to scratches due to specimen manufacture.

It follows that the fretting scars had interlocking topographies with limited tangential clearance. Obviously, a surface pair as in Fig. 8 has tangential fretting scar (bump vs. depression) interactions, if tangential movement is large enough. It seems that numerous individual interactions may take place due to the vast number of interlocking bumps and depressions in the fretting scar pair. If surface sliding brings interlocked bump vs. depression pairs into contact, it happens at a certain contact angle, which depends on the geometry of the interacting surface features (Fig. 8B–D). Contact angles were typically in the range of 10°–20°, though they may also occur in a much larger 5°–45° range. In height, bumps and depressions ranged from 5 to 100 μm and in width from 50 to 1000 μm. Similar interacting bumps and depressions were reported in a previous study with tests made in partial slip

conditions [6], where fretting wear scar interactions were thought to have a major impact on raising the local stress level due to reaction forces caused by tangential fretting scar interaction.

The fretting scar topographies from measurements 33→50 and 33→20 showed that material transfer can also occur in the opposite direction, from the bronze transfer layer on the surface of the specimen to the surface of the pad. Bumps may also be sheared and then relocated on the same surface. Fig. 9 shows protruding pieces of bronze on the surface of the fretting pad with sharp edges (close to 90°). In measurement 33→50, such reverse material transfer and material relocation may be related to an abrupt increase in δ_a. Some interlocked bumps may have been sheared due to an increase in relative surface sliding. In measurement 33→20, the phenomenon may be related to an unstable Q_a at the end of the experiment (Fig. 6A).

There was no evidence of the bronze test pad having macroscopically ploughed into the surface of the steel specimen. In fact, the bronze pad was heavily damaged, and the sphere was more or less worn and deformed to a planar surface, obviously because quenched and tempered steel has a much greater yield strength and hardness than bronze. It is unlikely that the curved fretting loop with this material pair and loading conditions resulted from macroscopic ploughing effects. On the contrary, similar tangentially interlocked fretting scars were found such as those observed also in the study by Mulvihill et al. [9].

3.4. Fretting scar interaction scheme

The previous section showed that fretting loading caused severe damage to the bronze pad and possible formation of interlocked fretting scars which is shown schematically in Fig. 10A–C. Fig. 10D–F shows interaction between interlocked bumps and depressions when surfaces are fretted. If relative surface sliding is extensive enough, interactions may contribute to non-Coulomb friction. The surface topographies shown here are measured (Fig. 8D). There is about a 14-μm tangential clearance or room for free sliding before interaction between interlocked bumps and depressions. Such surface comparison is not precise, because the surfaces were unstressed when the fretting scar profiles were measured, and because the correct relative vertical positions of the surfaces were not known. However, if surfaces are brought closer together, there is then less clearance. In this measurement, δ_a was about 33 μm, which means that the surface sliding amplitude in the middle of the contact was about 25 μm. This value is based on an analytical solution for surface sliding with ideal sphere-on-plane geometry (Eq. (1)) and assuming a friction coefficient of 1.0, which corresponds to the measured $F\mu_{max}$. We can conclude that the clearance of the interacting asperities is less than the relative surface sliding ($\sim$14 μm < $\sim$25 μm); consequently, some form of tangential fretting scar interaction can occur.

4. Discussion

So far we have shown that fretting loops are non-Coulomb, and that fretting scars contain numerous interlocked bumps and depressions that result in some form of tangential fretting scar interaction. Measured results also show that non-Coulomb friction did not fully develop in the initial fretting cycles but matured gradually as the the fretting load cycles increased in number. The interactions between bumps and depressions are not fully understood. However, the fretting scar interaction scheme with interlocked fretting scar topographies and clearances (Fig. 10) can be used to explain the experimental observations of frictional behaviour (Sections 3.1 and 3.2). A sudden reduction in δ_a should result in less fretting scar interaction and lead to reduced μ_{max}. A sudden increase in δ_a results in over-stressed bumps and depressions, causing them to deform or even wipe out under shear, which also leads to a temporary decrease in μ_{max}. We can speculate that the severity of the bumps and depressions wipe out and the magnitude of the temporary reduction in μ_{max} are depend on the absolute value of increase in the displacement amplitude. A gradual increase in μ_{max} in constant gross sliding conditions can be explained by continuous fretting wear or fretting damage process, which continuously modifies the contact interface leading to the formation of interlocked fretting scar topographies specific to these operating conditions. This is also consistent with the

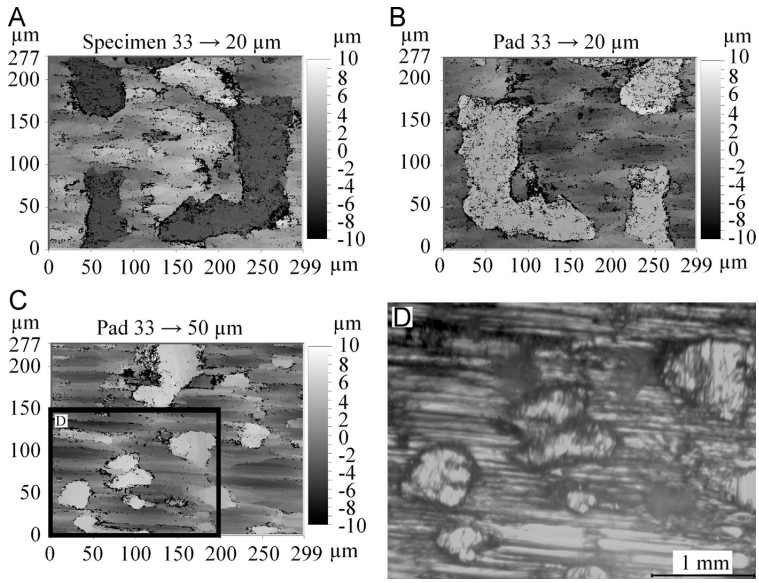

Fig. 9. Bronze material transfer particles on the surface of the fretting pad in measurement 33→50. (A–C: profilometer images and D: optical microscope image).

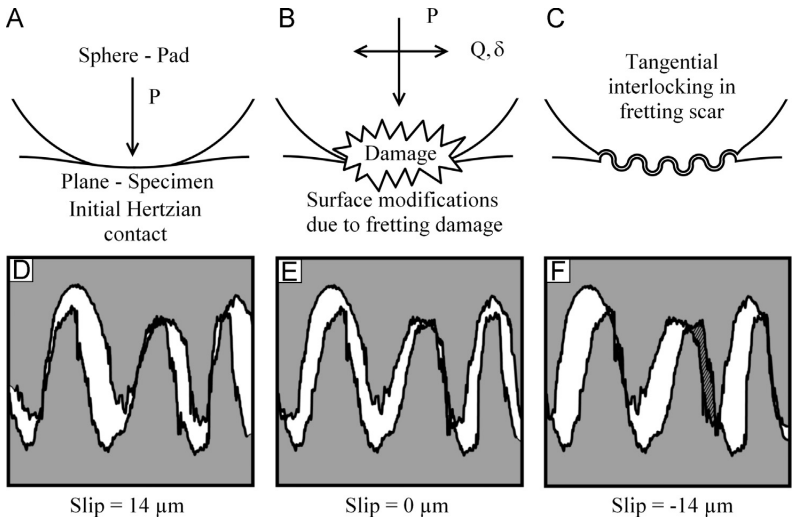

Fig. 10. Schematics of fretting scar interactions.

observation that μ_{max} could not be permanently reduced by manipulating δ_a. When δ_a is continuously changing between two values within a few tens of load cycles, μ_{max} increases or decreases when δ_a increases or decreases, because the fretting process does not have enough time (load cycles) to modify interlocked fretting scars. Consequently, fretting wear damage occurring in a bronze–steel contact may be the key factor leading to the observed non-Coulomb friction phenomenon.

Mechanical interlocking in interacting bumps and depressions may cause relative frictional surface sliding in a slightly upward direction due to the contact angles (Figs.8 and 10). This increases the Q required to propagate surface sliding compared to frictional sliding on an ideally flat surface, as proposed by Mulvihill et al. [9]. In such conditions, non-Coulomb friction behaviour follows even if the friction coefficient (μ) is constant. By employing the wear scar interaction model of Mulvihill et al. with the measured values for μ_{max} and a bump/depression contact angle of 20°, a Coulomb friction coefficient in the range of 0.5–0.7 is sufficient to produce the measured non-Coulomb effect. Such a value is feasible within the scope of the measured data. If such a mechanism is solely responsible for the non-Coulomb effect, the interactions with the steepest contact angles would have to carry a significant proportion of the non-Coulomb tangential load to compensate for the weaker effect of the shallower angles. The non-Coulomb phenomenon was explained by macroscopic ploughing effects by Fouvry et al. [23] and Lavella et al. [15]; however, their results showed that the pad penetrated into the surface of the specimen. This was not observed in our study, which is obvious because the sphere was made of bronze, a much softer material than the steel specimen. The similarity is that the non-Coulomb behaviour was related to fretting damage and mechanical interlocking in the tangential direction, and the obvious difference is in the size scale. Another possible explanation is that the real contact area increases as the fretting movement approaches its extreme position due to fretting scar interactions, thereby increasing the force required to shear adhesive junctions. Such an explanation means that the friction coefficient is changing and leading to non-Coulomb behaviour. Some non-Coulomb behaviour may result from a plasticity-related phenomenon within the bronze fretting pad or in the interaction of the bumps and depressions, as suggested by Zhou et al. [26]. Multiple mechanisms may also be operating simultaneously to bring about overall non-Coulomb tangential behaviour. It is unlikely that all non-Coulomb friction observations can be explained accurately with the same mechanisms, because they may strongly depend on parameters such as the material pair, contact geometry, and severity of the load. One factor not considered in this study was the role of loose wear particles. They may contribute to non-Coulomb friction, especially in spaces between interacting bumps and depressions.

Non-Coulomb tangential behaviour gives rise to non-linear contact behaviour where surface sliding commences at relatively low forces, and where the contact then stiffens when the fretting movement approaches its extreme position. Non-Coulomb behaviour could perhaps be modelled by adding interlocked bumps and depressions to otherwise ideal surfaces. However, that would be very demanding computationally, especially in industrial-scale applications. A more straightforward method would be to model the friction coefficient as a function of slip and use ideal surfaces, an approach that might give a reasonably accurate total tangential response. However, this method has the drawback that it ignores the concentrating effect of bump-depression interactions on normal and tangential tractions. Such work is left for future studies.

5. Conclusions

Fretting experiments were performed with an aluminium bronze vs. quenched and tempered steel pair in gross sliding conditions under high normal loads. The following conclusions were drawn:

- The fretting loops showed non-Coulomb friction behaviour with the friction force increasing steeply when the fretting movement approached its extreme position. The behaviour evolved in the early stages of the experiments and persisted for the test duration of 2.8×10^6 load cycles; however, the fretting loops gradually changed shape from “hooked” ends to a parallelogram.
- A single sudden increase or decrease in the tangential displacement amplitude leads to a temporary reduction in the maximum friction force. However, this reduction was not permanent,

because the maximum friction force gradually reverted to its value prior to any changes, typically within 5000 load cycles.

- Continuously changing tangential displacement amplitude led to a different behaviour pattern. Reducing the tangential displacement led to a decrease in the maximum friction force, and increasing the tangential displacement amplitude led to an increase in the maximum friction force.
- The minimum friction force depended slightly on the value of the tangential displacement amplitude; however, it was not greatly affected by the suddenness of change in its value.
- The fretting scars had multiple interlocked bumps and depressions, resulting from a gradual propagation of fretting wear damage, and material transfer.
- Non-Coulomb friction behaviour, and especially the properties of the maximum friction force, can be explained in terms of fretting scar interactions. These interactions, however, are not yet fully understood.

Acknowledgements

This study was conducted as part of the ScarFace Research Project (Tekes decision no. 40205/12). We are grateful for the financial support provided by Tekes - the Finnish Funding Agency for Innovation, Wärtsilä Finland Oy, Nome Oy, and Global Boiler Works Oy.

References

[1] Hills DA, Nowell D. Mechanics of fretting fatigue. Dordrecht: Kluwer Academic Publishers; 1994.
[2] Johnson KL. Contact mechanics. Cambridge: Cambridge University Press; 1985.
[3] Dundurs J. Discussion of edge-bonded dissimilar orthogonal elastic wedges under normal and shear loading. J Appl Mech 1969;36:650–2.
[4] Munisamy RL, Hills DA, Nowell D. Static axisymmetric Hertzian contacts subject to shearing forces. J Appl Mech Trans ASME, 61; 1994; 278–83.
[5] Mindlin RD. Compliance of elastic bodies in contact. J Appl Mech 1949;16:259–68.
[6] Hintikka J, Lehtovaara A, Mäntylä A. Fretting fatigue and friction of quenched and tempered steel in dry contact with aluminum bronze. Wear 2013;308: 155–65.
[7] Kartal M, Mulvihill D, Nowell D, Hills D. Determination of the frictional properties of titanium and nickel alloys using the digital image correlation method. Exp Mech 2011;51:359–71.
[8] Lee H, Mall S, Murray K. Fretting wear behavior of Cu–Al coating on Ti-6Al-4V substrate under dry and wet (lubricated) contact condition. Tribol Lett 2007;28:19–25.
[9] Mulvihill DM, Kartal ME, Olver AV, Nowell D, Hills DA. Investigation of non-Coulomb friction behaviour in reciprocating sliding. Wear 2011;271:802–16.
[10] Kartal ME, Mulvihill DM, Nowell D, Hills DA. Measurements of pressure and area dependent tangential contact stiffness between rough surfaces using digital image correlation. Tribol Int 2011;44:1188–98.
[11] Bolton W. Mechatronics. 5th ed.. Harlow: Pearson; 2011.
[12] Kubota M, Kuwada K, Tanaka Y, Kondo Y. Mechanism of reduction of fretting fatigue limit caused by hydrogen gas in SUS304 austenitic stainless steel. Tribol Int 2011;44:1495–502.
[13] Wavish PM, Houghton D, Ding J, Leen SB, Williams EJ, McColl. IR. A multiaxial fretting fatigue test for spline coupling contact. FFEMS 2009;32:325–45.
[14] Pasanen A, Järvisalo S, Lehtovaara A, Rabb R. Development of a test device for the evaluation of fretting in point contact. Lubr Sci 2009;21:41–52.
[15] Lavella M, Botto D. Fretting wear characterization by point contact of nickel superalloy interfaces. Wear 2011;271:1543–51.
[16] Ren Wanbin, Cui Li, Chen Jinbao, Ma Xiaoming, Zhang Xinyun. Fretting behavior of au plated copper contacts induced by high frequency vibration. In: Proceedings of the IEEE 58th Holm conference on electrical contacts; 2012. pp. 1–7.
[17] Mohrbacher H, Celis J, Roos JR. Laboratory testing of displacement and load induced fretting. Tribol Int 1995;28:269–78.
[18] Mohd Tobi AL, Ding J, Bandak G, Leen SB, Shipway. PH. A study on the interaction between fretting wear and cyclic plasticity for Ti–6Al–4V. Wear 2009;267:270–82.
[19] Filippi S, Gola MM, Akay A. Measurement of tangential contact hysteresis during microslip. J Tribol 2004;126:482–9.
[20] Rybiak R, Fouvry S, Bonnet B. Fretting wear of stainless steels under variable temperature conditions: introduction of a 'composite' wear law. Wear 2010;268:413–23.
[21] Sabeya GRYN, Paris J, Denape J. Fretting wear of a coated titanium alloy under free displacement. Wear 2008;264:166–76.
[22] Jin O, Mall S, Sanders JH, Sharma SK. Durability of Cu–Al coating on Ti–6Al–4V substrate under fretting fatigue. Surf Coat Technol 2006;201:1704–10.
[23] Fouvry S, Duó P, Perruchaut. P. A quantitative approach of Ti–6Al–4V fretting damage: friction, wear and crack nucleation. Wear 2004;257:916–29.
[24] Jin O, Mall S. Effects of slip on fretting behavior: experiments and analyses. Wear 2004;256:671–84.
[25] Degat PR, Zhou ZR, Vincent L. Fretting cracking behaviour on pre-stressed aluminium alloy specimens. Tribol Int 1997;30:215–23.
[26] Zhou ZR, Gu SR, Vincent. L. An investigation of the fretting wear of two aluminium alloys. Tribol Int 1997;30:1–7.
[27] Liu E, Blanpain B, Celis J. Fretting friction and wear of polycrystalline diamond coatings. Diam Relat Mater 1996;5:649–53.
[28] Wang D, Zhang D, Ge S. Effect of displacement amplitude on fretting fatigue behavior of hoisting rope wires in low cycle fatigue. Tribol Int 2012;52: 178–89.
[29] Wang D, Zhang D, Zhao W, Ge S. Quantitative analyses of fretting fatigue damages of mine rope wires in different corrosive media. Mater Sci Eng: A 2014;596:80–8.
[30] Mollenhauer K, Tschoeke H. Handbook of diesel engines. Berlin: Springer eBooks; 2010.
[31] Cortez R, Mall S, Calcaterra JR. Investigation of variable amplitude loading on fretting fatigue behavior of Ti–6Al–4V. Int J Fatigue 1999;21:709–17.
[32] Kondo Y, Sakae C, Kubota M, Kitahara H, Yanagihara K. Fretting fatigue under variable loading below fretting fatigue limit. Fatigue Fract Eng Mater Struct 2006;29:191–9.
[33] Jin O, Mall S, Lee H. Investigation into cumulative damage rules to predict fretting fatigue Life of Ti-6Al-4V under two-level block loading condition. J Eng Mater Technol 2003;125:315–23.
[34] Paulin C, Fouvry S, Deyber. S. Wear kinetics of Ti–6Al–4V under constant and variable fretting sliding conditions. Wear 2005;259:292–9.
[35] Liskiewicz T, Fouvry S, Wendler B. Impact of variable loading conditions on fretting wear. Surf Coat Technol 2003;163-164:465–71.
[36] Hintikka J, Lehtovaara A, Lönnqvist C. Effect of start-up schemes and amplitude of tangential motion on friction behavior in fretting point contact. Tribol Int 2011;44:1535–43.

Publication IV

Fretting-induced friction and wear in large flat-on-flat contact with quenched and tempered steel

by

J Hintikka, A Lehtovaara and A Mäntylä

Tribology International, 92 (2015), 191-202

doi:10.1016/j.triboint.2015.06.008

Tribology International 92 (2015) 191–202

Contents lists available at ScienceDirect

Tribology International

journal homepage: www.elsevier.com/locate/triboint

Fretting-induced friction and wear in large flat-on-flat contact with quenched and tempered steel

Jouko Hintikka [a,*], Arto Lehtovaara [a], Antti Mäntylä [b]

[a] Department of Materials Science, Tampere University of Technology, PO Box 589, 33101 Tampere, Finland
[b] Research & Development, Wärtsilä Finland Oy, PO Box 244, 65101 Vaasa, Finland

ARTICLE INFO

Article history:
Received 10 March 2015
Received in revised form
13 May 2015
Accepted 2 June 2015
Available online 20 June 2015

Keywords:
Fretting
Friction
Wear
Steel

ABSTRACT

Fretting may cause severe surface damage and lead to unexpected fatigue failure. Our test apparatus was designed based on reciprocating, large, annular flat-on-flat contact without any edge effects in the direction of the fretting movement. Fretting wear tests were run with quenched and tempered steel with different normal pressures and sliding amplitudes under gross sliding conditions. The development of the friction coefficient and total wear mass depended mostly on the accumulated sliding distance. Initially, friction and wear were highly adhesive but gradually changed to abrasive due to third body accumulation in the interface.

1. Introduction

Reciprocating tangential loading of contacting bodies can lead to small-amplitude rubbing of surfaces also known as fretting. Reciprocating surface sliding induces fretting wear, which can be detected by the appearance of oxide wear debris and material transfer. For example, fretted steel contacts produce brown oxides of fine, powdery texture. In fretting conditions, the coefficient of friction (COF) is often high, which may lead to high tangential traction, enhancing near-surface stresses. Fretting fatigue can occur if rubbing of surfaces is accompanied with sufficiently high cyclic stresses. Furthermore fretting is efficient in nucleating surface cracks, and in general causes surface degradation, potentially reducing component endurance under fretting fatigue conditions. Further details about the mechanics of fretting and contacts can be found in [1,2].

Designing components to last a huge number of load cycles can be very challenging due to the uncertainty of the frictional behaviour and surface degradation induced by fretting. Stress calculations are commonly done assuming an initial ideal geometry [3–8], disregarding surface degradation and changes in the contact geometries. In fretting conditions, wear is typically evaluated with the Archard wear formalism, where worn material is assumed to disappear [9,10]. However, observations of fretting scars have shown that such assumptions have their limitations [11–13]. Fretting wear and fretting-induced surface modifications may well play an important role in unexpected fretting failures, which can occur under relatively low nominal loads. For example, quenched and tempered steel (QT) with a high fatigue strength may fail in fretting conditions with a 25% lower nominal fatigue load because of fretting wear damage, which leads to tangentially interlocked fretting scar topographies [14]. Such unpredictable fretting behaviour poses a serious challenge to risk management in industries, such as diesel engineering. The engines include many highly loaded, clamped, sub-assemblies where the demand to increase engine performance leads to large-scale exploitation of the fatigue strength of materials.

Godet [15,16] introduced the concept of third body approach for velocity accommodation in dry frictional interfaces, and the concept has been further developed by other researchers [13,17–19]. It has been suggested that the contact of first bodies (S_1 and S_5) is separated by naturally occurring third-body screens (S_2 and S_4) and by a third-body bulk (S_3) in the middle. The movement is accommodated by different mechanisms in S_i: elastic M_1, rupture M_2, shear M_3, and rolling M_4, resulting in a total of 20 velocity accommodation mechanisms (S_iM_i). In fretting conditions, such mechanisms play an important role in friction and wear behaviour, because short-motion amplitudes may be accommodated even without surface sliding, and because third bodies are easily trapped in the contact, enabling these additional modes of velocity accommodation [13].

Berthier et al. proposed that wear particle ejection rather than wear particle formation drives fretting wear [13]. Iwabutchi studied the role of iron oxides in fretting wear and discovered that artificially

* Corresponding author. Tel.: +358 3 311511.
E-mail address: jouko.hintikka@tut.fi (J. Hintikka).

http://dx.doi.org/10.1016/j.triboint.2015.06.008
0301-679X/

added oxide particles could either protectively or harmfully contribute to the resulting wear, depending on the normal load and displacement amplitude [20]. Merhej et al. investigated the effect of the Hertz contact size on fretting wear rate and on friction by using different radii spheres while maintaining a constant maximum pressure [21]. They found that the rate of fretting wear (and COF) decreased dramatically when the sphere radius was increased from 8 mm to 50 mm. These wear and friction observations were explained by entrapment of wear particles in the contact, which was more pronounced with large contacts. A similar contact size effect on fretting wear was reported by Warmuth et al. [22]. Varenberg et al. showed that wear particle ejection was enhanced by pores in the contacting surface providing spaces where wear debris could accumulate [23]. Hence the size of the contact and its surface microgeometry may strongly affect third-body mechanics and its effect on the friction and wear of the interface.

Fretting apparatuses can be categorized by their type of contact and loading conditions. Plain fretting testers have no bulk fatigue loading, and they are mostly designed for studying friction and wear [24–27]; however, they can also be used to study fretting fatigue, especially crack nucleation [5,6,10,12]. Dedicated fretting fatigue test rigs [3,4,8,28,29] are often based on a bridge type design [30] with a linear loading scheme, though some testers use a bending load [31–33]. Fretting fatigue rigs are often capable of measuring friction and wear. Both complete and incomplete contacts are used in fretting research. Complete contacts offer a contact size that is independent of the normal load but typically includes major edge effects, such as local pressure peaks due to abrupt changes in the contact geometry, i.e., punch against flat [1,2]. Incomplete contacts, such as Hertzian contacts, have distributed values for normal and tangential tractions and for surface sliding, which are often well-defined and can be solved using analytical equations in initial and ideal conditions [1,2].

A vast majority of testers are based on linear fretting movement between a small pad against a large specimen, resulting in a very small contact area and significant local tractions and stress gradients. These apparatuses cover certain industrial applications and provide useful experimental data for researchers. However, they have limitations for studying large planar surfaces, where nominal normal pressures are low and without significant edge effects. Such contacts are common in large, heavy-duty, combustion engines and machines. Fretting conditions with apparently constant normal and tangential tractions without any edge effects in the direction of surface sliding can be created by using annular, flat-on-flat contacts under axisymmetric loading. Such apparatuses have recently been employed by Leidich et al. [34] with single contact design, and by Mulvihill et al. [27] who preferred dual contact design; however, the first prototypes of such devices were introduced already in the 1930s and 50s [30].

This study introduces a new plain fretting test rig and the key findings from the first test runs made with a pair of tempered and quenched high-strength steel. The test rig is based on axisymmetric reciprocating, annular, flat-on-flat contact conditions. Special features of the test rig are its single large contact with adjustable alignment without any clearances. In addition precise control of the fretting movement is achieved by measuring the displacements in multiple directions and adjusting the specimen alignment on the run. The apparatus is capable of testing large and uniformly loaded planar contacts at pressure and sliding amplitude levels common in pressure fits and bolted joins in assemblies in largescale heavy-duty combustion engines and machines.

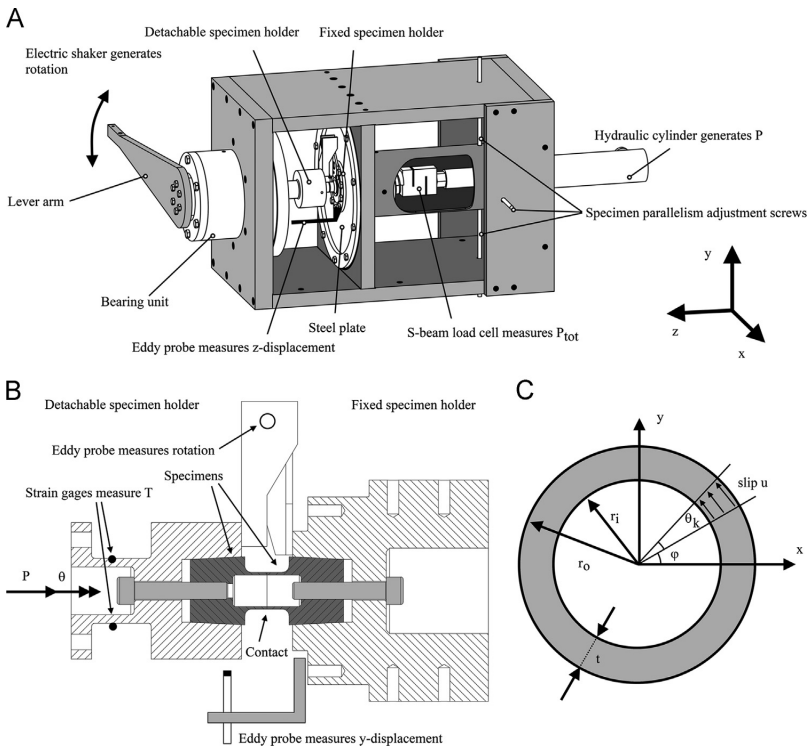

Fig. 1. (A) Fretting apparatus, (B) specimens and specimen holders, and (C) contact type.

2. Experimental

2.1. Test rig design

The design of our apparatus is illustrated in Fig. 1A and B. Specimens are attached to specimen holders with a conical seat forming a precise and clearance-free fixture. One specimen holder is detachable and the other is fixed. The total normal force P_{tot} (1×10^3 to 30×10^3 N) is generated with a hydraulic cylinder, which forces the two specimens together by deforming the steel plate in the axial direction. The steel plate deforms relatively easily in this direction and retains a high radial stiffness, which with adjustment screws allows fine-tuning of the parallelism of the planar specimen surfaces without any clearances. The reciprocating movement θ (3×10^{-4} to 100×10^{-4} rad) is generated with an electric shaker via a lever arm, which rotates the main shaft. The main shaft is supported by clearance-free, preloaded, conical bearings, which provide high radial stiffness. The detachable specimen holder is fixed with screws to the end of the main shaft. A rigid and clearance-free structure allows testing of fretting under conditions in which both the rotation amplitude and surface pressures are accurately controlled.

The axial z-displacement of the fixed specimen holder was measured with an eddy current probe, and the data was used to determine the force required to deform the steel plate. The total normal force P_{tot} was measured from the end of the piston rod with an s-beam load cell. The actual normal force P affecting the specimens was the measured total normal force minus the force needed to deform the steel plate, which was separately calibrated. The detachable specimen holder measured the torque with strain gages in a full Wheatstone bridge configuration. The angle of the rotation θ of the detachable specimen in relation to the fixed specimen holder was measured with an eddy current probe. Though the loading was ideally pure rotation, the x- and y-displacements ($w_{x,y}$) between the specimen holders were measured with two eddy current probes.

Torque, rotation, and x- and y-displacements were measured at 5000 Hz sampling frequency, and the normal force and z-displacement at 10 Hz sampling frequency. The tests were carried out as a rotation amplitude controlled system, where the rotation signal was used as the feedback signal for the electric shaker control unit.

2.2. The test specimens

The test device was designed using an axisymmetrically loaded, annular, flat-on-flat contact configuration of tubular specimens, where relative surface sliding was obtained by cyclic rotational movement. The shape of the specimen at the contact location was a tube with inner and outer radii r_i and r_o and wall thickness t, as shown in Figs. 1C and 2A. The length of the tubular part was 10 mm.

The tube-ended specimens were loaded with a normal load P and a reciprocating rotation θ, which was then resisted by the torque T due to friction (Fig. 1B and C). Specimen elastic deformations were included in the measured rotation. The rotation at the contact interface θ_k was calculated using Eq. (1), where k is the compliance of the specimen under torque.

$$\theta_k = (\theta - k \cdot T) \tag{1}$$

Assuming constant Coulomb conditions, the COF can be calculated from the measured torque T and the normal pressure distribution $p(r)$.

$$COF_T = T / \left[2\pi \int_{r_i}^{r_o} r^2 \times p(r) dr \right] \tag{2}$$

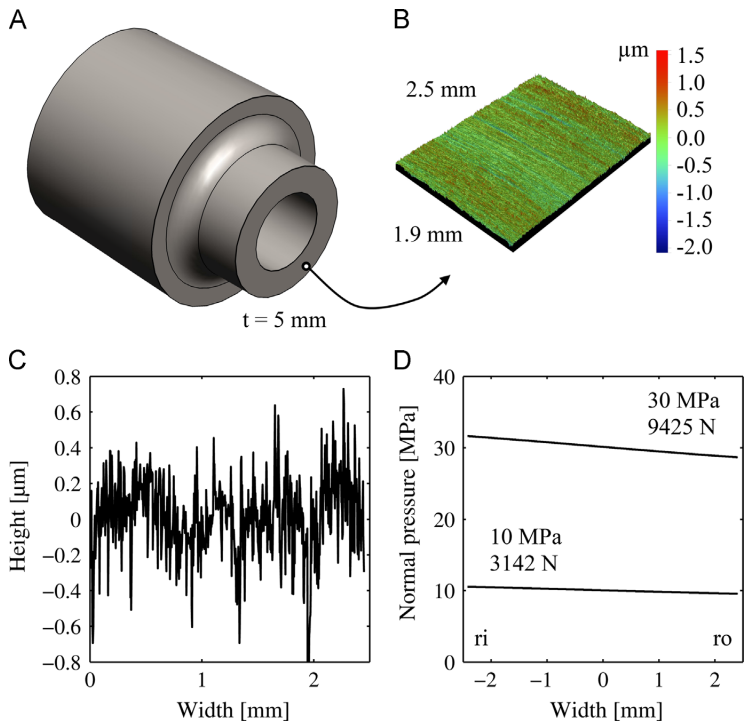

Fig. 2. (A) Specimen, (B) and (C) measured surface geometry, and (D) calculated normal pressure distributions.

The frictional energy dissipation, *Ed*, is the work done by frictional surface sliding during one load cycle, and it can be calculated from the measured torque and rotation data, and it corresponds to the area inside the fretting loop as follows:

$$Ed = \oint T d\theta \tag{3}$$

The *COF* can be determined also from the measured frictional energy dissipation *Ed*, $p(r)$ and the rotation amplitude θ_a as follows:

$$COF_{Ed} = Ed / \left[8\pi \int_{r_i}^{r_o} r^2 \times \theta_a \times p(r) dr \right] \tag{4}$$

These equations can be simplified when $p(r)$ is approximated to be a constant [34]. The surface sliding can be calculated from θ_k and the radius r (Eq. (5)). Though the loading of the specimens was rotational, there may have been a radial sliding component due to uneven tangential traction. In such conditions, the sliding distribution in the contact can be approximated with Eqs. (6) and (7), where $w_{x,y}$ is the *x*- and *y*-displacement of the specimen, respectively, and where φ is the angle of observation.

$$u_r = \theta_k \cdot r \tag{5}$$

$$u_x = w_x - u_r \times \sin(\phi) \tag{6}$$

$$u_y = w_y + u_r \times \cos(\phi) \tag{7}$$

The specimens were manufactured from a quenched and tempered steel (EN 10083-1-34CrNiMo6+QT) circular rod with a diameter of 45 mm (design shown in Fig. 2A). The radii of the tubular section were $r_i = 7.5$ mm and $r_o = 12.5$ mm and the wall thickness $t = 5$ mm. The compliance of the specimens under torque (k) was determined using a finite element method (Abaqus), and it had a value of 11.6×10^{-6} rad/N m. The specimens were manufactured by turning, and the contact surface was fine-ground so that the grinding scratches were circular. The surfaces were examined by 3D profilometry (Wyco NT1100), and an example of the surface topography is shown in Fig. 2B and C. The geometric and material properties are listed in Table 1, where S_a is 3D surface roughness corresponding to the arithmetic mean of the absolute value of the surface departures from the average plane, S_q is the corresponding root-mean-squared roughness, and S_z is the maximum peak-to-valley height as the average of ten extreme data points. Additionally, S_y and S_u are the yield and ultimate strengths, respectively, E is the modulus of elasticity, and ν is Poisson's ratio. The specimens were cleaned before and after fretting tests in acetone using an ultrasonic cleaning device.

The normal pressure of the contact was examined by using a finite element method (Abaqus). In the contact of ideal planar surfaces, the normal pressure is highest at the inner edge and drops gradually toward the outer edge, albeit by only a 5% deviation from the nominal pressure (Fig. 2D), whose effect on the calculated COF is about 0.8% and could be ignored with specimen dimensions we used. The results shown later were calculated using a constant normal pressure approximation.

The annular contact formed a closed circle in the direction of the fretting movement; hence there were no stress gradients or edge effects in the sliding direction, which are always included in linear fretting tests with a pad vs. specimen contact configuration. Fairly constant sliding conditions were achieved across the wall thickness by using a large tube radius per wall thickness ratio. A constant initial nominal pressure without edge effects in the width direction could also be obtained by using identical specimens with wall thicknesses of 5 mm. Such a contact is capable of simulating large and uniformly loaded planar contacts at pressure and sliding amplitude levels common in pressure fits and bolted joins related to assemblies in large-scale heavy-duty combustion engines and machines.

Table 1
Specimen properties.

S_y [MPa]	S_u [MPa]	E [GPa]	ν [–]
994	1075	210	0.27

S_a [μm]	S_q [μm]	S_z [μm]
0.17–0.24	0.22–0.32	1.8–5.3

2.3. Experiment procedure

First, specimens were tightened with screws to the specimen holders, and the detachable specimen holder was then fixed to the main shaft. The specimens were then gently brought into contact, and uniformity of surface pressure was confirmed by using a pressure sensitive film (Fuji Prescale), and any observable error in the parallelism was balanced out. After that a desired surface pressure was applied, and the experiment was started by linearly increasing the rotational loading from zero to the target level within a predefined start-up time of 10 s, resulting in 400 load cycles with a loading frequency of 40 Hz. Optionally, the parallelism of the contact surfaces can be adjusted on the run by minimizing the measured *x*- and *y*-displacements.

Because the measured parameters were recorded from the full duration of the test, each fretting cycle could be analysed. Additional parameters such as COF and frictional energy dissipation were calculated in data post processing. Post-test inspection of the specimens allowed characterization of fretting-induced surface degradation and wear.

2.4. Measurements

Fretting tests were run at three normal pressure levels, 10 MPa, 30 MPa, and 50 MPa, and at five sliding amplitudes (u_a), ranging from 5 μm up to 65 μm, which was calculated with an average radius of 10 mm. The loading frequency was 40 Hz. Three sets of experiments were run. In set-1 and set-2, the test duration (N_{LC}) was 3.0×10^6 load cycles. The option to adjust the parallelism of the fretting contact on the run was used in set-2. Each experiment in set-1 was run continuously from start to finish, whereas in set-2 each experiment was halted for the night and resumed the following day without removal of the normal pressure. In set-3, the test duration was shorter: 1.0×10^4 and 1.0×10^5 load cycles. Short duration tests provide insight into the mechanism of fretting damage at different stages of the experiment. The test matrix with a total of 21 measurements is shown in Table 2. Experiments were performed in ambient laboratory atmosphere at temperatures ranging from 25 °C to 30 °C and at a relative humidity of 22% to 44%.

The specimens were weighed (Precisa EP 420A) before and after fretting tests, and their wear mass was calculated as the

Table 2
Test matrix.

Set	Pressure (MPa)	N_{LC}	u_a [μm]
1	10	3e6	5, 20, 35, 50, 65
	30	3e6	5, 20, 35, 50, 65
2	10	3e6	20, 35, 50
	30	3e6	20, 35, 50
	50	3e6	20, 35, 50
3	10	1e4	35
	10	1e5	35

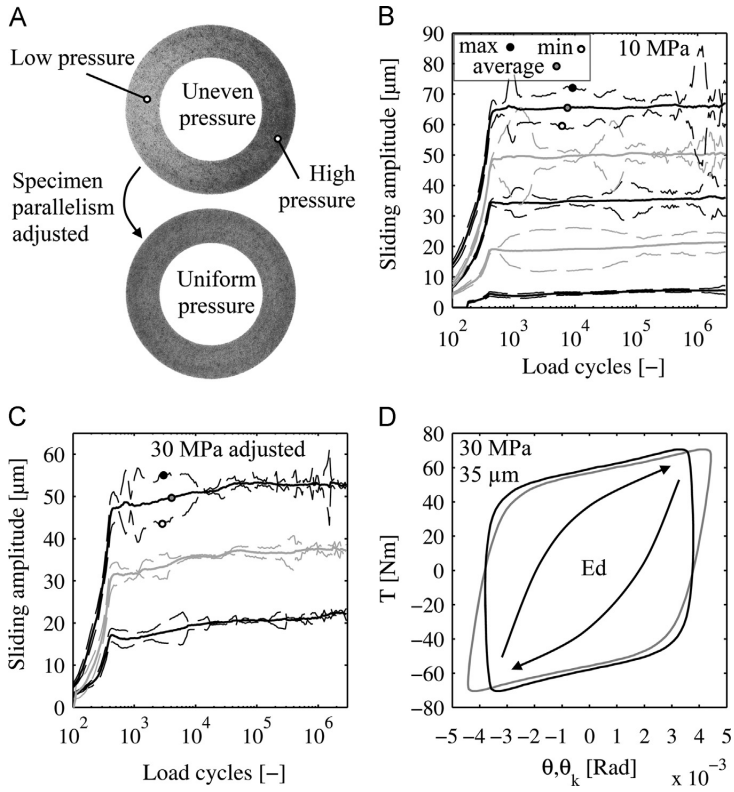

Fig. 3. Fretting apparatus performance.

difference between those values. Two specimens were rubbed against one another; hence the total wear mass loss was calculated as a sum of the mass losses from both specimens. Each specimen was heated up to 105 °C before weighting, eliminating thus any error due to air humidity. Each scaling was done three times with a reference weight, and the average value was calculated. This procedure had a maximum error of about 2 mg for the total mass loss (1 mg for a single specimen).

3. Results

3.1. Measured signals and test rig performance

The quality of the collected data and capabilities of the apparatus are illustrated in Fig. 3. The surface pressure was adjusted to be even by using a pressure sensitive film before a test was started (Fig. 3A). Examples of measured sliding amplitude values from the full duration fretting tests (set-1 and set-2) are shown in Fig. 3B and C, respectively. The *x*- and *y*-displacements in the rotating specimen holder showed extra fretting movement, which was used to calculate minimum, average, and maximum sliding amplitudes using Eqs. (5)–(7). The average deviation from the pure rotational sliding amplitude varied in a range of 6% to16% in set-1; however, up to 40% deviations occurred momentarily. In set-2, adjustment of the specimen parallelism reduced the corresponding deviation down to 1% to 5%. Because in all tests the deviation was miniscule right after the start-up, it was caused by changes in the frictional interface resulting in unevenly distributed tangential traction in the interface (φ, r). It was shown later that the interface experienced significant adhesive wear damage at the beginning of the tests, which led to the above conditions. The normal force remained closely within its set values and showed only a few hundred Newton changes during the test, corresponding to a maximum of 5% deviation.

Rotation and torque data were recorded at good resolution, as shown by the precisely measured fretting loop in Fig. 3D. The grey fretting loop includes elastic deformation, which in the black loop is eliminated using Eq.(1). The vertical ends of the black fretting loop demonstrate that the elasticity was accurately removed. It is crucial to measure fretting loops accurately, because analysis of frictional behaviour is based on its interpretation. For example, the area inside the fretting loop corresponds to the frictional work (*Ed*) of a single fretting load cycle, and the shape of the fretting loop can be used to study the development of friction during fretting sliding [27,35].

3.2. Fretting scar observations

In all the tests, small amounts of wear particles were ejected from the outer edge of the contact, except at the lowest sliding amplitude. The texture of this ejected debris was fine, powdery, reddish brown, ‘cocoa’ typical of fretted steel contacts. After the tests, the contact surfaces were covered in powdery oxides, indicating tendency to wear particle entrapment. Wear debris was removed by pressurized air and by gently rubbing with a paper tissue and finally with an ultrasonic cleaning device. After cleaning, the fretting scar looked brown/grey, reminiscent of a

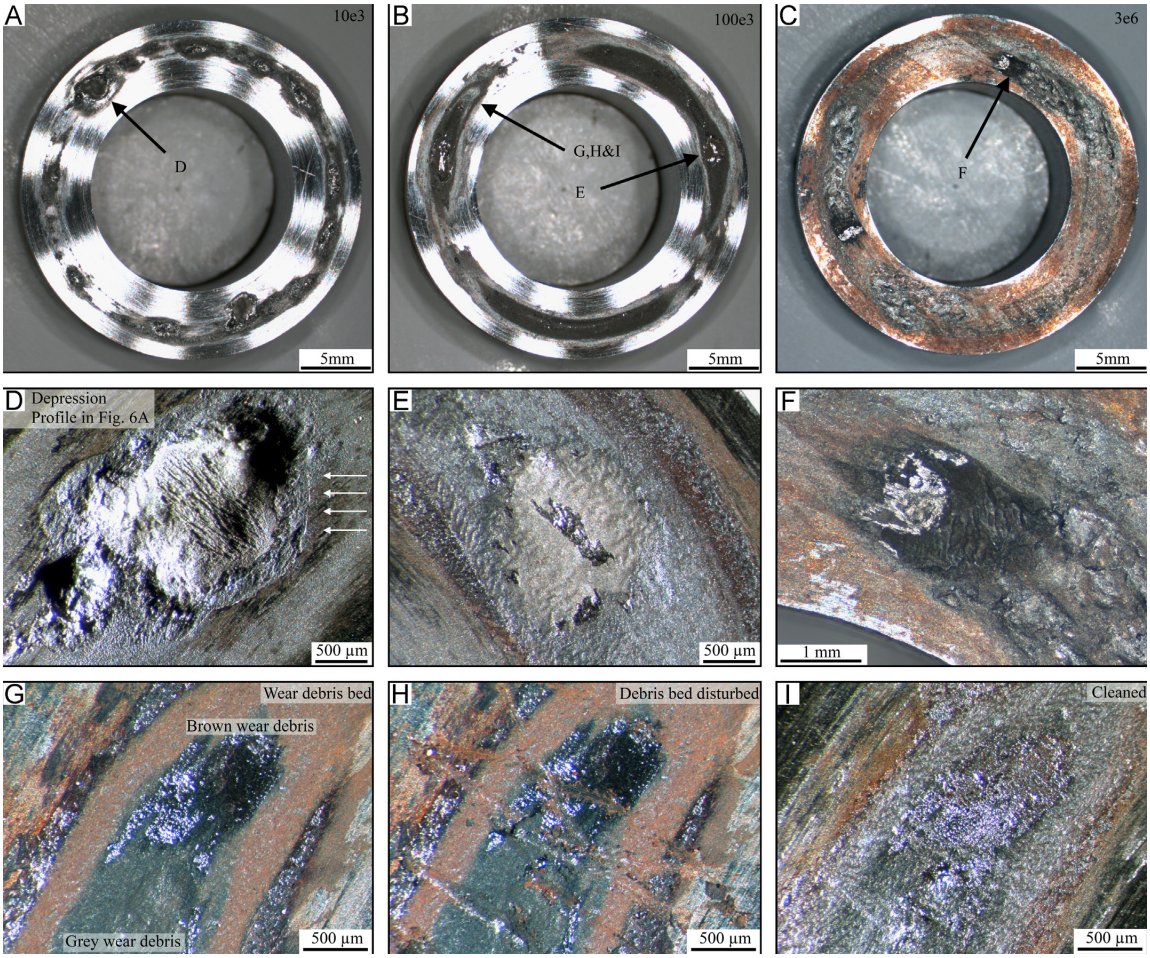

Fig. 4. Fretting damage after different test durations under 10 MPa, ~35 μm sliding amplitude loading. (For interpretation of the references to color in this figure legend, the reader is referred to the web version of this article.)

layer of varying degrees of hard-to-remove oxidation. This also indicates that the naturally occurring third body particles generated in the interface (third-body screens and third-body bulk) enabled additional velocity accommodation mechanisms.

3.2.1. Optical microscopy

One of the loading conditions (10 MPa, ~35 μm) was fretted for a duration of 1.0×10^4, 1.0×10^5 and full 3.0×10^6 load cycles, and the observed fretting damage is illustrated in Fig. 4A–C. The shortest test duration showed severe adhesive wear and material transfer. The most severe example is illustrated in Fig. 4D, showing a location where material was torn from one surface and adhering to the counter surface (shown in the profilometry section). The contact had two of these, a few millimetre sized, material transfer locations, resembling failed spot welds; however, such material transfer occurred throughout the interface on a smaller scale, producing the wear scar shown in Fig. 4A. When the contact was fretted for 1.0×10^5 load cycles, wear damage was more abrasive, and the interface was filled with wear debris. Again a few millimetre sized spots were identified (Fig. 4E), which were the remnants of the initial material transfer, similar to that observed after the 1.0×10^4 load cycles. The contact shows little evidence of severe adhesive wear, indicating that the initially adhesive wear damage had changed to abrasive wear. Remnants of large adhesion spots were identified also in the full duration test (Fig. 4F); however, entrapped wear debris produced further, brown, abrasive fretting wear and oxidation.

An example of powdery third bodies, observed after 1.0×10^5 load cycles, is illustrated in Fig. 4G–I. The specimen was carefully detached from the apparatus, and some locations were imaged before any cleaning, showing beds of brown and grey wear debris (Fig. 4G). These beds were then mechanically scratched with tweezers tips (Fig. 4H) and cleaned (Fig. 4I), exposing a damaged surface underneath. Such debris beds covered also intact surfaces (not shown). This indicates that an accumulating third body effectively reduces direct interaction between the first bodies and explains why adhesive wear changed to more abrasive wear.

Examples of surface damage in different loading conditions after 3.0×10^6 fretting load cycles are shown in Fig. 5. The magnitude of surface degradation depended strongly on the sliding amplitude and normal pressure. With the lowest sliding amplitudes, fretting damage occurred mostly in the annular area inside the nominal contact

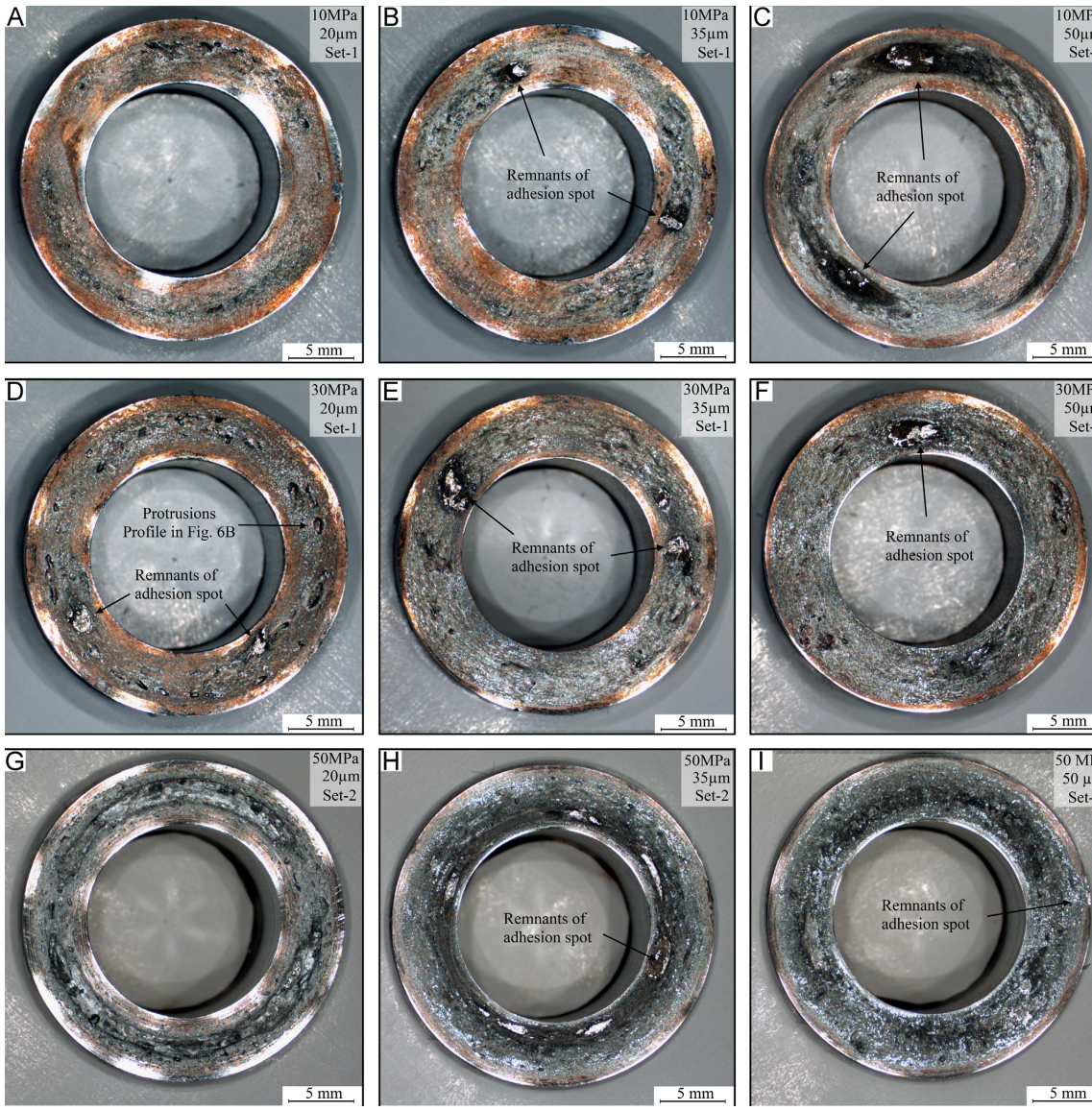

Fig. 5. Fretting scars with all normal pressures and different sliding amplitudes.

(Fig. 5A, D and G), because frictional heating in the interface caused the specimen surfaces to bulge in the central annulus, concentrating contact on a narrow area. Increasing the sliding amplitude spread fretting damage over the whole contact surface due to wear. We suspect that the spreading of fretting damage was also affected by third body-first body interaction after a sufficient number of wear particles had accumulated in the interface. In all cases, the damage at both contact surfaces was strikingly similar (Figs. 4C and 5B).

The fretting scar changed colour from reddish brown to dark grey and metallic grey, when the sliding amplitude and normal pressure were increased, indicating changes in the composition of the third-body screens. All fretting scars showed multiple depressions and protrusions of different shapes and sizes (Fig. 5D) forming tangential interlocking, as illustrated in the profilometry section. Often markedly large, a few millimetre sized spots were found in the interface. Many protrusions, depressions, spots are remnants of the initial adhesive wear and material transfer, which occurred at the beginning of the tests (Fig. 4A–F). The large size (millimetre scale) of the damage zones (adhesion spots, protrusions, and depressions) illustrates the usefulness of large test contacts, because such damage may be very hard to reproduce with small test geometries. A more comprehensive look at the surface degradation is worth a separate study.

3.2.2. *Profilometry*

The profiles of the different surface damage locations were measured on both surfaces and some examples are shown in

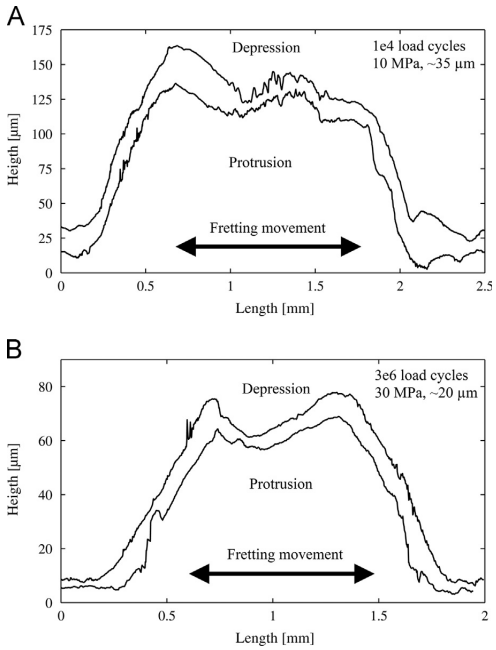

Fig. 6. Examples of tangentially interlocked protrusions and depressions.

Fig. 6, where Fig. 6A and B correspond to Figs. 4D and 5D, respectively. The 2D profiles shown here were extracted from 3D profiles in the direction of the fretting movement. After 1.0×10^4 fretting load cycles, the surface profiles showed significant tangential interlocking. Clearly, the protrusion had transferred from the counter surface and produced a depression. These interlocked protrusions and depressions were formed by high adhesive friction and resulted in material transfer at the early stages of the experiment. Even after 3.0×10^6 load cycles, the fretting scars showed tangentially interlocked protrusions and depressions (Fig. 6B), albeit not as severe and more oxidized than that observed after 1.0×10^4 load cycles. In other studies [27,35], such tangential interlocking has been linked to non-Coulomb friction behaviour. It is thus likely that the observed tangentially interlocked protrusions and depressions, in our study, may also have contributed to the observed non-Coulomb friction early in the experiments, an observation discussed in the next section.

3.3. Frictional behaviour

COF_T was calculated according to Eq. (2) and by using the measured maximum torque amplitude at the extreme ends of the fretting movement; consequently, COF_T corresponds to the maximum COF during a fretting cycle. COF_{Ed} was calculated from the measured frictional energy dissipation using Eq. (4), which corresponds to the average COF during a fretting cycle. The surface normal pressure was assumed to be constant for both COF_T and COF_{Ed}. All fretting loops were recorded, and the following observations were made.

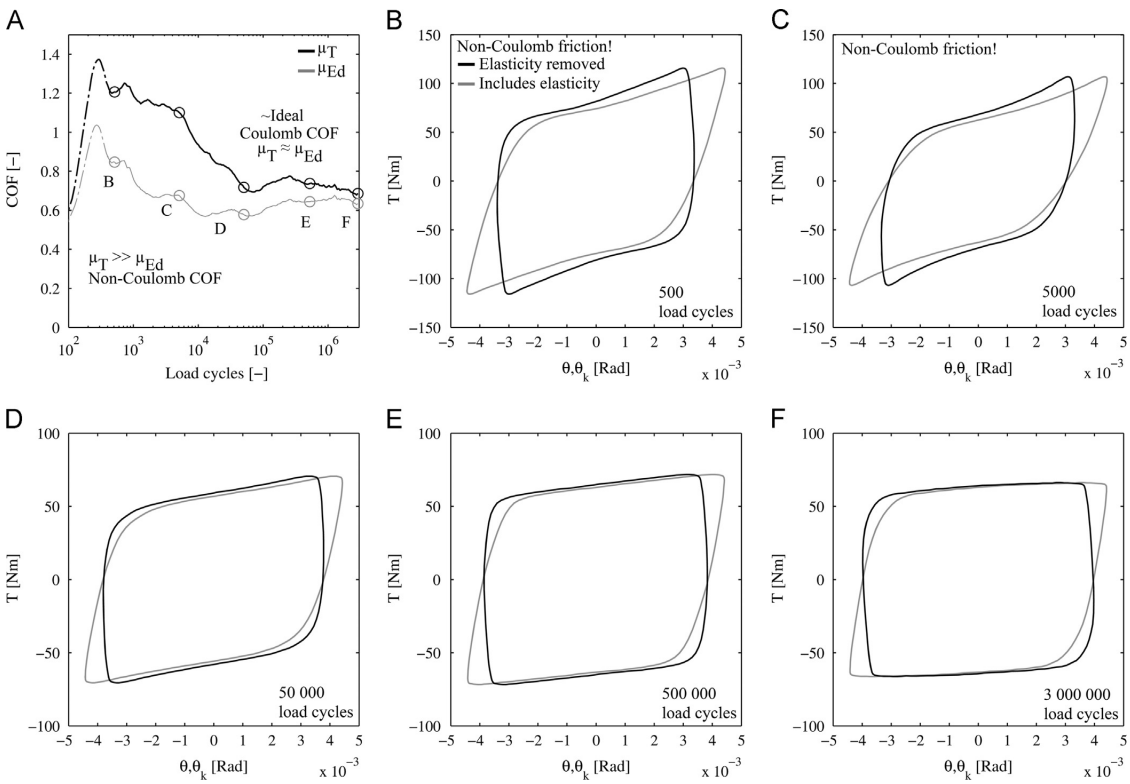

Fig. 7. Development of fretting loops during the experiment with a sliding amplitude of 35 μm and a normal pressure of 30 MPa. Grey loops with and black loops without elastic deformation.

3.3.1. Fretting loops

The very first fretting loops showed a near ideal Coulomb shape, which quickly changed to a non-Coulomb one during the start-up phase, as illustrated in Fig. 7 (30 MPa, sliding $\sim$35 μm). With these load parameters, the non-Coulomb behaviour lasted about 1.0×10^5 load cycles, during which the fretting loop gradually changed to rectangular, ideal Coulomb shape (Fig. 7D–F).Once the non-Coulomb phase ended, any further increase in the load cycles had little effect on the shape of the fretting loop. The non-Coulomb behaviour occurred when COF_T was much larger than COF_{Ed} (Fig. 7A), and when fretting scar observations showed adhesive wear and material transfer, which resulted in tangentially interlocked protrusions and depressions.

3.3.2. Coefficient of friction

Because frictional behaviour hardly changed between test sets 1 and 2, the sets are shown and discussed as a single entity. The development of COF_T and COF_{Ed} are shown in Fig. 8A–C as a function of load cycles, accumulated frictional energy dissipation (ΣEd), and accumulated surface sliding (ΣSliding), respectively. Both COF_T and COF_{Ed} peaked briefly at the beginning of the test, followed by a steep drop to steady state values. The high COF decayed exponentially (nearly linearly in a semi-logarithmic plot) to its steady state values as a function of ΣEd and ΣSliding without any significant dependence on the sliding amplitude. Similar shapes were observed in the COF curve at all normal pressures. Maximum COF conditions occurred always simultaneously with non-Coulomb friction conditions, where COF_T was significantly greater than COF_{Ed}.

All the measured maximum and steady state values of COF_T and COF_{Ed} are shown in Fig. 8D and E as a function of sliding amplitude, while the colour indicates normal pressure. The maximum values were in a range of 1.1 to 1.5 for COF_T and 0.9 to 1.1 for COF_{Ed}. The maximum COFs increased with increasing normal pressure. The steady state value for COF_T was in a range of 0.7 to 0.9, while COF_{Ed} showed slightly lower values, 0.6 to 0.8, which seem independent of the normal pressure and sliding amplitude. The error bars correspond to a $\pm$1 standard deviation.

Fig. 8F–G shows median values of ΣEd and ΣSliding for all measured normal pressure levels, when COF_T and COF_{Ed} have their maximum (peak) values and start of steady state (stabilization) values (indicated in black dots on the vertical lines in Figs. 8B and 9C). Fig. 8F shows that at the peak and stabilization of COFs the value of frictional energy dissipation (ΣEd) increases linearly (note semi-logarithmic scale) in all cases as a function of the normal pressure. In a corresponding case (Fig. 8G), the value of accumulated sliding (ΣSliding) is nearly independent of the normal pressure. COF_T peaked and stabilized approximately after 10 mm and 10 m, respectively, at all normal pressure and sliding amplitude levels ($\sim$10 mm and $\sim$100 mm in the case of COF_{Ed}). This shows that frictional behaviour correlates well with accumulated frictional work and especially well with accumulated sliding.

The accumulated frictional work or surface sliding distances required before COF stabilization may depend on the development of third-body layers in the interface. COF_{Ed} may well stabilize before COF_T, because a 'thin' third body (screens and bulk) may be sufficient to separate most of the interface contributing to COF_{Ed}, whereas diminution of tangential interaction between protrusions and depressions may require a thicker third-body layer, which contributes to COF_T. It is unclear how thick the accumulating third body was and whether it ever became thick enough to effectively reduce tangential interlocking. Consequently, the stabilization of COF_T may be affected by the wearing down of tangentially interlocked protrusions and depressions rather than by the increasing thickness of accumulated third-body layers.

In most cases, the COF peaked already in the start-up phase, while the sliding amplitude was still increasing, as illustrated by the coloured dots in Fig. 8A–C that indicate the end of the start-up phase and by the limited range of actual sliding amplitudes for the maximum COFs in Fig. 8D and E. Though Fig. 8D and E show that the maximum COFs reduced slightly as a function of the sliding amplitude, this is not certain because the COFs reduced also due to the rapid build-up of the ΣSliding. Therefore it may be that the maximum COFs are largely independent of the sliding amplitude; however experiments with a very short start-up phase are necessary for further study of maximum COF conditions.

Leidich et al. showed maximum COF in a range of 1.2 to 1.6 with 34CrNiMo6+QT vs. 16MnCr5E rotating, annular, flat-on-flat contact, with similar normal pressure levels than what was used in our study [34]. Iwabuchi illustrated COF values of about 0.8 in steady state gross sliding conditions with a S45C steel cylinder on flat contact [20]. Additionally, Hintikka et al. produced maximum COF in a range of 1.5 to 1.6, followed by a gradual reduction to about 0.8 with a sphere in plane contact in gross sliding conditions with a 34CrNiMo6+QT material pair [36]. Thus our new results with rotating, annular, flat-on flat contact correspond well with other studies performed with different type and size contacts.

3.4. Wear

The classic Archard formulation predicts a linear dependence of wear on a normal force and sliding distance [37]. Measured mass loss due to fretting wear is shown in Fig. 9 for all full-duration tests. The wear mass loss depended mostly on the accumulated sliding distance (or sliding amplitude). Surprisingly, the best fit slopes indicate that the normal load had little impact on the wear mass loss (Fig. 9A), a finding that contradicts the classic Archard wear model. Accumulated frictional energy dissipation has been shown to correlate with wear volume in conditions where wear particles are easily ejected [11,12]. Our study shows such correlation, yet a strong dependency remains on the normal force (Fig. 9B), indicating that a significant amount of frictional energy is dissipated in mechanisms such as velocity accommodation in third bodies, which do not contribute to the total wear in these test conditions. These wear findings agree with Berthier et al. [13], who stated that fretting wear is governed by wear particle ejection rather than their generation.

A detailed view of our results shows that wear was slightly higher in set-2 than in set-1. Adjusting the specimen parallelism may well have promoted wear particle ejection by momentarily interrupting the steady state velocity accommodation conditions, or that halting measurements in set-2 for several hours cooled down the apparatus. Increased temperature has been reported to reduce the rate of wear [38,39].

4. Discussion

Our fretting apparatus with axisymmetric loading conditions and a large, annular, flat-on-flat contact and low nominal pressure levels showed interesting results. Fretting loops were recorded with good accuracy, allowing precise analysis of frictional behaviour. Normal pressure could be adjusted uniformly before a test was started, though the conditions changed during the test due to progressive fretting damage. Natural changes in the contact interface may lead to a distribution of different values for tangential traction in the contact. Additional measurements in the *x*- and *y*-directions allowed accurate recording of the fretting movement. The magnitude of extra fretting movement components was controlled by fine-tuning the parallelism of the specimens on the run, though frictional behaviour remained mostly unaffected.

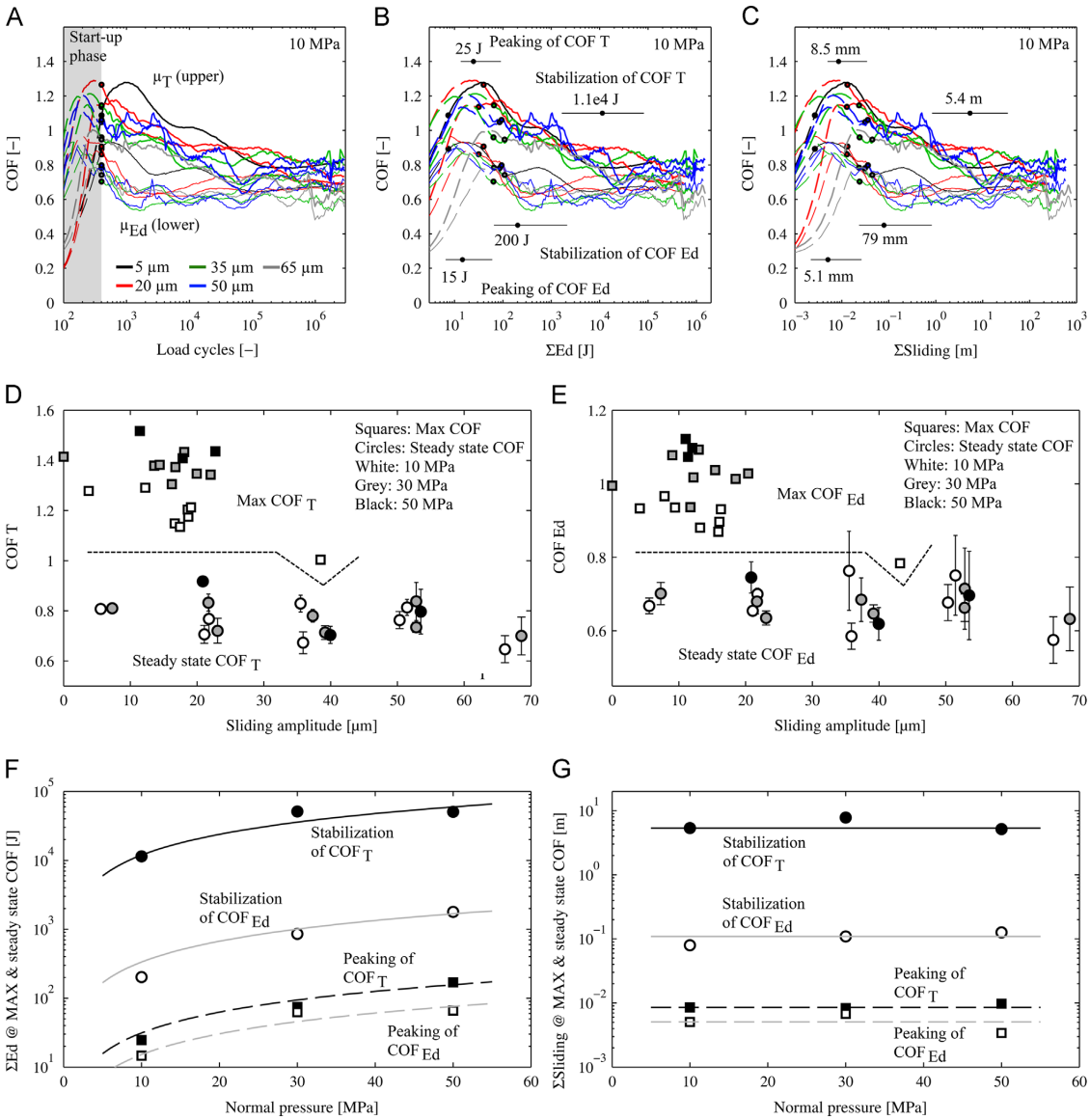

Fig. 8. Measured frictional behaviour in all full duration tests. (For interpretation of the references to color in this figure legend, the reader is referred to the web version of this article.)

The COF was high at the beginning of the experiment and dropped gradually to a significantly lower steady state value. As to COF_T, its maximum value was 70%to 90% greater than its steady state value, the corresponding difference being 40% to 50% for COF_{Ed}. A high initial COF occurred concurrently with a pronounced non-Coulomb shaped fretting loop. In addition, fretting scar observations revealed tangentially interlocked protrusions and depressions due to adhesive wear, which was pronounced at the early stages of the experiments; consequently, tangential interlocking is likely to contribute to non-Coulomb friction. Fretting wear produced wear particles that accumulated in the contact and formed oxide third-body screens and third-body bulk with only a small amount of them ejected from the contact. The drop in the COF can be explained by a gradual development of third-body layers and by a gradual wearing of tangentially interlocked protrusions and depressions due to third-body abrasion. The extent of fretting wear damage varied significantly as a function of loading parameters; however, at the end all tests produced a nearly identical steady state COF. This is not surprising with a third-body approach, because significant friction may originate from third bodies via velocity accommodation mechanisms.

The observed frictional behaviour introduces variable COF conditions in large-scale contacts, if the sliding amplitude is distributed unevenly around the contact zone both in partial slip and in gross sliding, because high COF conditions persist longer in low sliding zones, whereas high sliding zones achieve a steady

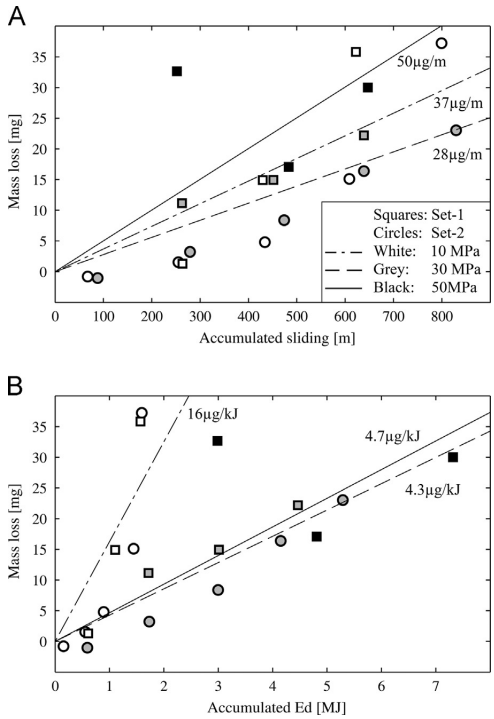

Fig. 9. Mass loss due to fretting wear as a function of accumulated surface sliding and accumulated frictional energy dissipation.

state faster in terms of accumulating sliding. This may concentrate tangential traction in low sliding locations and fretting fatigue load (and hence fatigue crack initiation) in low sliding locations and stick-slip-boundaries. COF_{Ed} is often preferred to COF_T, because it corresponds to such an average COF that actually produces frictional work. However, it is important to notice that COF_{Ed} underestimates the maximum tangential traction, which was up to 60% higher in most pronounced non-Coulomb conditions. Additionally, initially uniform and symmetric normal pressure and surface sliding conditions yielded uneven and asymmetric traction distribution due to adhesive wear, which concentrated surface damage on highly localized adhesion spots. Such contact conditions may further add to the surface stress near the adhesion spots, promoting further fretting fatigue crack nucleation. Such non-Coulomb friction conditions must be carefully analysed, because assuming ideal condition may lead to non-conservative fatigue calculation results.

The wear mass loss depended mostly on the sliding amplitude, which can be explained by the third-body approach. The wear rate may initially have been 'high', as indicated by the initial adhesive wear, which quickly saturated the contact with third bodies. In such conditions, fretting movement may be mostly accommodated by a third body, 'lowering' thus rubbing action on the first bodies and effectively changing initial adhesive wear towards abrasion. Wear may occur in third-body screens and third-body bulk, which, however, are regenerated continuously in a nearly closed cycle, interrupted only when a stray wear particle is ejected from the contact edge. Assuming that the ejection rate depends mostly on the sliding amplitude, it follows that the wear rate depends on the sliding amplitude. It is thus reasonable to assume that ejection depends on the sliding amplitude, because specimen movement enables wear particles to move. This behaviour may dominate especially in a rotating, annular, flat-on-flat contact, because fretting occurs in a closed circle with no edges in the sliding direction; consequently, wear particles must migrate perpendicular to the sliding direction before they can be ejected. Further study is required to fully understand the entrapment of wear particles.

Our apparatus warmed up markedly at the largest sliding amplitudes and a largest normal force. However, such natural increase in the friction temperature in the interface is an essential part of fretting, because it occurs also in industrial applications and must be studied as well. The effect of temperature on fretting wear and COF with stainless steels was studied by Rybiak et al. [38], who showed that the wear rate and COF dropped dramatically, accompanied by a glaze formation in the contact when the temperature exceeded 220 °C. Pearson et al. [39] showed similar results with a high-strength steel pair; however, the wear rate and COF dropped at temperatures above 85 °C and glaze formation initiated at 300 °C. Frictional heating may thus result in changes in the interface; however, we did not focus on it in our study. Frictional heating and third-body mechanics and their role in friction and wear must be studied further with new experiments, as should also initial adhesive wear damage, because such severe surface degradation accompanied with a high COF, may affect the start-up of fretting fatigue failures.

5. Conclusions

A new fretting test rig with axisymmetrically loaded, annular, flat-on-flat contact was designed, and the first test was successfully conducted with quenched and tempered steel specimens. The following conclusions were made:

- Maximum coefficient of friction values, based on maximum torque, peaked in a range of 1.1 to 1.5 and dropped then gradually to a range of 0.7 to 0.9 in steady state gross sliding conditions. The maximum coefficient of friction occurred simultaneously with non-Coulomb behaviour; however, the steady state values correspond to nearly ideal Coulomb behaviour. The development of friction coefficients correlated well with accumulated sliding and accumulated frictional energy dissipation.
- Tangentially interlocked surface depressions and protrusions were identified in optical profilometry; they were especially pronounced and metallic during non-Coulomb test conditions. Those were caused by initial adhesive wear and material transfer. Tangential interlocking of these protrusions and depressions led to non-Coulomb friction. Steady state friction occurred when a sufficient amount of wear particles accumulated and when the interlocked protrusions and depressions gradually wore off, reducing tangential interlocking.
- Wear mass loss was measured, and it depended mostly on the sliding distance (or amplitude), whereas normal pressure had less effect on it in our test conditions. The rate of wear particle ejection from the contact interface may govern the total wear mass loss rather than wear particle generation.
- Initially uniform normal pressure and surface sliding conditions led to highly uneven fretting wear damage due to the formation of adhesion spots. With increasing load cycles, wear particles gradually accumulated in the contact, resulting in abrasive wear and uniform fretting wear damage.
- Large, flat-on-flat contact resulted in wear damage observations which may be difficult to obtain with small Hertzian contacts. In some occasions the width of the adhesion spots exceeded 1 mm, being larger than the contact size used in conventional fretting testers. Furthermore the entrapment of the wear debris was pronounced with the large contact.

Acknowledgements

This study was conducted as part of the ScarFace Research Project (decision number 40205/12). We are grateful for the financial support provided by Tekes (Finnish Funding Agency for Technology and Innovation), Wärtsilä Finland Oy, Nome Oy, and Global Boiler Works Oy. We would also like to thank MSc Jouko Meriläinen for his contribution to the design of the apparatus and to bringing it online.

References

[1] Hills DA, Nowell D. Mechanics of fretting fatigue. Dordrecht: Kluwer Academic Publishers; 1994.
[2] Johnson KL. Contact mechanics. Cambridge: Cambridge University Press; 1985.
[3] Sabelkin V, Martinez SA, Mall S, Sathish S, Blodgett MP. Effects of shot-peening intensity on fretting fatigue crack-initiation behaviour of Ti–6Al–4V. Fatigue Fract Eng Mater Struct 2005;28:321–32.
[4] Hwang D, Cho S. Correlation between fretting and plain fatigue using fatigue damage gradient. J Mech Sci Technol 2013;28:2153.
[5] Alfredsson B, Cadario A. A study on fretting friction evolution and fretting fatigue crack initiation for a spherical contact. Int J Fatigue 2004;26:1037–52.
[6] Pasanen A, Järvisalo S, Lehtovaara A, Rabb R. Development of a test device for the evaluation of fretting in point contact. Lubr Sci 2009;21:41–52.
[7] Szolwinski MP, Farris TN. Observation, analysis and prediction of fretting fatigue in 2024-T351 aluminum alloy. Wear 1998;221:24–36.
[8] Walvekar AA, Leonard BD, Sadeghi F, Jalalahmadi B, Bolander N. An experimental study and fatigue damage model for fretting fatigue. Tribol Int 2014;79:183–96.
[9] McColl IR, Ding J, Leen SB. Finite element simulation and experimental validation of fretting wear. Wear 2004;256:1114–27.
[10] Mohd Tobi AL, Ding J, Bandak G, Leen SB, Shipway. PH. A study on the interaction between fretting wear and cyclic plasticity for Ti–6Al–4V. Wear 2009;267:270–82.
[11] Fouvry S, Kapsa P, Vincent L. Quantification of fretting damage. Wear 1996;200:186–205.
[12] Fouvry S, Duó P, Perruchaut P. A quantitative approach of Ti–6Al–4V fretting damage: friction, wear and crack nucleation. Wear 2004;257:916–29.
[13] Berthier Y, Vincent L, Godet M. Velocity accommodation in fretting. Wear 1988;125:25–38.
[14] Hintikka J, Lehtovaara A, Mäntylä A. Fretting fatigue and friction of quenched and tempered steel in dry contact with aluminum bronze. Wear 2013;308:155–65.
[15] Godet M. The third-body approach: a mechanical view of wear. Wear 1984;100:437–52.
[16] Godet M. Third-bodies in tribology. Wear 1990;136:29–45.
[17] Berthier Y, Godet M, Brendle M. Velocity accommodation in friction. Tribol Trans 1989;32:490.
[18] Berthier Y. Experimental evidence for friction and wear modelling. Wear 1990;139:77–92.
[19] Iordanoff I, Berthier Y, Descartes S, Heshmat H. A review of recent approaches for modeling solid third bodies. J Tribol 2002;124:725–35.
[20] Iwabuchi A. The role of oxide particles in the fretting wear of mild steel. Wear 1991;151:301–11.
[21] Merhej R, Fouvry S. Contact size effect on fretting wear behaviour: application to an AISI 52100/AISI 52100 interface. Lubr Sci 2009;21:83–102.
[22] Warmuth AR, Pearson SR, Shipway PH, Sun. W. The effect of contact geometry on fretting wear rates and mechanisms for a high strength steel. Wear 2013;301:491–500.
[23] Varenberg M, Halperin G, Etsion I. Different aspects of the role of wear debris in fretting wear. Wear 2002;252:902–10.
[24] Sabeya GRYN, Paris J-, Denape J. Fretting wear of a coated titanium alloy under free displacement. Wear 2008;264:166–76.
[25] Mohrbacher H, Celis J-, Roos JR. Laboratory testing of displacement and load induced fretting. Tribol Int 1995;28:269–78.
[26] Filippi S, Gola MM, Akay A. Measurement of tangential contact hysteresis during microslip. J Tribol 2004;126:482–9.
[27] Mulvihill DM, Kartal ME, Olver AV, Nowell D, Hills DA. Investigation of non-Coulomb friction behaviour in reciprocating sliding. Wear 2011;271:802–16.
[28] Jin O, Mall S. Effects of independent pad displacement on fretting fatigue behavior of Ti–6Al–4V. Wear 2002;253:585–96.
[29] Meriaux J, Fouvry S, Kubiak KJ, Deyber S. Characterization of crack nucleation in TA6V under fretting–fatigue loading using the potential drop technique. Int J Fatigue 2010;32:1658–68.
[30] Waterhouse RB. Fretting corrosion. 1st ed.. Oxford: Pergamon Press; 1972.
[31] Peng JF, Song C, Shen MX, Zheng JF, Zhou ZR, Zhu MH. An experimental study on bending fretting fatigue characteristics of 316L austenitic stainless steel. Tribol Int 2011;44:1417–26.
[32] Juoksukangas J, Lehtovaara A, Mäntylä A. Development of a complete contact fretting test device. J Eng Tribol 2012;227:570.
[33] Kubota M, Tanaka Y, Kondo Y. The effect of hydrogen gas environment on fretting fatigue strength of materials used for hydrogen utilization machines. Tribol Int 2009;42:1352–9.
[34] Leidich E, Maiwald A, Vidner J. A proposal for a fretting wear criterion for coated systems with complete contact based on accumulated friction energy density. Wear 2013;297:903–10.
[35] Hintikka J, Lehtovaara A, Mäntylä A. Non-Coulomb friction in gross sliding fretting conditions with aluminium bronze against quenched and tempered steel. Tribol Int 2014;79:151–61.
[36] Hintikka J, Lehtovaara A, Lönnqvist C. Effect of start-up schemes and amplitude of tangential motion on friction behavior in fretting point contact. Tribol Int 2011;44:1535–43.
[37] Archard JF. Contact and rubbing of flat surfaces. J Appl Phys 1953;24:981–8.
[38] Rybiak R, Fouvry S, Bonnet B. Fretting wear of stainless steels under variable temperature conditions: introduction of a ‘composite’ wear law. Wear 2010;268:413–23.
[39] Pearson SR, Shipway PH, Abere JO, Hewitt. RAA. The effect of temperature on wear and friction of a high strength steel in fretting. Wear 2013;303:622–31.

Publication V

Normal displacements in non-Coulomb friction condi-tions during fretting

by

J Hintikka, A Lehtovaara and A Mäntylä

Tribology International, 94 (2016), 633-639

doi:10.1016/j.triboint.2015.10.029

Tribology International 94 (2016) 633–639

Contents lists available at ScienceDirect

Tribology International

journal homepage: www.elsevier.com/locate/triboint

Normal displacements in non-Coulomb friction conditions during fretting

Jouko Hintikka [a,*], Arto Lehtovaara [a], Antti Mäntylä [b]

[a] Department of Materials Science, Tampere University of Technology, P.O. Box 589, 33101 Tampere, Finland
[b] Research & Development, Wärtsilä Finland Oy, P.O. Box 244, 65101 Vaasa, Finland

ARTICLE INFO

Article history:
Received 30 June 2015
Received in revised form
16 September 2015
Accepted 23 October 2015
Available online 1 November 2015

Keywords:
Fretting
Friction
Wear

ABSTRACT

Non-Coulomb friction may occur in gross sliding fretting conditions, in which the tangential force increases as the fretting movement approaches its extreme position and produces 'hooked' fretting loops. Uncertainties in frictional behaviour make the design of highly loaded contacts against fretting a challenging task. Experiments were made with quenched and tempered steel, and cyclic normal displacements were discovered during non-Coulomb friction conditions. Normal displacement and non-Coulomb friction were caused by tangential fretting scar interactions between protrusions and depressions formed by material transfer. Tangential interlocking leads to inclined sliding conditions, which produce loading components in both tangential and normal directions; this explains most non-Coulomb friction.

1. Introduction

Fretting occurs when contacting surfaces are under short-amplitude reciprocating sliding motion. The rubbing of surfaces leads to fretting wear, characterized by the occurrence of powdery oxides. Furthermore, fretting efficiently produces small surface cracks and may cause surface degradation such as material transfer and fretting-induced increase in surface roughness. The coefficient of friction (COF) is often near unity and may cause high tangential tractions, which again may enhance the near surface fatigue load and generate fretting fatigue. Furthermore, surface degradation may compromise component fatigue performance under fretting. A more comprehensive description of fretting and contacts is available in [1,2].

Many studies have reported frictional behaviour in fretting, including steels [3–10] and aeronautical alloys [4,5,11,12]. Development of the COF is closely related to fretting wear. During the first tens of load cycles, the COF has a relatively low value, which, however, rapidly increases to greater values due to subsequent load cycles [3–7,9–12]. This has been explained by wear of naturally occurring oxide and contaminant films leading to rubbing action between the bulk materials. At this stage, wear and friction are typically adhesive, and material transfer may occur [3,7,8,10,12–18]. Gradual propagation of fretting wear produces wear debris, which is crushed by the rubbing action and which then oxidizes in the air. For example, in a steel–steel contact this results in fine-textured, reddish-brown wear debris. These particles tend to get entrapped in the interface [19], entrapment being more pronounced with large contacts [8,20]. Accumulation of wear particles leads to a gradual change in the wear mechanism from adhesion to abrasion [13,14]. Often the COF increases directly from the initial low values to steady state values (~0.9) [6]; however, some materials such as quenched and tempered steel pairs produce a 'friction peak' during which the COF may reach a high value (~1.5), last for a few thousands of load cycles, and then gradually drop to typical steady state values of about 0.9 [9,18]. The accumulation of wear debris and development of third body screens effect changes in the wear mechanism and in the development of the COF by changing the velocity accommodation mechanisms [19].

In ideal conditions, the tangential force remains at a constant value during the gross sliding phase, producing a rectangular fretting loop [1]. Many studies, including various materials, have shown non-Coulomb friction in which the tangential force increases during the gross sliding phase within one load cycle and leads to 'hook'-shaped fretting loops [7,15–18,21–26]. They have been suggested to have been caused by fretting-induced wear damage in the interface, which forms tangentially interlocked, variously sized protrusions and depressions. Macroscopic interlocking has been reported to occur with incomplete contacts, where the fretting pad ploughed a trench into the specimen via plastic deformation [11] and/or wear [7,17]. In such conditions, tangential interlocking causes non-Coulomb friction as the pad

* Corresponding author. Tel.: +358 3 311511.
E-mail address: jouko.hintikka@tut.fi (J. Hintikka).

http://dx.doi.org/10.1016/j.triboint.2015.10.029
0301-679X/

makes contact with the end of the trench while the fretting movement approaches its extreme positions. On a micro-scale, interlocking occurs when adhesive fretting wear and material transfer create tangentially interlocked protrusions and depressions within the contact. In these conditions, non-Coulomb friction is caused by tangential interactions between the sides of those protrusions and depressions and has been reported with annular contacts [18,21], sphere on plane contact [15], and cylinder on sheet contact [16]. Mulvihill et al. studied the non-Coulomb phenomenon in detail and showed that a curved fretting loop could be reproduced with an inclined sliding model, which represents tangentially interlocked protrusions and depressions while retaining a constant COF value [21]. Hintikka et al. showed that with a quenched and tempered steel material pair, non-Coulomb behaviour was most pronounced during the first few thousands of load cycles, when wear damage showed severe material transfer. Gradually declining non-Coulomb behaviour occurred simultaneously with a change in the wear mechanism to abrasion due to accumulation of entrapped wear particles [18].

The phenomenon of non-Coulomb friction has been explained by tangentially interlocked protrusions and depressions, because such fretting scar features have been observed in post-test inspection of specimens under a surface profilometer [9,15,17,18,21]. The only measured parameter during the experiments that shows non-Coulomb behaviour is the tangential force or torque. However, there are other possible explanations for non-Coulomb increase in tangential load, such as the Bauschinger effect [27], whereby the material yields easily when the loading direction is changed, followed by work hardening. The tangentially interlocked fretting scar interaction model, such as that presented in [21], suggests that in non-Coulomb friction conditions there should also be cyclic normal displacements or a cyclic normal force because of the sloped edges of protrusions and depressions that result in inclined sliding. In conventional fretting tests with an ideally constant normal load, all cyclic phenomena in the normal direction are typically ignored.

Large proportion of experimental investigations on fretting have been made using Hertzian contacts resulting in a small contact area which has significant sliding, traction and stress gradients. Hertzian contacts are generally convenient in experiments and many analytical equations are readily available for analysis of test results increasing further their usefulness. Although Hertzian contacts cover certain industrial applications, those have limitations for studying fretting in the case of large planar surfaces, which are common in large, heavy-duty, combustion engines and machines. Large flat-on-flat contacts are characterized by modest normal pressure and shallow sliding, traction, and stress gradients. Annular flat-on-flat contact, under axisymmetric loading, produces nearly constant normal and tangential tractions without any edge effects in the direction of surface sliding, and as such it has a good correspondence to industrial scale contacts.

Quenched and tempered steel is commonly used for demanding engineering applications under high fatigue loads, such as diesel engines. The demand to increase engine performance leads to high utilization of the fatigue strength of the materials. Highly loaded contacts pose a fretting risk, which is amplified by the fact that the COF is often high and possibly subject to uncertain phenomena such as non-Coulomb friction, which interferes with proper simulation of such contact interfaces. A better understanding of the friction phenomenon helps to evaluate the fretting risk of engine components. A test rig based on annular flat-on-flat [18] contact was upgraded to measure normal displacements, and a series of tests was performed using quenched and tempered steel specimens in gross sliding fretting conditions. This study focused on normal displacement in non-Coulomb friction conditions.

2. Experimental

2.1. Apparatus design

Fretting apparatus with annular, flat-on-flat contact was used in the experiments (Fig. 1A). The device has been presented in detail [18]; thus only a brief summary is given here. Fretting contact occurred between axisymmetric specimens, one of which was attached to the detachable specimen holder and the other to the fixed specimen holder with a clearance-free conical seat. The detachable specimen holder was bolted to the end of the main shaft, which was subjected to cyclic rotation via the lever arm. The fixed specimen holder was attached to the apparatus frame with a steel plate that allowed fine tuning of the uniformity of the fretting contacts' normal pressure by tightening and loosening the adjustment screws. A normal load was generated with the hydraulic cylinder which deforms the steel plate in z-direction, and the uniformity of the normal pressure was measured with a pressure sensitive film (Fuji prescale). An electric shaker generated the fretting movement, and its control unit used the measured rotation amplitude as a feedback signal.

The x-, y-, and z-displacements and the rotation (θ) between the specimen holders were measured with 4 eddy current probes. The normal force at the contact was calculated as the total normal force (P_{tot}), measured with the s-beam load cell, minus the force required to press the specimens together. The torque (T) was calibrated using dead weights and measured from the detachable specimen holder with strain gauges in a full Wheatstone bridge configuration. An extra z-displacement measurement was added to the apparatus to measure normal displacements during fretting tests by replacing the conventional specimen tightening screws with custom made ones (Fig. 1B). The screw in the fixed specimen holder was drilled hollow, and the inside was partially threaded.

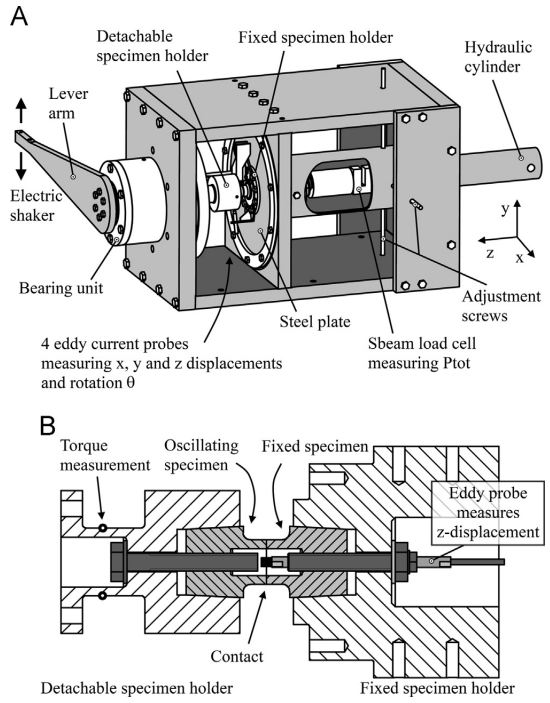

Fig. 1. Fretting apparatus design (A) and normal displacement measurement (B).

An eddy current probe was inserted through the modified screw so that the the sensor head was located inside the specimens. This enabled measurement of the z-displacement close to the contact and from the neutral axis of the apparatus, which minimized the effect of vibration and elastic deformation under fretting loading conditions (Fig. 1B). Cyclic signals were collected at 5 kHz frequency, whereas static signals were collected at a lower 10 Hz frequency. With a loading frequency of 40 Hz, each fretting loop was recorded at 125 measurement points.

2.2. Specimens

The specimen cross section and contact are shown in Fig. 1B. The specimen was tubular near the contact, with inner (r_i) and outer (r_o) radii of 7.5 mm and 12.5 mm, respectively. The length of the tubular section was approximately 10 mm. The specimen was turned into shape, and its contact surface was fine-ground in such a way as to produce circular scratches. The scratching marks were thus collinear with the direction of the fretting movement. The material was a quenched and tempered steel rod, 45 mm in diameter (EN 10083-1-34CrNiMo6+QT). The material and surface roughness data are shown in Table 1. The following abbreviations are used: the yield strength (S_y), the ultimate strength (S_u), Poisson's ratio (ν), the 3D surface roughness calculated as the arithmetic mean of the absolute value of surface departures from the average plane (S_a), the corresponding root mean squared roughness (S_q), and the maximum peak-to-valley height calculated using the averages of five lowest and five largest surface departures (S_z). Specimen surface profiles were measured with a 3D-profilometer (Wyco NT1100), after the specimens had been cleaned in acetone with an ultrasonic washing device.

2.3. Calculations

The rotation at the interface θ_k was calculated as the measured rotation θ minus the shear deformation due to the specimen compliance k (11.6×10^{-6} rad/N m) and torque T as follows:

$$\theta_k = \theta - k \times T \tag{1}$$

Sliding was calculated from this corrected rotation at an average distance (r_a) of 10 mm as follows:

$$u = \theta_k \times r_a \tag{2}$$

The ideal Coulomb COF was calculated using two methods. First, it was calculated from the measured maximum torque and normal pressure distribution $p(r)$ as follows:

$$\mathrm{COF}_T = T_{max} \Big/ \left[2\pi \int_{r_i}^{r_o} r^2 \times p(r) dr\right] \tag{3}$$

Additionally, the COF was calculated from the frictional energy dissipation Ed, normal pressure distribution $p(r)$, and the rotation amplitude θ_a as follows:

$$\mathrm{COF}_{Ed} = \mathrm{Ed} \Big/ \left[8\pi \int_{r_i}^{r_o} r^2 \times \theta_a \times p(r) dr\right] \tag{4}$$

The normal pressure distribution was estimated to be evenly distributed, which led to approximately 0.8% error in both COF_T and COF_{Ed} [18]. Furthermore, Eq. (4) assumes that the transition from stick to gross sliding occurs instantaneously; however a brief period of partial slip exists. The significance of the partial slip was investigated using FEM (Abaqus) and it had less than 1% effect on the calculated COF_{Ed} and no effect at all on the COF_T, with the used normal loads and sliding amplitudes. Hence in ideal Coulomb conditions, both COFs are approximately equal; however in non-Coulomb conditions $\mathrm{COF}_T > \mathrm{COF}_{Ed}$. The difference between the two COFs correlates with the magnitude of the non-Coulomb friction, because the COF_T corresponds to the maximum COF, whereas the COF_{Ed} represents an average COF during a fretting cycle [18].

Table 1
Specimen properties.

S_y [MPa]	S_u [MPa]	E [GPa]	ν [dimensionless]
994	1075	210	0.27
S_a [μm]	S_q [μm]	S_z [μm]	
0.21–0.24	0.27–0.32	2.3–5.3	

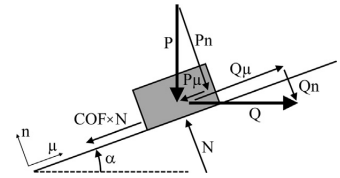

Fig. 2. Inclined sliding model.

Mulvihill et al. [21] proposed a simple inclined sliding model for non-Coulomb friction conditions. In a simple slider on an inclined frictional plane system (Fig. 2), the Q/P-ratio can be solved as a function of the angle of the gradient α and the ideal Coulomb COF for forward sliding with Eq. (5), disregarding any dynamic effects. For reverse sliding, the angle of the gradient and Eq. (5) must be inversed. Under inclined sliding conditions the Q/P-ratio does not represent Coulomb COF.

$$\frac{Q}{P} = \frac{\mathrm{COF} \times \cos(\alpha) + \sin(\alpha)}{\cos(\alpha) - \mathrm{COF} \times \sin(\alpha)} \tag{5}$$

2.4. Measurements

Gross sliding fretting tests were run with three target sliding amplitudes (20 μm, 35 μm, and 50 μm) and at three normal pressures (10 MPa, 35 MPa, and 50 MPa), resulting in a total of 9 test points, which were run at 40-Hz loading frequency for 3×10^6 load cycles. Furthermore, two short duration tests were run with 35-μm sliding amplitude and 30-MPa normal pressure (10×10^3 and 100×10^3 load cycles). The actual sliding amplitude depends on specimen compliance, which varies as a function of friction torque (Eqs. (1) and (2)) [18]. Because this compliance was estimated before the tests, the target values corresponded closely with the realized ones. The specimens were attached to the apparatus, their parallelism was corrected, and the target surface normal pressure was applied. The sliding amplitude was then increased linearly from zero to the target level in the first 10 s (400 load cycles). The parallelism of the contacting surfaces was periodically corrected by minimizing the x- and y-displacements. Measurements were run in ambient laboratory atmosphere at 24–28 °C and at a relative humidity of 8–24%.

3. Results

3.1. Fretting scars

Since fretting scars and frictional behaviour have been analysed more comprehensively before [18], only observations essential to the non-Coulomb phenomenon are summarized here. Short duration tests revealed that severe adhesive wear and material transfer occurred during the early stages of the experiments (Fig. 3). Material transfer caused detachment of material to form depressions and deposition to form protrusions. The profile of these depressions and protrusions retain a high degree of conformity, because the fretting

movement was of limited magnitude and had zero net tangential displacement. The protrusions and depressions may collide under fretting movement, and the interaction is characterized by the angle of the gradient α. Fig. 3B–D illustrate angles of the gradient ranging between 3° and 18° and variation in the shape and size of individual protrusions and depressions. Adhesive wear changed gradually to abrasion, because entrapped wear particles accumulated in the interface [19].

3.2. Friction coefficient

Fig. 4A shows an example of the development of COFs during the fretting test. The difference between the COFs ($\Delta COF = COF_T - COF_{Ed}$) was pronounced during the first 10^5 load cycles. The development of θ–T-fretting loops, illustrated in Fig. 4B–D, show that the greater the ΔCOF, the more pronounced was the non-Coulomb shape of the fretting loops. Therefore, the ΔCOF was used to indicate the severity of the non-Coulomb friction conditions. The duration of this non-Coulomb phase depended mostly on the accumulated sliding distance, though nearly ideal Coulomb conditions prevailed after about 10^5 load cycles with the 50-μm sliding amplitude.

3.3. Normal displacements

The absolute value of measured z-displacement was affected by thermal effects such as heat expansion, hence the u–z-fretting loops shown here were 'zeroed' so that the cyclic oscillation occurs around origin. An example of measured normal displacement (z) as a function of relative surface sliding is shown in Fig. 5, which corresponds to the measurement in Fig. 4. Fig. 5B–D shows that the specimens experienced normal displacement strongly dependent on the phase of the fretting movement. When the movement approached its extreme positions, normal displacement increased, and when the sliding direction changed, normal displacement diminished only to increase again when sliding approached its opposite extreme position and formed 'u-shaped' u–z-fretting loops. The magnitude of the normal displacements (Δz) depended strongly on the ΔCOF and the existence of non-Coulomb friction conditions. These z-displacements were caused by the fretting process itself, and there was no external source providing any excitation in the z-direction.

Fig. 6 illustrates the relation between the ΔCOF and Δz. In Fig. 6A, the two are normalized with their maximum values for convenience (ΔCOF^* and Δz^*) and plotted as a function of load cycles, showing clearly a close correlation. Initially, Δz and the ΔCOF increased, peaked, and then gradually decreased nearly simultaneously. Fig. 6B–D shows the ΔCOF as a function of Δz for 20–μm, 35–μm, and 50–μm sliding amplitudes, respectively at all normal pressures. Each data point in these graphs corresponds to a different number of load cycles. The colour indicates the normal

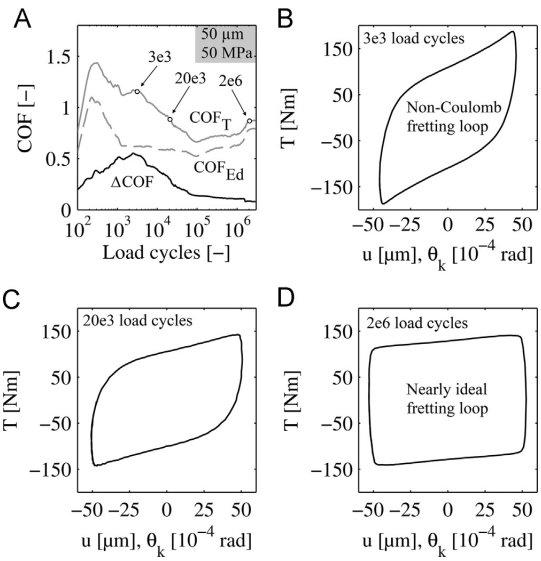

Fig. 4. Evolution of COFs and θ–T-fretting loops.

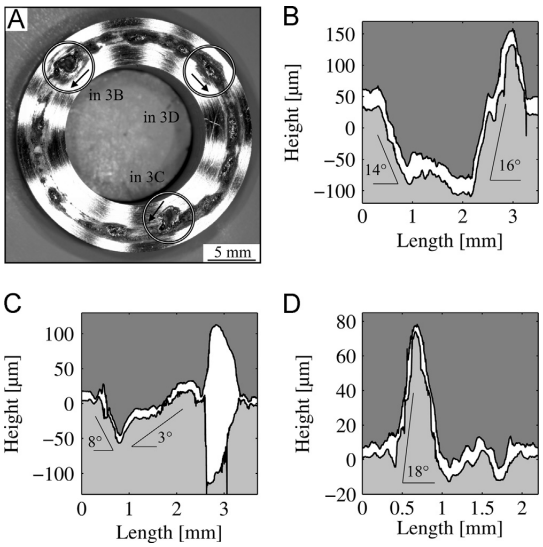

Fig. 3. Tangentially interlocked protrusions and depressions due to material transfer after 10^4 fretting load cycles (35 μm and 30 MPa).

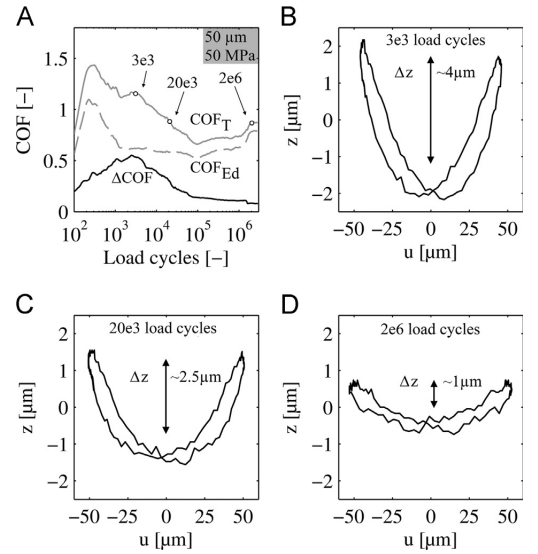

Fig. 5. Evolution of COFs and u–z-fretting loops.

pressure, and the line composition indicates whether the data was before or after the end of the 400-cycle start-up phase. During start-up, the ΔCOF increased steeply from zero (dash dot lines), whereas Δz built up with a slight delay. The initial developments of the ΔCOF and Δz may be related to the formation of adhesive friction spots and their failure under shear, which produced the tangentially interlocked protrusions and depressions via material transfer. After start-up, Δz and the ΔCOF first increased, peaked, and then dropped gradually back to zero, showing linear dependence unaffected by normal pressure. In all the experiments, the maximum value of the ΔCOF remained in a range of 0.4–0.6. However, the higher the sliding amplitude, the higher was the maximum of Δz.

Measured normal displacements were most pronounced during highly non-Coulomb friction conditions. A gradual change towards nearly ideal Coulomb friction conditions occurred simultaneously with diminishing normal displacements. Therefore, these phenomena clearly correlate, and it is reasonable to assume that they are caused by the same underlying mechanism.

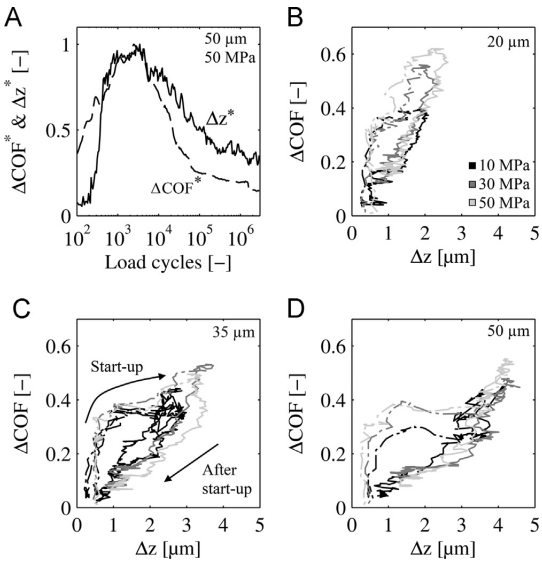

Fig. 6. Development of ΔCOF vs Δz.

3.4. Asperity interaction scheme

It has been suggested that non-Coulomb friction originates from tangential fretting scar interactions. Tangential interaction occurs when the sides of an interlocked protrusion depression collide as fretting sliding approaches its extreme position during forward and reverse movement. Fretting scar topographies have shown that the sides of protrusions and depressions have varying angles of gradient (α). When such protrusion vs. depression interaction occurs, the angle of the gradient introduces inclined sliding and generates both tangential and normal components of force and displacement, as shown in Fig. 7.

The design of our fretting apparatus allows small normal displacements to occur without noticeable difference in the normal force. The location of the eddy current probes measuring the relative displacements and rotation between the contacting bodies corresponds roughly to the reference points RP1 and RP2. The displacement data in the z-direction was used to estimate the normal movement between the specimen surfaces. The angles of the gradient α, which correspond to individual protrusion vs depression interactions during the fretting test, were unknown, though they could be measured by post-test profilometry. The measured normal displacement (z) and surface sliding (u) data enabled approximation of a kind of effective angle of the gradient α_{eff} (Fig. 7C).This was achieved by fitting a 2-degree polynomial function to the u–z-data, and the angle of the gradient α_{eff} was then calculated from the derivate of the fitted function.

Fig. 8A shows an example of a u–z-fretting loop with best-fit 2-degree polynomial fit. We observed that α_{eff} increased when the fretting movement approached its extreme position. The maximum angle at the end of the movement corresponds to the COF_T according to the Eq. (5). An example of the development of the calculated max α_{eff} as a function of load cycles is shown in Fig. 8B. The max α_{eff} was largest during the most severe non-Coulomb conditions in the early parts of the experiment (~2000 load cycles) and then gradually diminished when the non-Coulomb friction conditions subsided. Fig. 8C shows max α_{eff} vs. ΔCOF plots at all normal pressures and sliding amplitudes, whereas each data point corresponds to a different number of load cycles. This illustrates a strong linear correlation between the development of max α_{eff} and ΔCOF, and that it was nearly independent of normal pressure and sliding amplitude. Interestingly, the measured α_{eff}, which occurred during severe non-Coulomb conditions, is of about the same order of magnitude than the angles observed in post-test profilometry (Fig. 3).

Eq. (5) was used to calculate the $COF_{T\alpha}$ with the measured α_{eff} and COF_{Ed} used as input values. According to the fretting scar asperity interaction scheme, the $COF_{T\alpha}$ corresponds to the COF_T.

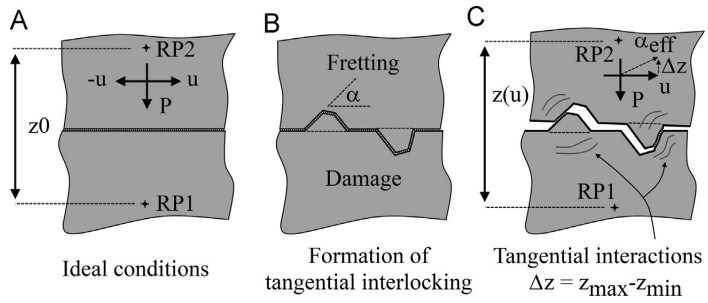

Fig. 7. Normal displacement in non-Coulomb friction.

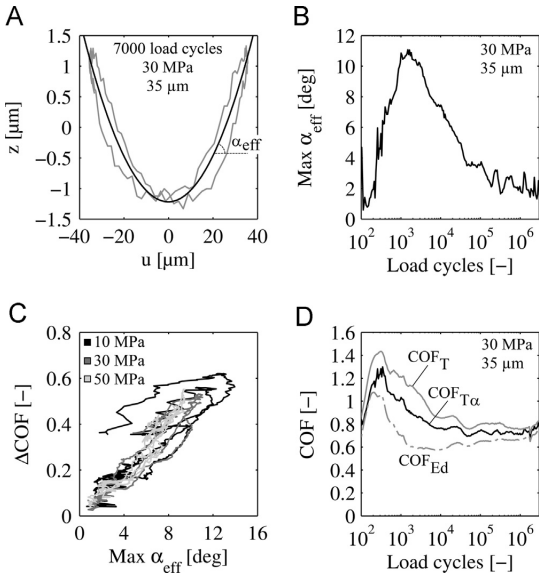

Fig. 8. Effective tangential interaction angle α and $COF_{T\alpha}$.

An example of the development of the $COF_{T\alpha}$ as a function of load cycles is shown in Fig. 8D. The calculated $COF_{T\alpha}$ developed values close to the measured COF_T, though the latter showed consistently somewhat greater values. This indicates that a significant proportion of the non-Coulomb friction phenomenon can be explained by the protrusion vs depressions tangential interaction scheme and with the simple inclined sliding model.

Δz was shown to increase when the sliding amplitude was increased, while the normal pressure had no effect on it (Fig. 6). Such behaviour is consistent with the asperity interaction scheme, because any increase in tangential movement amplitude leads to increased normal displacements due to inclined sliding. Furthermore, the COF_T (or ΔCOF) was reported mostly independent of normal pressure and sliding amplitude, which is also consistent with the asperity interaction scheme, because the Q/P-ratio depends only on the values of α and COF (Eq. 5). Most changes in the values of the COF_T are explained by variations in the max α_{eff}, which was illustrated in Fig. 8C.

4. Discussion

The results showed that fretting scar tangential interactions cause both non-Coulomb friction and normal displacements. In the non-Coulomb friction condition, the net effect of all individual protrusion vs. depression tangential interactions was measured. The forces and displacements related to individual interactions remain unknown. Profilometric observations showed that the shapes and sizes and interaction angles (α) of protrusions and depressions varied. The angle of the gradient related to tangential interactions introduced a non-linear effect on the tangential force, whereby steep angles probably had a larger impact than shallow ones. Furthermore, elastic/plastic deformations occurring close to individual protrusion vs. depression interactions were included in the measured displacements. The measured α_{eff} represents a kind of average angle at best and explains partly why the COF_T has slightly greater values than the $COF_{T\alpha}$.

Ideal inclined sliding can occur only if the angle of the gradient is sufficiently low, which can be determined from Eq. (5) ($\alpha_{lim}=a\tan(1/COF)$). It follows that with a maximum measured COF_{Ed} of about 1.1, this α_{lim} is about 43°, a limit that was not exceeded. However, it follows that if such large gradient angles should exist, relative surface sliding would grind to a halt. In such conditions, fretting movement must be accommodated by some other mechanism, such as elastic/plastic deformations or failure of the tangentially interlocked protrusion vs depression pair.

Because Δz and the ΔCOF diminished as a function of load cycles, the results depend also on the gradual wearing down of the initial material transfer spots and on the accumulation of entrapped wear particles in the interface. For example, wearing down of interlocked protrusions and depressions may introduce clearances, which accommodate surface sliding without any tangential interaction. Furthermore, wear debris in the interface accommodates displacements and provides load carrying capacity. Some of these effects are included in the measured values of α_{eff} and COF_{ED}, though it is uncertain whether their effect has properly been taken into account in the inclined sliding model. Obviously, there are phenomena related to the non-Coulomb phenomenon that warrants further study.

The tangential fretting scar interaction model implies that the COF_{Ed} is the true coefficient of friction to describe friction between contacting materials. Geometric interlocking pushes the tangential force to levels higher than predicted by ideal Coulomb conditions, and it is not purely friction. The COF_T is a kind of 'pseudo' COF yet a useful parameter, because it represents measured tangential loads assuming flat surfaces, and such assumptions are regularly made in analysis of contact conditions. It is not obvious which one of the COFs should be used in the analysis of contact conditions if non-Coulomb friction occurs. The usage of average COF or COF_{Ed} might lead to significant underestimation of tangential tractions and contact stresses, which may be detrimental if there is a risk of fretting fatigue. On the other hand the COF_T may be unrealistically large in certain cases.

The extent of normal displacements depends on the design of the apparatus and on its stiffness in the normal direction. Our test rig allowed a few micrometre normal displacements to occur with insignificant increase in the normal force. In apparatus stiff in the normal direction, tangential interactions should cause observable changes in the normal force with little normal displacements. In such conditions, the non-Coulomb effect may be even stronger. Because the interactions between protrusions and depression were capable of producing the non-Coulomb effect, these locations were under much higher loads than those produced in ideal conditions. Local hot spots due to tangential fretting scar interactions may accelerate fatigue crack initiation, though this is a topic for further study.

5. Conclusions

Our fretting test rig was upgraded to be able to measure normal displacement between specimens. Fretting tests were run with quenched and tempered steel under gross sliding conditions. Friction and normal displacements were measured with different sliding amplitudes and normal pressures. The following conclusions were drawn:

- Non-Coulomb friction was measured where the maximum friction coefficient was much larger than the average friction coefficient. This resulted in a hook-shaped fretting loop.
- The specimens were experiencing cyclic normal displacements simultaneously with non-Coulomb friction conditions. When the fretting movement approached its extreme positions, normal displacement increased and produced a 'u-shaped' curve during a fretting cycle.

- Initial adhesive wear and material transfer formed tangentially interlocked protrusions and depressions.
- The effective angle of gradient, related to inclined sliding due to protrusion vs. depression interactions, was evaluated from sliding and normal displacement data. The magnitude of the non-Coulomb effect depended on this angle.
- Friction conditions gradually changed to nearly ideal Coulomb friction as a function of load cycles, followed by simultaneously diminishing normal displacements. The wear mechanism also changed from adhesive to abrasive due to a gradual accumulation of entrapped wear debris, which also wore down any protrusions and depressions.

Acknowledgements

This study was conducted as part of the ScarFace research project. We are grateful for the financial support provided by Tekes (Finnish Funding Agency for Innovation, Decision number 40205/12), Wärtsilä Finland Oy, Nome Oy, and Global Boiler Works Oy.

References

[1] Nowell D Hills DA. Mechanics of fretting fatigue. Dordrecht: Kluwer Academic Publishers; 1994.
[2] Johnson KL. Contact mechanics. Cambridge: Cambridge University Press; 1985.
[3] Chaudhry V, Kailas SV. Fretting studies on self-mated stainless steel and chromium carbide coated surfaces under controlled environment conditions. Wear 2013;301:524–39.
[4] Hirsch MR, Neu RW. A simple model for friction evolution infretting. Wear 2013;301:517–23.
[5] Kubiak KJ, Liskiewicz TW, Mathia TG. Surface morphology in engineering applications: Influence of roughness on sliding and wear in dry fretting. Tribol Int 2011;44:1427–32.
[6] Ramesh R, Gnanamoorthy R. Effect of hardness on fretting wear behaviour of structural steel, En 24, against bearing steel, En 31. Mater Des 2007;28:1447–52.
[7] Rybiak R, Fouvry S, Bonnet B. Fretting wear of stainless steels under variable temperature conditions: introduction of a 'composite' wear law. Wear 2010;268:413–23.
[8] Warmuth AR, Pearson SR, Shipway PH, Sun W. The effect of contact geometry on fretting wear rates and mechanisms for a high strengthsteel. Wear 2013;301:491–500.
[9] Hintikka J, Lehtovaara A, Lönnqvist C. Effect of start-up schemes and amplitude of tangential motion on friction behavior in fretting point contact. Tribol Int 2011;44:1535–43.
[10] Leidich E, Maiwald A, Vidner J. A proposal for a fretting wear criterion for coated systems with complete contact based on accumulated friction energy density. Wear 2013;297:903–10.
[11] Fouvry S, Duó P, Perruchaut P. A quantitative approach of Ti–6Al–4V fretting damage: friction, wear and crack nucleation. Wear 2004;257:916–29.
[12] Mubarak Ali M, Raman S Ganesh Sundara, Pathak SD, Gnanamoorthy R. Influence of plasma nitriding on fretting wear behaviour of Ti–6Al–4V. Tribol Int 2010;43:152–60.
[13] Freimanis AJ, Segall AE, Conway JC, Whitney EJ. Elevated temperature evaluation of fretting and metal transfer between coated titanium components. Tribol Trans 2000;43:653–8.
[14] de Baets P, Strijckmans K. Thin layer activation for measuring fretting wear and material transfer in iron alloys. Tribol Int 1996;29:307–12.
[15] Hintikka J, Lehtovaara A, Mäntylä A. Non-Coulomb friction in gross sliding fretting conditions with aluminium bronze against quenched and tempered steel. Tribol Int 2014;79:151–61.
[16] Hirsch MR, Neu RW. Fretting damage in thin sheets: analysis of an experimental configuration. Tribol Int 2011;44:1503–10.
[17] Lavella M, Botto D. Fretting wear characterization by point contact of nickel superalloy interfaces. Wear 2011;271:1543–51.
[18] Hintikka J, Lehtovaara A, Mäntylä A. Fretting-induced friction and wear in large flat-on-flat contact with quenched and tempered steel. Tribol Int 2015;92:191–202.
[19] Berthier Y, Vincent L, Godet M. Velocity accommodation in fretting. Wear 1988;125:25–38.
[20] Merhej R, Fouvry S. Contact size effect on fretting wear behaviour: application to an AISI 52100/AISI 52100 interface. Lubr Sci 2009;21:83–102.
[21] Mulvihill DM, Kartal ME, Olver AV, Nowell D, Hills DA. Investigation of non-Coulomb friction behaviour in reciprocating sliding. Wear 2011;271:802–16.
[22] Jin O, Mall S. Effects of slip on fretting behavior: experiments and analyses. Wear 2004;256:671–84.
[23] Jin O, Mall S, Sanders JH, Sharma SK. Durability of Cu–Al coating on Ti–6Al–4V substrate under fretting fatigue. Surf Coat Technol 2006;201:1704–10.
[24] Degat PR, Zhou ZR, Vincent L. Fretting cracking behaviour on pre-stressed aluminium alloy specimens. Tribol Int 1997;30:215–23.
[25] Kartal M, Mulvihill D, Nowell D, Hills D. Determination of the frictional properties of titanium and nickel alloys using the digital image correlation method. Exp Mech 2011;51:359–71.
[26] Zhou ZR, Gu SR, Vincent L. An investigation of the fretting wear of two aluminium alloys. Tribol Int 1997;30:1–7.
[27] Hosford William F. Mechanical behavior of materials. New York: Cambridge University Press; 2005.

Publication VI

Third particle ejection effects on wear with quenched and tempered steel fretting contact

by

J Hintikka, A Lehtovaara and A Mäntylä

Tribology Transactions, Accepted author version

DOI:10.1080/10402004.2016.1146813

Third particle ejection effects on wear with quenched and tempered steel fretting contact

Jouko Hintikka [a,*], Arto Lehtovaara [a], Antti Mäntylä [b]
* Corresponding author: Phone: +358 3 311511, Email: jouko.hintikka@tut.fi
[a] Department of Materials Science, Tampere University of Technology
PO Box 589, 33101 Tampere, Finland
[b] Research & Development, Wärtsilä Finland Oy,
PO Box 244, 65101 Vaasa, Finland

ABSTRACT

The design and life prediction of fretting wear sensitive mechanical components remains a challenge. In the present work the role of wear particle movements under conditions of axisymmetric loading of an annular, flat-on-flat contact were investigated using self-mated quenched and tempered steel specimens. Total fretting wear significantly increased when loose wear particles were periodically removed from the interface, and this effect increased as a function of the sliding amplitude. Additionally, increased wear was measured when grooves perpendicular to the sliding direction were added to the interface. Increasing the rate of wear debris ejection leads to increased wear rate because naturally occurring, entrapped third body particles significantly reduce the wear. The shape of fretting loops and values of the average and the maximum coefficient of friction remained unaffected by the removal of entrapped wear debris and by the introduction of the grooves.

Keywords: fretting; unlubricated wear; unlubricated friction; wear debris; third body

INTRODUCTION

Fretting stands for reciprocating surface sliding and wear damage associated with it. Fretting wear and especially fretting fatigue are considered a severe damage mechanism. Fretting damage can accumulate out of sight inside an interface and potentially lead to an unexpected and catastrophic component failure. On steel surfaces, fretting can be detected by the appearance of reddish-brown oxidised wear debris of powdery texture, though such observation requires opening the contact. Design against fretting is made difficult by the fact that there are major uncertainties in the friction and wear behaviour of contacts under a fretting load. (Waterhouse (1) and Hills et al (2))

The motion between contacting first bodies is accommodated via various mechanisms in the interface (i.e., shear and rolling) and further velocity accommodation is enabled by loose and sticking wear debris beds (Berthier et al (3), Berthier (4) and Godet (5,6)). Velocity accommodation via oxide wear particle layers is especially important in fretting conditions because sliding amplitudes are low, and because wear particles tend to get entrapped in the interface (Berthier et al (7)). In such conditions, wear is dictated by the rate of the ejection rather than generation of wear particles. Velocity accommodation in third particles has been studied further in powder lubrication (Iordanoff et al (8), Heshmat (9) and Haff (10)). Because powders have lubricating properties, they can be used to control wear and friction. They provide lift under sliding conditions and retain a load carrying capacity even in static conditions, which may be crucial in fretting.

The role of entrapped wear debris on fretting wear using a flat-on-flat steel contact has been studied, including “open and shut” tests, in which the interface was periodically opened and cleaned of wear debris and in which artificial oxide particles were added in the contact (Colombié et al (11)). They showed that naturally occurring and artificially added beds of oxide particles reduce wear in the first bodies, because the powdery third body has a load carrying capacity that separates the first bodies and accommodated velocity. Fretting wear studies with different radii spheres against flat (Merhej et al (12)) and cylinder against flat (Warmuth et al (13)) have showed that the wear rate reduced when the contact size was increased. These fretting wear observations were explained by the wear reducing properties of the entrapped wear particles, which are more pronounced with larger contacts. Fretting experiments with quenched and tempered steel with large axisymmetrically loaded, annular, flat-on-flat contacts showed wear depending mostly on the sliding amplitude while a normal force had only a slight effect (Hintikka et al (14)). This was also explained by the entrapment of wear particles in the interface, which was assumed especially pronounced due to the large annular contact without any contact edges in the direction of the fretting movement. Furthermore, because pores in the interface affect the accumulation of wear…

Nomenclature

Symbol	*Explanation*
At-%	Percentage of atoms
COF	Coefficient of friction
COF_{Ed}	Average COF
COF_T	Maximum COF
E	Modulus of elasticity
Ed	Frictional energy dissipation
k	Specimen compliance
N_{Cle}	Number of contact cleanings
$p(r,j)$	Normal pressure distribution
p_n	Nominal normal pressure
P	Normal force at specimen
P_{tot}	Total normal force
r	Radius
r_a	Average radius (10 mm)
r_i	Inner radius (7.5 mm)
r_o	Outer radius (12.5 mm)
S_a	3D average surface roughness
S_u	Ultimate stress
S_y	Yield stress (0.2 %)
S_q	3D root mean squared roughness
S_z	3D max peak to valley distance
W_{Cle}	Mass loss due to contact cleaning
W_{LC}	Mass loss due to load cycles
W_{tot}	Total mass loss
T	Torque
u	Sliding
u_a	Sliding amplitude
x,y,z	Coordinate system
j	Angle around specimen
q	Rotation
q_a	Rotation amplitude
q_k	Corrected rotation
n	Poisson's ratio

Abbr.	
Cle	Contact cleaning tests
EDS	Energy dispersive X-ray spectroscopy
Gro_6	Tests with grooved specimens
Gro_{12}	(6 and 12 grooves)
SEM	Scanning electron microscope
Sta	Tests with standard specimens

…particles in it (Varenberg et al (15)), surface topography such as surface roughness contributes to the entrapment of these particles.

The propagation of wear damage may not be linear as a function of the loading parameters, and transitions may occur in wear rate (Blau (16)). Calculating the wear rate from pre- and post-test measurements may be misleading if the running-in or wear-in effects are pronounced. Changes in wear rate occur also in fretting wear, where wear may initially be adhesive and then gradually change to abrasive due to entrapped wear particles (Colombié et al (11) and Hintikka et al (14)).
The rate of fretting wear has been shown to depend on loose wear particles entrapped in the contact; therefore, modifying the conditions of entrapped wear particles may entail changes in the resulting wear. This study focused with two approaches on the role of loose wear particles and their ejection in the wear of a fretted steel vs. steel contact in gross sliding conditions. In the first test series, loose wear debris was periodically removed from the interface and its effect on the wear was measured including multiple sliding amplitudes and two normal loads. In the second test series, the effect of specimen geometry on the resulting wear was studied.

EXPERIMENTAL

Apparatus design

A fretting apparatus based on an axisymmetrically loaded, annular, flat-on-flat, contact was used (Fig. 1A); described in detail elsewhere (Hintikka et al (14)). The contact occurred between two "tubular" specimens, one attached to a detachable specimen holder and the other to a fixed specimen holder with a conical clearance free fixture. The detachable specimen holder was attached to the end of the main shaft and the fixed specimen holder to the apparatus' frame with a steel plate. Contact was created by driving the fixed specimen holder and the steel plate in the *z*-direction with a hydraulic cylinder. The uniformity of the normal pressure was confirmed using a pressure sensitive film (Fuji prescale), and any error was corrected before the fretting test was started by adjusting the parallelism of the specimens (adjustments screws). Fretting movement was achieved by reciprocating rotational movement of the detachable specimen holder via the lever arm moved by an electric shaker. Measurements were run under controlled rotation amplitude using measured rotation as a feedback signal.

The *x*-, *y*-, *z*-displacements and rotation q between the two specimen holders were measured with 4 eddy current probes. Under ideal conditions, *x*- and *y*-displacements do not exist; however, changes in the interface will eventually result in uneven traction distribution causing such extra displacements. The total normal force P_{tot} was measured from the end of the piston rod with an s-beam load cell. The normal force at the specimens P was calculated as the total normal force minus the force required deforming the steel plate and the adjustment screws in the *z*-direction, which was separately calibrated. The frictional torque T was measured with strain gauges from the detachable specimen holder. Cyclic and static signals were measured at 5 kHz and 10 Hz frequencies, respectively.

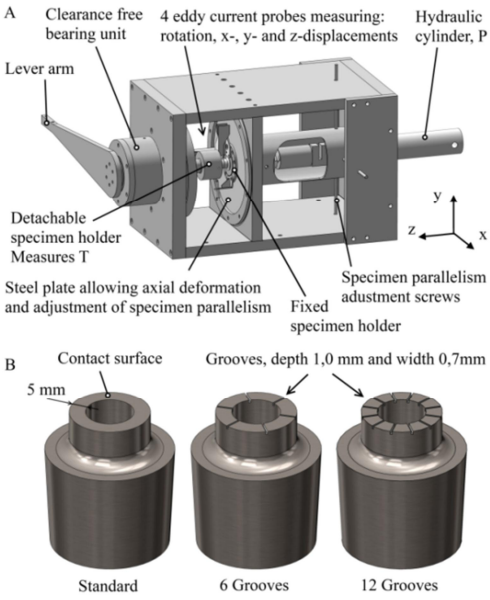

Figure 1 – Test rig and specimen design

Measured signals were recorded covering the entire experiment duration. One second long samples (40 cycles) were collected from the full duration data at exponentially increasing time intervals. The first five subsequent fretting load cycles were identified from each data sample, from which an average fretting loop was calculated. In the case of static signals, such as the normal load, the average value was calculated from the whole sample duration. The calculated average values were used in the further analysis.

Calculations

The rotation at the interface was calculated as the measured rotation q minus the shear deformation due to specimen compliance k (11.6×10^{-6} rad/Nm) under the frictional torque T as follows:

$$q_k = q - k \cdot T \tag{1}$$

The surface sliding was estimated using an average distance r_a of 10 mm as follows:

$$u = q_k \cdot r_a \tag{2}$$

Assuming that the COF is uniformly distributed, it can be calculated from the measured torque and the normal pressure distribution $p(r,\varphi)$ as follows:

$$COF_T = T / \left[\int_0^{2\pi} \int_{r_i}^{r_o} p(r,\varphi)\, dr\, d\varphi \right] \tag{3}$$

Each fretting cycle produces frictional work Ed due to frictional rubbing of surfaces. The COF was also calculated from the measured frictional energy dissipation Ed, the normal pressure distribution $p(r,\varphi)$ and the rotation amplitude q_a as follows:

$$COF_{Ed} = \frac{Ed}{4 \cdot q_a} / \left[\int_0^{2\pi} \int_{r_i}^{r_o} p(r,\varphi)\, dr\, d\varphi \right] \tag{4}$$

COF_{Ed} represents the average COF during one load cycle. In this study, COF_T was calculated using the amplitude of measured T, hence COF_T represent the maximum COF during one load cycle. In ideal conditions COF_{Ed} is equal to COF_T; however, under no called non-Coulomb friction conditions COF_T is greater than COF_{Ed} (Mulvihill et al (17), and Hintikka et al (14, 18, 19)).

Specimens

The specimens were made of a quenched and tempered steel rod (EN 10083-1-34CrNiMo6+QT, D 45 mm; design shown in Fig. 1B). Three kinds of specimens were used: standard annular specimens and ones with the contacting surface modified with 6 and 12 grooves. The specimens were turned to shape, and the annular contact surface was fine-ground so that the grinding scratches were circular. The grooves were made before the final fine-grinding of the contact surface. The material and surface roughness data is compiled in Table 1. Specimens were cleaned in an ultrasonic cleaning device with acetone before and after the fretting tests.

Table 1 – Specimen properties

S_y [MPa]	S_u [MPa]	E [GPa]	n
994	1075	210	0.27
S_a [µm]	S_q [µm]	S_z [µm]	
0.17–0.36	0.22–0.74	1.8–10.7	

In tests with grooved specimens the nominal contact area was reduced by about 7 % and 13 % in the case of 6 and 12 grooves, respectively; hence the increase in the nominal surface pressure was quite low. Additionally, the contact between grooved and standard specimens introduced a local pressure concentration due to edge effects, leading to a further local increase in the surface normal pressure. The contact pressure distribution was estimated with the finite element method (Abaqus) using an approximately 100-µm element size. In ideal conditions, the local maximum pressure is infinite at the edge of the groove; however, it drops steeply close to nominal values. The impact of the actual, non-uniform surface pressure distribution on the calculated COF was estimated to deviate only about 1% compared to the contact of standard specimens (Eqs. 3 and 4). The FEM

model did not accurately reproduce the peak surface pressure; however, its effect on the COF was negligible because the peak pressure was confined to a very small area. Hence all tests were analysed using a constant normal pressure approximation.

Furthermore, increased wearing may occur at the location of the normal pressure peaks. This leads to gradual change in the specimen geometry resulting in curved contact surfaces and change towards constant normal pressure conditions. Analytical solution for the geometry of a rigid punch against an elastic half-plane, producing constant normal pressure (Hills et al (2)), was compared to the sharp edged punch geometry. Using grooved specimen dimensions, the volume difference corresponded to wear masses of 0.7 mg and 0.3 mg for specimen with 6 and 12 grooves respectively. Hence, the wearing down of normal pressure peaks, near groove edges, cannot have a major impact on the resulting wear.

Measurements

The experiment procedure was as follows. First, specimens were attached to the apparatus, specimen parallelism was confirmed, and the desired surface normal pressure was applied. Then the sliding amplitude was increased linearly within 400 load cycles from zero to the target level. The loading frequency was 40 Hz. The parallelism of the contacting surfaces was periodically adjusted by minimizing *x*- and *y*-displacements. Experiments were run in standard, monitored laboratory atmosphere (temperature 24˚C - 30˚C and humidity 7 % - 44 %).

A series of fretting tests were run by rubbing two standard specimens against each other for $3.0 \cdot 10^6$ load cycles at 10 MPa, 30 MPa, and 50 MPa nominal normal pressures and 5, 20, 35, 50, and 65-µm sliding amplitudes (reported in detail elsewhere by Hintikka et al (14)). A total of 19 tests were done, including reruns with identical test parameters, and these tests are named here as tests with standard specimens (Sta). Two new test series were performed: contact cleaning tests (Cle) and tests with grooved contact geometry (Gro). The wear results of the new test series were compared with those of the Sta tests.

In the contact cleaning tests (Cle), the contact was opened and cleaned after each $216 \cdot 10^3$ load cycles (90 min at 40 Hz) without removing the specimens from the apparatus. The test duration was $3.0 \cdot 10^6$ load cycles hence a total of 14 contact cleanings was done in each test. Contact cleaning was done as follows: first, the experiment was started as described above, and the contact was fretted for $216 \cdot 10^3$ load cycles. The contact was then opened by removing the normal force, and the interface was blasted with pressurized air, and the contact surfaces were rubbed with paper tissue soaked in acetone. This procedure removed a large proportion of loose wear debris from the interface. The design of the apparatus (no clearances) allowed opening and closing of the contact so that movement occurred only in the *z*-direction without disturbing the relative orientation (*x, y*) of the contacting surfaces. Experiments were made with a normal pressure of 10 MPa and 30 MPa and with various sliding amplitudes (7 tests).

In the Gro_6 and Gro_{12} tests, one standard specimen was fretted against one grooved specimen and the index refers to the number of grooves (Fig. 1B). Adding grooves to the interface may increase the probability of wear particle ejection because of the edges introduced perpendicular to the direction of the fretting movement. The grooves provide space for wear particles to accumulate, and their open ends allow the particles to trickle out. The test duration was $3.0 \cdot 10^6$ load cycles. Experiments were made with a normal force of 9425 N, corresponding to 30 MPa of normal pressure with standard specimens, and with various sliding amplitudes (6 tests). The normal force was chosen the same as that used in the Sta tests because Archard wear formalism predicts that the wear volume loss depends on the normal force rather than the surface pressure (Archard (20)). The test matrix is summarized in Table 2, where each row includes multiple experiments with different sliding amplitudes. Each test point was a separate measurement and was done using new specimens.

Table 2 – Test matrix

Series	P[N]	p_n [MPa]	u_a [µm]
Sta	3142	10	5, 20, 35, 50, 65
Sta	9425	30	5, 20, 35, 50, 65
Sta	15708	50	20, 35, 50
Cle	3142	10	20, 35, 50
Cle	9425	30	5, 20, 35, 50
Gro_6	9425	32.1	20, 35, 50
Gro_{12}	9425	34.6	20, 35, 50

Specimens were weighed prior and after tests with precision scales (Precisa EP 420A). Each specimen was warmed to 105˚C removing adhered moisture. Weighing was done three times with a reference weight and the average value was calculated. At each test point, mass loss was calculated as the sum of the mass losses of both specimens. The wear debris was analysed using X-ray diffractometer (Panalytical Empyrean), and the fretting scars were investigated using scanning electron microscope (SEM, Philips XL-30) and an energy dispersive X-ray spectroscopy (EDS,

EDAX DX 4). Surface profiles were measured with a white light vertical scanning interferometer (Wyco NT1100). The surface roughness values of fretted surfaces were measured from three different locations from each specimen. For each test point the average values were calculated covering both involved specimens. The dimensions of profiled areas were 3.8 mm × 4.6 mm, representing a total of 17 % of the combined contact area.

RESULTS

Friction coefficient

Fig. 2 shows fretting loops from all test series, which were extracted at 216×10^3 load cycles corresponding to the first contact cleaning in the Cle tests. Fig. 2A shows the last fretting loop before the experiment was halted for the first contact cleaning with a solid black line. After the contact cleaning, the fretting loop gradually develops as the rotation amplitude approaches its target value during the mid-experiment start-up phase (dashed grey lines), and then stabilizes to nearly identical shape what existed prior contact cleaning (dashed black line). Fig. 2B, 2C and 2D compares fretting loops from Cle, Gro_6 and Gro_{12} test series against the Sta tests, illustrating that the fretting loop shapes were nearly identical.

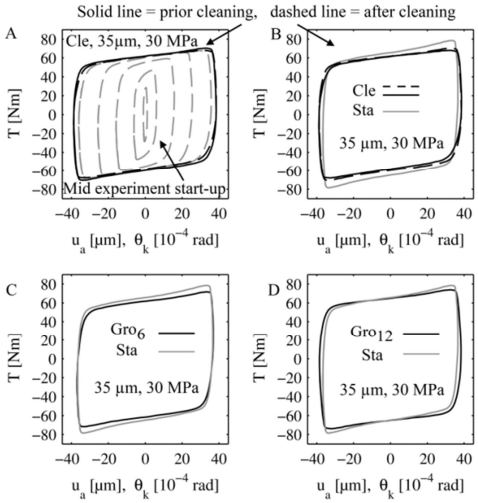

Figure 2 – Fretting loops after 216×10^3 load cycles

The overall frictional behaviour, including values of COFs and shapes of fretting loops, related to the Sta tests was described in detail elsewhere (Hintikka et al (14)). In standard tests, the COF_T was observed as initially high, in the range of 1.2 to 1.5, followed by a sharp drop to steady state values in the range of 0.6 to 0.8. The COF_{Ed} showed similar behaviour, though its maximum value was in the range of 0.9 to 1.1 and dropped to 0.6 - 0.7 in steady state conditions. Additionally, the initial high COF conditions were characterized by non-Coulomb friction conditions, where the COF value depended on the specimens' rotational position during a fretting cycle (Fig. 2). In non-Coulomb conditions, $COF_T > COF_{Ed}$, as can be seen in the COF graphs in Fig. 3.

Fig. 3A compares friction results between Sta and Cle tests. After the first start-up, frictional behaviour was nearly identical between the two, which is obvious because the test conditions were identical. Subsequent start-ups after each cleaning produced no extra peaking in the COF, its value remaining mostly unaffected by contact cleaning, which stabilized at about its steady state value. However, there were small abrupt changes in the COFs due to the cleaning, which is illustrated in greater detail in Fig. 3B showing the first six contact cleanings. It may be that after each mid-experiment cleaning enough loose wear debris and hard to-remove third body screens remained in the interface to maintain steady state friction conditions. The mid-experiment start-up phases were excluded from this graph. Similarly the Gro tests produced a COF nearly identical to that observed in the Sta tests which is illustrated in Fig. 3C.

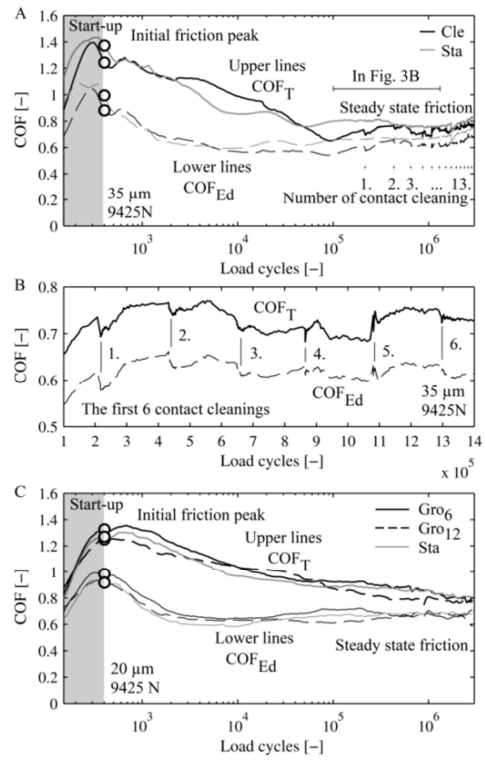

Figure 3 – COF in Cle tests (A&B) and Gro_6 and Gro_{12} tests (C)

It follows from the friction results that any difference in the entrapped third body particles, between the three test series, caused no marked differences in the fretting loop shapes or in the values of COF_T or COF_{Ed}. Therefore, any differences in the wear results, which are shown next, cannot be explained by changes in frictional behaviour because it remained unchanged.

Fretting wear

The mass losses of Cle tests are compared against Sta test in Fig. 4. First, Sta tests produced wear mass loss mostly dependent on the accumulated sliding distance or sliding amplitude, whereas the normal load had only a low impact on it. Compared to the Sta tests, Cle tests produced three to four times greater mass losses at 3142 N and 9425 N normal loads (Fig. 4A). In them, mass loss depended mostly on the accumulated sliding distance, and normal load had only a minimal effect.

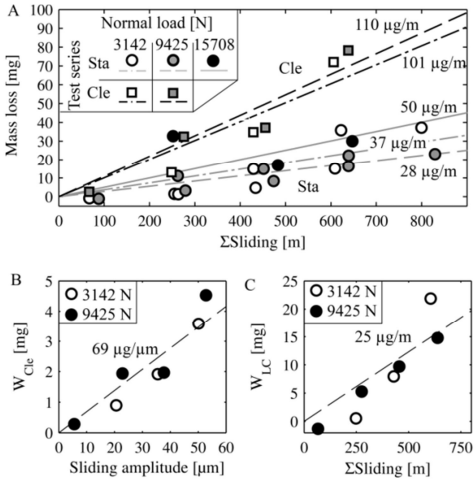

Figure 4 - Mass loss due to fretting wear in Cle tests

Each test point in the Cle tests was subjected to a total of 13 cleanings during the test and once after the test, whereas in Sta tests they were cleaned once after the test. It follows that the number of contact cleanings (N_{Cle}) was 1 and 14 for Sta and Cle test series, respectively. The contribution of each cleaning on the wear mass was approximated by assuming that the total wear mass (W_{tot}) is the combination of gradual wear due to load cycles and sliding amplitude (W_{LC}) and the sum of the masses due to cleaning (W_{Cle}), as shown in Eq. 5.

$$W_{tot} = W_{LC} + N_{Cle} \cdot W_{Cle} \quad (5)$$

The calculated values for W_{LC} and W_{Cle} are shown in Fig. 4B and 4C. The wear due to load cycles (W_{LC}) and each contact cleaning (W_{Cle}) were approximately linearly dependent on the sliding amplitude and accumulated sliding distance, respectively, and those were independent of the normal load. Hence the wear enhancing effect of cleanings increased as a function of the sliding amplitude.

In annular flat-on-flat contact, wear particles may be ejected naturally only from the inner and outer edges of the contact. This however requires that the wear particles migrates perpendicular to the fretting direction. The grooved specimens introduced additional edges, from which the wear particles may be ejected after migrating parallel to the fretting. Wear results from Gro_6 and Gro_{12} tests are compiled in Fig. 5, showing that using grooved specimens increases wear significantly. Wear increased approximately linearly as a function of the accumulated sliding distance. Furthermore, wearing was greater with 12 grooves than with 6 grooves. The wear increasing effect of the grooves is clearly illustrated in Fig. 5B, showing the measured wear rates from Sta, Gro_6 and Gro_{12} tests. The wear rate was calculated as mass loss divided by the accumulated sliding distance. The observed increase in the wear cannot be explained by the local pressure peaks near to the groove edges, because rounding of the interface may explain only about 1 mg mass loss, which is insignificant in comparison to the measured wear mass losses. Furthermore, the grooves changed the nominal contact area and nominal contact pressure only by a small amount (~10%).

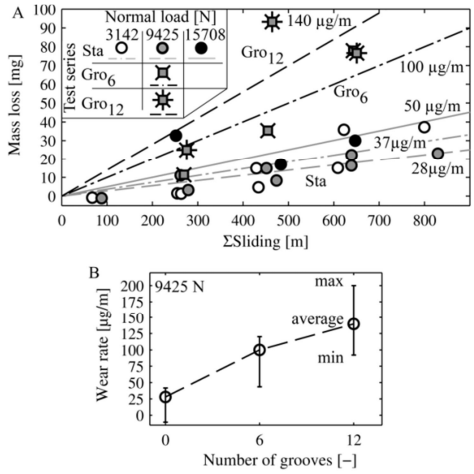

Figure 5 - Mass loss due to fretting wear in Gro_6 and Gro_{12} tests

The ejected wear debris was analysed using x-ray diffractometer covering the Gro tests and some of the Sta tests. Wear debris was composed of hematite (α-Fe_2O_3) and trace amounts of iron

(steel particles). This result is typical for fretted steel contacts (Waterhouse (1)).

Fretting scars

A compilation of SEM micrographs and EDS results, including samples from all test series, is shown in Fig.6. The elemental composition of the fretting scar surface was mostly iron with small amount of alloying elements corresponding to quenched and tempered steel, with varying amounts of oxygen. Therefore, only the percentage of oxygen atoms (*At-%*) is shown, indicating the level of oxidation.

The specimen surfaces were covered with a layer of oxide wear particles as shown in Fig. 6A. The oxygen content was approximately 40 *At-%* indicating a high level of oxidation. It may be that the oxide layer is composed of agglomerated hematite, or other iron oxides, and steel particles. Basically, this kind of oxide layer was found in all tests, and represents a typical fretted surface in this study.

Fig. 6B shows an example of the wear track on a standard specimen which was fretted with a grooved specimen. It was observed that section of surface, related to the location of the groove edge, was mostly clean of oxides (8 *At-%*); however regions further away from the groove edge were covered in oxides, comparable to other test series (43 *At-%*). Interestingly the width of the clean area is approximately twice the sliding amplitude (100 µm). This demonstrates that oxides are removed efficiently at the edge perpendicular to the fretting direction. Fig. 6C shows an example of cracking in the specimen surface and spot from which metal particle had detached. Detachment of metallic particles due to surface fatigue is one source of fresh wear particles. Mostly metallic, compacted wear debris was observed as shown in Fig. 6D and 6F. Such layers were composed of, approximately 1 µm sized, mostly metallic steel particles which had agglomerated, indicating that fresh wear particles were generated at this site. Metallic wear debris agglomerates were found from most specimens, typically in a form of few spots which sizes varied from few to few tens of square millimetres. It is likely that these kinds of metal agglomerates gradually changed to highly oxidized layers.

In a previous study adhesive wear resulting in material transfer was reported to occur during the first few thousands of load cycles (Hintikka et al (14,19)). An example of material transfer layer is shown in Fig. 6E. The initial material transfer lead to tangential fretting scar interlocking and it had a profound effect on the COF (Hintikka et al (19)). There was no evidence of further material transfer after the first few thousands of load cycles; however the initial adhesive wear followed by gradual wearing down of metallic transfer layers is part of the fretting wear phenomenon.

Examples of the measured surface profiles from Gro_6 and Gro_{12} tests are shown in Fig. 7. Some surface profiles showed gentle curvature near grooves which may have been caused by the initial normal pressure distribution which is illustrated in Fig. 7A (Gro_6, 35 µm, 9425 N). However the wear track profile is characterized by protrusions and depressions introducing extra normal pressure peaks. The wear tracks illustrated frequently wearing which clearly did not follow the shape of a constant normal pressure distribution as illustrated in Fig. 7B (Gro_{12}, 50 µm and 9425 N). Though some rounding of the groove edges occurred, it did not have significant contribution to the overall wear and it did not occur systematically. The specimens did not wear under the grooves, resulting in strips of nearly intact surfaces. Theoretical wear depths (dashed lines), calculated using the measured weight loss, specimen nominal contact area and steel density, shows close match to measured wear depth. This also verifies that the mass losses were measured with good accuracy.

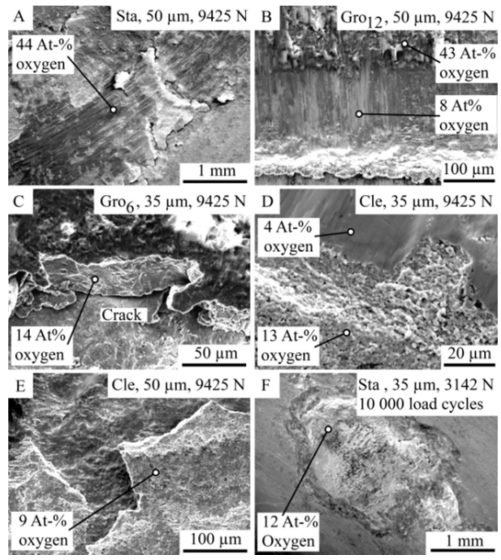

Figure 6 – Fretting scar micrographs (SEM and EDS)

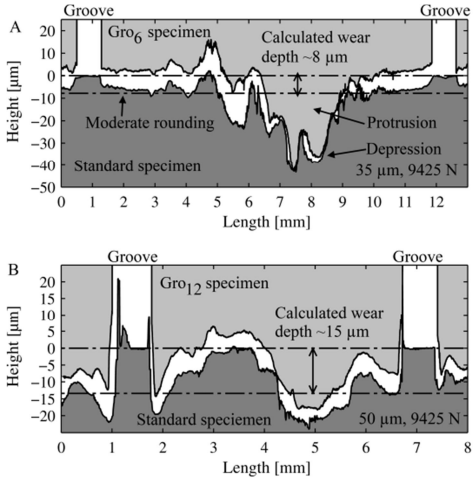

Figure 7 - Wear scar profiles in Gro_6 and Gro_{12} tests

Fretting increased the specimen surface roughness and the resulting S_a was dependent on the test series, normal load and sliding amplitude as shown in Fig. 8A. Typically the S_a increased as a function of sliding amplitude and normal load in all test series. Additionally, S_a was lower in Sta tests than in Gro or Cle tests, which can be attributed partly to lower wear mass loss in the Sta tests.

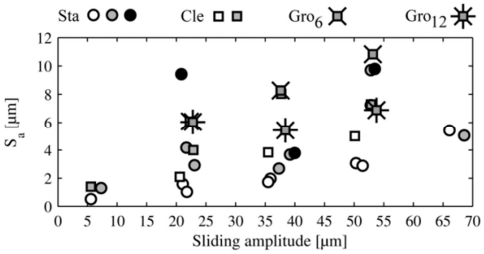

Figure 8 – Surface roughness after fretting tests

DISCUSSION

Experiments showed that oxide wear particles (hematite) were entrapped and ejected from the interface. Additionally, the specimens were covered in hard to remove iron oxide and metallic particle agglomerates. The wear results of this study are conveniently explained by the velocity accommodation in the third bodies, which is known to be pronounced in fretting conditions. The idea being that the first bodies are separated by third body screens and third body bulk in the middle. The fretting movement between first bodies is accommodated, at least partly in the third bodies providing protection against wear.

The Cle tests illustrated that removal of entrapped wear debris lead to significant increase in wear, and that the effect increased linearly as a function of sliding amplitude, while normal load had unobservable effect on it. In the scheme of velocity accommodation, the cleaning removed much of the third body bulk, resulting temporary increase in wear rate. The thickness of the third body bulk would then increase due to the entrapment of wear particles and wear rate would gradually recover back to lower values. Although this explains the increased wear in comparison to the Sta test, it does not explain why the wear increasing effect was depended on the sliding amplitude. A possible explanation would be that the amount of entrapped wear debris, which was removed in each cleaning, increased as a function of sliding amplitude. In such conditions Fig. 4B may also represent the amount of entrapped wear debris which was removed in each leaning. Such behaviour may be explained by the velocity accommodation scheme, assuming that the greater the sliding amplitude the thicker the third body bulk needs to be, before a certain level of wear reduction is achieved.

The same mechanism may be also used to explain the wear results from the Gro tests. The reciprocating shearing of wear particles in the interface provided some velocity accommodation. This shearing occurred in the fretting direction, though there may be some randomness in the movement of individual wear particles due to interactions between other wear particles and the specimens' surfaces. This enables migration of wear particles which is suspected to occur mostly in the fretting direction; however it may occur in any direction. A wear particle may only be ejected when it is at a free edge. It follows that ejection of wear particles occurs more frequently at the edges perpendicular to fretting direction. Additionally, it was observed that area next to the groove edge was relatively clean from oxides. The width of this 'clean' area was approximately twice as large as the sliding amplitude, which may imply that the edge of the groove scraped off entrapped adhering third bodies, potentially increasing the ejection rate. Overall, the introduction of grooves increased wear particle ejection rate, reducing the thickness of the third body bulk and the wear protection it offers, leading to an overall increase in wear. Because all test series showed approximately linear dependency between mass loss and sliding amplitude it is suspected that the flowing of wear particles towards parallel and perpendicular edges was mostly dependent on the sliding amplitude. In cylinder against flat contact configuration wear rate reduced when the contact width was increased, while the contact length remained at a constant value, suggesting that the contact size itself plays a role (Warmuth et al (13)). In this study the grooves were equally spaced thus increasing the number of grooves reduced the

distance between grooves. The average distance which a wear particle needs to migrate before encountering a contact edge is dependent on this distance, suggesting that the contact size effect on fretting wear is dependent on the distance between contact edges in the fretting direction.

The wear mass loss was mostly independent of the normal load in both the Sta and Cle tests contradicting classic Archard theory (Archard (20)). In steady state velocity accommodation conditions the wear depends on the wear particle ejection. Increasing the rate of contact cleanings and or the number of grooves might bring about the expected normal load dependency. Additionally, direct observations of the thickness of the third body bulk, under fretting conditions, might shed more light on the velocity accommodation mechanics. Such experimental investigation is left for future study.

CONCLUSIONS

Gross sliding fretting wear tests were run with annular, flat-on-flat contact, using quenched and tempered steel specimens. The effect of loose wear particles on wear rate was studied by running tests in which loose wear particles were periodically removed from the interface; in addition, tests were run with grooved contact surfaces. The following conclusions were drawn:

1. The fretting loop shapes and values of the average and the maximum coefficient of friction remained unaffected by the contact cleaning and by the use of grooved specimen geometry.

2. Loose wear particles in the interface protect against wear. Removing them from the interface increased wear rate significantly. This effect increased approximately linearly as a function of the sliding amplitude. Normal load had no marked effect on wear in the test conditions.

3. Specimen geometry had a strong effect on wear rate because grooves perpendicular to the sliding motion increased wear rate. The wear promoting effect of the grooves increased when the number of grooves was increased.

ACNOWLEDGEMENTS

This study was conducted as part of the SCarFace research project. We are grateful for the financial support provided by Tekes (Finnish Funding Agency for Technology and Innovation, decision number 40205/12), Wärtsilä Finland Oy, Nome Oy, and Global Boiler Works Oy. The authors give their thanks to MSc. Ville Oksanen for providing SEM images and EDS data and MSc. Leo Hyvärinen for the X-ray diffractometry measurements.

REFERENCES

(1) Waterhouse R.B. (1972),"Fretting corrosion," Pergamon press, Oxford, ISBN 0 08 16902 3

(2) Hills D.A Nowell D (1994), "Mechanics of fretting fatigue," Kluwer Academic Publishers, Dordrecht, ISBN 0-7923-2866-3.

(3) Berthier, Y., Godet, M., Brendle, M. (1989), "Velocity accommodation in friction." *Tribology Trasactions*, 32, pp 490.

(4) Berthier, Y. (1990), "Experimental evidence for friction and wear modelling," *Wear*, **139**, pp 77-92.

(5) Godet, M. (1984), "The third-body approach: A mechanical view of wear," *Wear*, **100**, pp 437-452.

(6) Godet, M. (1990), "Third-bodies in tribology," *Wear*, **136**, pp 29-45.

(7) Berthier, Y., Vincent, L., Godet, M. (1988), "Velocity accommodation in fretting," *Wear*, **125**, pp 25-38.

(8) Iordanoff, I., Berthier, Y., Descartes, S., Heshmat, H. (2002), "A Review of Recent Approaches for Modeling Solid Third Bodies," *Journal of Tribology*, **124**, pp 725-735.

(9) Heshmat, H. (1991), "The Rheology and Hydrodynamics of Dry Powder Lubrication," *Tribology Transactions*, **34**, pp 433-439.

(10) Haff, P.K. (1983), "Grain flow as a fluid-mechanical phenomenon," *Journal of Fluid Mechanics*, **134**, pp 401-430.

(11) Colombié, C., Berthier, Y., Floquet, A., Vincent, L., Godet, M. (1984), "Fretting: Load Carrying Capacity of Wear Debris," *Journal of Tribology*, **106**, pp 194-201.

(12) Merhej, R., Fouvry, S. (2009), "Contact size effect on fretting wear behaviour: application to an AISI 52100/AISI 52100 interface," *Lubrication Science*, **21**, pp 83-102.

(13) Warmuth, A.R., Pearson, S.R., Shipway, P.H., Sun, W. (2013), "The effect of contact geometry on fretting wear rates and mechanisms for a high strength steel," *Wear*, **301**, pp 491-500.

(14) Hintikka, J., Lehtovaara, A., Mäntylä, A. (2014), "Fretting-induced friction and wear in large flat-on-flat contact with quenched and tempered steel," *Tribology International*, **92**, pp. 191–202.

(15) Varenberg, M., Halperin, G., Etsion, I. (2002), "Different aspects of the role of wear debris in fretting wear," *Wear*, **252**, pp 902-910.

(16) Blau, P.J. (2015), "How common is the steady-state? The implications of wear transitions for materials selection and design," *Wear*, **332-333**, pp. 1120-1128.

(17) Mulvihill, D.M., Kartal, M.E., Olver, A.V., Nowell, D., Hills, D.A. (2011), "Investigation of non-Coulomb friction behaviour in reciprocating sliding," *Wear*, **271**, pp 802-816.

(18) Hintikka, J., Lehtovaara, A., Mäntylä, A. (2014), "Non-Coulomb friction in gross sliding fretting conditions with aluminium bronze against quenched and tempered steel," *Tribology International*, **79**, pp 151-161.

(19) Hintikka, J., Lehtovaara, A., Mäntylä, A. (2016), "Normal displacements in non-Coulomb friction conditions during fretting," *Tribology International*, **94**, pp. 633–639.

(20) Archard, J.F. (1953), "Contact and Rubbing of Flat Surfaces," *Journal of Applied Physics*, **24**, pp 981-988.

Tampereen teknillinen yliopisto
PL 527
33101 Tampere

Tampere University of Technology
P.O.B. 527
FI-33101 Tampere, Finland

ISBN 978-952-15-3766-0
ISSN 1459-2045